Mesoscopic materials studied with advanced X-ray scattering methods

Dissertation

zur Erlangung des Doktorgrades
an der Fakultät für Mathematik, Informatik und
Naturwissenschaften
Fachbereich Physik
der Universität Hamburg

vorgelegt von

NASTASIA MUKHARAMOVA

Hamburg
2020

Gutachter/in der Dissertation:	Prof. Dr. Ivan A. Vartaniants Prof. Dr. Christian G. Schroer
Gutachter/in der Disputation:	Prof. Dr. Ivan A. Vartaniants Prof. Dr. Christian G. Schroer Prof. Dr. Edgar Weckert Prof. Dr. Andreas Stierle Prof. Dr. Daniela Pfannkuche
Vorsitzender des Prüfungskommission:	Prof. Dr. Daniela Pfannkuche
Datum der Disputation:	18 September 2020
Vorsitzender Fach-Promotionsausschusses PHYSIK:	Prof. Dr. Wolfgang Hansen
Leiter des Fachbereichs PHYSIK:	Prof. Dr. Michael Potthoff
Dekan der Fakultät MIN:	Prof. Dr. Heinrich Graener

Zusammenfassung

Mesoskopische Materialien bilden die Brücke zwischen der Quantenwelt der atomarer Systeme und der klassischen Welt der makroskopischen Systeme. Die charakteristische Längenskala solcher Strukturen liegt im Bereich von 100 nm bis 1 µm, was mit Wellenlängen des sichtbaren Lichts vergleichbar ist. Diese Nähe führt häufig zu ungewöhnlichen optischen und elektrischen Eigenschaften, die in den makroskopischen Systemen nicht beobachtet werden. Die Möglichkeit, solche einzigartigen Materialien in der Elektronik, Photonik und Nanotechnologie einzusetzen, motiviert das wachsende wissenschaftliche Interesse an der mesoskopischen Physik.

Die physikalischen, mechanischen und chemischen Eigenschaften der mesoskopischen Materialien sind das Resultat ihrer Nanostruktur. In-situ Untersuchungen der Struktur und Dynamik mesoskaliger Systeme sind ein herausforderndes experimentelles Problem. Aufgrund der kurzen Wellenlänge und der hohen Eindringtiefe ist Röntgenstrahlung ein hervorragendes Werkzeug für strukturelle Untersuchungen mesoskopischer Objekte. Die neue Generation von Röntgenquellen wie Synchrotrons oder Freie-Elektronen-Laser bietet eine Vielzahl leistungsstarker Methoden wie Röntgennanodiffraktion Kleinwinkel-Röntgenstreuung unter streifendem Einfall, Winkel-Röntgen-Kreuzkorrelationsanalyse und zeitaufgelöste Röntgendiffraktion. Die vorliegende Arbeit konzentriert sich auf die Anwendung dieser Methoden auf mesoskopische Systeme und umfasst drei separate Projekte.

Im ersten Projekt werden mithilfe der Röntgen-Nanodiffraktion Domänen und Domänengrenzen in mesokristallinen Übergittern von PbS-Nanokristallen untersucht. Diese Methode wurde durch eine neuartige Winkel-Röntgenkreuzkorrelationsanalyse ergänzt, die benutzt wurde, um die Orientierungsordnung innerhalb der Domänen und in der Nähe der Domänengrenzen aufzuklären. Das zweite Projekt nutzt in-situ-Röntgendiffraktion unter streifendem Einfall zur Untersuchung der strukturellen Entwicklung kolloidaler Polystyrolkristalle unter trockenen Sinterbedingungen. Eine detaillierte Analyse der Bragg-Peaks des kolloidalen Kristalls ermöglichte es, die Transformation der kolloidalen Partikelform während des Erhitzens der Probe aufzudecken. Diese beiden Experimente wurden am Messplatz P10 des PETRA III Speicherringes durchgefhrt.

Für das dritte Projekt wurde ein pump-probe -Experiment an einem Röntgen-Freie-Elektronen-Laser zur Untersuchung der durch den Infrarotlaser angeregten Dynamik in kolloidalen Kristallen durchgeführt. Kolloidale Kristalle wurden mit Hilfe eines Infrarotlaser mit variabler Leistung angeregt und die nachfolgende Dynamik mit einer Zeitauflösung von Pikosekunden gemessen. Abhängig von der Intensität des Pumplasers wurden zwei Regime der Laser-Materie-Wechselwirkung erreicht. Für eine niedrige Pumplaserintensitt wurden die im kolloidalen Kristall angeregten Schwingungsmoden unter Verwendung der Lamb-Theorie analysiert. Höhere Pumplaserintensitäten führten

zur Erzeugung eines einzigartigen periodischen Plasmas in der Probe. Die experimentellen Daten konnten mit Hilfe einer kombinierten Simulation

Abstract

Mesoscopic materials form the bridge between the quantum world of atomic systems and the classical world of macroscopic systems. The characteristic length scale of such structures is in the range of hundreds of nanometers which is comparable to visible light wavelengths. This proximity often leads to unusual optical and conducting properties that are not observed in the macroscopic systems. The possibility of using such unique materials in electronics, photonics, and nanotechnology motivates the growing scientific interest to mesoscopic physics.

The physical, mechanical and chemical properties of the mesoscopic materials originate in their nanostructure. *In-situ* probing of the structure and dynamics of mesoscale systems is a challenging experimental problem. Due to short wavelength and high penetration depth X-rays offer a great opportunity for structural studies of mesoscopic objects. New generation of X-ray sources such as synchrotrons or free-electron lasers offers a variety of powerful tools such as X-ray nanodiffraction, grazing-incidence small-angle X-ray scattering, angular X-ray cross-correlation analysis and time-resolved X-ray diffraction. The present Thesis is focused on applying these methods to mesoscopic systems and includes three separate projects.

In the first project, X-ray nanodiffraction is used to study domains and domain boundaries in mesocrystalline superlattices of PbS nanocrystals. This method was complemented with novel angular X-ray cross-correlation analysis which unraveled the orientational order inside the domains and near the domain boundaries. The second project focuses on the structural evolution of the polystyrene colloidal crystals under dry sintering conditions studied using *in-situ* grazing incidence X-ray scattering. The detailed analysis of the Bragg peaks from the colloidal crystal allowed to reveal the colloidal particle shape transformation during heating of the sample. These two experiments were performed at P10 beamline at PETRA III synchrotron radiation source.

The third project is devoted to the studies of the infrared laser-induced dynamics in the colloidal crystal using a pump-probe setup at an X-ray free-electron laser. Colloidal crystals were pumped with infrared laser of varying power and the subsequent dynamics was measured with picosecond time resolution. Depending on the pump laser intensity two regimes of laser-matter interaction were accessed. For low pump laser intensity, the vibrational modes excited in the colloidal crystal were analyzed using Lamb theory. Higher pump laser intensities resulted in the generation of a unique periodic plasma in the sample. Combined simulation of the femtosecond plasma dynamics and a hydrodynamic shock wave were performed to explain the experimental data.

Hiermit erklre ich an Eides statt, dass ich die vorliegende Dissertationsschrift selbst verfasst und keine anderen als die angegebenen Quellen und Hilfsmittel benutzt habe.

I hereby declare, on oath, that I have written the present dissertation by my own and have not used other than the acknowledged resources and aids.

Hamburg
Unterschrift (Signature)

Contents

1 Introduction **4**

2 Modern sources of coherent X-ray radiation **7**

2.1 Synchrotron sources 9

2.2 Free-electron lasers 13

3 Advanced X-ray scattering techniques **17**

3.1 X-ray interaction with a material 18

3.1.1 X-ray absorption 18

3.1.2 X-ray scattering at a single electron 19

3.2 X-ray scattering at an atom 23

3.3 Scattering from a crystal in kinematical approximation 24

3.4 Grazing Incidence Small Angle X-ray Scattering 28

3.5 Angular X-ray Cross-Correlation Analysis 32

4 Structure and properties of mesoscopic materials **37**

4.1 Crystalline structures and defects 38

4.1.1 Crystallographic defects 39

4.2 Colloidal crystals 42

4.3 Mesocrystals 45

5 Revealing grain boundaries and defect formation in nanocrystal superlattices by nanodiffraction **49**

5.1 Experiment 50

5.2 Definition of crystalline domains and their orientation 51

5.3 Determination of the nanocrystal orientation in the superlattice 54

5.4 Nanocrystal orientational disorder 58

5.5 Structural configurations and facet-induced interactions 59

5.6 Compression of the superlattice near domain boundaries 61

5.7 Rotation of the superlattice near domain boundaries 63

5.8 Conclusions 66

6 Unravelling structural rearrangement of polymer colloidal crystals under dry sintering conditions 67
6.1 Experiment . . . 68
6.2 GTSAXS analysis and simulations . . . 70
6.3 Temperature evolution of GTSAXS peak parameters . . . 71
6.4 Conclusions . . . 77

7 Probing dynamics in colloidal crystals with pump-probe experiments at LCLS 79
7.1 Pump-probe experiments on solid samples . . . 80
7.2 Experiment . . . 82
7.2.1 Experimental setup . . . 82
7.2.2 Infrared laser calibration . . . 83
7.2.3 Data analysis . . . 84
7.3 Experimental results . . . 86
7.4 Model simulations . . . 89
7.5 Discussion . . . 92
7.6 Conclusions . . . 92

8 Femtosecond laser produced periodic plasma in a colloidal crystal probed by XFEL radiation 94
8.1 Physics of femtosecond pulse laser-matter interaction . . . 95
8.1.1 Strong field ionisation . . . 95
8.1.2 Heating of electrons during the laser pulse propagation . . . 102
8.1.3 Skin effect . . . 103
8.1.4 Two-temperature model . . . 106
8.1.5 Ablation and shock wave propagation . . . 107
8.2 Experiment . . . 110
8.2.1 Experimental results . . . 110
8.3 Ionization of the colloidal crystal . . . 112
8.3.1 PIConGPU simulation details . . . 114
8.3.2 PIConGPU simulation results . . . 114
8.3.3 PIConGPU simulations coupled to HELIOS simulations . . . 118
8.4 Ablation and shock wave propagation inside the colloidal crystal . . . 119
8.5 Discussion . . . 125
8.6 Conclusions . . . 126

9 Summary 128

Appendix A PIConGPU simulations 166

Appendix B HELIOS simulations 169

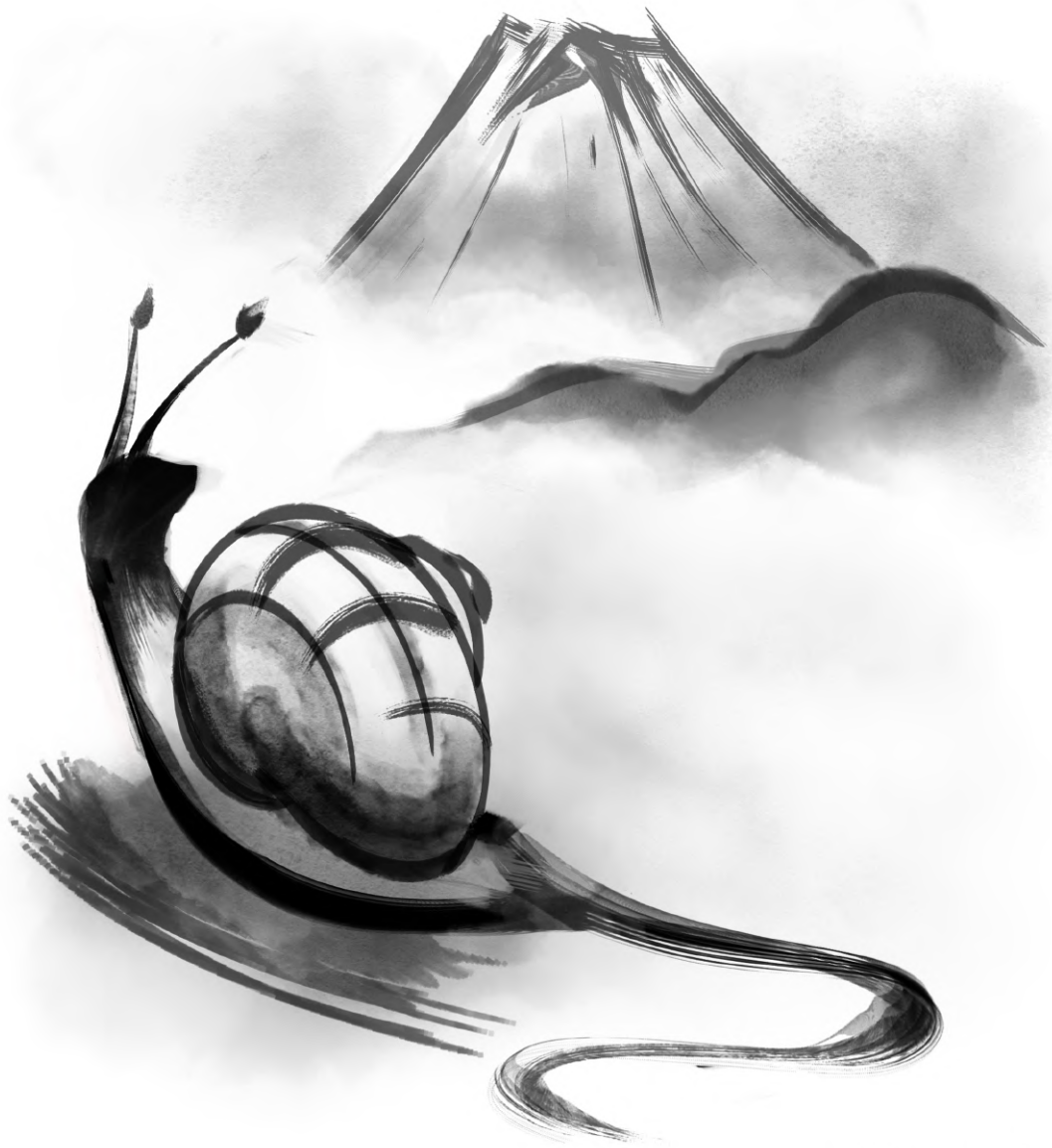

Little snail
inch by inch, climb
Mount Fuji!

Kobayashi Issa

Chapter 1

Introduction

Mesoscopic physics is a subdiscipline of condensed matter physics that deals with materials with a size ranging from tens of nanometers up to micrometers. The physical properties of such systems often differ from those of large-scale bulk materials, which stimulated recent extensive studies [1]. Due to their unique optical properties, these novel materials are particularly promising for various applications, including field-effect transistors, light-emitting diodes, photodiodes, and photovoltaic cells and could have serious implications for modern photonics [2, 3]. The material nanostructure plays a critical role in these functionalities and therefore is of great interest for design and applications of these novel systems. Structural investigations of mesoscopic materials are often performed using imaging techniques of visible light microscopy, but the resolution of these techniques is generally limited by the wave nature of light. Higher spatial resolution can be achieved in electron microscopy by using shorter De-Broglie wavelength of electrons. However, due to the small penetration depth of electrons, the sample thickness is limited to below 100 nm.

In this sense, experimental methods using X-ray scattering offer great possibilities for the *in-situ* research of mesoscopic materials. These methods allow to obtain high-resolution images and follow dynamics of a bulk structure without destroying the sample. Examples of these experimental techniques are X-ray diffraction, Small-angle X-ray scattering [4] or more sophisticated imaging techniques such as coherent diffractive imaging [5–7], ptychography [8, 9] and X-ray photon correlation spectroscopy [10]. In this thesis we used Grazing-Incidence Transmission Small Angle X-ray Scattering (GTSAXS) [11] and the Angular X-ray Cross-Correlation Analysis (AXCCA) [12, 13] to study colloidal crystals and mesocrystals. These techniques can be applied to solid or liquid samples, and are particularly useful for monitoring phase transitions or local orientational order of the sample [14–16].

These experimental techniques profoundly advanced with recent development of the bright sources of X-ray radiation such as the third generation synchrotrons and free electron lasers (FELs). The examples of third and fourth generation sources include PE-

TRA III [17] in Germany, MAX IV [18] in Sweden, ESRF [19] in France, Spring8 [20] in Japan, or APS [21] in the USA. Synchrotron based techniques are widely used in nearly every branch of science such as biology, chemistry, physics, nanotechnology, geology, and medicine. X-ray free electron lasers (FELs) such as FLASH [22] and XFEL [23] in Germany, LCLS [24] in the USA, and SACLA [25] in Japan are the new kind of X-ray radiation sources. They provide coherent femtosecond pulses of enormous brightness, which enable groundbreaking experiments revealing fundamental processes in materials and technology. These experiments demonstrated three-dimensional imaging of a virus (single particle imaging [26, 27]), investigation of excited states a molecule [28], or measuring ultrafast phase transitions [29, 30].

With the rapid development of laser sources producing ultrashort infrared pulses with intensity up to 10^{20} W/cm^2 [31], studies of matter under extreme conditions enter further unexplored regimes. The fundamental property of such high-power lasers is the creation of plasma at extreme temperature and pressure, which causes a shock compression of the material. The shock wave speed is in the range of several kilometers per second, therefore, a method providing picosecond resolution is required for the *in-situ* measurements of the shock-induced dynamics. One of the approaches allowing accurate time resolved measurements is pump-probe technique, when the sample is probed at a well-known time delay after interaction with a pump laser pulse. In the first pump-probe schemes, an optical laser pulse was splitted into a pump pulse and a probe pulse using a beam splitter. However, the wavelength of the probe pulse limits the resolution of the experiment.

In order to overcome this limit, the high-energy radiation is used to probe the systems under study. Recent developments of the FEL-based pump-probe technique opened new possibilities for investigating laser-induced dynamics and phase transitions [32, 33]. In combination with ultra-bright femtosecond pulses, produced by modern FELs, pump-probe technique became an essential tool to probe structures of short-living photoinduced states in different materials [28], measuring charge density waves [34], exploring laser-induced phase transitions [29, 30], and high pressure states of matter [35, 36].

Thesis outline. In this Thesis I focus on studies of mesoscopic materials with advanced X-ray scattering methods. Chapter 2 is a historical overview on the development of different X-ray radiation sources. The basics of X-ray interaction with matter and description of advanced scattering methods are discussed in Chapter 3. A brief introduction on the growth techniques and structural properties of mesoscopic materials is provided in Chapter 4. Chapter 5 is focused on using AXCCA to reveal the defect structure of lead sulfide mesocrystals. In Chapter 6 the GTSAXS method was applied to study the colloidal crystal rearrangement under dry sintering conditions. Both experiments were performed at PETRA III synchrotron facility. Chapters 7 and 8 describe a pump-probe experiment performed at the LCLS on a colloidal crystal sample.

Chapter 7 is focused on the theoretical and experimental studies of the laser-induced vibrations of the colloidal crystal. In Chapter 8, first, a general theory of laser-matter interaction is described with an emphasis on the ultrashort powerful laser pulses. Further experimental studies of the periodic plasma created from the colloidal crystal are presented. The sample dynamics observed in this experiment was interpreted using the theory introduced in Chapter 8. Finally, Summary concludes the obtained results and provides an outlook for further studies.

Chapter 2

Modern sources of coherent X-ray radiation

X-ray is a high-energy electromagnetic radiation with a wavelength in the region of an Ångström (10^{-10} m). The first paper written on X-rays is called "On a new kind of ray: A preliminary communication" and it was submitted to Würzburg's Physical-Medical Society journal by German scientist Wilhelm Röntgen in 1895 [37]. He named it X-radiation to signify an unknown type of radiation, but in many languages X-rays are referred to as Röntgen radiation. In this paper, Röntgen described that X-rays could pass through books and papers on his desk. The ability of X-rays to penetrate into matter, together with the short wavelength similar to the atomic and molecular dimensions, makes X-rays an extremely useful tool for probing the structure of matter. This fascinating properties of X-ray radiation led to extensive development of X-ray science and X-ray sources in the last century.

Röntgen discovered X-rays while experimenting with a Crookes tube, which was the first non-dedicated X-ray tube. These tubes were further developed by William Coolidge and became the first widely used source reliably producing X-rays. The spectrum of radiation emitted by an X-ray tube can be described as a continuous curve with several intense spikes (see Fig. 2.1). Such shape is caused by the fact that in the X-ray tube, radiation is produced in two separate processes: the bremsstrahlung and the characteristic radiation. During the bremsstrahlung process, electromagnetic radiation is produced by the deceleration of an electron by an atomic nucleus. This process produces a continuous part of the emitted spectrum. The second process is the characteristic radiation, which is emitted by the atoms in the anode, ionized due to the electron-atom collisions. When bound electrons are ejected from the inner shell due to the photoelectric effect, they leave behind core holes that are filled by the electrons from the outer shells, and the energy of the emitted photon is precisely determined by the energy difference between the higher and lower states. This leads to the characteristic spikes in the spectrum of the emitted radiation (see Fig. 2.1).

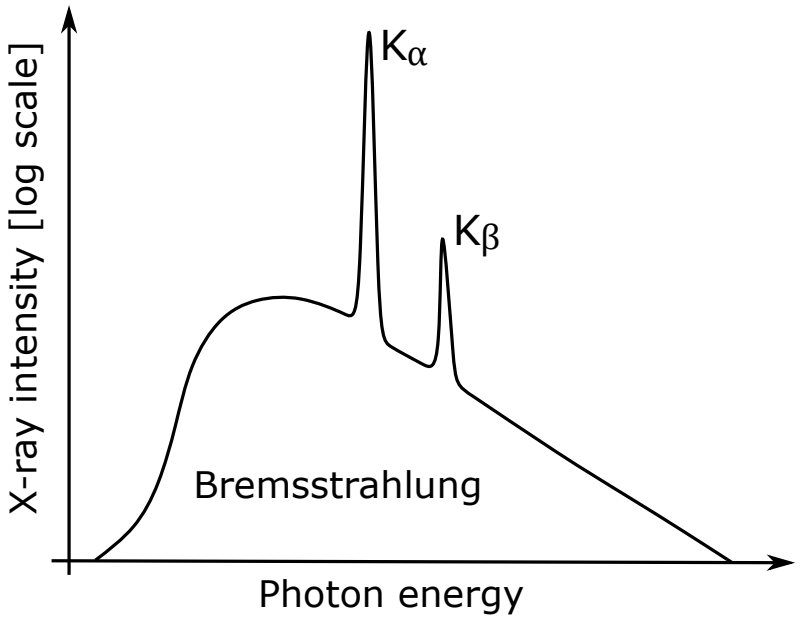

Figure 2.1: The spectrum from an X-ray tube.

X-ray tubes have played a significant role in the various fields of material science. In particular, first experiments studying diffraction on crystals were performed on the X-ray tube [38, 39]. These experiments established a very successful field of X-ray crystallography. Nowadays, the use of X-rays tubes has widely extended to medical and industrial applications, for example, in computed tomography scanners, airport luggage scanners, and industrial inspection. The intensity of X-ray radiation is typically characterized by the spectral photon flux [40]

$$F(\lambda) = \frac{Photons}{(second)(0.1\%\, bandwidth)}, \tag{2.1}$$

where λ is the radiation wavelength. However, when comparing X-ray sources, an important measure is brightness

$$B(\lambda) = \frac{F(\lambda)}{(2\pi)^2(\varepsilon_x)(\varepsilon_y)}, \tag{2.2}$$

where $\varepsilon_{x,y}$ is photon emittance. The emittance is defined as $\varepsilon_{x,y} = \sigma_{x,y}\sigma'_{x,y}$, where $\sigma_{x,y}$ and $\sigma'_{x,y}$ are size and divergence of the X-ray source, respectively.

X-ray tubes are small and cheap, however, they have both low brightness and low coherent flux because they emit radiation incoherently and in all directions. The brightness of the modern X-ray tubes is in the range $10^7 - 10^{12}$ ph/(s·mm^2·mrad^2·0.1%) and it was overcome by the invention of the synchrotron radiation sources which increased the possible brightness of the emitted radiation by orders of magnitude. The limits of the X-ray science were further pushed by the development of the next generation X-ray sources – free electron lasers (FELs). These sources will be discussed in detail in the

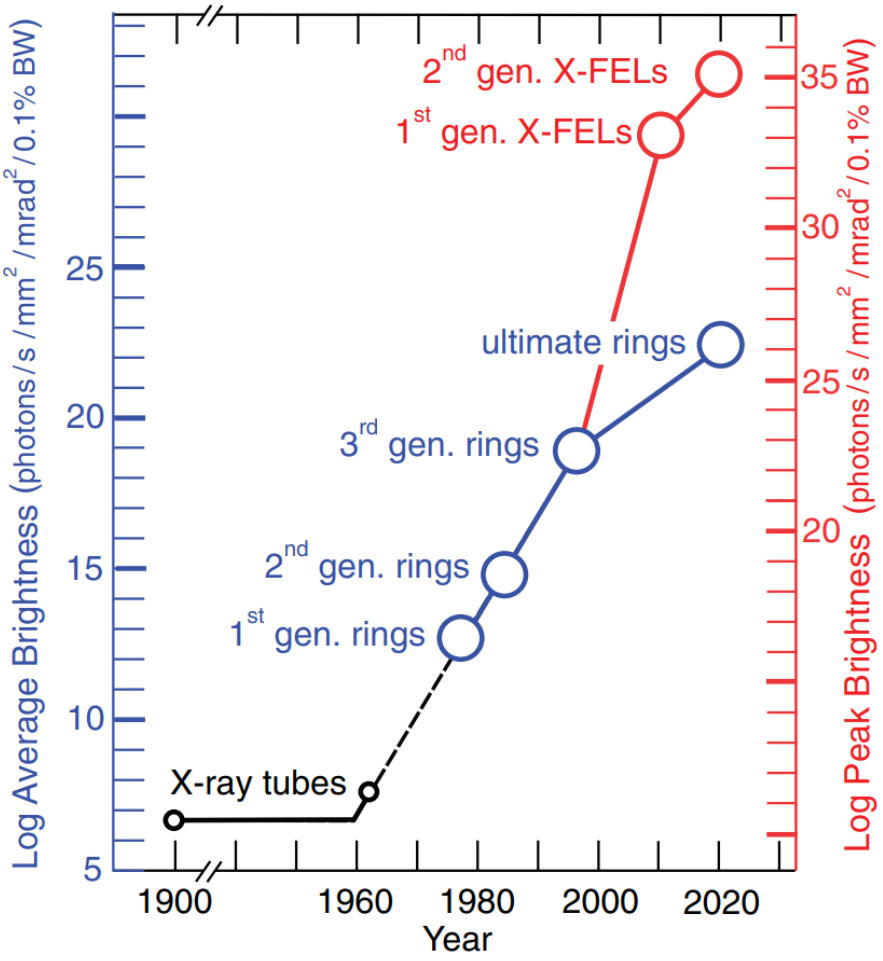

Figure 2.2: Historical and projected future increase in average brightness of storage rings (blue) and peak brightness of XFELs (red). This Figure was adapted from Reference [41].

next sections.

2.1 Synchrotron sources

Nowadays, the working horse for production of the X-ray radiation is a synchrotron light source. During the last century, four generations of synchrotron light sources were developed. The evolution of peak brightness from X-ray tubes to synchrotron and FELs is shown in Fig. 2.2.

In a synchrotron, charged particles such as electrons or positrons are accelerated to relativistic speed and are circulating in a storage ring. The particles are going through strong magnetic fields where their trajectory is bent by the Lorentz force. As a result, bremsstrahlung radiation is emitted by particles.

The history of synchrotron light sources begins in the 40s when it was discovered that in betatrons charged particles emit electromagnetic waves in a wide range of energies [42, 43]. First, this radiation was considered parasitic, but in the 60s, it was

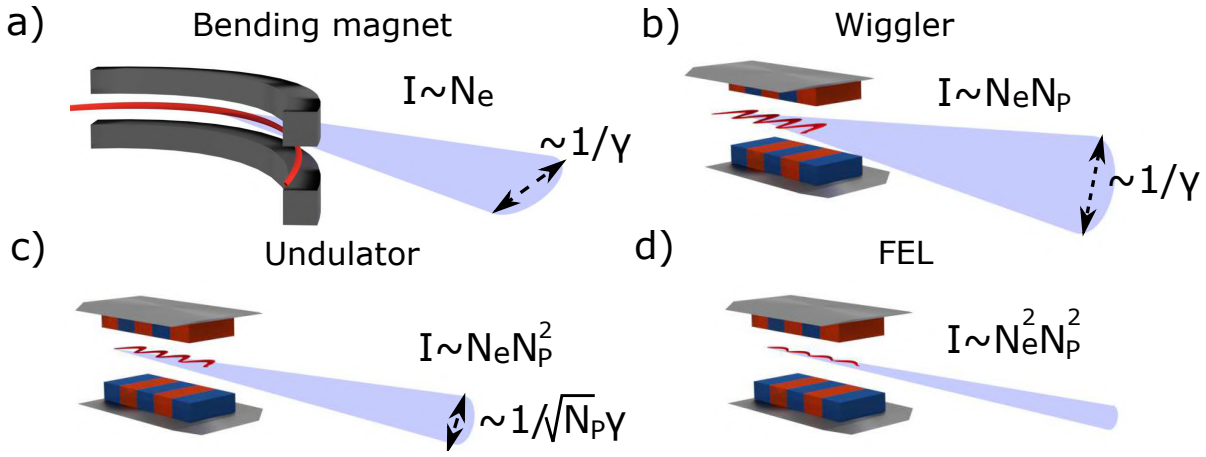

Figure 2.3: Principles of X-ray generation in bending magnet (a), wiggler (b), undulator (c) and Free Electron Laser (d). The electron beam is red and the X-ray beam is visualized here in blue.

already used for a variety of studies [44, 45]. Thus, first-generation synchrotrons are non-specialized X-ray sources in which electromagnetic radiation occurs as a side effect when changing the trajectory of charged particles in bending magnets (see Fig. 2.3(a)).

It turned out that synchrotron radiation has significantly higher brightness in comparison to X-ray tubes (up to 10^{15} - 10^{16} ph/(s·mm^2·mrad^2·0.1%)). Due to relativistic effects, the radiation is concentrated inside the cone with a radiation opening angle $\theta \sim 1/\gamma$, where $\gamma = 1/\sqrt{1-(v/c)^2}$ is the relativistic Lorentz factor, v is the electron velocity, and c is speed of light in vacuum. As a result, the vertical divergence of the X-ray radiation is $2/\gamma$, and the horizontal divergence is determined by the electron trajectory inside the magnet (see Fig. 2.3(a)).

The second generation of synchrotron sources is specially optimized for the radiation generation. The first synchrotron of the second generation, Tantalus, operated by the University of Wisconsin-Madison, was commissioned in the end of the 60s [46]. First generation synchrotron sources were dedicated to particle physics experiments, and they used low particle current, but second generation synchrotrons were designed for much higher current. Thus, development of the dedicated synchrotron sources allowed to increase brightness up to 10^{15} ph/(s·mm^2·mrad^2·0.1%) (see Fig. 2.2).

A further upgrade of the synchrotron light sources was conceived and optimized to produce brilliant X-rays. Third generation synchrotrons typically reliant upon undulators and their brightness reaches up to 10^{21} ph/(s·mm^2·mrad^2·0.1%) (see Fig. 2.2). The first third generation synchrotron was a ESRF 6 GeV storage ring in Grenoble, which started operation in 1994 [19]. The other examples of the third generation synchrotrons are 7 GeV APS in Chicago [21], 8 GeV SPring-8 in Japan [47] and 6 GeV PETRA III in Hamburg [17].

Two main types of insertion devices used in synchrotrons are wigglers and undulators [48, 49]. Wiggler is a periodic structure of N_p dipole magnets (see Fig. 2.3(b)). Inside the wiggler, the electron beam oscillates (wiggles) and emits electromagnetic

waves at every turn. Brightness of the radiation in wiggler is proportional to the number of magnets N_p and the number of electrons N_e, those $I \sim N_e N_p$. Another insertion device is an undulator, which is also a set dipole magnets (see Fig. 2.3(c)). In order to characterize the insertion devices, an undulator parameter is used [4]

$$K_u = \frac{eB_0\lambda_u}{2\pi m_e c^2} = 0.934 B_0[\mathrm{T}]\lambda_u[\mathrm{cm}], \tag{2.3}$$

where B_0 is the magnetic field, λ_u is the period of the magnetic system, e and m_e are the electron charge and rest mass, respectively. This parameter characterizes the electron motion and allows to distinguish between different insertion devices

$$\begin{cases} K_u \gg 1 \rightarrow \text{wiggler}\,, \\ K_u \sim 1 \rightarrow \text{undulator}\,. \end{cases} \tag{2.4}$$

If $K \sim 1$ the angular deviation of an electron bunch is comparable with the radiation opening angle θ. As a result, the constructive interference happens, therefore the intensity of undulator radiation is proportional to the square the number of undulator periods $I \sim N_e N_p^2$. Another important difference between undulators and wigglers is the value of the opening angle. While wigglers emit radiation with an opening angle $\theta \sim 1/\gamma$ undulator radiation is confined in a much narrower angle $\theta \sim 1/\sqrt{N_p}\gamma$ which depends on a number of magnets (see Fig. 2.3). Due to constructive interfetrence between N_p individual magnet periods undulators have a narrow bandwidth in comparison to other insertion devices. Because of the same reason the wavelength of the radiation emitted by undulator can be expressed as [50]

$$\lambda_n = \frac{\lambda_u}{2\gamma^2 n}(1 + \frac{K_u^2}{2} + \gamma^2\theta^2)^{-1}\,, \tag{2.5}$$

where n is the number of the harmonics, and θ is the off-axis angle. The degree of monochromaticity of the undulator radiation can be estimated as $\Delta\lambda/\lambda \sim 1/(nN_p) \approx 10^{-2}$.

The low emittance and high brightness of the third generation synchrotron sources allowed to exploit coherence properties of X-ray radiation. There are many imaging techniques based on the coherent properties of the beam such as coherent X-ray diffraction imaging (CXDI) [51], ptychography [8, 9], X-ray photon correlation spectroscopy (XPCS) [10], in-line holography [52, 53] and Fourier transform holography (FTH) [54, 55]. Also the high degree of coherence allows tight focusing of the synchrotron beam (down to nanometer range) without spatial filtering of flux [56]. However, only 1 % of the synchrotron beam is sufficiently coherent to be used in coherence-based applications, and the strong spatial filtering of the radiation is required [57]. Therefore, the sources with the higher degree of coherence are strongly desirable.

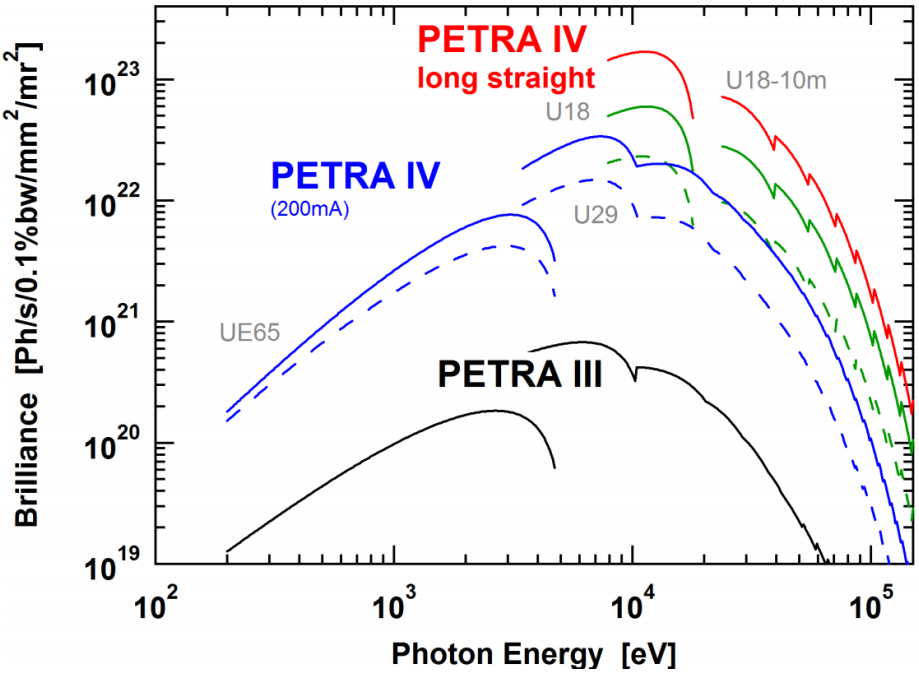

Figure 2.4: Brightness of PETRA IV for a storage ring current of 200 mA (blue, green, and red curves) in comparison with PETRA III (black curves) for a storage ring current of 100 mA. This figure was adapted from Reference [58].

In order to further increase the brightness and coherent fraction of the emitted radiation, synchrotron sources of the fourth generation were developed. According to the Eq.(2.2) the brightness is inversely proportional to the emittance. For the third generation synchrotron sources the main limiting factor was the size of the electron bunch in the horizontal direction, which depends on the bending magnet parameters. Typical emittance of the third generation synchrotron sources is about 1 – 5 nm·rad in the horizontal direction and about 5 – 50 pm·rad in the vertical direction. Thus, in order to optimize the source parameters in is necessary to obtain the horizontal and vertical emittance of the same order of magnitude. The minimum value of the photon beam emittance $\lambda/4\pi$ is determined by the wave nature of light [59]. If the electron beam emittance is decreased up this value

$$\varepsilon_e < \varepsilon_p = \frac{\lambda}{4\pi}, \tag{2.6}$$

the source can be called a diffraction-limited source. It is important to note that this equation is valid only for radiation described by the Gaussian functions. For the the far-field region and resonant conditions radiation is described by a sinc-function, and therefore emittance of single-electron undulator radiation is $\lambda/2\pi$ [60].

In the fourth generation synchrotrons low emittance in the horizontal direction is obtained by focusing the electron beam using the so-called multi-bend achromat scheme [64]. In this scheme, several (typically 7) bending magnets (instead of 2) are

Table 2.1: The present and planned fourth generation sources target parameters [18, 58, 61–63].

Source	MAX IV	ESRF-EBS	APSU	PETRA IV
Energy, GeV	3	6	6	6
ε_x (pm · rad)	250	150	40	10-30
Current, mA	500	200	200	200
Brightness, ph/(s·mm^2·mrad^2·0.1%)	$4 \cdot 10^{21}$	10^{22}	$2 \cdot 10^{22}$	10^{23}
Coherent fraction ($\lambda = 1\mathring{A}$)	~ 0.1	~ 0.3	~ 0.1	~ 0.4

put together in an achromat. The first fully operational fourth generation synchrotrons were MAX IV opened in 2016 [18], and ESRF [62] which got the first beam in 2020. Existing synchrotron sources such as PETRA III [58], and APS [61] are planning upgrades based on the multi-bend achromat concept. The target parameter for these upgrades are shown in Table 2.1. As can be seen from this Table, PETRA IV can reach by far the smallest emittance and thus the highest brightness, compared to other planned fourth-generation synchrotron radiation sources. This can be obtained because of the large storage ring radius. This upgrade would allow increasing the brightness of the existing facilities by 2-3 orders of magnitude and increase the coherent fraction more than by one order of magnitude (see Table 2.1 and Fig. 2.4).

2.2 Free-electron lasers

Further increase of brightness was achieved by the development of the new concept of the X-ray sources – Free-Electron Laser (FELs). It was initially suggested by Madey in 1971 [65], and soon the performance of the first FEL in the infrared domain was demonstrated [66]. Further, the concept of Self-Amplified Spontaneous Emission (SASE) process allowed the create X-ray FELs (or XFELs). This concept was proposed independently by two groups of scientists: A. Kondratenko and E. Saldin in 1980 [67] and by R. Bonifacio, C. Pellegrini, J. Murphy and L. M. Narducci in 1984 [68, 69].

The difference between the undulators in synchrotrons and SASE FELs is the following. In both of them, electrons are compressed into bunches, of about 20 – 100 ps in synchrotrons and 10 – 100 fs in the FELs. In the synchrotrons, electrons in the bunch move through the undulator with purely random positional order. In long undulators of FELs, on the other hand, radiation emitted by the electron beam modulates the current of that beam into microbunches, causing even higher radiation power via a positive feedback loop (see Fig. 2.5). Due to the small size of the microbunch, all electrons emit radiation coherently, thus the intensity of the radiation is proportional to the square of the number of electrons $I \sim N_e^2 N_p^2$ (see Fig. 2.3). The formation of the microbunches is undergoing three stages (see Fig. 2.5). First, electrons have random longitudinal positional order – shot noise, but during the SASE process, the radiation

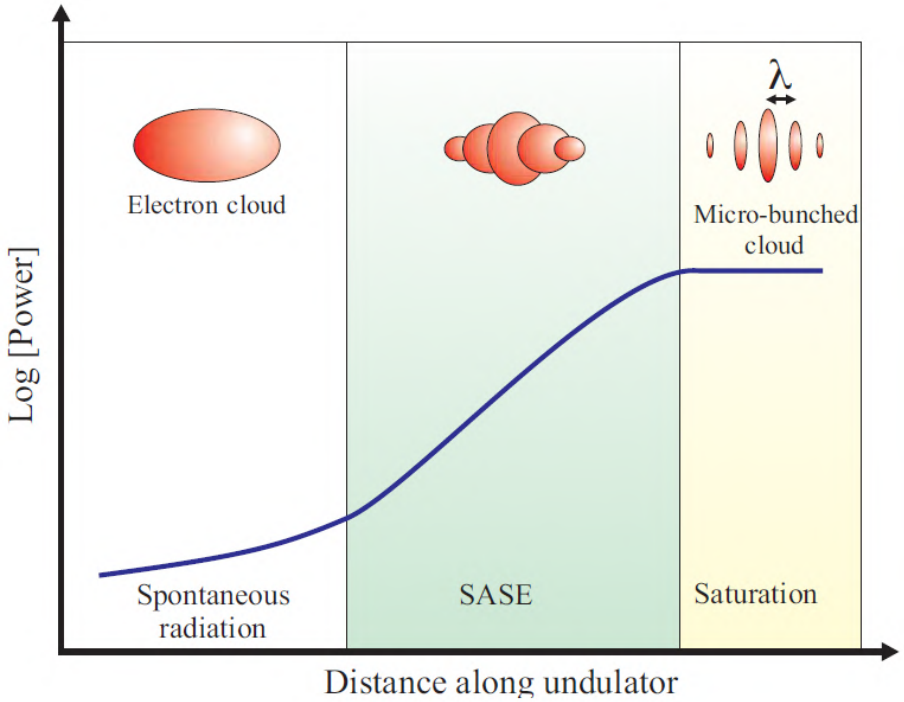

Figure 2.5: Schematic of the power radiated by an electron cloud as it propagates through a long undulator. This figure was adapted from Reference [4].

produced by electrons is accelerating or slowing down some of the electrons. Thus, despite the repulsive Coulomb forces, the electrons form microbunches, separated by the length of radiation wavelength. Due to the formation of the microbunches, the radiated power grows exponentially (see Fig. 2.5). This regime of the operation is called a linear regime. At a, certain point, the microbunches are fully formed and the exponential power growth stops. It is called FEL saturation. Beyond this point radiation power can be extracted at best linearly as a function of the undulator length by properly adjusting unduator paramter K.

The invention of the XFELs allowed to increase coherence up to 80% [70, 71] and peak brightness by 10 orders of magnitude, up to 10^{34} ph/(s·mm^2·mrad^2·0.1%) (see Fig. 2.2). The first FELs demonstrating SASE principle was FLASH in Hamburg [22]. Soon many other SASE XFELs such as LCLS [24], SACLA [25], European XFEL [23] Swiss FEL [72] and PAL – XFEL [73] started operation.

In the SASE FELs, the startup process is stochastic, which leads to the lack of temporal coherence. In order to achieve better temporal coherence, the a new improvement was proposed. This is the concept of seeding where electrons are structured by an external electromagnetic radiation. To successfully modulate the electron beam the seed power should be stronger than thee shot-noise power of the electron beam, which depends linearly on the radiation frequency. There are two main schemes of the seeded FELs – external seeding or high-gain harmonic generation (HGHG) and self seeding [74]. In the HGHG scheme the beam is first modulated by an external seed

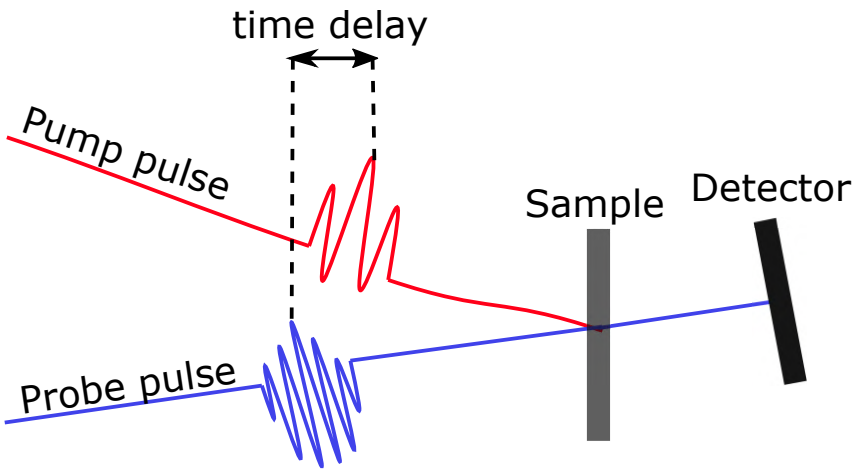

Figure 2.6: The scheme of a typical pump-probe experiment.

laser, further the energy modulation is converted into a current modulation by a dispersive section, and at the last stage FEL is tuned to one of the higher harmonics in the radiator section. The HGHG scheme can be generalized to a cascade system with more than one frequency multiplication. This scheme was first proposed by Yu [75] and tested in Brookhaven [76]. Later the first seeded-FEL source FERMI operating with wavelength down to 4 nm was commissioned at the Sincrotrone Trieste Laboratory [77].

The limitation of the HGHG seeding scheme is the lack of power of the conventional lasers, which makes impossible seeding at X-ray wavelength. This problem was partly solved by invention of the so-called echo-enable harmonic generation (EEHG) FEL scheme [78, 79]. In this scheme a more complex configuration with two modulators and dispersive sections is used to achieve strong overcompression of the electron beam, which allows much higher harmonic conversion in the HGHG stage. However, the practical use of EEHG is limited to wavelengths larger than 1 nm.

Another concept called "self-seeding" was invented in the 2012 [80]. In the self seeding at the first stage the undulator is operating in SASE regime, then the photon beam is filtered through a monochromator and is used as a seed. The initial self-seeding concept as described in Ref. [80], required a long electron bypass line, where control over the electron beam properties was achieved by many quadrupole and sextupole magnets. The problem of a long electron bypass was successfully solved by Geloni, Kocharyan, and Saldin in 2011 [81]. They proposed using the transmission around the stop band of a Bragg reflection instead of grating monochromators. The self-seeding method was successfully realized at LCLS in both soft and hard X-ray regimes [82, 83], and this allowed to increase the temporal coherence of the beam.

XFELs provide extremely intense coherent femtosecond X-ray pulses, which allows performing new kind of experiments. One of the application is the biomolecular imaging [84, 85], and single particle imaging (SPI) [27, 86]. Another exciting application of the ultrashort XFEL pulse is the performance of the pump-probe experiments when the

sample is first pumped by the conventional infrared laser and after some time delay the dynamics is measured by the probe pulse. The typical scheme of the pump-probe experiment is shown in Fig. 2.6. This kind of experiments is used to reveal the dynamics of plasma – matter interactions [87, 88], ionisation process, dynamics of shock compression [29, 89], ultrafast phase transition [35, 90], and laser – induced molecular dynamics [28, 91].

Chapter 3

Advanced X-ray scattering techniques

This thesis is mostly concentrated on the elastic scattering of X-ray photons, which is discussed further in detail. There are two different approaches to the description of X-ray diffraction, kinematic and dynamic. In the kinematical theory, also known as the first Born approximation, scattering is considered to be weak. Therefore only single scattering events for each photon are considered. In the dynamical theory, multiple scattering events are taken into account, and the resulting mathematics is more complex. There are also approaches such as distorted wave Born approximation (DWBA) [92], which take into account multiple scattering events.

Various techniques of X-ray scattering are based on kinematical diffraction theory. It allows solving the three-dimensional structure of different complex crystalline materials such as natural minerals and metals or artificially prepared mesocrystals. Kinematical diffraction theory led to development of the protein crystallography [93] which allowed to solve the structure of proteins and other biomolecules. Also, different imaging techniques such as Coherent X-ray Diffractive Imaging (CXDI) [51] use kinematical approximation. However, these techniques require sophisticated iterative phasing algorithms because phase information is lost during the measurement process.

This chapter is focused on various X-ray scattering methods and derivation of the essential equations. First, the basics of X-ray interaction with a single electron i.e. absorption and scattering is provided. Further, the X-ray interaction with crystalline structures is described within kinematical approximation. Then two advanced X-ray scattering methods, namely Grazing Incidence Small Angle X-ray Scattering (GISAXS) and Angular X-ray Cross-Correlation Analysis (AXCCA) are discussed in detail.

3.1 X-ray interaction with a material

3.1.1 X-ray absorption

When an X-ray photon interacts with an atom it can be either scattered or absorbed. Let us, first, consider the absorption process following Reference [4]. The absorption process obeys the Beer-Lambert-Bouguer law, which was first discovered by Pierre Bouguer before 1729 while looking at red wine [94]

$$-dI = \mu I(z)dz\,, \tag{3.1}$$

where μ is the linear absorption coefficient and $I(z)$ is the X-ray intensity at the position z inside the sample. The solution of the differential Equation (3.1) is the following

$$I(z) = I_0 \exp(-\mu z)\,, \tag{3.2}$$

where I_0 the incident beam intensity $I_0 = I(z = 0)$. Linear absorption coefficient depends on the atomic number density ρ_{at} and the absorption cross-section σ_a as

$$\mu = \rho_{at}\sigma_a\,. \tag{3.3}$$

The absorption cross-section is defined by the photon energy E and the atomic number Z of the absorber as $\sigma_a \sim Z^4/E^3$. However, at a characteristic energy, the so-called K-edge energy, there is a disccontinious rise in the cross-section due ionisation of an electron from a K shell (see Fig. 3.1).

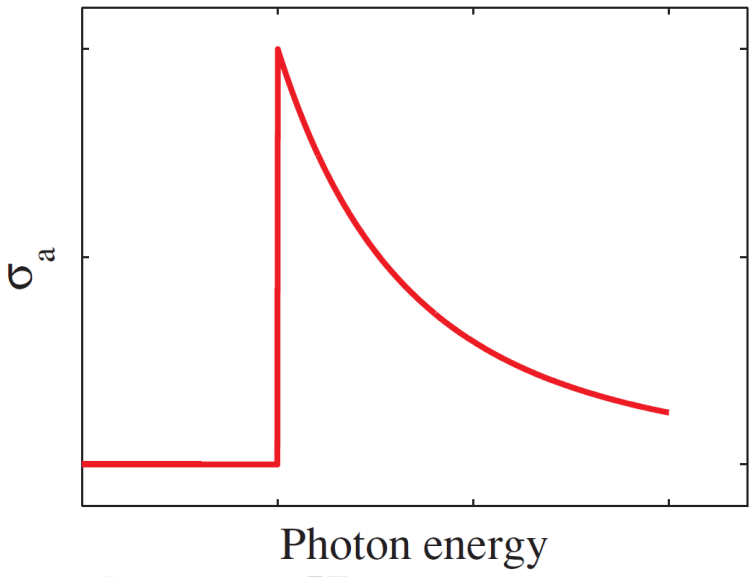

Figure 3.1: The absorption cross-section for a K electron on a linear scale. This figure was adapted from Reference [4].

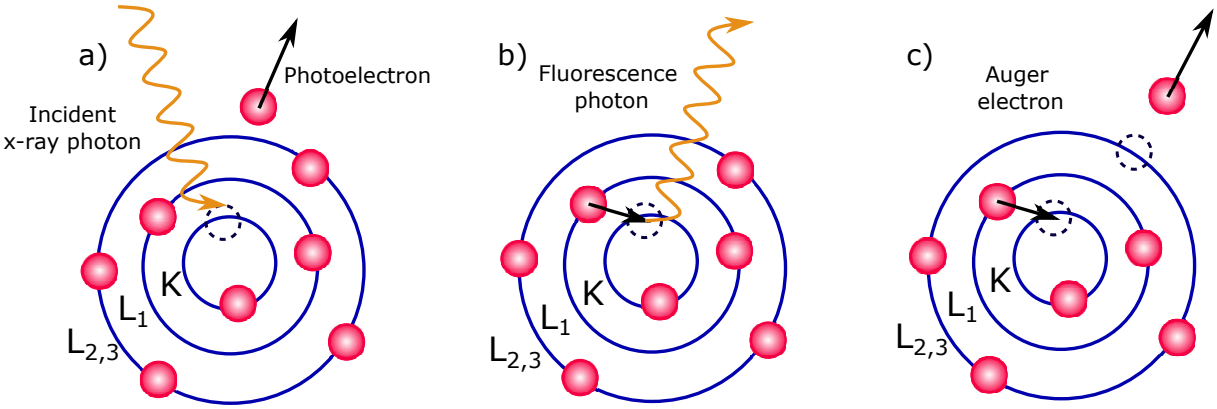

Figure 3.2: Two scenarios following a photoionization process. (a) Incident X-ray photon is interacting with an electron from an inner shell and ionizing the atom. The vacancy is further filled with an electron from an outer shell, followed by fluorencence photon emission (b) or Auger electron ejection (c).

During the absorption process, an X-ray photon is transferring its energy to the electron in the inner shell. This process is called photoelectric absorption. The electron is further knocked out of its shell and thus a hole is created. This hole is later filled by an electron from an outer shell, and the emitted energy can be used in two different ways. An atom can emit a photon with an energy equal to the difference between binding energies of the shells. This process is called fluorescence radiation. Another scenario is when the energy is transferred to another electron from an outer shell, ionizing it. The ionized electron is called an Auger electron, and this process is an Auger process. The processes described above are schematically demonstrated in Fig. 3.2.

It is worth to notice that the X-ray absorption phenomenon has various applications. The first application was demonstrated by Röntgen when he visualized the bone structure of a human hand. This approach was further developed, and now it is used in techniques such as tomography [95] or radiography [96]. Also, there are many different spectroscopy techniques, such as Extended X-Ray Absorption Fine Structure (EXAFS), X-ray Absorption Near Edge Structure (XANES), fluorescence spectroscopy and Auger spectroscopy [4].

3.1.2 X-ray scattering at a single electron

Now we turn our attention to X-ray scattering, and first, we consider elastic scattering also called Thomson scattering. The calculation of the differential cross section for elastic scattering was provided by Thomson in 1906 according to classical theory. The same result can be obtained using quantum field theory, which was demonstrated by Dirac in 1927. We will describe Thomson scattering following Reference [97] and we will use the CGS unit system in this section.

The most simple case is the collision of a single photon with a single free charged particle. The proton mass is 1836 times heavier then the electron mass, thus protons

are accelerated much less, and we consider only scattering on an electron. We consider an incoming polarized electromagnetic field in the form of electromagnetic plane wave

$$\mathbf{E}_{\text{in}}(\mathbf{r}, t) = E_0 \mathbf{p} e^{-i\omega t}\,, \tag{3.4}$$

where $\mathbf{p}$ is the polarization vector. Plane wave is coming to the charged particle with a dipole moment

$$\mathbf{d} = \sum e_i \mathbf{r}_i\,. \tag{3.5}$$

The dipole is accelerated by an electric field $\mathbf{E}_{\text{in}}$, and obeys the Coulomb's law

$$\mathbf{F} = e\mathbf{E}_{\text{in}}\,. \tag{3.6}$$

The acceleration of a charged particle can be obtained from the Newton's second law of motion

$$\mathbf{a} = \frac{\mathbf{F}}{m_e}\,. \tag{3.7}$$

Combining all of the above, the second time derivative of the dipole moment of an electron $\ddot{\mathbf{d}}$ can be written in the form

$$\ddot{\mathbf{d}} = e\mathbf{a} = e\frac{\mathbf{F}}{m_e} = \frac{e^2}{m_e}\mathbf{E}_{\text{in}}\,, \tag{3.8}$$

where e and m_e are electron charge and mass respectively.

The electromagnetic field emitted by a moving dipole in vacuum can be written in the form of:

$$\mathbf{E} = \frac{3\mathbf{n}(\mathbf{n}\cdot\mathbf{d}) - \mathbf{d}}{R_0^3} + \frac{3\mathbf{n}(\mathbf{n}\cdot\dot{\mathbf{d}}) - \dot{\mathbf{d}}}{cR_0^2} + \frac{\mathbf{n}(\mathbf{n}\cdot\ddot{\mathbf{d}}) - \ddot{\mathbf{d}}}{c^2 R_0}\,. \tag{3.9}$$

Here R_0 and $\mathbf{n}$ is the distance and unit vector towards the observer, and c is the speed of light. This equation is simplified if the field is considered at distances much larger than the wavelength, and first two terms of the Equation (3.9) can be neglected. Using the vector triple product rule we obtain

$$\mathbf{E} = \frac{1}{c^2 R_0}[[\ddot{\mathbf{d}}\mathbf{n}]\mathbf{n}]\,. \tag{3.10}$$

The magnetic field of the plane wave is derived from the electric field as

$$\mathbf{H} = [\mathbf{n}, \mathbf{E}] = \frac{1}{c^2 R_0}[\ddot{\mathbf{d}}\mathbf{n}]\,. \tag{3.11}$$

The directional energy flux is represented by the Poynting vector defined as $\mathbf{S} = c/4\pi[\mathbf{EH}]$. In the time domain, the electric and magnetic fields are oscillating, and we are interested in the average emitted power. If we consider an oscillating electric field

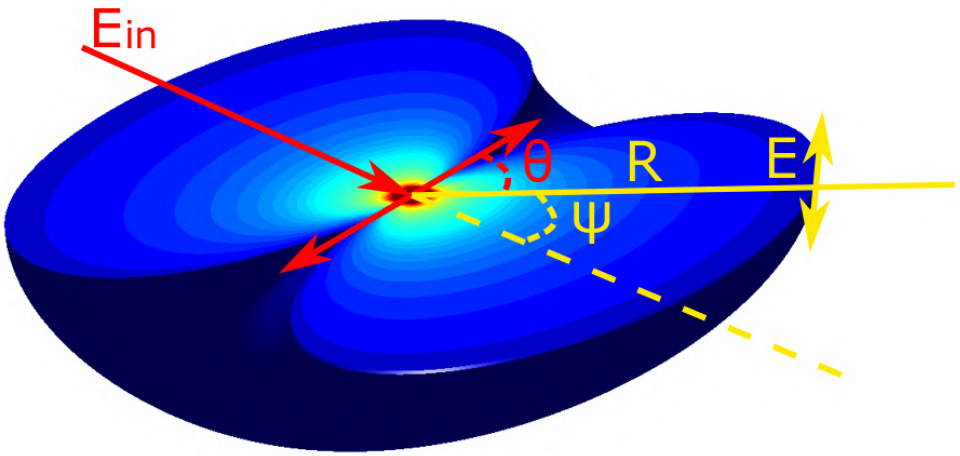

Figure 3.3: The scheme of the angular dependence of Thomson scattering. Scattering is illustrated as a surface of constant intensity. The direction of the incident electric field is shown by red, and the emitted electric field is shown by yellow. The polarization angles θ and ψ are marked by red and yellow, respectively.

the Poynting vector is

$$\mathbf{S} = \frac{c}{8\pi}[\mathbf{EH}] = \frac{c}{8\pi}|\mathbf{H}|^2\mathbf{n}\,. \tag{3.12}$$

The intensity of the radiation dI in the solid angle $d\Omega$ is defined as an energy going through the area $R_0^2 d\Omega$. Combining Equation (3.11) with Equation (3.12) we obtain

$$dI = \frac{c}{8\pi}|\mathbf{H}|^2 R_0^2 d\Omega = \frac{1}{8\pi c^3}[\ddot{\mathbf{d}}\mathbf{n}]^2 d\Omega = \frac{\ddot{\mathbf{d}}^2}{8\pi c^3}\sin^2\theta d\Omega\,, \tag{3.13}$$

where θ is the angle between the $\ddot{\mathbf{d}}$ and $\mathbf{n}$ vectors. From the Equation (3.13) it is obvious that intensity emitted by the oscillating dipole depends only on a second time derivative of the dipole moment $\ddot{\mathbf{d}}$.

Combining Equation (3.8) with Equation (3.13) we obtain

$$dI = \frac{e^4}{8\pi m_e^2 c^3} E_0^2 \sin^2\theta d\Omega = \frac{c}{8\pi} r_0^2 E_0^2 \sin^2\theta d\Omega\,, \tag{3.14}$$

where $r_0 = e^2/m_e c^2 = 2.82 \cdot 10^{-13}$ cm is the classical electron radius. The scattering process is described by the differential scattering cross-section

$$\frac{d\sigma}{d\Omega} = \frac{I_{sc}}{\Phi_0 \Delta\Omega}\,, \tag{3.15}$$

where the I_{sc} is number of scattered photons per solid angle $\Delta\Omega$ and Φ_0 is the flux of an incident beam. Considering all of the above the differential cross section of Thomson scattering is defined as

$$\frac{d\sigma}{d\Omega} = r_0^2 \sin^2\theta\,. \tag{3.16}$$

The quantity $\sin^2\theta$ is known as the polarization factor P. If the direction of oscil-

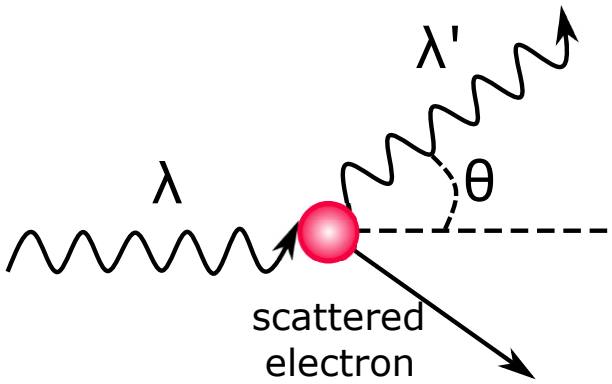

Figure 3.4: Scheme of the Compton scattering. A photon with the wavelength λ is coming to an electron, and a new photon with the wavelength λ' is scattered at the angle θ.

lation of the electric field is normal to the scattering plane, it is called σ – polarization and if the oscillations occur in-plane it is called π – polarization. In the case of σ – polarization, the polarization factor is equal to one, and in the case of π – polarization it is given by the angle $\psi = 90 - \theta$. In the case of unpolarized source, both contributions are equal

$$P = \begin{cases} 1,\ \sigma\text{– polarization}\,, \\ \cos^2\psi,\ \pi\text{– polarization}\,, \\ \frac{1+\cos^2\psi}{2},\ \text{unpolarized light}\,. \end{cases} \tag{3.17}$$

The intensity distribution of Thomson scattering has a doughnut shape, and it is shown in Fig. 3.3.

In the beginning of the 20th century inelastic scattering was discovered by Arthur Holly Compton [98]. Although classical electromagnetism predicted that the wavelength of scattered rays should be equal to the initial wavelength, the wavelength of the scattered rays was longer. This effect is now called the Compton effect. It is important because it cannot be explained purely by the wave theory and gave support for the emerging quantum theory.

The Compton wavelength is derived considering the conservation of energy and momentum during the collision. Therefore, the shift of the wavelength $\Delta\lambda$ is

$$\Delta\lambda = \frac{h}{m_e c}(1 - \cos\theta)\,, \tag{3.18}$$

where h is the Planck constant and θ is the scattering angle. The constant $h/m_e c = 2.43 \cdot 10^{-12}$ m is known as the Compton wavelength of an electron.

The differential cross section for the photon scattered from a single electron in lowest order of quantum electrodynamics is expressed by Klein-Nishina formula [99]. It yields the Thomson scattering at low frequencies and Compton scattering at high frequencies. It is worth to notice that Compton scattering is incoherent.

3.2 X-ray scattering at an atom

Now we will discuss the scattering from an atom following Reference [4]. In the kinematical theory an atom is considered as a set of electrons. Let us consider electron density of an atom in two points, at the distance $\mathbf{r}$ from each other. The difference in the considered position of electron density causes the phase difference $\Delta'\varphi(\mathbf{r})$ of the scattered waves

$$\Delta'\varphi(\mathbf{r}) = \mathbf{k}_\mathrm{i} \cdot \mathbf{r} - \mathbf{k}_\mathrm{f} \cdot \mathbf{r} = -\mathbf{q} \cdot \mathbf{r}, \tag{3.19}$$

where $\mathbf{k}_\mathrm{i}$ and $\mathbf{k}_\mathrm{f}$ are wavevectors of the incident and scattered fields, and $\mathbf{q} = \mathbf{k}_\mathrm{f} - \mathbf{k}_\mathrm{i}$ is known as the scattering vector. Scattering on an atom is schematically shown in Fig, 3.5.

The electron distribution in the atom is described by the electron density distribution function $\rho(\mathbf{r})$, which defines the probability of finding an electron in a certain position $\mathbf{r}$. The resulting scattering amplitude is proportional to a coherent sum of scattering from all electrons in an atom

$$A(\mathbf{q}) = -r_e f_0(\mathbf{q}) = -r_e \int \rho(\mathbf{r}) e^{-i\mathbf{q}\mathbf{r}} d^3\mathbf{r}, \tag{3.20}$$

where $f_0(\mathbf{q})$ is called the atomic form factor. As can be seen from Equation (3.20) the scattering amplitude is the Fourier transform of the electron density distribution. The atomic form factor defines the probability of elastic scattering from the atom $P = |f_0(\mathbf{q})|^2$, which yields to the correction of the Thomson scattering equation. Thus, the intensity scattered at an atom is directly proportional to P.

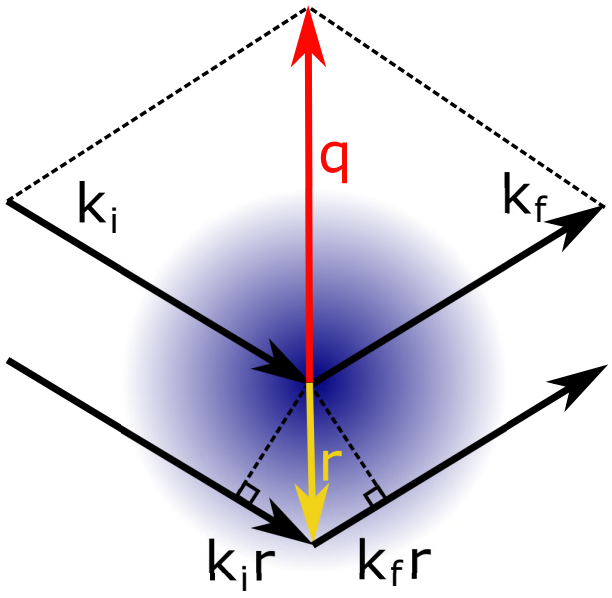

Figure 3.5: Schematic representation of scattering from an atom. The wavevectors of the incident and the scattered waves are denoted as $\mathbf{k}_\mathrm{i}$ and $\mathbf{k}_\mathrm{f}$. The phase difference between is given by $\mathbf{k}_\mathrm{i} \cdot \mathbf{r}$ and $\mathbf{k}_\mathrm{f} \cdot \mathbf{r}$.

It is important to note that up to now we assumed completely free electrons. However, electrons in the atom are bound, therefore we should introduce more accurate treatment of the atomic scattering factor:

$$f(\mathbf{q},\omega) = f_0(\mathbf{q}) + f'(\omega) + if''(\omega)\,, \tag{3.21}$$

Here $f'(\omega)$ and $f''(\omega)$ are the real and imaginary parts of the so-called dispersion correction. The angular dependence of the dispersion correction values is much smaller than that for $f(\mathbf{q})$ but they strongly depend on the ω. When ω is close to the one of the resonant frequencies in atom, the total scattering increases dramatically. The imaginary part of the dispersion correction represents the absorption and is proportional to the absorption cross-section σ_a. Here sign convention for the $f''(\omega)$ is negative, but sometimes in other texts sign convention is positive. The dispersion correction values are given in the International Tables For Crystallography [100].

3.3 Scattering from a crystal in kinematical approximation

Now we turn our attention to the X-ray scattering (or diffraction) by crystals, following Reference [51]. This is one of the most remarkable phenomenon in X-ray science, discovered by Max von Laue in 1912 [101] and explained theoretically by William Bragg in 1913 [39]. Since many materials can form crystals, the X-ray diffraction is widely used to determine the crystalline structure.

An ideal crystal is defined as an infinitely repeated periodic arrangement of identical structural elements such as single or several atoms, molecules etc., [102] (see Fig. 3.6). Positions of these elements in the structure are characterized by the translational vector $\mathbf{R}_\mathrm{n}$, which is defined by three linearly independent space vectors $\mathbf{a}_1$, $\mathbf{a}_2$, and $\mathbf{a}_3$

$$\mathbf{R}_\mathrm{n} = n_1\mathbf{a}_1 + n_2\mathbf{a}_2 + n_3\mathbf{a}_3\,, \tag{3.22}$$

where n_1, n_2, and n_3 are integer numbers. Vectors $\mathbf{a}_1$, $\mathbf{a}_2$, and $\mathbf{a}_3$ form a so-called unit cell and the structure formed by the translational symmetry is called crystal lattice (see Fig. 3.6). If the resulting volume of the unit cell reaches its minimum, it is called the primitive unit cell defined by the primitive lattice vectors. Generally, crystal lattice has not only translational symmetry but also a number of point symmetries which define 14 distinct types of lattices, known as Bravais lattices. It is important to note that the presence of point symmetries affects the mechanical, optical and electrical properties of the crystal.

The periodicity of the crystal lattice defines the periodicity of the electron density. It can be expressed as the convolution of an electron density of a unit cell $\rho_{uc}(\mathbf{r})$ with

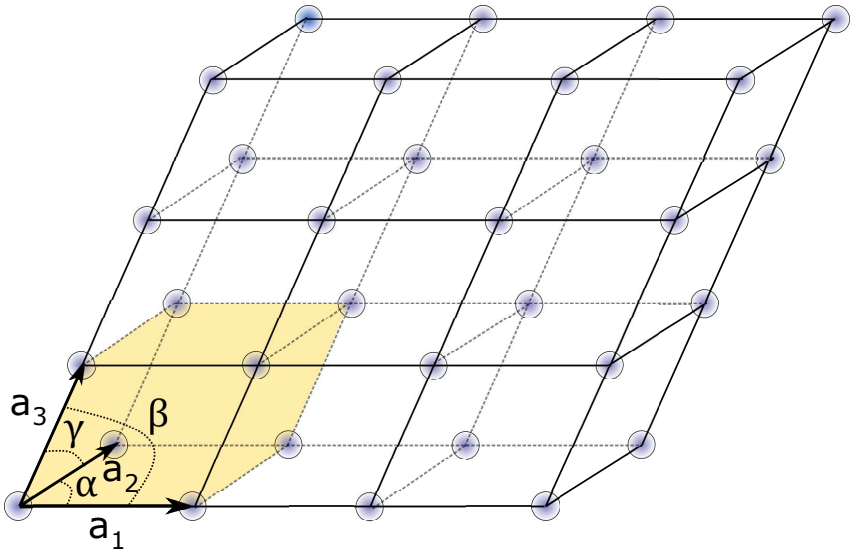

Figure 3.6: Schematic representation of a crystal lattice. The unit cell defined by basic vectors $\mathbf{a}_1$, $\mathbf{a}_2$ and $\mathbf{a}_3$ is shaded yellow.

lattice periodicity function

$$\rho(\mathbf{r}) = \rho_{uc}(\mathbf{r}) * \sum_{\mathbf{n}} \delta(\mathbf{r} - \mathbf{R}_\mathrm{n}) \cdot s(\mathbf{r}) \,, \tag{3.23}$$

where $s(\mathbf{r})$ is the shape function defined as 1 inside the crystal and 0 outside. $\sum_{\mathbf{n}}$ denotes the summation over all possible integer vectors $\mathbf{n} = \{n_1, n_2, n_3\}$.

As was shown in the previous section, the scattering amplitude is connected with the electron density through the Fourier transform

$$A(\mathbf{q}) = -r_e \int \rho(\mathbf{r}) e^{i\mathbf{q}\mathbf{r}} d^3\mathbf{r} \,. \tag{3.24}$$

Thus, to describe the properties of the scattering from crystals, the concept of reciprocal lattice was developed by P. P. Ewald in 1913 [103]. The position of each point in the reciprocal lattice is defined by the vector $\mathbf{G}_\mathrm{n}$, which satisfies the condition

$$e^{i\mathbf{G}_\mathrm{n}\mathbf{R}_\mathrm{n}} = 1 \,, \tag{3.25}$$

and its basis vectors are defined as follows

$$\mathbf{b}_1 = 2\pi \frac{\mathbf{a}_2 \times \mathbf{a}_3}{\mathbf{a}_1 \cdot (\mathbf{a}_2 \times \mathbf{a}_3)} \,;\; \mathbf{b}_2 = 2\pi \frac{\mathbf{a}_3 \times \mathbf{a}_1}{\mathbf{a}_1 \cdot (\mathbf{a}_2 \times \mathbf{a}_3)} \,;\; \mathbf{b}_3 = 2\pi \frac{\mathbf{a}_1 \times \mathbf{a}_2}{\mathbf{a}_1 \cdot (\mathbf{a}_2 \times \mathbf{a}_3)} \,. \tag{3.26}$$

Thus, each node in the reciprocal lattice is defined as

$$\mathbf{G}_\mathrm{n} = \mathbf{G}_\mathrm{hkl} = h\mathbf{b}_1 + k\mathbf{b}_2 + l\mathbf{b}_3 \,, \tag{3.27}$$

where hkl are integers also known as Miller indices.

Combining Eq. (3.25) with Eq. (3.24) and applying the Fourier convolution theorem, the resulting scattering amplitude than can be expressed as [51]

$$A(\mathbf{q}) = -r_e F_{uc}(\mathbf{q}) \cdot \Big[\frac{(2\pi)^3}{V_{uc}} \sum_{\mathrm{hkl}} \delta(\mathbf{q} - \mathbf{G}_{\mathrm{hkl}})\Big] * s'(\mathbf{q})\,. \tag{3.28}$$

The first term $F_{uc}(\mathbf{q})$ is the unit cell structure factor defined as

$$F_{uc}(\mathbf{q}) = \sum_j f_j(\mathbf{q}) e^{-W_j(\mathbf{q})} e^{i\mathbf{q}\mathbf{r}_\mathrm{j}}\,. \tag{3.29}$$

Here $f_j(\mathbf{q})$ and $\mathbf{r}_\mathrm{j}$ are the atomic form factor and the position of the jth atom in the unit cell. The thermal oscillation of atoms is taken into account by Debye-Waller factor $W_j(\mathbf{q})$ [104].

In Eq. (3.28) $s'(\mathbf{q})$ is the Fourier transform of a shape function, which takes into account a finite size of a crystal and causes an additional intensity distribution in the vicinity of each Bragg peak. In the case of the crystal of rectangular cuboid shape

$$s_{rect}(\mathbf{q}) = \begin{cases} 1\,,\ -L_1/2 < x < L_1/2\,,\ -L_2/2 < y < L_2/2\ ,-L_3/2 < z < L_3/2\,, \\ 1/2\,,\ x = \pm L_1/2\,,\ y = \pm L_2/2\,,\ z = \pm L_3/2\,, \\ 0\,,\ \text{otherwise}\,, \end{cases} \tag{3.30}$$

where L_1, L_2, and L_3 are length width and height of the crystal, respectively. The Fourier transform of s_{rect} is a sinc function

$$s'(\mathbf{q}) = C\Big[L_1 \frac{\sin(\mathbf{q}_\mathrm{x} L_1/2)}{\mathbf{q}_\mathrm{x} L_1/2}\Big]\Big[L_2 \frac{\sin(\mathbf{q}_\mathrm{y} L_2/2)}{\mathbf{q}_\mathrm{y} L_2/2}\Big]\Big[L_3 \frac{\sin(\mathbf{q}_\mathrm{z} L_3/2)}{\mathbf{q}_\mathrm{z} L_3/2}\Big]\,, \tag{3.31}$$

where C is a constant. From Eq. (3.28) and Eq. (3.31) we can conclude that the intensity in the peak center is proportional to the square of the crystal volume V

$$I_{peak} = |AA^*| \sim L_1^2 L_2^2 L_3^2 = V^2\,. \tag{3.32}$$

From Eq. (3.31) we can see that the size of the peak is inversly proportional to the crystal size in the corresponding direction, therefore the integrated intensity of the Bragg peak I_{int} is directly proportional to the crystal volume $I_{int} \sim V$. In the case of a more complicated crystal shape the exact equation describing the peak shape may vary slightly but the tendency is the same. It is worth to notice that in the case of infinite crystal the sinc function reduces to delta function.

Now let us discuss the second component in the Eq. (3.28). It is obvious that it takes nonzero values only if the scattering vector is equal to one of the reciprocal lattice

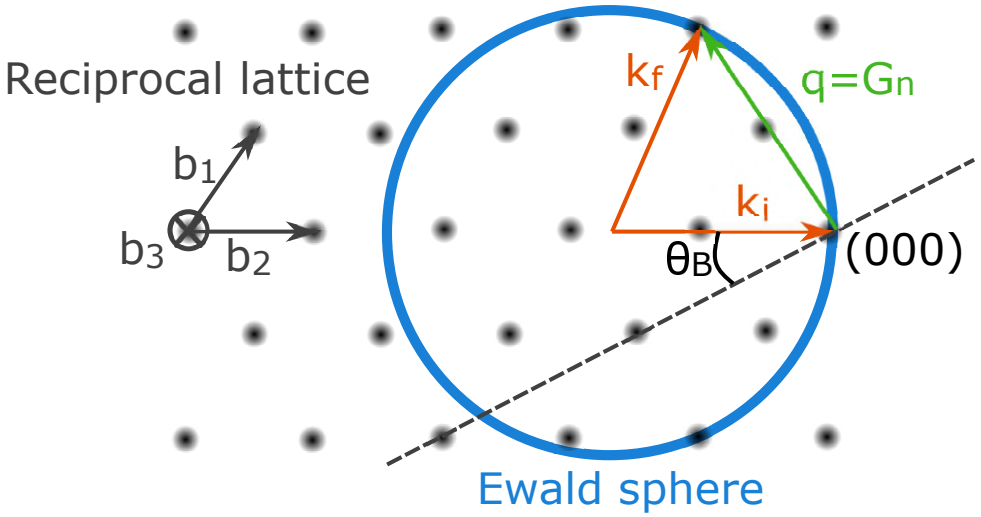

Figure 3.7: Schematic representation of the Ewald sphere. Reciprocal lattice points of a crystal with the basis vectors $\mathbf{b}_1$; $\mathbf{b}_2$; $\mathbf{b}_3$ are shown by grey dots. Scattering vector $\mathbf{k}_i$ points at the origin of the reciprocal space (000), and vectors $\mathbf{k}_f$ and $\mathbf{q}$ form the scattering triangle. The thickness of the circle indicates the bandwidth of the incident radiation $\Delta\mathbf{k}_i$.

vectors

$$\mathbf{q} = \mathbf{G}_{hkl}\,, \tag{3.33}$$

which is called Laue diffraction condition.

The Laue diffraction condition can be represented graphically in a very elegant way using Ewald construction (see Fig 3.7). A monochromatic beam is coming to the sample with the incident wave vector $\mathbf{k}_i$. This vector points to the origin of the reciprocal space (000) and forms an angle θ_B with the crystalline planes. The vector $\mathbf{k}_f$ starts at the same point as $\mathbf{k}_i$ and ends at the position of the detector. A sphere of radius $|\mathbf{k}| = |\mathbf{k}_i| = |\mathbf{k}_f| = 2\pi/\lambda$ and origin at the beginning of wave vectors is called the Ewald sphere. It represents all achievable points in the reciprocal space and the thickness of the sphere is defined by the monochromaticity of the incident radiation. The vectors $\mathbf{k}_i$, $\mathbf{k}_f$ and $\mathbf{q} = \mathbf{k}_f - \mathbf{k}_i$ form a triangle which represents the momentum conservation law. As can be seen from Fig. 3.7 if the Ewald sphere intersects with a reciprocal lattice point, the Laue condition is fulfilled, and the Bragg peak is observed at the detector. The absolute value of the $\mathbf{G}_{hkl}$ can be geometrically obtained from the Laue condition and Fig. 3.7

$$|\mathbf{G}_{hkl}| = 2|\mathbf{k}| \sin\theta_B\,. \tag{3.34}$$

Each point in the reciprocal space corresponds to the group of parallel equidistant crystallographic planes. The interplanar distance is defined by the modulus of the reciprocal lattice vector

$$d_{hkl} = \frac{2\pi}{|\mathbf{G}_{hkl}|}\,. \tag{3.35}$$

Combining Eq. (3.34) and Eq. (3.35) we obtain the Bragg's law

$$n\lambda = 2d_{hkl}\sin\theta_B\,. \tag{3.36}$$

3.4 Grazing Incidence Small Angle X-ray Scattering

Grazing Incidence Small–Angle X-ray Scattering (GISAXS) is a scattering technique that combines concepts from transmission small-angle scattering, grazing-incidence diffraction, and diffuse reflectometry. It uses the form factors and structure factors from small–angle scattering, the scattering geometry from grazing incidence diffraction and the scattering theory of the distorted wave Born approximation (DWBA) [92, 105, 106]. The DWBA was first introduced by S. Sinha in 1988 [92] and GISAXS was experimentally realized in 1989 by Joanna Levine and Jerry Cohen [107] to study the dewetting of gold deposited on a glass surface. Further, this method was improved by Naudon [108] in 1995 to study metal agglomerates on surfaces and in buried interfaces [109]. Recently different modifications of GISAXS such as Grazing Incidence Wide–Angle X-ray Scattering (GIWAXS) or Grazing Incidence Transmission Small–Angle X-ray Scattering (GTSAXS) were reported [11, 110]. It is worth to notice that grazing incidence can be experimentally realized using neutrons (grazing incidence small–angle neutron scattering, GISANS).

Here we provide a basic theoretical description of Grazing Incidence Small Angle X-ray Scattering (GISAXS) and Grazing Incidence Transmission Small Angle X-ray Scattering (GTSAXS), following [11, 106]. The typical scheme of a scattering experiment is shown in Fig. 3.8. Let us consider a grazing incidence X-ray diffraction experiment with a wavelength λ coming to the sample under the angle α_i. Here only the elastic scattering is taken into account, therefore the wavevectors are defines as $|\mathbf{k}_\mathrm{i}| = |\mathbf{k}_\mathrm{f}| = 2\pi/\lambda$ and the scattering vector is defined as $\mathbf{q} = \mathbf{k}_\mathrm{f} - \mathbf{k}_\mathrm{i}$. Considering the scattering geometry, we obtain the following equations for the projections of the scattering vector

$$q_x = k_0[\cos(2\theta_f)\cos(\alpha_f) - \cos(\alpha_i)]\,, \tag{3.37}$$

$$q_y = k_0\sin(2\theta_f)\cos(\alpha_f)\,, \tag{3.38}$$

$$q_z = k_0[\sin(\alpha_f) + \sin(\alpha_i)]\,, \tag{3.39}$$

where $k_0 = |\mathbf{k}_\mathrm{f}| = |\mathbf{k}_\mathrm{i}|$, and α_f and $2\theta_f$ are in-plane and out-of-plane scattering angles

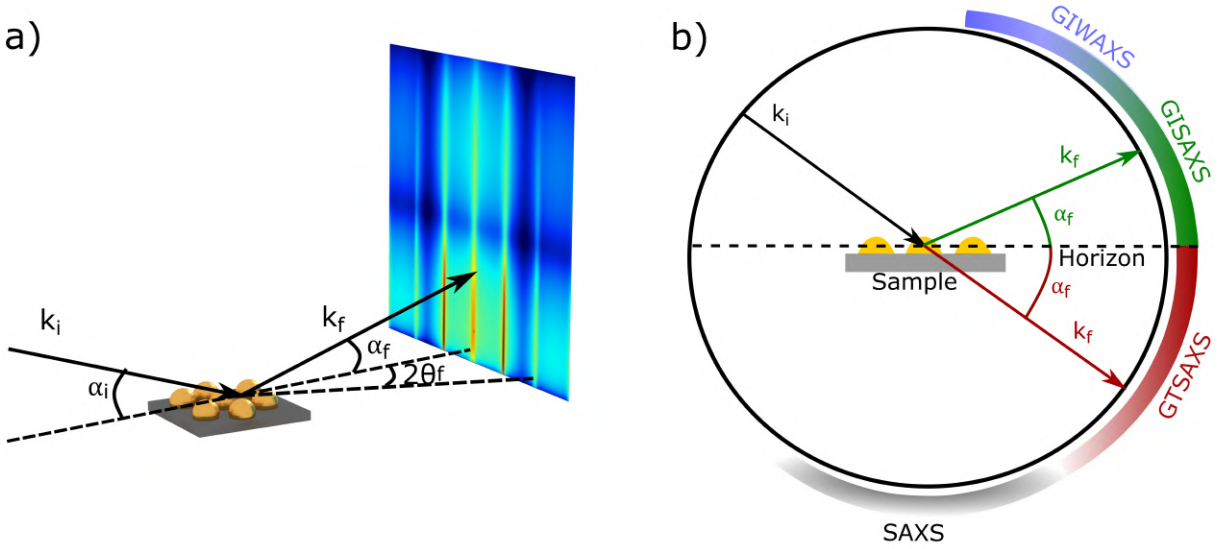

Figure 3.8: (a) Scheme of scattering geometry of the GISAXS experiment. The incident beam with a wave vector k_i enters the sample surface at a grazing angle α_i. The scattered beam with a wave vector k_f is defined by the in-plane and out-of-plane scattering angles $2\theta_f$ and α_f, respectively.(b) A two-dimensional Ewald sphere illustration of the GIWAXS, GISAXS, GTSAXS and SAXS regimes. The dashed line marks the horizon. The rather large grazing incident angle shown is for illustrative purposes. The figure was adapted from Reference [11].

of the $\mathbf{k}_f$. The lateral component is defined as

$$q_{||} = \sqrt{q_x^2 + q_y^2}\,. \tag{3.40}$$

By using the specular scattering, we are sensitive to a depth information only, but measuring the lateral scattering component makes it possible to investigate the in-plane structure of the sample.

In order to analyze the obtained scattering, the Distorted Wave Born Approximation (DWBA) is used [92]. According to the DWBA theory, in total, four scattering amplitudes contribute to the resulting scattering signal from a single particle:

- the amplitude of kinematical scattering in a particle described by the first Born approximation,
- the reflection from a substrate followed by the scattering event in a particle,
- the scattering in a particle followed by the reflection from a substrate,
- the reflection from a substrate followed by the scattering event and subsequent reflection from the substrate.

These scattering channels are schematically shown in Fig. 3.9. Following DWBA formalism the resulting scattering amplitudes for the particle on top of a substrate can be calculated as follows

$$A_1(\mathbf{q}) = \int S(\mathbf{r}) e^{-i(\mathbf{q}_{||}+\mathbf{q}_{z,1})\mathbf{r}} dr\,, \tag{3.41}$$

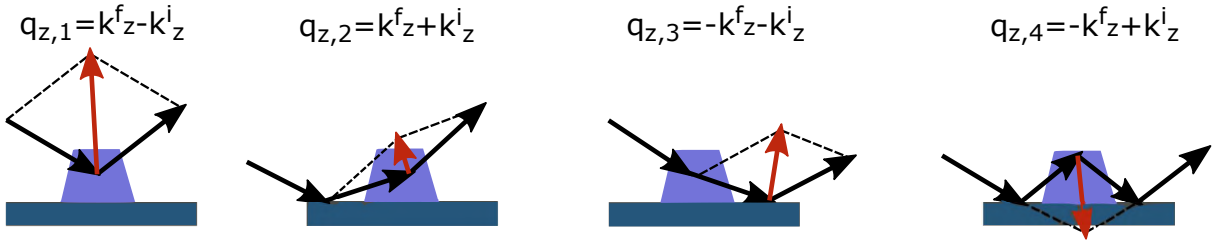

Figure 3.9: The four terms of scattering considered in DWBA in the GISAXS geometry. The first term corresponds to the simple Born approximation.

$$A_2(\mathbf{q}) = R(\alpha_i) \int S(\mathbf{r}) e^{-i(\mathbf{q}_{||}+\mathbf{q}_{z,2})\mathbf{r}} dr\,, \tag{3.42}$$

$$A_3(\mathbf{q}) = R(\alpha_f) \int S(\mathbf{r}) e^{-i(\mathbf{q}_{||}+\mathbf{q}_{z,3})\mathbf{r}} dr\,, \tag{3.43}$$

$$A_4(\mathbf{q}) = R(\alpha_i)R(\alpha_f) \int S(\mathbf{r}) e^{-i(q_{||}+\mathbf{q}_{z,4})\mathbf{r}} dr\,. \tag{3.44}$$

where $S(r)$ is the shape function of the particle, and $\mathbf{q}_{z,1}$, $\mathbf{q}_{z,2}$, $\mathbf{q}_{z,3}$ and $\mathbf{q}_{z,4}$ are defined as follows

$$\mathbf{q}_{z,1} = \mathbf{k}^f_z - \mathbf{k}^i_z\,, \tag{3.45}$$

$$\mathbf{q}_{z,2} = \mathbf{k}^f_z + \mathbf{k}^i_z\,, \tag{3.46}$$

$$\mathbf{q}_{z,3} = -\mathbf{k}^f_z - \mathbf{k}^i_z\,, \tag{3.47}$$

$$\mathbf{q}_{z,4} = -\mathbf{k}^f_z + \mathbf{k}^i_z\,. \tag{3.48}$$

$R(\alpha)$ is a reflection coefficient which is defined through the Fresnel equation

$$R(\alpha) = \frac{k_z - \tilde{k_z}}{k_z + \tilde{k_z}}\,, \tag{3.49}$$

where k_z and $\tilde{k_z}$ are z-components of the wave vector in a vacuum and substrate media, respectively. $\tilde{k_z}$ is defined as

$$\tilde{k_z} = -n_s^2 k_0^2 - |k_{||}|^2\,, \tag{3.50}$$

where $n_s = 1 - \delta_s - i\beta_s$ is the complex refractive index of the substrate and $k_{||}$ is the out-of-plane wavevector component.

Each scattering amplitude is a Fourier transform of the shape function, or the form factor of a particle. One of the most common cases is a form factor of a sphere with radius R normalized to its volume, which can be represented as [111]

$$F(\mathbf{q})_{sphere} = \left(\frac{3[\sin(|\mathbf{q}|R) - |\mathbf{q}|R\cos(|\mathbf{q}|R)]}{(|\mathbf{q}|R)^3} \right)^2. \tag{3.51}$$

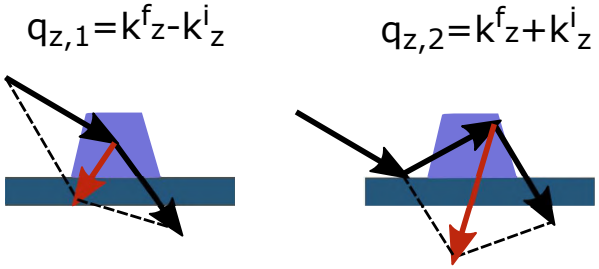

Figure 3.10: The two terms of scattering considered in DWBA in the GTSAXS geometry. The first term corresponds to the simple Born approximation.

Thus, the scattering amplitude of one particle $A_p(\mathbf{q})$ is defined as [106]

$$A_p(\mathbf{q}) = A_1(\mathbf{q}) + A_2(\mathbf{q}) + A_3(\mathbf{q}) + A_4(\mathbf{q}) = \\ = F(\mathbf{q}_{||}, \mathbf{q}_{z,1}) + R(\alpha_i)F(\mathbf{q}_{||}, \mathbf{q}_{z,2}) + R(\alpha_f)F(\mathbf{q}_{||}, \mathbf{q}_{z,3}) + R(\alpha_i)R(\alpha_f)F(\mathbf{q}_{||}, \mathbf{q}_{z,4})\,. \quad (3.52)$$

An important limitation of a GISAXS technique is that it is not possible to probe q_z close to zero [112–114]. An alternative is GTSAXS, another variation of the grazing-incidence technique. In the GTSAXS geometry, the scattering signal below the sample horizon is considered [11]. In that geometry, it is possible to probe very small q_z and also negative q_z. In GTSAXS geometry only the first two scattering channels contribute to the resulting scattering amplitude of a single particle (see Fig 3.10)

$$A_1(\mathbf{q}) = \int S(\boldsymbol{r}) e^{-i(\mathbf{q}_{||}+\mathbf{q}_{z,1})\mathbf{r}} dr\,, \quad (3.53)$$

$$A_2(\mathbf{q}) = R(\alpha_i) \int S(\boldsymbol{r}) e^{-i(\mathbf{q}_{||}+\mathbf{q}_{z,2})\mathbf{r}} dr\,, \quad (3.54)$$

and the scattering amplitude of one particle $A_p(\mathbf{q})$ is defined as

$$A_p(\mathbf{q}) = A_1(\mathbf{q}) + A_2(\mathbf{q}) = F(\mathbf{q}_{||}, \mathbf{q}_{z,1}) + R(\alpha_i)F(\mathbf{q}_{||}, \mathbf{q}_{z,2})\,. \quad (3.55)$$

In the case of N monodisperse particles, the total scattering amplitude A_{tot} is the sum of the scattering amplitudes from each particle with a radius-vector $\mathbf{r}_i$

$$A_{tot} = A_p \sum_{i=1}^{N} \exp -i\mathbf{q}\mathbf{r}_i\,. \quad (3.56)$$

The intensity distribution is calculated as $I(\mathbf{q}) = |A_{tot}(\mathbf{q})|^2$.

Comparison of three different scattering techniques (GISAXS, GTSAXS, and SAXS) in terms of experimental and data analysis challenges is shown in Table 3.1. It is well seen that GTSAXS combines features of the GISAXS (fast measurements) and conventional SAXS (scattering unperturbed by special corrections). Another advantage of GTSAXS is that due to just two scattering channels, the reconstruction of reciprocal

Table 3.1: Comparison of GISAXS, GTSAXS, and SAXS

	GISAXS	GTSAXS	SAXS
Sample	Thin film	Thin film	Any
Beam size	Focused	Focused	Any
Incinence angle	Small enough for strong reflection signal	Large enough to avoid refraction	Any
Collection time	Fast	Fast	Long
Signal	Strong	Strong	Weak
Modeling	4 scattering amplitudes	2 scattering amplitudes	Born approximation
Analysis	Difficult	Relatively easy	Easy

space may be obtained much faster and easier than for GISAXS.

Due to the rapid improvement of the synchrotron sources in the last decades, GISAXS became an extremely useful technique for the investigation of the dynamic structural changes in physical and chemical processes at surfaces and in films. GISAXS was used for the investigation of nanostructured surfaces by Hexemer and Müller-Buschbaum [110, 115], and was successfully applied to investigate the surface and bulk morphology of polymer films [116, 117], surface roughness, and roughness correlations [118–120]. Also, it was reported on the research of the lithographically produced structures [121, 122]. An important advantage of the grazing incidence geometry is that due to the large beam footprint on the sample, less measurement time is needed, which opens the possibility of *in-situ* measurements. It was reported on the *ex–situ* and *in–situ* studies of active layer of solar cells [123–125]. GISAXS technique is widely used for the studies of the deposition growth kinetics of different materials [126, 127]. Also, this method was shown to be highly useful for investigation of the mesocrystal self–assembly growth [16]. In the future, GISAXS techniques may be used for characterizing biological samples, such as proteins, peptides, or viruses attached to surfaces or in lipid layers.

3.5 Angular X-ray Cross-Correlation Analysis

In this section, we discuss Angular X-ray Cross Correlation Analysis (AXCCA), a novel method capable of the angular distribution analysis of the diffracted intensity, also known as the Fluctuation X-ray Scattering (FXS). This method was first introduced by Z. Kam [128, 129] to study the structure of bioparticles by analyzing angular correlations of the scattered intensity. Soon the first experimental realization of the AXCCA was performed using the optical light scattering on the colloidal systems [130, 131].

Here we briefly summarize the main concepts of the AXCCA following [132]. Let us consider a transmission X-ray diffraction experiment with an X-ray wavelength λ.

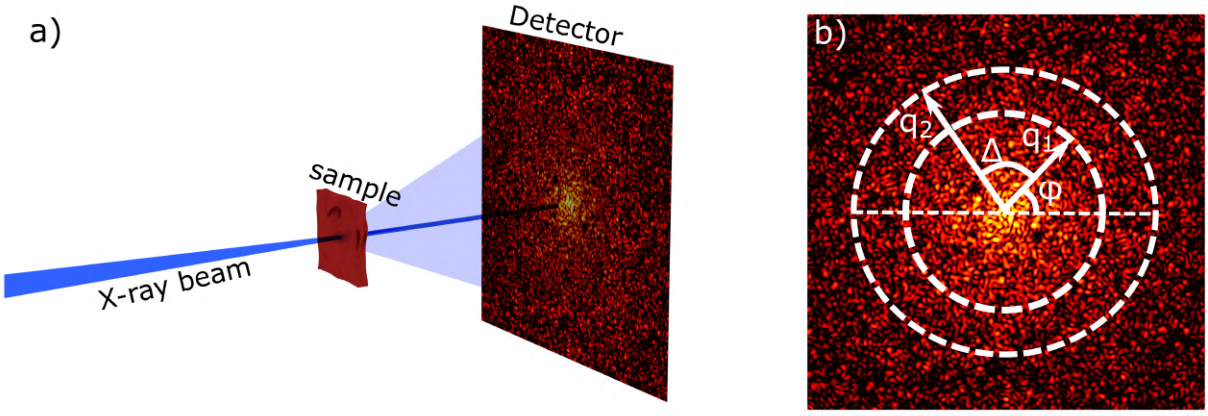

Figure 3.11: a) Scheme of the transmission geometry diffraction experiment. The detector is positioned downstream from the sample perpendicular to the incoming X-ray beam. The intensity of the diffraction pattern is coded by color. b) Outline of the CCF calculation. White arrows point to the momentum transfer values q_1 and q_2. The angle Δ between these Bragg peaks is shown.

The diffraction pattern is recorded by the 2D detector located perpendicular to the incident beam as shown in Fig. 3.11a. The scattering vector is defined as $\mathbf{Q} = \mathbf{k}_f - \mathbf{k}_i$. Here only the elastic scattering is taken into account, therefore $|\mathbf{k}_i| = |\mathbf{k}_f| = 2\pi/\lambda$ and the scattering vector is defined as $\mathbf{Q} = \frac{4\pi}{\lambda}\sin(\theta)$, where 2θ is the scattering angle. Let's introduce the cylindrical coordinates $\mathbf{Q} = \mathbf{Q}(q, \varphi, q_z)$, where q_z is perpendicular to the detector. Thus the scattered intensity at the detector can be written as $I(q, \varphi)$.

AXCCA is based on the analysis of a two-point angular cross-correlation function (CCF) [12, 13, 133]. The two-point CCF can be calculated for each diffraction pattern as

$$C(q_1, q_2, \Delta) = \langle I(q_1, \varphi) I(q_2, \varphi + \Delta) \rangle_\varphi \,, \tag{3.57}$$

where $0 \leq \Delta \leq 2\pi$ is the angular coordinate and $\langle ... \rangle_\varphi$ denotes the average over the angle φ

$$\langle f(\varphi) \rangle_\varphi = \frac{1}{2\pi} \int_0^{2\pi} f(\varphi) d\varphi \,. \tag{3.58}$$

All values used in this definition are shown in Fig. 3.11b. Here we should note that consideration of third and higher order CCFs is possible.

Often the scattering intensity is normalized in different ways:

$$I_{norm}(q, \varphi) = I(q, \varphi) - \langle I(q, \varphi) \rangle_\varphi \,, \quad I_{norm}(q, \varphi) = \frac{I(q, \varphi)}{\langle I(q, \varphi) \rangle_\varphi}$$
$$\text{or} \quad I_{norm}(q, \varphi) = \frac{I(q, \varphi) - \langle I(q, \varphi) \rangle_\varphi}{\langle I(q, \varphi) \rangle_\varphi} \,. \tag{3.59}$$

In order to investigate the symmetry properties of the CCF let us expand it into the Fourier series

$$C(q_1, q_2, \Delta) = \sum_n C_n(q_1, q_2) e^{-in\Delta}\,, \tag{3.60}$$

with the complex Fourier coefficients

$$C_n(q_1, q_2) = \frac{1}{2\pi} \int_0^{2\pi} C(q_1, q_2, \Delta) e^{-in\Delta} d\Delta\,. \tag{3.61}$$

By substituting Eq. (3.57) in Eq. (3.61) and applying the convolution theorem we get

$$C_n(q_1, q_2) = I_n^*(q_1) I_n(q_2)\,, \tag{3.62}$$

where I_n are the Fourier coefficients of the intensity and asterisk denotes the complex conjugate. In particular case, when the orientational order in the system is characterized by a single length scale, one may consider $q_1 = q_2$ and $C(q, \Delta) = C(q, q, \Delta)$. Thus, information about the complex phase of the Fourier components of the $I_n(q)$ is lost, and Eq. (3.62) is reduced to

$$C_n(q) = |I_n(q)^2|\,. \tag{3.63}$$

In practice it is common to deal with CCFs averaged over many realizations of the system

$$\langle C(q_1, q_2, \Delta) \rangle = \frac{1}{N} \sum_{i=1}^{N} C^i(q_1, q_2, \Delta)\,. \tag{3.64}$$

where N is the total number of the diffraction patterns corresponding to different realizations of the system. Due to the linearity property of the Fourier transform, the Fourier coefficients also can be averaged

$$\langle C_n(q_1, q_2, \Delta) \rangle = \frac{1}{N} \sum_{i=1}^{N} C_n^i(q_1, q_2, \Delta)\,. \tag{3.65}$$

It is important to note that while the direct averaging of the diffraction patterns causes the smearing of a signal, the averaging of the CCFs enhances symmetry features.

While working on the experimental data, different issues should be addressed. First, experimentally obtained diffraction patterns contain features that block the scattering signal, such as detector gaps, beamstop, beamstop holder, etc. In order to take their presence into account,a mask function should be introduced

$$M(q, \varphi) = \begin{cases} 0, & \text{gaps, beamstop, etc.} \\ 1, & \text{otherwise}\,. \end{cases} \tag{3.66}$$

The CCF becomes

$$C(q_1, q_2, \Delta) = \int_{-\pi}^{\pi} I(q_1, \varphi) M(q_1, \varphi) I(q_2, \varphi + \Delta) M(q_2, \varphi + \Delta)\,. \tag{3.67}$$

Another experimental challenge is finding accurately the center of the diffraction pattern. As can be seen from Fig. 3.11, if the center of the polar coordinate system does not coincide with the center of the diffraction pattern, the angular intensity $I(q, \varphi)$ has some additional modulations. These modulations may lead to the unphysical low-frequency harmonics in the CCFs. To find the center of the diffraction pattern a calibration standard such as silver behenate powder can be used. This material has diffraction with well-visible Debye-Scherrer rings, and thus the position of the direct beam at the detector as well as the sample to detector distance may be accurately determined.

Also, due to the recent development of the gain-switching detectors (such as AGIPD, Jungfrau or ePix) it is important to note that AXCCA is extremely sensitive to the proper detector calibration. Without the proper calibration, these detectors can have different unphysical features, for example, increased intensity near the detector gaps. As soon as detector gaps are typically symmetrical in respect to the position of the direct beam, this may lead to the not-existing symmetry of the CCF and enhancement of its Fourier components. As soon as such detectors have multiple gains, and these features can not be treated as a regular background, the proper detector calibration is crucial for the successful performance of AXCCA.

One of the problems which can be solved by AXCCA is related to the reconstruction of the shape of an individual particle from the scattering of an ensemble of identical particles [134]. Let us consider the basic problem when the 2D structure of the particle is revealed. The reconstruction of the shape of the 2D particle by the AXCCA method consists of two steps - calculating angular cross-correlation functions, and then reconstruction of the particle shape in direct space using various iterative algorithms to solve the phase problem [135–138]. This method was studied theoretically [13, 139–144] and experimentally. It allowed to reveal the complicated shape structure of nanoparticles [145, 146]. In the case of a 3D structure the reconstruction process more challenging however knowledge about the symmetry of particles can simplify the problem of the 3D structure recovery. Thus, it is possible to determine the shape of an individual three-dimensional particle [128, 129, 147] and this method was successfully applied for reconstructing the polystyrene particles composed of two polystyrene spheres of equal diameter about 90 nm [148].

In the last decade, it was shown that AXCCA is capable of providing insights on hidden symmetries, such as bond-orientational order or partial alignment of particles in the system [132]. The AXCCA is widely used for the studies of orientational ordering in magnetic structures: in multilayer Co/Pd films [149] and in cylindrical domains in heterostructures CoPd/IrMn [150]. In [151, 152] it was demonstrated that the AXCCA

is capable of identifying additional information from powder diffraction data, that can be used to determine the structure of polycrystalline samples. Also, it was shown that using electron and X-ray diffraction, one can study orientational order in amorphous systems, using three- and four-particle correlation functions [153].AXCCA is widely exploited for the analysis of phase transitions of partially ordered systems such as colloids, liquid crystals and polymers. It was reported on the studies of the local ordering in colloidal crystals consisting of spherical polymer particles [12, 154, 155] and a change in the structure of colloidal crystals under the action of pressure [156]. Angular correlation analysis was successfully applied to analyze the orientational order in the liquid crystals during the smectic – hexatic phase transition [15, 157]. AXCCA is used to reveal the orientational order evolution of the solvated molecules excited by the laser pulse [91]. It is possible to use the angular correlation analysis for the studies of the polycrystalline samples such as polycrystalline polymer poly- (3-hexylteophene) films with the addition of gold nanoparticles [158–160]. Also, this method was shown to be highly useful to study the orientation of the nanoparticles with respect to the superlattice in mesocrystals [14, 161].

Chapter 4

Structure and properties of mesoscopic materials

Mesoscopic materials are nowadays receiving growing attention motivated largely by the various possible applications in electronics industry, nanofabrication and nanotechnology [1]. The optical and mechanical properties of mesoscopic materials are strongly affected by the orientational order and defects of the crystalline structure. A detailed understanding of the defect origin is expected to improve the design of the nanocrystal – based devices.

One of the novel examples of mesoscopic material is a mesocrystal. The tremendous potential of mesocrystals is the application for electrode materials, such as catalysts, sensors, light-emitting diodes (LEDs), or electrodes in Li-ion batteries [162]. Photodetectors based on mesocrystals may be an effective substitute for the silicon-based devices, which can not be used for the infrared light [2]. Another exiting mesoscopic material is a colloidal crystal. For the colloidal crystals, very promising is the possibility of obtaining a complete photonic band gap, which would allow to inhibit unwanted spontaneous emission and manipulate the flow of light [163]. Also, colloidal crystals have shown phononic band gaps in the gigahertz (GHz) frequency range, corresponding to picosecond timescale [164–166]. Combination of both photonic and phononic band gaps can be used for ultrafast manipulation and control of electromagnetic waves by hypersonic (GHz) acoustic waves [167].

In this chapter the structural, electrical, and optical properties of the mesoscopic materials are discussed. The first section is focused on the crystalline structures, and in particular, close-packed structures, common for mesocrystals and colloidal crystals. Different types of defects in crystal structures, such as point, line, planar, or volume defects are described. In section two and three we discuss in detail colloidal crystals and mesocrystals, respectively. A historical overview on investigation of these materials is provided and modern growth techniques are reviewed.

4.1 Crystalline structures and defects

The crystalline structure of any material can be described in terms of Bravais lattice, named after a French physicist Auguste Bravais. In three-dimensional space, Bravais lattices are obtained by combining the seven lattice systems shown in Table 4.1 with one of the 4 possible centering types - primitive, base-centered, body-centered and face-centered. From all combinations, 14 unique Bravais lattices can be constructed. In this thesis, we study two kinds of structures, colloidal crystals, and mesocrystals. The lattice types often observed in mesocrystals are face-centered cubic *(fcc)* [161], body-centered-cubic *(bcc)*, body-centered-tetragonal *(bct)* [14] and hexagonal close-packed (*hcp*) [168] structures, depending on the organic ligand. However, in general other structures are also possible. The colloidal crystals used in our work are prepared from the spherical colloidal particles, thus they tend to reach the highest possible average density, or, in other words, to form a close-packed structure [169], which is described below.

Historically the problem of close-packing of spheres was discussed in regard to piling cannonballs on ships. Sir Walter Raleigh posed this problem to the mathematician Thomas Harriot around 1587 before the expedition to America. Later, it was proven by Carl Friedrich Gauss that the highest possible average density of a lattice packing is $\pi/(3\sqrt{2}) = 0.74048$. This packing density can be achieved when spherical particles form plain hexagonal layers, and these layers occupy three specific positions A, B and C in respect to each other. These positions are schematically shown in Fig. 4.1a. The layer at the bottom is called A (black), and the above layer can occupy only one of the two possible positions B (blue) or C (red). This stacking results in the two different common close-packed structures: *fcc* with a stacking sequence ABCABCABC (see Fig. 4.1b) and *hcp* with a stacking sequence ABABABAB (see Fig. 4.1c). The displacement of crystal planes in the lateral directions causes the formation of the random hexagonal close-packed *rhcp* structure.

Table 4.1: Seven different lattice types. Here, a_1; a_2; a_3 are the unit cell parameters, α; β; γ are the angles between the basis vectors (see Fig. 3.6).

Lattice system		Edge lengths	Axial angles
Cubic		$a_1 = a_2 = a_3$	$\alpha = \beta = \gamma = 90°$
Tetragonal		$a_1 = a_2 \neq a_3$	$\alpha = \beta = \gamma = 90°$
Orthorhombic		$a_1 \neq a_2 \neq a_3$	$\alpha = \beta = \gamma = 90°$
Hexagonal	Rhombohedral	$a_1 = a_2 = a_3$	$\alpha = \beta = \gamma \neq 90°$
	Hexagonal	$a_1 = a_2$	$\alpha = \beta = 90°, \gamma = 120°$
Monoclinic		$a_1 \neq a_2 \neq a_3$	$\alpha = \gamma = 90°, \beta \neq 90°$
Triclinic		$a_1 \neq a_2 \neq a_3$	$\alpha \neq \beta \neq \gamma$

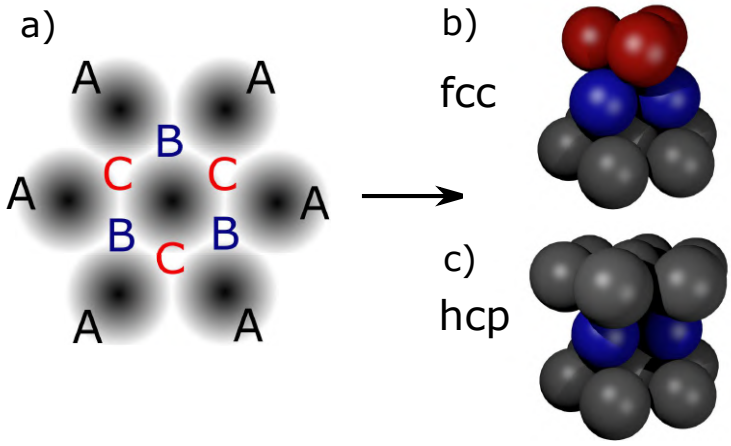

Figure 4.1: (a) Top view of three possible positions, denoted as A, B, and C, in a hexagonal close-packed layers. Side view on *hcp* (b) and *fcc* (c) structures.

4.1.1 Crystallographic defects

An interruption of regular patterns in crystalline solids is known as a crystallographic defect. The defects appear due to the inaccuracy of the positions of atoms in a perfect periodic crystal structure caused by the fluctuations of energy at $T > 0$ K. The defect states strongly influence on the properties of solids, such as optical properties, charge carrier mobility, and play an important role in plastic deformation of the crystal. The geometrical properties define four main types of crystallographic defects – point, line, planar and bulk defects.

Point defects

Point (zero-dimensional) defects occur only at or around a single lattice point and are not extended in space in any dimension. The most common types of point defects are:

Vacancy defect or Schottky defect, is vacant lattice sites which would be occupied in a perfect crystal (see Fig. 4.2a).

Interstitial defect is an extra atom that occupy a site in the crystal structure (see Fig. 4.2a).

Frenkel pair is a nearby pair of vacancy and interstitial defects.

Substitutional defect is the presence of an atom that is not supposed to be anywhere in the crystal (see Fig. 4.2b). If the radius of the substitutional atom is significantly different from the radius of a regular atom, the equilibrium position of atoms near the defect can be shifted away from the lattice site. The presence of the substitutional defect is common in semiconductor materials, since it allows the fine tuning of the energy band gap.

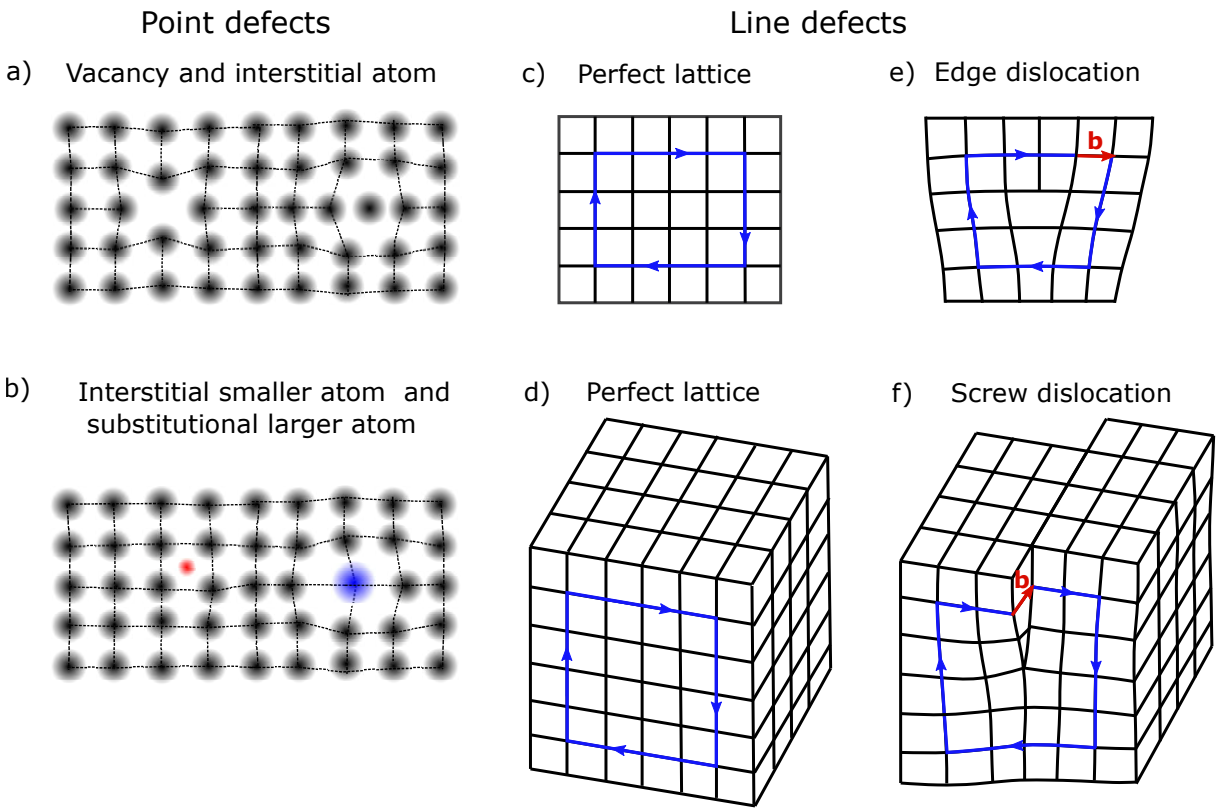

Figure 4.2: Schematic representation of the point and line defects in crystals. Three kinds of point defects, such as vacancies, interstitial atom (a), and substitutional atoms (b) are shown. Line defects include the edge (c,e) and screw dislocation (d,f). The Burgers vector is shown in (e,f) by the red arrow.

Antisite defect occurs when atoms of different type exchange positions in an ordered alloy or compound.

Point defects result in the displacement of the neighboring atoms from their equilibrium positions, thus leading to the appearance of the forbidden peaks and diffuse scattering in resulting diffraction pattern.

Line defects

Line (one-dimensional) defects are defined as defects whose size in one direction is much larger than the lattice parameter, and in the other two, is comparable with it. There are two types of line defects, dislocations, and disclinations. Dislocations are expressed by the unequal number of atoms in neighboring parts of the crystal and appear during the plastic deformation of crystals. Dislocations are characterized by a Burgers vector [102]:

$$\oint_{\Gamma} d\mathbf{u} = -\mathbf{b}, \tag{4.1}$$

where $\mathbf{u}(\mathbf{r})$ is the displacement vector field, which describes the shift of the atoms from their positions, and Γ is a closed contour around the dislocation. Thus two types of dislocations, namely edge and screw dislocations, can be defined (see Fig. 4.2(c-f)). As

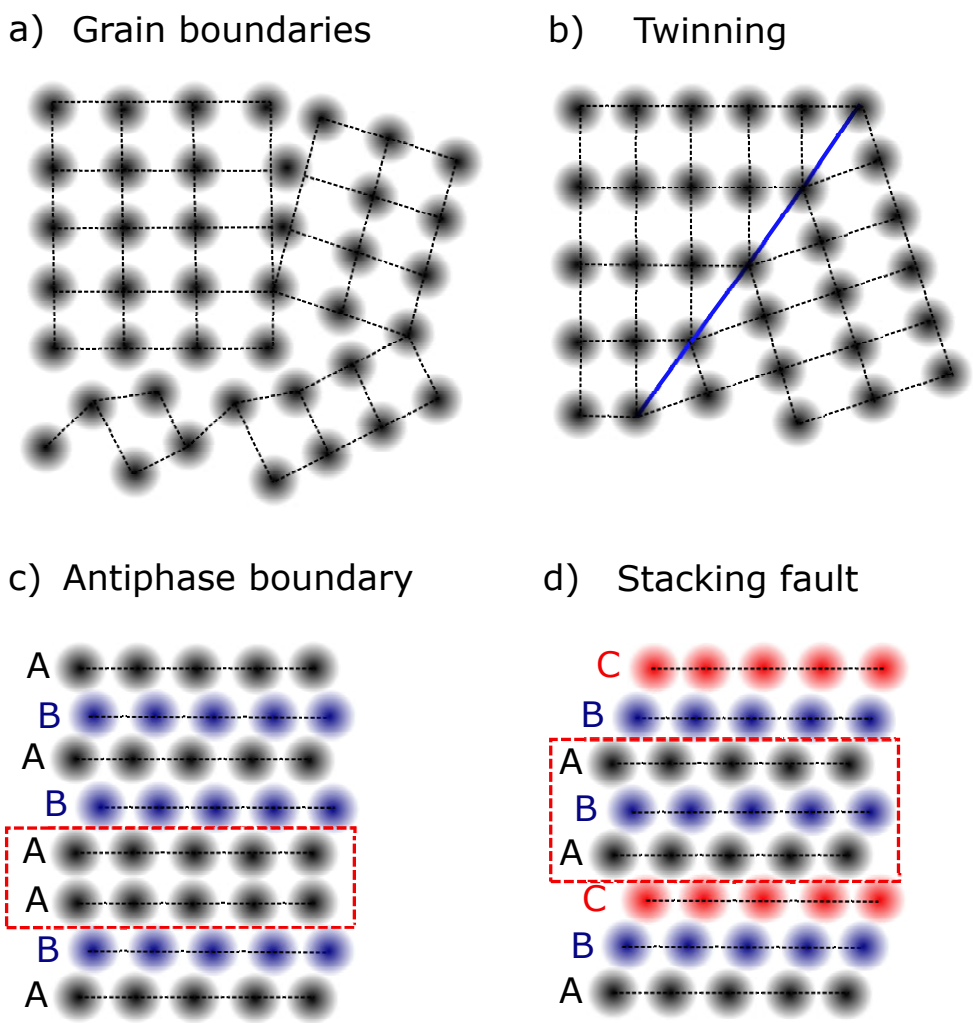

Figure 4.3: Schematic representation of the different kinds of planar defects in crystals, grain boundaries (a), twinning (b), antiphase boundary (c), and stacking faults (d). The most common example of stacking fault is found in *hcp* (e) and *fcc* (f) structures.

illustrated in Fig. 4.2(c-f) for the edge dislocation, the Burgers vector is perpendicular to the dislocation line, and for the screw dislocation, the Burgers vector is parallel to it. For all other cases, dislocations are called mixed, and they can be decomposed into screw and edge components. The other type of the line defect is disclination – topological line defect in which rotational symmetry is violated.

A general planar or two-dimensional defect is a grain boundary, which is an abrupt change of the crystallographic direction of the lattice (see Fig. 4.3a). Three of the most common planar defects are described below:

Twinning is a type of a grain boundary when a plane of mirror symmetry is introduced in the ordering of a crystal (see Fig. 4.3b)

Antiphase boundaries for hexagonal-close packed (*hcp*) structure are shown in Fig. 4.3c. If a perfect ordering is ABABABAB (hexagonal close-packed crystal), an antiphase boundary takes the form of ABAABABA.

Stacking faults is also very common for close-packed structures. The stacking fault is a local deviation of the stacking sequence of layers in a crystal. An example is shown in Fig. 4.3d, when the perfect ABCABCABC structure became ABCABABC stacking sequence. The presence of the stacking fault leads to the formation of a random close-packed hexagonal structure *rhcp*.

The crystal surface also can be called a plane defect, which causes streaks in reciprocal space called crystal truncation rods (CTR).

Bulk defects

The last type of defects is bulk or three-dimensional defects. They include such as pores, voids, cracks, or clustered impurities.

4.2 Colloidal crystals

A colloidal solution consists of particles ranging between 1 nm and 1000 nanometers in diameter suspended throughout another substance. A colloid has a dispersed phase (the suspended particles) and a continuous phase (the medium of suspension), unlike a solution whose solute and solvent constitute only one phase. The subject of interface and colloid science was first introduced in the 1840s by the Italian chemist Francesco Selmi [170]. A daily life example of a colloid is milk, an emulsified colloid of liquid butterfat globules dispersed within a water-based solution. To qualify as a colloid, the mixture must be one that does not settle or would take a very long time to sediment appreciably. Brownian motion, originating from the thermal energy, is a feature of colloidal particles that counteracts their sedimentation. The colloids are an exciting model system for atoms because both systems are governed by the similar statistical mechanics [171, 172].

The interaction of the colloidal particles in the solution can be approximated by the superposition of different interparticle forces, such as electrostatic interaction, van der Waals forces, or steric forces. The electrostatic interaction occurs due to the electrical charge carried by the colloidal particles. The van der Waals forces appear due to an interaction between two dipoles, permanent or induced [173, 174]. Thus, the short-range and attractive van der Waals forces are always present unless the refractive indexes of the dispersed and continuous phases are matched. Steric forces are nonbonding interactions between polymer-covered surfaces or in solutions containing non-adsorbing polymer. Steric effects result in repulsive forces or an attractive depletion force [175]. Also, the volume of a particle is inaccessible to other particles in the system which is called an excluded volume repulsion effect.

One of the most remarkable phenomena of the colloids is the self-organization from fluid-like structures to those exhibiting long-range spatial and/or orientational order

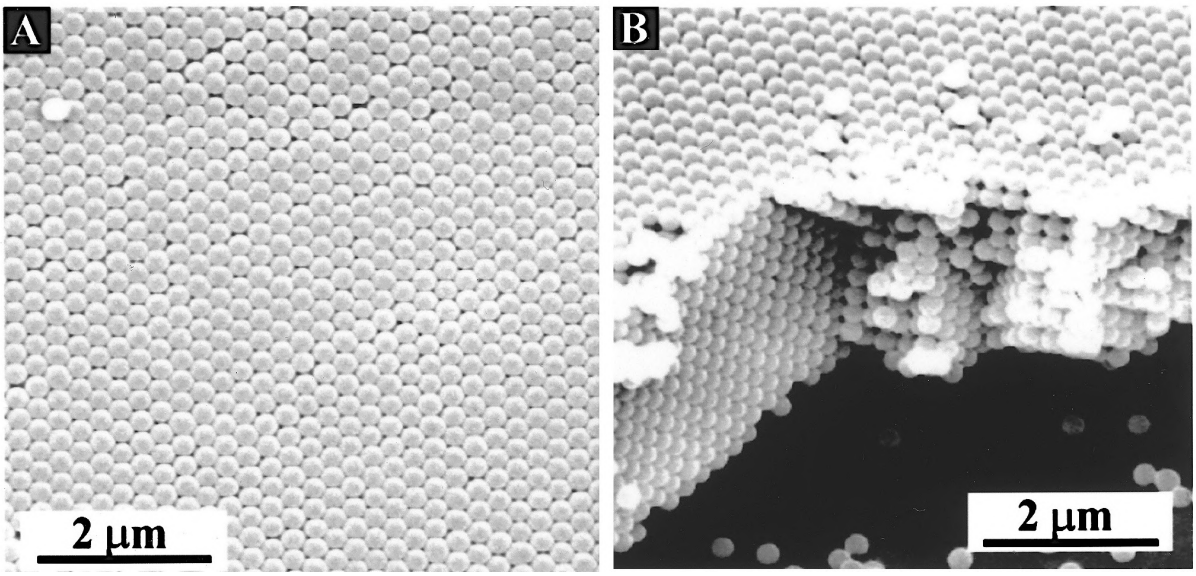

Figure 4.4: Typical scanning electron micrograph (SEM) of a silica colloidal crystal prepared using vertical deposition method from the top view (a) and side view (b). Figure was adapted from Reference [181].

(colloidal crystals and colloidal liquid crystals). For the colloidal particles, the transition occurs from a fluid state to the crystal, typically accompanied by the decease of temperature [176, 177]. Thus a colloidal crystal, a highly ordered array of particles, can be formed. This was confirmed by early computer simulations in the 1950s, and later the first colloidal crystals were observed in the systems of charged latex particles [178]. A scanning electron micrograph of a colloidal crystal is shown in Fig. 4.4. One of the natural examples of such self-organization of the colloidal particles is the precious opal. The internal structure of these gemstones consists of highly ordered close-packed arrays of amorphous colloidal spheres of silicon dioxide, which are formed after years of sedimentation and compression under hydrostatic and gravitational forces [179, 180].

Colloidal crystals have a possibility of obtaining a complete photonic band gap, and due to that feature, they can be used as photonic crystals, periodic optical nanostructures that affect the motion of photons. The photonic band-gap in the periodic dielectric structures was first discovered by the English physicist Lord Rayleigh in 1887 [182], and the research interest grew further with the work by Eli Yablonovitch and Sajeev John in 1987 [183, 184], who also invented the term 'photonic crystal'. Nowadays, natural and artificial photonic crystals are the focus of many investigations [185–188], and also they are in widespread use for commercial applications. For example, one-dimensional photonic crystals are applied in the form of thin-film optics or even for color changing paints and inks [189–191]. Three-dimensional photonic crystals may be useful for various applications, such as optical chips [192] or more efficient photovoltaic cells [193].

The functional properties of the colloidal crystal are influenced by the crystal quality and, in particular, defects in the crystal structure. However, the fabrication process

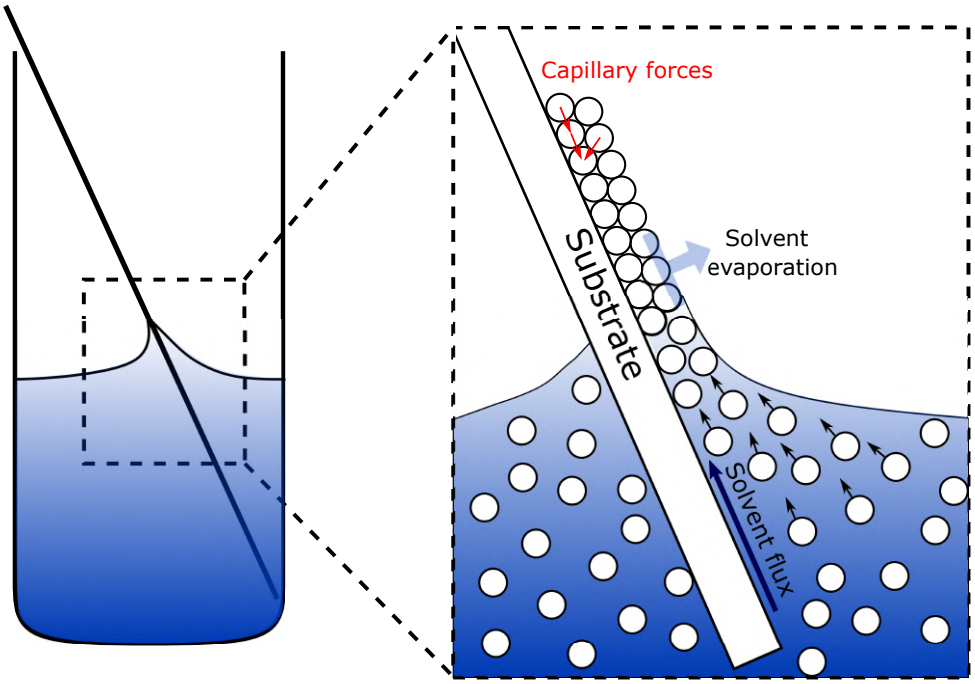

Figure 4.5: Schematic outline of the vertical deposition, the common procedure to assemble colloidal crystals into 3D crystalline structures. Figure was adapted from Reference [194].

of the 2D and 3D colloidal crystals faces some major challenges. One of them is producing high-quality colloidal crystals to prevent scattering losses which are blurring the crystal properties. The second challenge is inventing such a designing process that can robustly mass-produce cheap photonic crystals. Thus, self-organized colloidal crystals are promising cheap alternative for photonic crystal production.

Colloidal crystals can be prepared artificially using several methods of which the most convenient are sedimentation in a gravitational field, or controlled evaporation of the solvent. During sedimentation under the gravitational field the particles slowly settle at the bottom of the solution. The settling is counterbalanced by the Brownian diffusion of the particles, therefore only the limited control of the sedimentation speed of the particles can be achieved. Furthermore, crystallization nuclei form at different locations, which results in a polycrystalline structure with different domain sizes.

The second commonly used growth technique is the controlled drying of a dispersion containing a low concentration of monodisperse colloids. The colloidal particles are driven by the convective flow to the meniscus and pulled together by strong capillary forces they form a close-packed structure on the substrate. The schematic representation of the process is shown in Figure. 4.5 for the most commonly used convective assembly setup, the vertical deposition setup. This setup was first introduced by Jiang et al. [181] and was improved over the years [195, 196]. In this method, the thickness and uniformity of the colloidal crystals can be controlled by several experimental factors such as the particle flux, particle size and material, volume fraction, solvent, substrate material, and orientation, humidity, temperature and temperature gradient.

Thus, much higher control over the crystal quality can be achieved compared to the sedimentation method.

Colloidal crystals grown using the vertical deposition method form a close-packed structure consisting of hexagonal layers of spheres stacked on top of each other. The two simplest periodic sequences of these layers form an *hcp* or *fcc* structures, described in detail in the previous section. The hexagonal order of spheres is well seen at the SEM image of the colloidal crystal in Figure 4.4. Due to the small free-energy difference between *fcc* and *hcp* [197, 198] a random mixture of these two stacking types, so-called random hexagonal close-packed (*rhcp*) structure, might be observed [199, 200]. Also, the self-assembly process can result in other types of defects such as point defects, line defects, planar defect and bulk defects. These different types of defects observed in self-assembly structures (such as colloidal crystals or mesocrystals) are also described in the previous section.

The research presented in this thesis deals with the colloidal crystals prepared from polystyrene spheres by the vertical deposition method (see Figure 4.5). In Chapter 5 the structural rearrangement of polystyrene colloidal crystals under dry sintering conditions has been revealed by *in situ* grazing incidence X-ray scattering and in Chapter 8 we discuss the IR pump–X-ray probe diffraction experiment performed at XFEL on a periodic polystyrene colloidal crystals.

4.3 Mesocrystals

Mesocrystal is an abbreviation for mesoscopically structured crystal, a material consisting of numerous nanocrystals (NCs) with a typical size of 1 nm – 1000 nm, which are periodically arranged in a superlattice. In this form, nanocrystals are spatially separated, unlike in the form of oriented aggregation of nanoparticles (see Figure 4.6). These structures were named "mesocrystals" by Helmut Cölfen in 2005 during his studies on biominerals [201]. The unique crystallographically hierarchical structure is the criterion for determining whether a material is mesocrystal. However, the term mesocrystal had been used before for crystalline materials of mesoscopic size or of mesoporous structure [202, 203]. Mesocrystal can be composed from monodispersed or polydispersed nanoparticles. The unique features and physical properties of mesocrystals made them promising in many different applications, such as photocatalysts, electrodes, optoelectronics, biomedical materials, and lightweight structural materials.

Mesocrystals are often viewed as large-scale analogs to crystalline lattices of atoms. In line with this analogy, homogenous NC ensembles crystallize in common structures, such as *fcc*, *bcc*, *bct*, or *hcp* arrangements [16, 204–207]. Such ordered superlattices are held together by directional forces between adjacent nanocrystals, which span a wide

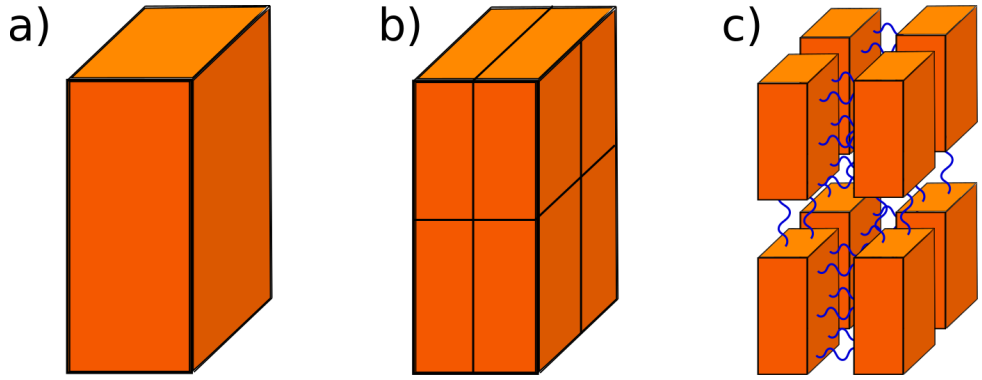

Figure 4.6: Schematic outline of the single crystal (a), oriented aggregation of nanoparticles (b), and mesocrystal (c). The borders of the monocrystalline domains are shown by the black lines and organic ligands by the blue lines.

spectrum from weak van-der-Waals interactions to ionic and covalent bonds [204, 208, 209]. The nanoparticles in the mesocrystal are faceted single crystals (for e.g. truncated cubes). Anisotropic, facet-specific interactions invoke the orientational order of NCs into mesocrystalline assemblies with a global angular correlation between the superlattice and the atomic lattices of its NCs [14, 210]. When these interactions are weakened, e.g. due to stress induced by polydisperse NCs or by uniaxial strain applied to the superlattice, defects occur which lead to the manifestation of grain boundaries and polycrystallinity [211, 212].

In this thesis, we focus on Coupled Organic-Inorganic Nanostructures (COINs) composed from the PbS nanoparticles connected via organic surfactants, which shall be referred to as ligands hereafter. The electron levels of the nanoparticles are discrete, and conducting properties of nanocrystals strongly depend on the size of the particle. Nanostructures discussed in this thesis have two types of coupling between nanoparticles and ligands: electronic coupling via potentially near-resonant alignment of suitable energy levels, and chemical coupling through a strong binding interaction [3]. The conducting properties of such structures are determined by the energy alignment between the highest hole level ($1S_h$) and lower electron level ($1S_e$) of the nanoparticle, and the highest occupied molecular orbital (HOMO) and lowest unoccupied molecular orbital (LUMO) of the organic ligand. Different possible configurations of this alignment are shown in Fig. 4.7. Typical ligands used in the mesocrystal synthesis are big organic molecules, for example, oleic acid. Such molecules have a wide HOMO–LUMO gap, and it often results in a type-I alignment in which the photo-generated excitation is confined to the NC (see Fig. 4.7). However, some NCs (e.g. CdSe or CdS) like have relatively low ($1S_h$) states, which may result in a type-IIa alignment. In inorganic-inorganic PbSe-CdSe/CdS, a type-IIb alignment in which the hole is confined to the core but the electron migrates to the ligand is also possible.

The transport properties of the mesocrystal depend on the misalignment of the energy levels in one nanoparticle. The energy transport has maximum efficiency when

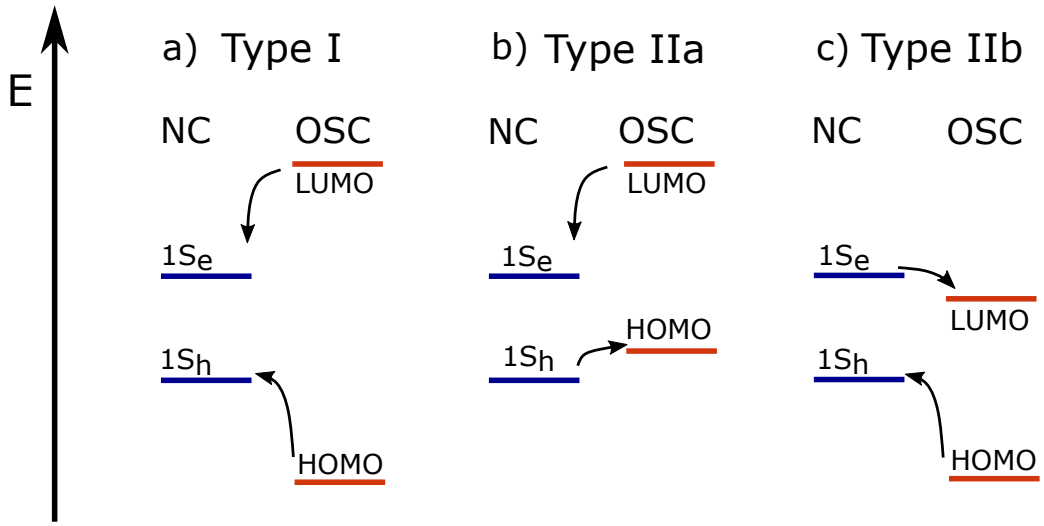

Figure 4.7: Schematic outline of the energy alignment between the highest hole level ($1S_h$) and lowest electron level ($1S_e$) of the nanocrystal (NC) and the highest occupied molecular orbital (HOMO) and lowest unoccupied molecular orbital (LUMO) of the organic semiconductor (OSC). Three different types of the energy alignment are shown. Figure was adapted from Reference [3].

the resonance between the neighboring nanoparticles occurs, and energy levels coincide. This parameter is influenced by the size variation of the nanoparticles and defects in the mesocrystal. Thus, a detailed understanding of the mesocrystal formation processes is expected to improve the design of nanocrystal superlattices with tailored mechanical, electric, and optical properties.

The formation mechanisms of various nanostructured materials have been studied for several decades, but the dedicated investigation of the mesocrystals only started about ten years ago. Since then, based on the studies of the mesocrystal structure, the classification of the mesocrystal formation principles was developed. Mesocrystals can be formed by various methods such as nanoparticle alignment by organic matrix, ordering by physical fields, formation with mineral bridges, and self-similar growth [213, 214]. The alignment by the organic matrix (biomineralization) is how mesocrystals are produced in nature. Examples of naturally formed mesocrystals are sea urchin spines [215], nacre [216], corals [217–220], or eggshells [221]. The presence of mesocrystals in nature proves the evolutionary advantages of such structures.

Artificially synthesized mesocrystals are typically inorganic nanoparticles connected via organic ligands. In most cases, mesocrystals are formed in the solution ordered by physical fields like tensorial polarization forces and dipole fields. Another common method for mesocrystal formation is the self-organization of nanoparticles, which are stabilized by organic molecules. The only requirement for these is a confined space where nanoparticles have no choice but to align with each other. These method was used to compose mesocrystal from different materials, such as Ag, Au, PbS, PbSe, CeO2, FePt, CoPt3, Fe3O4, PbSe/Au, Fe2O3/PbSe, PbSe/Pd, CdSe/PbSe, etc [222–

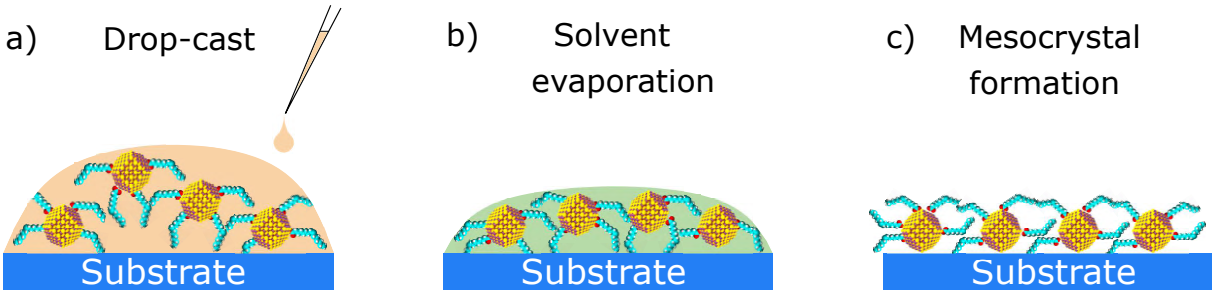

Figure 4.8: Schematic outline of the mesocrystal synthesis via drop-casting.(a) A small droplet is distributed over a solid or liquid surface, (b) followed by the controlled solvent evaporation and (c) formation of the mesocrystal.

227]. The scheme of the drop-casting, one of the several evaporation-induced self-assembly techniques, is shown on Fig. 4.8. First, a small droplet of the dilute dispersion of the nanoparticles is spread over a solid or liquid surface. The second stage is the controlled evaporation of the carrier solvent, followed by the mesocrystal formation. During the last stage, nanoparicles are forming an array or superlattice which is characterized by a high degree of directional and orientational order.

The research presented in this thesis is focused on the COINs prepared by drop-casting from PbS nanocrystals linked by oleic acid. The orientational order and defect formation of COINs was studied experimentally, using X-ray scattering methods. The experiment and the results are discussed in the next chapter.

Chapter 5

Revealing grain boundaries and defect formation in nanocrystal superlattices by nanodiffraction

Mesocrystals, or superlattices of inorganic nanocrystals (NCs) are often viewed as large-scale analogs to crystalline lattices of atoms. In line with this analogy, homogenous NC ensembles crystallize in common close-packed structures i.e. face-centered cubic (*fcc*), or hexagonal close-packed (*hcp*) arrangements. Anisotropic, facet-specific interactions invoke orientational order of NCs into mesocrystalline assemblies with a global angular correlation between the superlattice and the atomic lattices of its NCs. When these interactions are weakened, e.g., due to stress induced by polydispersity of NCs or by uniaxial strain applied to the superlattice, defects occur which leads to the manifestation of grain boundaries and polycrystallinity. Specifically, in view of the previously found correlations between the orientation of individual NCs and the superlattice, are these correlations preserved through grain boundaries, and, if so, in which way [16, 208, 209]? How does the structure change close to the grain boundaries? Addressing these fundamental questions on structure formation would also shed light on the intriguing question to which degree superlattices of NCs serve as a model for atomic crystalline systems and where this analogy ends [228].

Results of this chapter are based on Reference [161]. This chapter is focused on the studies of the the Coupled Organic-Inorganic Nanostructures (COINs) prepared from PbS particles linked by oleic acid (discussed in detail in Chapter 4). Angular X-ray cross–correlation analysis (AXCCA) in conjunction with a nanofocused X-ray beam was performed to reveal the structure and orientational order in superlattices near grain boundaries. The X-ray scattering experiments were performed at the Coherence Beamline P10 of the PETRA III synchrotron facility.

5.1 Experiment

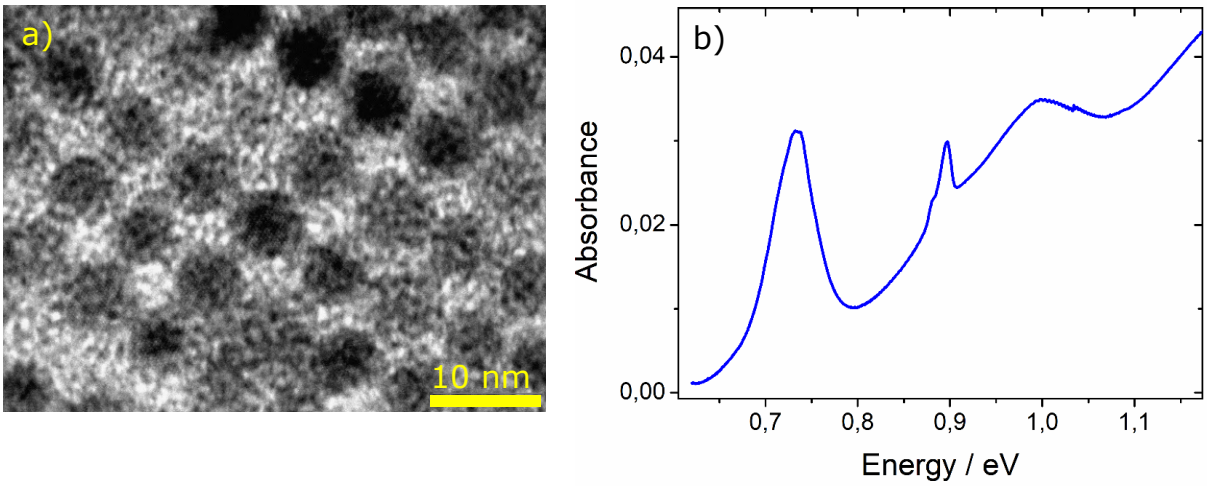

Figure 5.1: Transmission electron micrograph (a) and absorption spectrum (b) of the PbS NCs used in this study.

PbS nanocrystals of about 6.8 nm in size capped with oleic acid were synthesized following Weidman et al. [229]. The NCs were drop-cast from a hexane:octane (9:1) solution onto 5×5 mm^2 Si frames with a 500×500 µm^2 window consisting of a 50 nm-thick Si_3N_4 membrane (PLANO). The size of the PbS NCs was estimated by analysis of the absorption spectra, shown in Figure 5.1b. According to the empirical formula, the first excitonic transition at 730 meV corresponds to the average particle diameter of 6.8 nm [230]. This value is also corroborated by the transmission electron micrograph in Figure 5.1a. These samples were provided by Dr. Marcus Scheele from Tübingen University.

The X-ray diffraction experiment was performed at the Coherence Beamline P10 of the PETRA III synchrotron radiation source at DESY. The nanodiffraction endstation GINIX was used to focus an X-ray beam with energy E = 13.8 keV (λ = 0.898 Å) down to 400×400 nm^2 size with KB-mirrors [231]. The depth of the X-ray focus was about 0.5 mm. The sample was positioned perpendicular to the incoming X-ray beam as shown in Figure 5.2.

An area of 30×30 µm^2 was scanned to analyze the spatial variations of the structure of the samples. Within this scanning region, 14641 diffraction patterns were collected on a 121×121 raster grid with about 250 nm step size in both directions perpendicular to the incident beam. Each diffraction pattern was collected with an exposure time of 0.3 second to stay below the threshold of radiation damage, which was assessed by repeating the scanning procedure several times on the same position of the sample. A two-dimensional detector Eiger 4M (2070×2167 pixels with 75×75 µm^2 size) was positioned downstream at a distance of 41 cm from the sample and shifted so to have the transmitted beam close to a corner. Thus small-angle as well as wide-angle X-ray

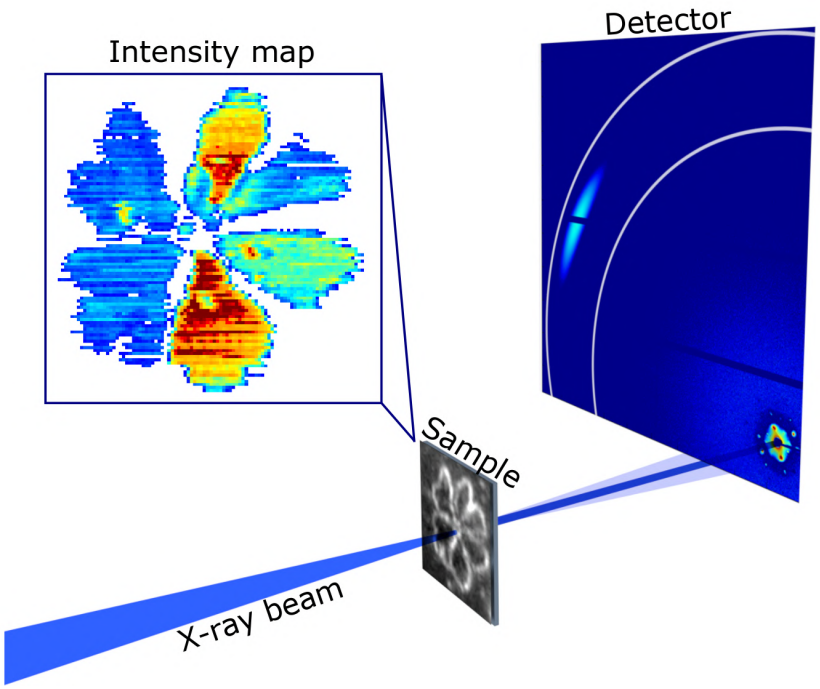

Figure 5.2: Scheme of the diffraction experiment. The sample is scanned by a nanofocused X-ray beam with the size of 400 × 400 nm^2 in transverse direction. The detector is positioned 41 cm downstream from the sample in transmission geometry and is shifted from the optical axis of the beam to measure simultaneously SL and AL Bragg peaks. The scanned map of the WAXS peak intensity between two lines marked on the detector is shown as an inset.

scattering (SAXS and WAXS) were simultaneously measured. With this geometry a part of reciprocal space in wide-angle scattering was accessible and it was possible to detect the scattering signal from the NC superlattice (SL) as well as from PbS atomic lattice (AL) simultaneously.

5.2 Definition of crystalline domains and their orientation

In order to determine the superlattice structure, SAXS and WAXS scattering of each measured diffraction pattern was analyzed. Figure 5.3a,b displays an X-ray scanning image of a polycrystalline superlattice of PbS NCs, utilizing the positions of SL peaks at $q_{SL} = 0.083$ Å^{-1} (Figure 5.3a) and of the AL peaks at $q_{AL} = 2.12$ Å^{-1} (Figure 5.3b). Throughout this chapter, all reflections, planes or crystallographic directions referring to superlattice of the PbS NCs will be denoted with the index $_{SL}$ and $_{AL}$ references to the atomic lattice. Spatial positions of the sample with the same angular orientation of peaks in SAXS (Figure 5.3d-h) and WAXS (Figure 5.3i-m) diffraction patterns are indicated by the same color and specified by diffraction patterns averaged over these areas. Grey color stands for areas with scattering signal but without a well-defined angular orientation. A comparison with an optical micrograph of the sample (Fig-

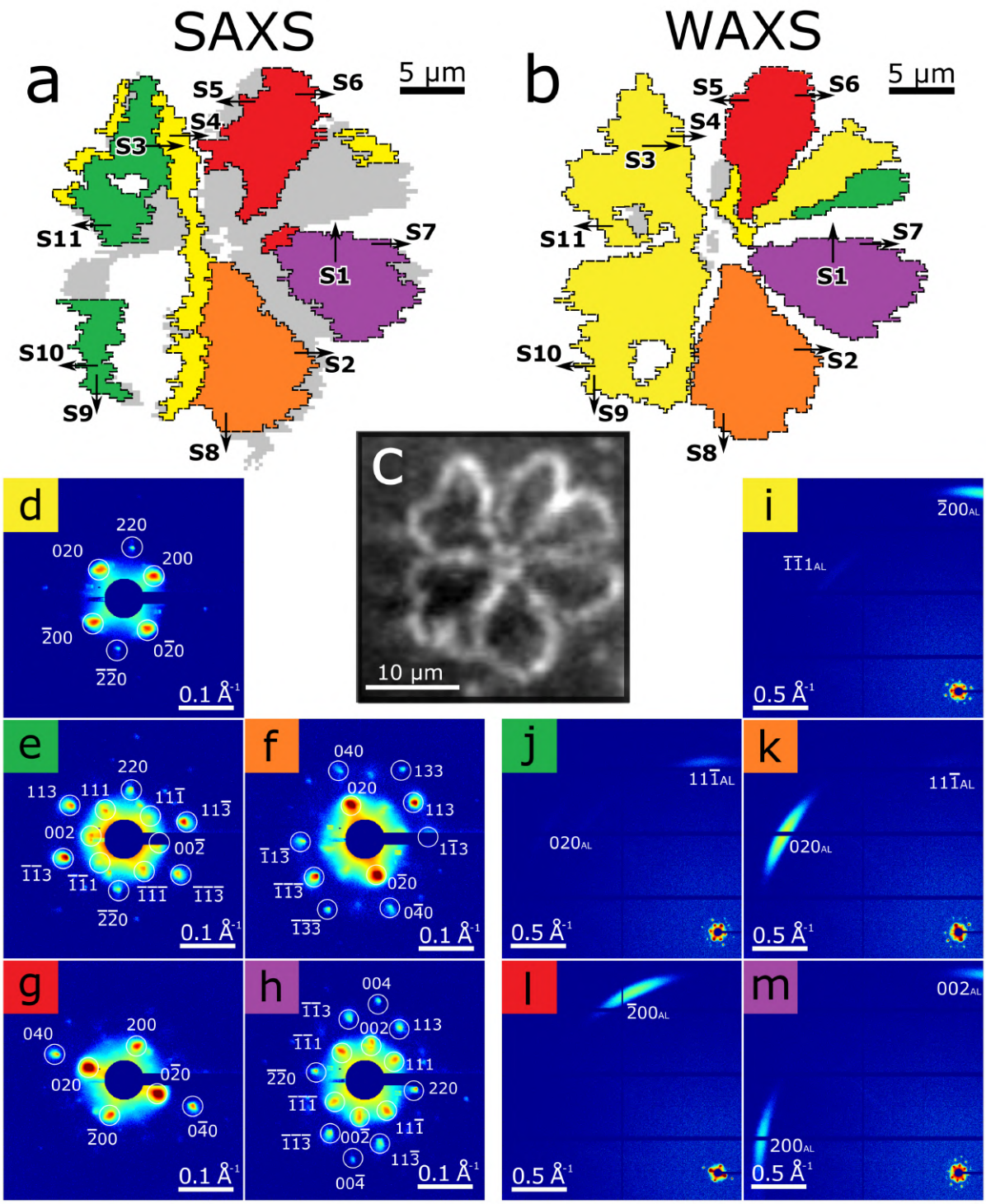

Figure 5.3: Spatially resolved maps of a mesocrystalline superlattice of PbS NCs, showing the domain structure. Each color corresponds to different orientations of the peaks at $q_{SL} = 0.083$ Å^{-1} for the SL (a) and the peaks at $q_{AL} = 2.12$ Å^{-1} for the AL (b). Grey color stands for areas with SAXS or WAXS scattering present but without well-defined orientation, while white areas correspond to parts without any scattering. Black arrows refer to specific scans across the grain boundaries. (c) An optical micrograph of the same sample. (d-m) Average SAXS (d-h) and WAXS (i-m) diffraction patterns with the corresponding peak indexing for each colored domain. The peaks are indexed under the assumption of an face-centered cubic *fcc* structure for the SL and a rock-salt structure of the NCs.

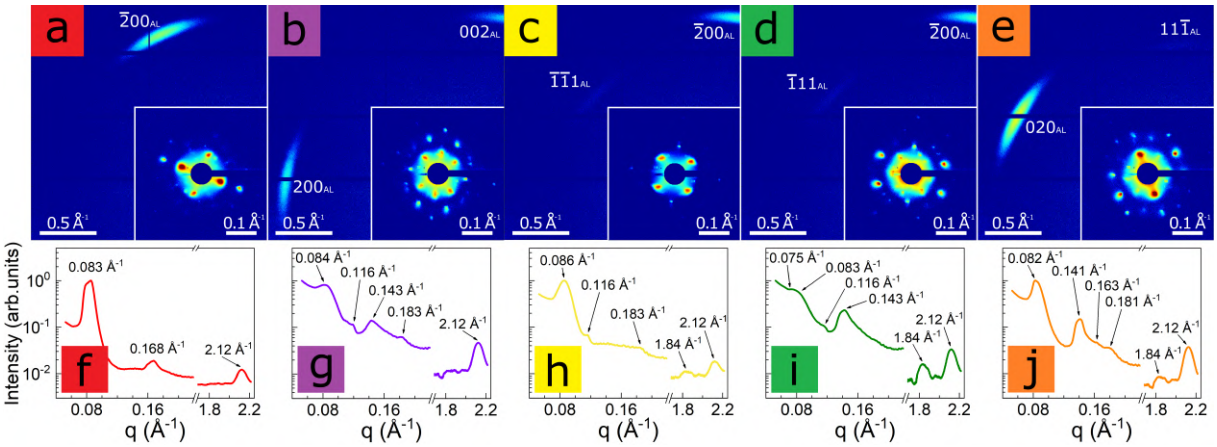

Figure 5.4: (a-e) Averaged scattering intensity of all diffraction patterns in each of the five domains defined in Figure 5.3a (color code is the same), all Bragg peaks are indexed according to an *fcc* structure; (f-j) Simulated diffraction patterns for all five domains.

ure 5.3c) shows very good resemblance between the spatially distributed scattering intensity and the real-space image.

From the color code, the domain structure of the superlattice of NCs with single-crystalline grains and areas of 50-100 µm^2 is easily visible. Five typical patterns for both SAXS (Figure 5.3d-h) and WAXS (Figure 5.3i-m) are sufficient to categorize all SAXS and WAXS patterns. Three domains, namely the red, orange and violet, exhibit nearly identical spatial dimensions in SAXS and WAXS. In contrast, the yellow WAXS domain coincides with two SAXS domains green and yellow. From here on, a discussion is focused on the SAXS domains.

In order to determine the superlattice structure, SAXS areas of the integrated diffraction patterns from the domains defined in Figure 5.3 were analyzed. The corresponding diffraction patterns and the calculated average radial intensity of the diffraction patterns within each domain is shown in Figure 5.4, where the q values are noted for the most prominent scattering peaks. The radial average of the WAXS region contains peaks at 1.84 Å^{-1} and 2.12 Å^{-1}, which are attributed to the 111_{AL} and 200_{AL} reflections of PbS, respectively. The positions of the SAXS peaks observed in the radial average for all domains are summarized in Table 5.1 and indexed according to a face-centered cubic (*fcc*) lattice. The corresponding unit cell parameter a for each reflection is also shown in the table.

The averaged unit cell parameter $\langle a \rangle$ slightly varies between different domains, but all values are within the standard deviation of the mean value. Thus, the superlattice structure can be described with high confidence as a face-centered cubic lattice with lattice constant $a = 150.1 \pm 3.0$ Å for all domains. The nearest-neighbor distance in this case is 106 Å. This value is consistent with the NC size of 68 ± 5 Å measured by optical spectroscopy and the length of the oleic acid of $\langle 19$Å$\rangle$ (on each NC) as detailed in Figure 5.1. The narrow size of all diffraction spots indicates that these parameters are uniform over each domain, and it is worth to note that there is excellent agreement

Table 5.1: The lattice constant in all five domains in Figure 5.3 based on the *fcc* lattice.

Domain	q_{exp}, Å^{-1}	h	k	l	a, Å	⟨a⟩, Å
Red	0.083	2	0	0	151.4	150.5±0.9
	0.168	4	0	0	149.6	
Purple	0.084	2	0	0	149.6	149.9±2.8
	0.116	2	2	0	153.2	
	0.143	3	1	1	145.7	
	0.183	3	3	1	151.3	
Yellow	0.086	2	0	0	146.1	150.2±3.0
	0.116	2	2	0	153.2	
	0.183	3	3	1	151.3	
Green	0.075	1	1	1	145.1	148.9±3.5
	0.083	2	0	0	151.4	
	0.116	2	2	0	153.2	
	0.143	3	1	1	145.7	
Orange	0.082	2	0	0	153.2	151.3±3.0
	0.141	3	1	1	146.5	
	0.163	4	0	0	154.2	
	0.181	3	3	1	151.3	

with these q–values in all domains of the sample.

5.3 Determination of the nanocrystal orientation in the superlattice

To determine correlations between the superlattice structure and the orientation of its NCs, two different approaches were applied. The first is an Angular Cross-Correlation Analysis (AXCCA) approach discussed in Chapter 3 and second is the direct modelling of the diffraction patterns. AXCCA is based on the analysis of a two-point angular cross-correlation function (CCF) that can be calculated for each diffraction pattern as

$$C(q_1, q_2, \Delta) = \langle I(q_1, \varphi) I(q_2, \varphi + \Delta) \rangle_\varphi \,, \tag{5.1}$$

where $I(q, \varphi)$ is the intensity at the point (q, φ) of the diffraction pattern and φ is the angular coordinate around a Debye-Scherrer ring. The intensities of the momentum transfer $q_1 = q_{200}^{SL} = 0.83$ Å^{-1}, $q_2 = q_{200}^{AL} = 2.12$ Å^{-1} for the yellow and red domains, and $q_1 = q_{311}^{SL} = 0.143$ Å^{-1}, $q_2 = q_{200}^{AL} = 2.12$ Å^{-1} for the green, purple and orange domains were correlated. All values used in this definition are shown in Figure 5.5. To obtain statistically meaningful data, CCFs were averaged over all diffraction patterns from different spatial positions within each domain of the sample.

In Figure 5.6, the relative orientations of the NCs in the sample are determined us-

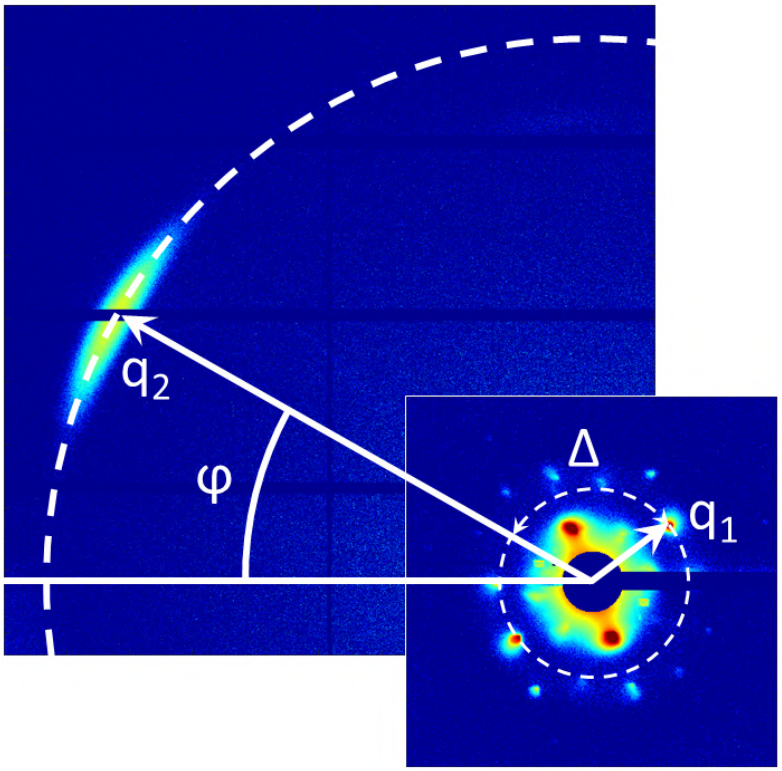

Figure 5.5: Outline of the CCF calculation. White arrows point to the Bragg reflections from the PbS AL and SL with momentum transfer values from the center of the pattern q_1 and q_2, respectively. The angle Δ between these Bragg peaks is shown. SAXS area is enlarged for better visibility.

ing AXCCA. The figure is structured as follows in the first row (Figure 5.6a-e) the cross correlation functions for all five domains are shown. The second row (Figure 5.6f-j) contains the corresponding WAXS and SAXS patterns integrated over all diffraction patterns. The q–values used in the analysis are indicated by the white dashed lines. The third row (Figure 5.6k-o) displays the simulated real space orientations for each domain of the SL based on the geometrical interpretation of the scattering data. Except for the red and purple domains, four correlation peaks are observed for each domain. For the red domain, there are only two peaks in the CCF due to the low intensity of one pair of SAXS peaks (see Figure 5.6a). This may be explained by a significant (5-10°) tilt of the SL with respect to the sample surface. However, the relative positions of the SAXS and WAXS peaks in this domain (Figure 5.6f) are similar to the yellow domain (see Figure 5.6h). For the purple domain, there are eight peaks in the CCF (Figure 5.6b) as this domain is characterized by the presence of two $\langle 200 \rangle_{AL}$ and four $\langle 311 \rangle_{SL}$ reflections (see Figure 5.6g). The CCFs for all domains except for the orange one are symmetric with respect to $\Delta = 0°$, indicating the symmetry of the angular position of the NCs with respect to the $\langle 110 \rangle_{SL}$ directions. The axis of symmetry for the red domain is marked at 0.3° under the assumption that its CCF resembles that of the yellow domain. The axis of symmetry for the orange domain is at 42°, which means that the NCs are not positioned symmetrically in the $(30\bar{1})_{SL}$ plane. This is further illustrated

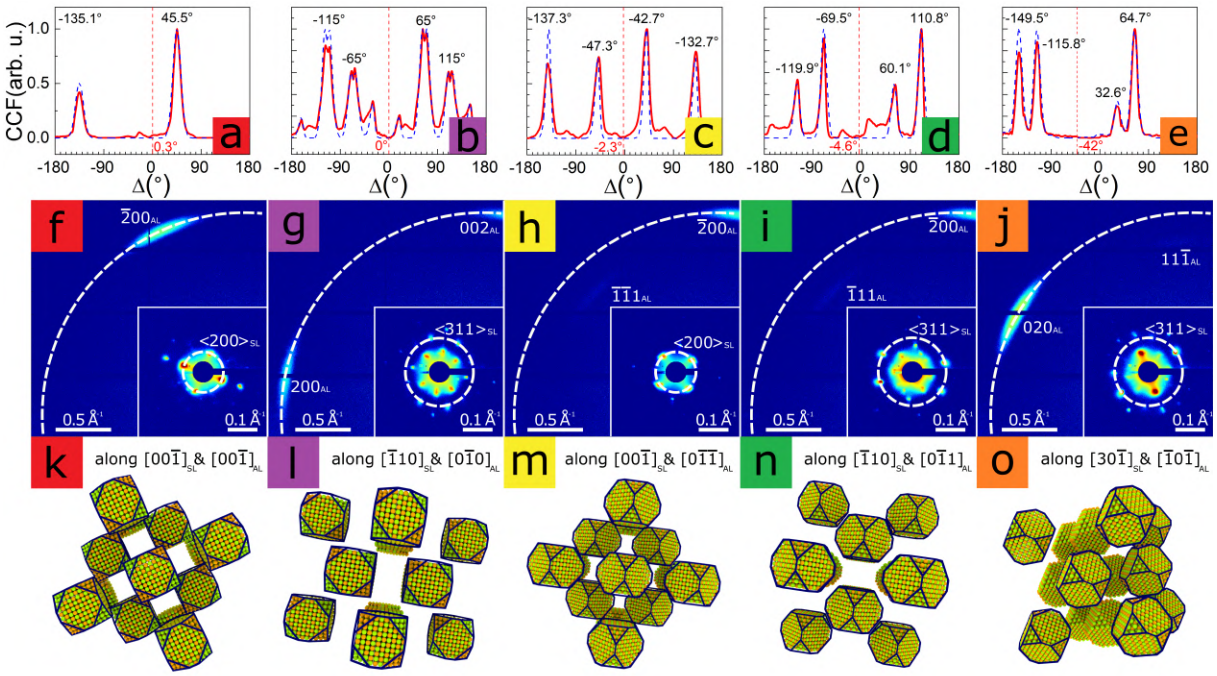

Figure 5.6: (a-e): Calculated CCFs (red lines) based on the experimental data and simulated CCFs (blue dashed lines) based on the model structures shown in (k-o) for all five domains. CCFs were calculated using the q-values described in the text. The analyzed q-values are also indicated by the white dashed lines in the SAXS and WAXS patterns (f-j). (f-j): Averaged WAXS intensity of diffraction patterns corresponding to each domain. Enlarged SAXS patterns are shown in the lower right corners (Note: The center of the WAXS pattern does not coincide with the center of the SAXS pattern due to the different scale). (k-o): Real space models of the superlattice and its constituting NCs based on the SAXS and WAXS patterns and CCFs for all five domains.

in Figure 5.6o by the asymmetric real space structure in this orientation.

The simulated CCFs (blue dashed curves) in Figure 5.6a-e were based on the determined real-space structures for all domains in 5.6k-o. The Bragg peaks in both WAXS and SAXS areas were assumed to have Gaussian shapes in the angular direction, and intensity on the corresponding ring was calculated as follows

$$I(\varphi) = \sum_i A_i \cdot \exp\left\{ -\frac{(\varphi - \varphi_i)^2}{2\sigma^2} \right\}, \tag{5.2}$$

where A_i is the intensity of the i-th Bragg peaks in the SAXS/WAXS area from the experimental data and σ is the angular size of the i-th SAXS/WAXS peak. The respective angular position of the SAXS/WAXS peaks were slightly varied in order to achieve better agreement of simulated and experimental data, and the small misorientation of the SL and AL was obtained. To simulate the effect of finite detector size the missing angular range for the WAXS signal was included. The good agreement between experimental and simulated CCFs supports the structural interpretation used to index Bragg peaks Figure 5.3d-h and serves as a basis to understand all further scattering patterns in this work, including individual patterns at grain boundaries.

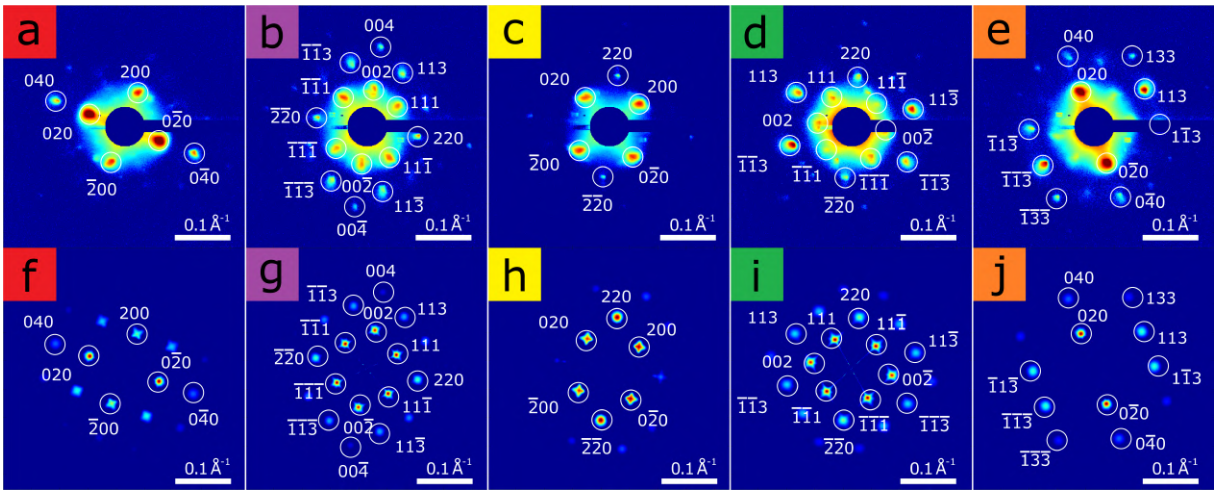

Figure 5.7: (a-e) Averaged SAXS diffraction patterns from each of the five domains defined in Figure 5.3a (color code is the same), all Bragg peaks are indexed according to an *fcc* structure; (f j) Corresponding simulated diffraction patterns for all five domains.

The determined orientations of the superlattice and the NCs with respect to the incident X-ray beam allowed us to reveal the relative orientation of the NCs in the superlattice unit cell. Modelled unit cells for all five domains are shown in Figure 5.6k-o, where the direction of the incident X-ray beam is perpendicular to the plane of the figure. All peaks are indexed assuming the incident X-ray beam to be along the $[00\bar{1}]_{SL}$ direction for the yellow domain, along the $[\bar{1}10]_{SL}$ direction for the green domain, along the $[30\bar{1}]_{SL}$ direction for the orange domain, along the $[00\bar{1}]_{SL}$ domain for the red domain, and along the $[\bar{1}10]_{SL}$ direction for the purple domain.

To confirm the suggested structure and orientations of the domains, the diffraction patterns of the superlattice were simulated, as shown in Figure 5.7f-j. In these simulations, the *fcc* superlattice was considered, with the experimentally obtained unit cell parameter a = 150 Å, and used the form factor of the NCs in nodes of the superlattice, which were approximated by spheres with normally distributed radii (65 Å mean radius and 5 Å standard deviation). The simulated SAXS patterns show a great resemblance to the experimental one, thus confirming the modeled orientations of the superlattice.

5.4 Nanocrystal orientational disorder

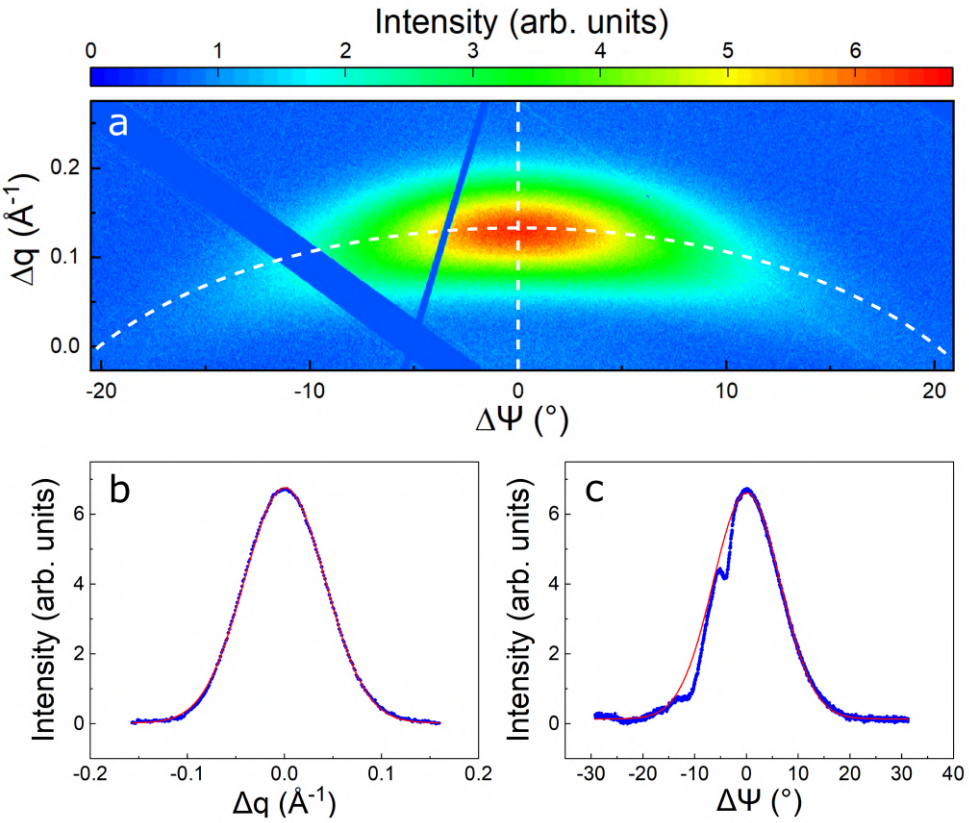

Figure 5.8: (a) Two-dimensional shape of the 200_{AL} diffraction peak averaged over diffraction patterns from the red domain. White dashed lines represent cross sections in radial and azimuthal directions. Radial (b) and azimuthal (c) profiles of the 200_{AL} peak, respectively. Blue points are experimental data, and red lines are Gaussian fits.

Texture is clearly seen from the diffraction patterns of the atomic lattice (Figure 5.3j-m), which indicates that in average, the individual nanocrystals are aligned in a certain way with respect to the crystallographic directions of the superlattice. The small deviations in orientation of NCs from this alignment can be described in terms of the misorientation angle $\Delta\Phi$. In order to obtain a statistical description of $\Delta\Phi$, the average diffraction pattern of each WAXS domain was considered. The enlarged part of the diffraction pattern averaged over the red domain, which contains 200_{AL} peak, is shown in Figure 5.8a. The radial and azimuthal cross sections of the averaged WAXS peak are shown in Figure 5.8b,c. Both cross sections are well-fit by Gaussian function, wherein the width of the diffraction peak in azimuthal direction is significantly larger than in the radial direction.

To quantitatively characterize angular disorder it was assumed that WAXS peak broadening is caused by two factors: Sherrer broadening due to the small size of the NCs and orientational disorder of the NCs in the lattice points of the SL. The first factor affects both radial and azimuthal width of the peak while the second one in-

Table 5.2: Determination of the orientational disorder in five domains.

Domain	Azimuthal FWHM, °	Radial FWHM, °	ΔΦ°
Red	13.1 ± 0.5	2.5 ± 0.1	12.9 ± 0.6
Purple	17.5 ± 1.2	2.5 ± 0.1	17.3 ± 1.2
Yellow	16.9 ± 0.8	2.5 ± 0.1	16.7 ± 0.8
Green	16.7 ± 1.5	2.6 ± 0.1	16.5 ± 1.4
Orange	13.1 ± 0.5	2.4 ± 0.1	12.9 ± 0.6

fluences only the azimuthal width of the peak. Assuming that these two factors are independent, it was estimated that the value of the orientational disorder $\Delta\Phi$ from the relationship between radial and azimuthal widths of the peak

$$\sigma_{az}^2 = \sigma_{rad}^2 + \Delta\Phi^2 \,, \tag{5.3}$$

where σ_{az} and σ_{rad} are FWHM values of the peak angular size in azimuthal and radial directions obtained from the gaussian fitting, respectively. The peak width in radial direction was converted to degrees for proper calculation.

Both angular and radial FWHM values calculated for all the domains are summarized in Table 5.2 together with evaluated values of the orientational disorder. Thus, the orientational disorder ($\Delta\Phi$) of the almost iso-oriented atomic lattices of NCs is roughly 15° in all domains, similar to the recently reported $\Delta\Phi$ for superlattices of tetrathiafulvalene-linked PbS NCs [14].

5.5 Structural configurations and facet-induced interactions

From the AXCCA analysis in Figure 5.6f-j, two different angular correlations were obtained, which apply to all domains of the sample (Figure 5.9). In the first configuration (Conf1, Figure 5.9a), the collinearities $[110]_{SL}||[100]_{AL}$ and $[001]_{SL}||[001]_{AL}$ were observed. The second configuration (Conf2, Figure 5.9b) is characterized by the collinearities $[110]_{SL}||100]_{AL}$ and $[001]_{SL}||[011]_{AL}$. It is worth to note that a single rotation of all NCs by 45° around the $[100]_{AL}$ transposes Conf1 into Conf2. While the purple and red domain are characterized by Conf1, the yellow, green and orange domain are examples for Conf2. To verify this for the orange domain, the SAXS and WAXS patterns for the superlattice were simulated, and they are shown in Figure 5.7e,j. From these simulations it was obtained that taking the incident beam directions along the $[30\bar{1}]_{SL}$ axis reproduces the SAXS pattern of the orange domain as well as the relative scattering intensities of the 200_{AL} and 111_{AL} Bragg peaks. Indicated by the relatively small intensity of the 111_{AL} Bragg peak, the $[30\bar{1}]_{SL}$ and $[\bar{1}0\bar{1}]_{AL}$ axes are not exactly

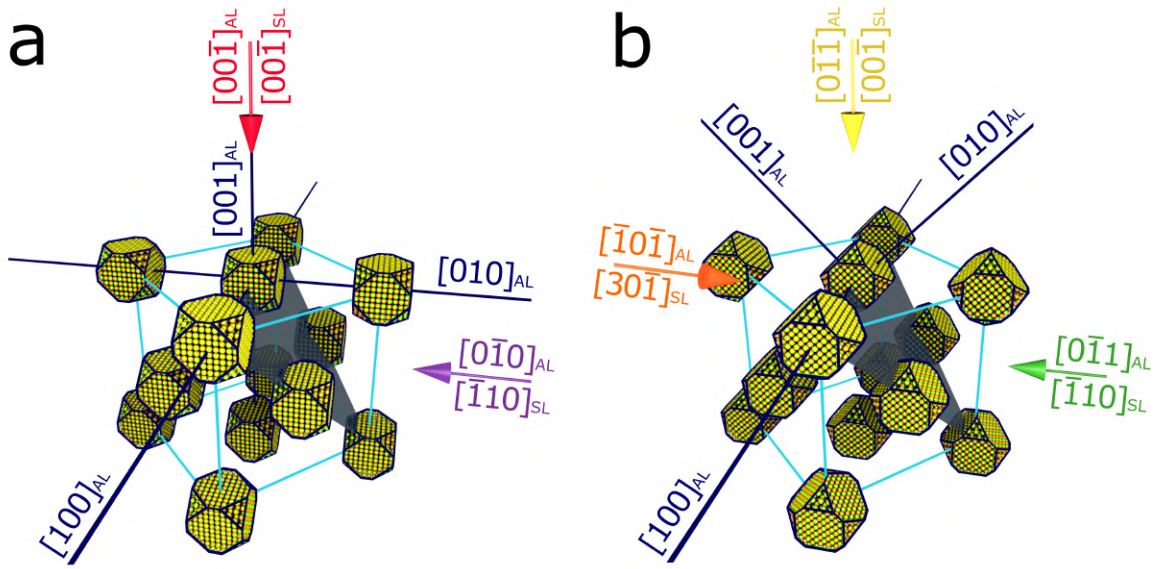

Figure 5.9: (a,b) Two different mesocrystalline configurations found in this work. Blue lines show the families of $\langle 100 \rangle_{AL}$ directions of the NCs. $(11\bar{1})_{SL}$ planes with the highest packing density of the NCs are shown in gray. Colored arrows display the direction of the incoming x-ray beam for each domain corresponding to the diffraction patterns in Figure 5.3.

collinear, but the difference is negligible when taking into account the calculated misorientation of the NCs, which is discussed in the previous section. The geometrical relationship between the red and purple domain as well as the yellow, green and orange domain is indicated with the corresponding colors in Figure 5.9a and Figure 5.9b, respectively.

Using an X-ray beam with 100 µm footprint, Li et al. have previously reported diffraction patterns from *fcc*-PbS NC superlattices exhibiting both configurations Conf1 and Conf2 simultaneously [207]. This was attributed to a mixed unit cell of the superlattice consisting of two groups of NCs with the two different angular correlations. In contrast, it the current experiment only domains with uniform angular correlation were observed. A possible explanation for these apparently contradicting findings is the much smaller X-ray foot print utilized by us, enabling the analysis of single-crystalline domains of the superlattice. Thus, the stability of the two configurations may be based on the maximization of ligand-ligand interactions between adjacent 100_{AL} and 111_{AL} facets separated by the nearest neighbor distance. In an SL with *fcc* structure, each NC is coordinated twelve-fold via its nearest neighbors along the twelve $\langle 110 \rangle_{SL}$ directions.

This is detailed in Figure 5.10 for both configurations by displaying three different 111_{SL} plane for each, which contain the central NC and six nearest neighbors. If a nearest neighbor directly faces the central NC with a 100_{AL} or 111_{AL} facet, the ligand molecules are represented in red and blue, respectively. Otherwise, the ligands between adjacent NCs are omitted for clarity. Conf1 stands out in that all twelve $\langle 110 \rangle_{SL}$

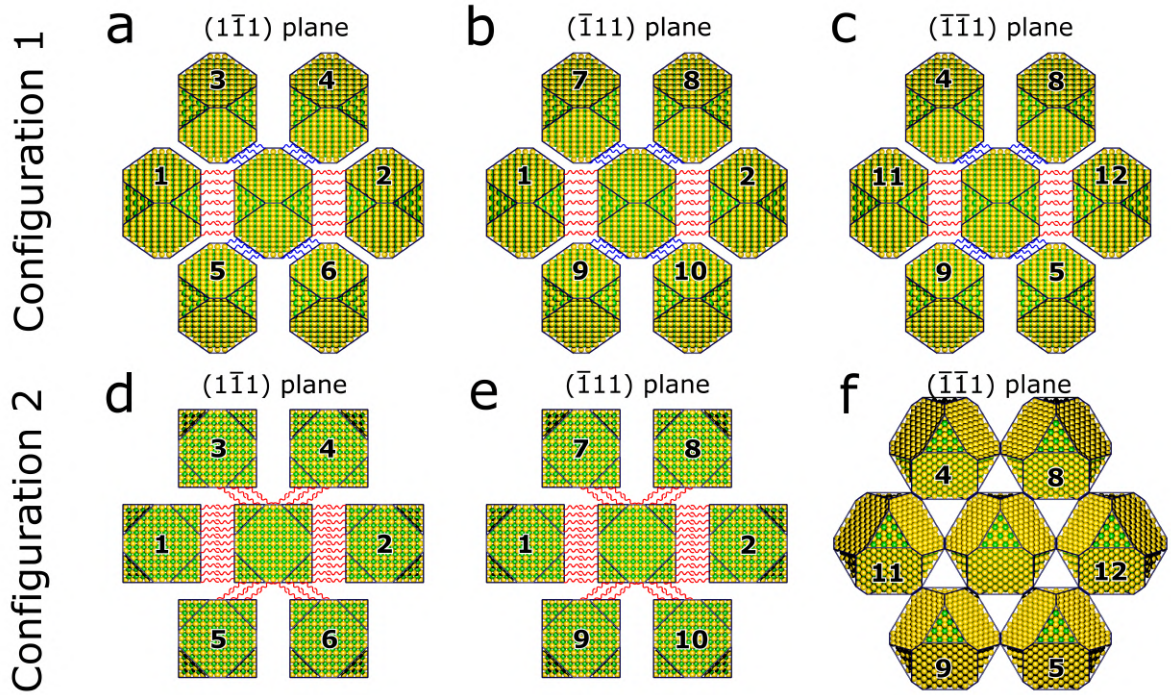

Figure 5.10: Three different 111 planes for each configuration shown in Figure 5.9. In each plane 6 nearest neighbor NCs out of 12 are visible. All 12 of the nearest neighbors of the central nanocrystal are numbered. The facet-facet interaction between central particle and other particles are shown by red (100-100 interactions) and blue (111-111 interactions) lines.

directions exhibit such ligand interactions, namely four 100_{AL}–100_{AL} and eight 111_{AL}-111_{AL} interactions (see Figure 5.10a–c). In contrast, Conf2 exhibit only ten such interactions, respectively, all of which occur exclusively between 100_{AL} facets (see Figure 5.10d–e). Since these facets are roughly 10^6 times more reactive than 111_{AL} facets, the smaller number of total interactions compared to Conf1 may be compensated by the larger number of specific 100_{AL}–100_{AL} interactions [232, 233].

5.6 Compression of the superlattice near domain boundaries

Now we turn our attention to the study of the SL structure close to domain boundaries. For each spatial position of our sample, the radial positions of $\langle 200 \rangle_{SL}$ and $\langle 311 \rangle_{SL}$ family of peaks were estimated. The calculated radial average for each diffraction pattern was fitted with a Gaussian function in the range of magnitudes of the scattering vector from 0.070 to 0.100 Å^{-1} for q_{200}^{SL} and from 0.130 to 0.160 Å^{-1} for q_{311}^{SL}. Figure 5.11a,b shows variations in the value of the q_{200}^{SL} and q_{311}^{SL} momentum transfer within the entire sample. The average value of q_{200}^{SL} in the center of each domain far from its boundary is 0.083 Å^{-1} (see Figure 5.11a), while near the edge its value increases up to 0.10 Å^{-1}. The length of the q_{311}^{SL} scattering vector also increases by about

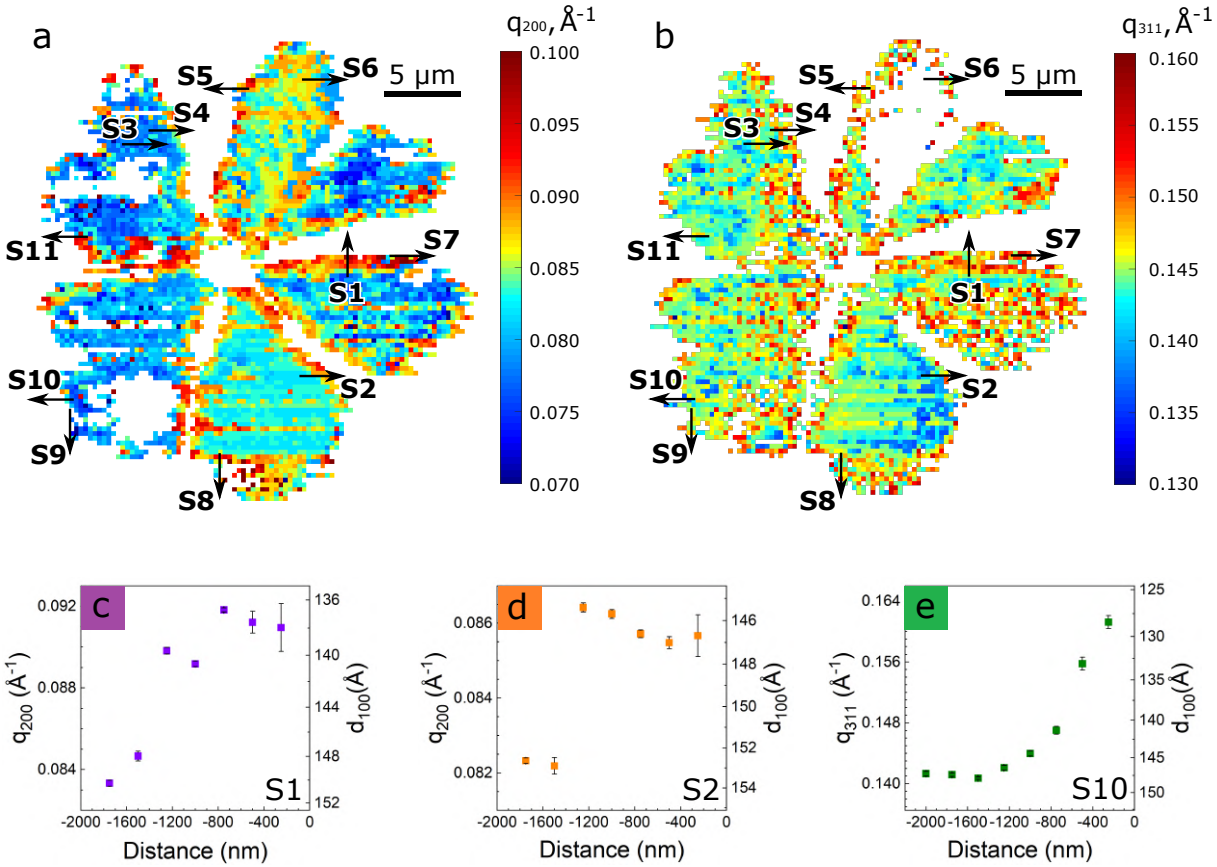

Figure 5.11: Spatial maps of the momentum transfer value for $\langle 200 \rangle_{SL}$ (a) and $\langle 311 \rangle_{SL}$ (b) reflections. The color code quantifies the value of q_{200}^{SL} (a) or q_{311}^{SL} (b). Black arrows refer to specific scans discussed in the text. Spatial variation in q_{200}^{SL} and q_{311}^{SL} between the bulk and the edge of domains for scans S1 (c) and S2 (d) and S10 (e) and calculated d_{100}^{SL}-spacing.

10% close to the domain boundaries. This indicates a compression of the superlattice as one approaches the domain boundary.

To verify our findings, radial averages were fitted more precisely with appropriate background subtraction for the grain boundary shown as scan S1, S2 and S10 in Figure 5.11c,d,e. Distances are relative to the edge of the domain (defined by the absence of the SAXS diffraction). At each point of the scans S1 and S2, the positions of the $\langle 200 \rangle_{SL}$ reflections were calculated and an increase of the momentum transfer by 10% and 5%, respectively was observed. The same trend was observed for the peaks of the $\langle 311 \rangle$ family. For the scan S10 the length of the scattering vector increases from about 0.141 Å^{-1} in the bulk of the domain up to about 0.162 Å^{-1} on the very edge that gives 13% shrinkage of the unit cell (see Figure 5.11e). Evidence for a contraction of the superlattice near domain boundaries is also found in a previous report based on electron microscopy (see Figure 1a therein) [234]. In this work the compression of the superlattice mostly in the direction of the surface tension force. In our work it was difficult to monitor the compression direction due to the low intensity of Bragg peaks near grain boundaries.

5.7 Rotation of the superlattice near domain boundaries

Now we focus on the analysis of the superlattice rotation near domain boundaries. In Figure 5.12, the changes in the orientation of the superlattice and of the NCs near grain boundaries observed along scan S2 marked in Figure 5.3a,b are analyzed. Scan S2 represents the approach from a mesocrystalline domain towards an area without any scattering (orange into white). The first row in Figure 5.12 is the experimental SAXS scattering patterns along the scan, and the second row is simulation of the SAXS scattering. From that simulations one can conclude that in scan S2, the superlattice undergoes an out-of-plane rotation around the $[010]_{SL}$ axis by 22°, and is simultaneously tilted by 7°. In the third row of Figure 5.12 the WAXS patterns along the scan S2 are shown. The q-rings corresponding to $q_{020}^{AL} = 2.12$ Å^{-1} and and $q_{111}^{AL} = 1.84$ Å^{-1} used in further analysis are marked by blue and red line, respectively. The azimuthal profiles of these q-rings are ahown in Figure 5.12m-p. The changes in the relative intensities of the 020_{AL} and $11\bar{1}_{AL}$ peaks indicate the rotation of the AL close to the domain boundary. These changes can be rationalized as the rotation of the NCs around $[010]_{SL}$ axis, thus the angular correlation is most likely preserved in this example. It was described in the previous section. that the shrinking of the lattice along this scan (see Figure 5.11d). Therefore, remarkably, although the orientation and lattice spacing of the superlattice changes drastically close to the edge of the sample, the angular correlation of the superlattice with the NCs is preserved until the scattering signal vanishes.

The scan S3 (Figure 5.13) is an example for a grain boundary between two mesocrystalline domains (green into yellow). In scan S3 the WAXS pattern remains practically unchanged, while the SAXS pattern exhibits a 90° rotation over a distance of 4 µm. This sequence of diffraction patterns can be rationalized as an out-of-plane rotation of both, the SL and AL, around the $[1\bar{1}0]_{SL}$ and $[001]_{AL}$ axes (which are collinear in the green and yellow domain) by 90° as detailed in Figure 5.13e,f. Importantly, the angular correlation between the SL and AL is thus preserved across this grain boundary.

Scans S1 and S4-S11 shown in Figure 5.3 were analyzed in the same way and it was found that the superlattice rotates by different angles at the grain boundaries. In all analyzed scans, the relative intensity of the SAXS peaks changes and some new peaks emerge. It is worth to note the following general trends: Near a grain boundary, the superlattice always experiences an out-of-plane rotation with typical values between 8-14°. For the orientation of the NCs, a clear trend is less obvious since the relatively broad Bragg reflections with a full width at half maximum of 15° (see Figure 5.8, Table 5.3) make small out-of-plane rotations difficult to monitor. For this reason, scan S2 as the most obvious example for the rotation of the atomic lattice near the grain boundaries is shown in detain in Figure 5.12. However, even despite this obstacle the disappearance of Bragg peaks of the AL was frequently observes while the SL rotates. This indicates either an out-of-plane rotation of the NCs or a fainting scattering signal

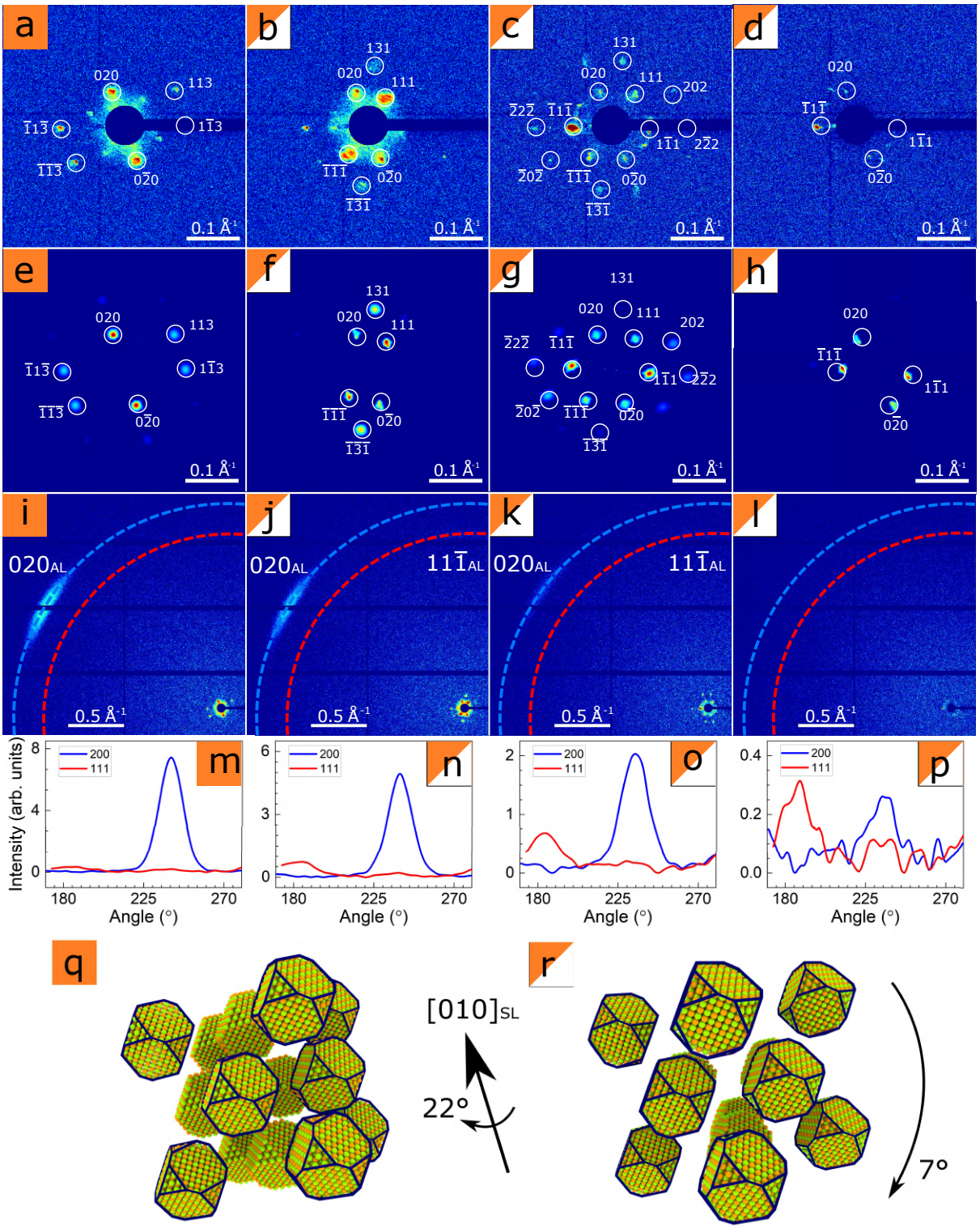

Figure 5.12: (a-d) Experimental and (e-h) simulated SAXS diffraction patterns from the Scan S2 from Figure 5.3a,b. The simulation starts from the SL oriented along $[30\bar{1}]_{SL}$ (e), and close to the edge of the domain superlattice is continuously rotated around $[010]_{SL}$ axis. (i-l) Experimental WAXS diffraction patterns from the Scan S2 from Figure 5.3a,b. The analyzed q-values are indicated by the blue dashed line for $q_{020}^{AL} = 2.12$ Å^{-1} and red dashed line for $q_{111}^{AL} = 1.84$ Å^{-1}. (m-p) Azimuthal profiles of the q-rings corresponding to $q_{020}^{AL} = 2.12$ Å^{-1} (blue) and $q_{111}^{AL} = 1.84$ Å^{-1} (red). The changes in the relative intensities of $[020]_{AL}$ and $[11\bar{1}]_{AL}$ indicates the rotation of the AL close to the edge of the domain.The unit cell rotates by 22° around the $[010]_{SL}$ direction and is additionally tilted by 7° out-of-plane as indicated in the schematic real space representations (q,r).

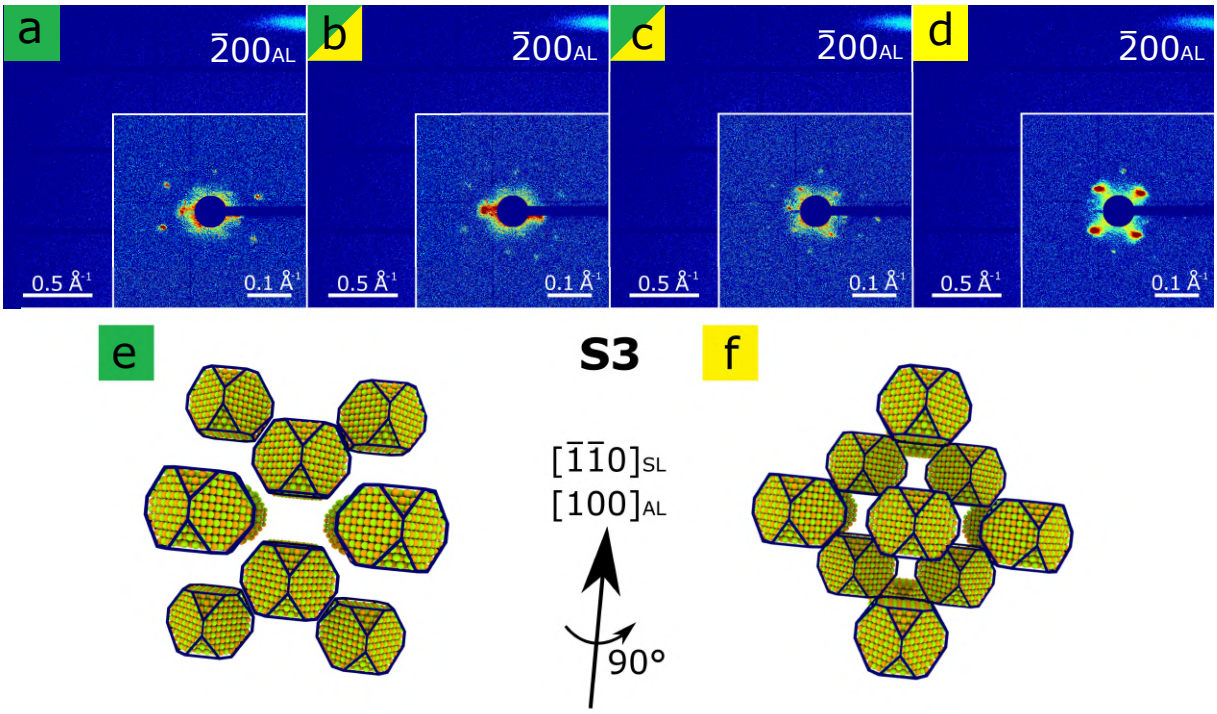

Figure 5.13: (a-d) Scan through the border between green and yellow domains of the SL (scan S3 in Figure 5.3a,b) performed with 1 µm step size. (e,f)) The unit cell rotates by 90° around the $[\bar{1}10]_{SL}$ and $[100]_{AL}$ directions, as indicated in the schematic real-space representations.

due to a thin material coverage at the edges of the sample. None of the scans show a pronounced in-plane rotation of the NCs. Thus, the typical grain boundary is characterized by an out-of-plane rotation of the mesocrystalline unit cell by 8-14°, a compression of the lattice constant by 5-10% and a preservation of the angular correlation between the superlattice and its constituting NCs. Domains of different angular correlation (e.g. yellow vs. red or green vs. purple) are separated by extended areas without long-range order of the superlattice and/or no material between these domains.

Obtained results allowed to conclude that facet-substrate interactions play a far more important role in the formation of grain boundaries. Each grain boundary studied by us in Figure 5.11, Figure 5.12 and Figure 5.13 is accompanied by an out-of-plane rotation of the superlattice and a preserved angular correlation with the atomic lattices of the NCs. Thus, the type and number of ligand-ligand interactions does not change in the vicinity of this structural defect, in contrast to the interactions with the substrate. Based on the observation that all grain boundaries are further characterized by a change of the lattice constant (Figure 5.11), one can conclude that the predominant driving force for the out-of-plane rotation of the superlattice is the reduction of stress or strain. A strategy towards mesocrystalline PbS NC superlattices with larger coherent domains should therefore aim at reducing stress/strain in the superlattice - e.g. by a narrower size distribution as well as maximizing interactions of the NCs with the surface of the substrate to prevent out-of-plane rotations. This may be achieved by coating the substrate with a self-assembled monolayer of a molecular species that

Table 5.3: Rotation angles for 9 scans through the domain boundaries

Scan	S1	S4	S5	S6	S7	S8	S9	S10	S11
Angle	14°	8°	10°	14°	10°	12°	9°	11°	9°

interacts strongly with the ligands of the NCs.

5.8 Conclusions

X-ray nanodiffraction in combination with Angular X-ray Cross-Correlation Analysis (AXCCA) was applied to study the formation and correlation of domain boundaries in mesocrystalline superlattices. Two distinct mesocrystalline polymorphs of PbS nanocrystal superlattices with face-centered cubic structure were identified, both of which exhibit a rigid iso-orientation of the nanocrystals (NCs) with the superlattice. This polymorphism is explained with the number of facet-specific ligand-ligand interactions, which are extraordinarily large for both structures.

Close to a grain boundary, the lattice shrinks and the superlattice undergoes an out-of-plane rotation, while the orientation of the NCs with respect to the superlattice remains unchanged. This out-of-plane rotation is probably caused by the stress or strain in the superlattice as evidenced by a 5-10% compression of the lattice constant during the rotation. The observation that correlations between adjacent NCs are preserved at the most of grain boundaries reveals the role of ligand-substrate interactions in the superlattice formation. Thus, the key to nanocrystal superlattices with improved long-range order are stronger particle-substrate interactions as the particle-particle interactions are advantageously strong.

Chapter 6

Unravelling structural rearrangement of polymer colloidal crystals under dry sintering conditions

Photonic crystals are optical structures with periodic modulations of medium dielectric susceptibility leading to the appearance of photonic band gaps [163]. The self-assembly of colloidal particles into 3D crystals provides a fabrication technique with the possibilities of tailoring the optical properties of a photonic crystal by changing the particle size [235]. The shape of the colloidal particles is responsible for the self-assembly of colloidal crystals [236–239], and it directly affects their dimensionality [240], phase behaviour [241, 242] and optical properties [243]. Thermal or chemical annealing can be used to modify the shape of self-assembled colloidal particles and, hence, tailor the photonic band gap properties of a colloidal crystal [244]. As a result of the annealing treatment, the spherical shape of a colloidal particle changes to a faceted shape, which provides a new route for the fabrication of polyhedral particles [245].

This chapter is based on Reference [246]. In this chapter, the results of an experiment performed on a polystyrene colloidal crystal at PETRA III synchrotron facility are discussed. *In-situ* grazing incidence X-ray scattering technique was employed to unravel the structural evolution of the sample. The formation of the colloidal crystals are discussed in detail in Chapter 4 and the grazing-incidence diffraction experiment is discussed in Chapter 3. As compared to standard transmission SAXS geometry, grazing incidence X-ray scattering is sensitive to both in-plane and out-of-plane structural order, and furthermore provides better control during thermal annealing due to the whole sample area forming a thermal contact. Therefore, this technique was chosen to reveal the structural rearrangement of polystyrene colloidal crystals under dry sintering conditions.

6.1 Experiment

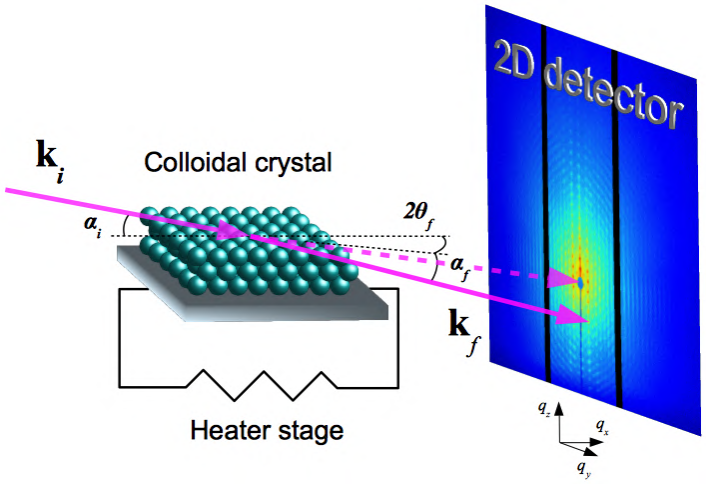

Figure 6.1: Scattering geometry of GTSAXS experiment. The incident beam with a wave vector $\mathbf{k}_i$ enters the sample surface at a grazing angle α_i. The scattered beam with a wave vector $\mathbf{k}_f$ is defined by the in-plane and out-of-plane scattering angles $2\theta_f$ and α_f, respectively.

Schematics and details of the experimental setup are presented in Fig. 6.1. X-ray scattering experiments were performed at the P10 coherence beamline of PETRA III synchrotron source at DESY, Hamburg. Incident X-ray beam with a photon energy of 7.74 keV was adjusted to 50×50 μm^2 size using beam-defining slits. The sample was aligned vertically on a 5-axis positioning stage such that the scattering plane was horizontal. Diffraction patterns were acquired using a 2D detector Pilatus 300K with an area of 487×619 pixels and a pixel size of 172 × 172 μm^2. The detector was positioned at 5.1 m distance downstream the sample. The incident angle α_i for the studied samples was adjusted to 0.5°, larger than the critical angles of the colloidal crystal and the substrate, which allowed to optimise the X-ray scattering signal without obscuring effects from the sample holder. The scattering patterns were acquired by collecting 100 detector frames with an exposure time of 1 second each. Our measurements benefited from high the incident flux of the synchrotron X-ray beam of 1.1×10^{11} photons/s/50×50 μm^2 and the fact that colloidal crystals were grown on thin glass coverslips of 170 μm thickness, providing relatively high transmission of 22% at normal incidence for the photon energy used in this experiment. Using grazing incidence geometry lowers the transmission of the samples significantly, resulting in values of the order of 10^{-5}. The air scattering background was eliminated by positioning the sample inside of a vacuum chamber and using an evacuated flight tube between sample and detector. To protect the detector from the transmitted beam and optimize the scattering signal acquisition at high q-values the beamstop (tungsten cylinder of 3 mm diameter) was positioned inside of the flight tube in front of the detector.

PS colloidal crystal films were fabricated by vertical deposition method [247]. Spher-

Table 6.1: Structural parameters of PS colloidal crystal samples at RT

Sample	A	B	C
D_{DLS}, nm	420	272	194
D_{GTSAXS}, nm	419	257	197
Polydispersity(DLS), %	2.1	4	3.5
c/a ratio	0.99	1.00	0.98
Packing	*rhcp*	*rhcp*	*rhcp*
hcp fraction	0.6	0.2	0.8
fcc fraction	0.4	0.8	0.2
Number of layers	30	70	60
Thickness, µm	10.3	14.7	9.7
Lateral domain size, µm	4.2	2.3	3.7
In-plane $\Delta d/d$, %	4.3	5.4	4.8
Out-of-plane $\Delta d/d$, %	5.1	6.8	3.5
In-plane mosaicity, mrad	51	68	35
Out-of-plane mosaicity, mrad	43	54	48

ical colloidal particles were synthesised by polymerization of an aqueous solution of styrene using potassium persulphate as initiator. Initial colloidal suspensions for the studied samples with particle diameter of 420, 272 and 194 nm (referred further as samples A, B and C, respectively) contained 0.8, 0.25 and 0.5% volume fraction of colloidal particles in water. Particle polydispersity values measured by dynamic light scattering (DLS) were 2.1, 4 and 3.5% (see Table 6.1). Thin glass substrates were immersed into colloidal suspensions and subsequently dried at 50°C for several days at ambient conditions. The fabricated colloidal crystal films consisted of 20-80 monolayers of PS spherical particles and typically exhibited a cracked texture composed of domains with an average size of 10 - 50 µm. The colloidal crystal samples were mounted to the sample holder using silver paste to assure a good thermal contact. The copper block of the sample holder was integrated into the vacuum chamber. Heating was supplied by two parallel connected heating elements integrated into the copper block, and the temperature was measured using two PT100 sensors embedded into the sample holder. The temperature and the heating power were controlled using a LakeShore 340 temperature controller. During measurements, the temperature of a sample was raised incrementally starting from room temperature (RT). After each temperature increment, a waiting time of 5 minutes was applied before collecting the data to reach thermal equilibrium within the sample.

6.2 GTSAXS analysis and simulations

To analyze the results the geometry of X-ray scattering experiment under grazing incidence conditions was considered. For the colloidal crystals studied in this work, the specularly reflected signal was hampered by surface roughness, that prevented us from using GISAXS geometry. Instead, the grazing incidence transmission small angle X-ray scattering (GTSAXS) geometry [11, 248] was employed, where only the forward transmitted part of a scattering pattern below the sample horizon ($\alpha_f < 0$) is analysed, as illustrated in Figure 6.1.

GTSAXS patterns measured at RT for the three colloidal crystals A, B and C, consisting of PS spherical particles of 420, 272 and 194 nm in diameter, are shown in Figure 6.2. Scattering patterns are displayed for the reciprocal space areas covering the same number of diffraction peaks, which corresponds to q-ranges 0.025×0.025, 0.041×0.041 and 0.050×0.050 Å^{-1} for the samples A, B and C, respectively. The achieved resolution in reciprocal space of 1.32×10^{-4} Å^{-1} was defined by the pixel size of the 2D detector and the sample-to-detector distance at 7.74 keV X-ray energy. Indexed sets of in-plane reflections of (110)-type and out-of-plane reflections of (001)-type employed for the analysis are depicted by rectangles. Dashed lines denote the q_y- and q_z-directions used to extract intensity profiles for fitting analysis. In the case of GTSAXS geometry the scattering pattern is dominated by the kinematical scattering contribution and less influenced by re-scattering channels inherent to conventional GISAXS measurement. In particular, the characteristic GISAXS features such as specular and Yoneda peaks [249] are not present in GTSAXS data. For all measured samples the central and side peaks along the q_z-direction reveal strong truncation rods which originate from the substrate scattering under grazing incidence angles. Due to variations of particle polydispersity and defect concentration different number of diffraction orders were observed for the studied colloidal crystals. For the sample A the diffraction peaks up to 13-th order were observed indicating a high structural quality. Meanwhile, for the sample B only 5 diffraction orders have been observed pointing to rather low quality of the sample, which can be related to high polydispersity of 4% (see Table 6.1). The sample C has revealed 7 diffraction orders, indicating an intermediate degree of long-range ordering.

In order to determine the structural parameters of colloidal samples the GTSAXS data were analysed by X-ray scattering simulations in the frame of Distorted Wave Born Approximation (DWBA) theory [7, 92, 105, 250, 251]. This theory is discussed in detail in Chapter 3. In the case of colloidal particles supported on a substrate, DWBA implies to consider the scattering amplitudes in a particle and at an interface between vacuum and substrate, as described by Fresnel reflection and transmission coefficients. To obtain quantitative sample characteristics, GTSAXS simulations were implemented as in-house developed Python scripts. Simulated patterns were calculated on 1600×1600 px^2 grid for the q-ranges corresponding to the GTSAXS data from

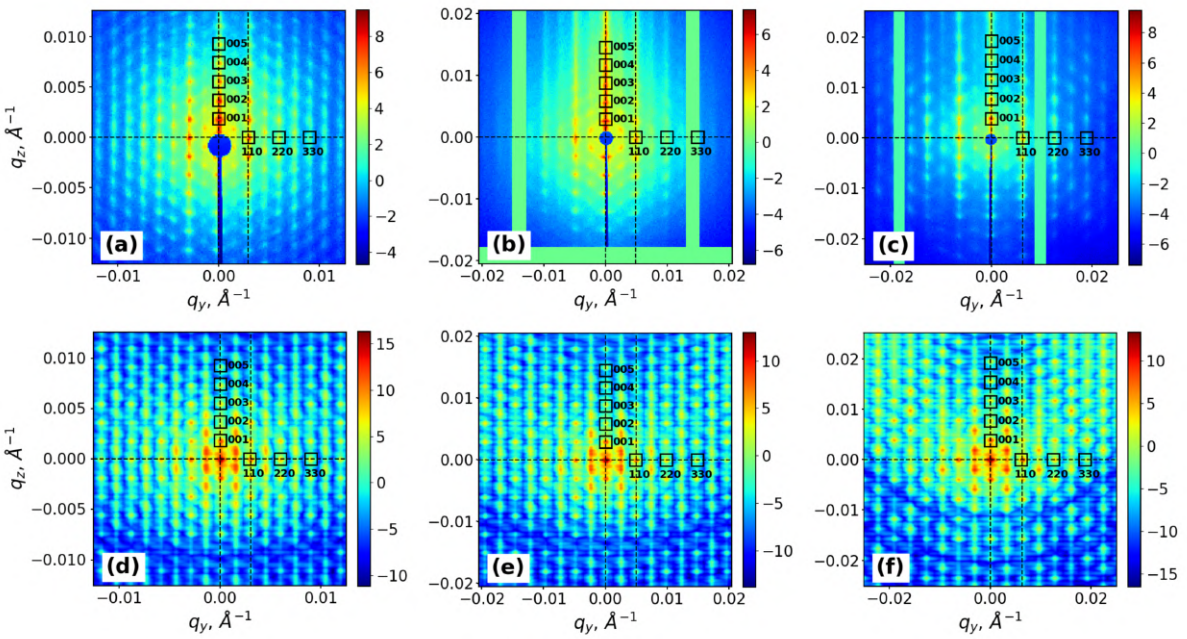

Figure 6.2: (a–c) Experimental and (d–f) simulated GTSAXS patterns for the three PS colloidal crystals (a,d) A, (b,e) B and (c,f) C at RT. Indexed sets of in-plane and out-of-plane reflections are marked by rectangles. Dashed lines indicate the directions of q_y- and q_z-profiles used for the analysis; vertical line across (-1-10) peak is not shown for better data visibility. A circular area around the direct beam was covered by the beamstop, and the vertical stripes of missing data are due to the gaps between detector tiles; horizontal stripe in (b) was not captured by the detector. Intensities are represented in logarithmic scale.

three PS colloidal crystals (Figure 6.2d–f). To simulate the total scattering amplitude from a colloidal crystal, the scattering amplitude from a single particle according to DWBA was calculated, which was then summed over the particles constituting a single layer and, lastly, the summation over a stack of particle layers was performed. The stacking of N_l particle layers in random hexagonal close-packed ($rhcp$) arrangement [252] was implemented by introducing n_{hcp} hexagonal close-packed hcp layers (layer sequence ABAB...) and $(N_l - n_{hcp})$ layers of face-centered cubic (fcc) structure (layer sequence ABCABC...). Peak broadening caused by lattice spacing variation was taken into account by a convolution of the simulated data with a Voigt function, which has also included the instrumental broadening due to the incident beam divergence of 4×28 µrad^2 (vertical$\times$ horizontal) [246].

6.3 Temperature evolution of GTSAXS peak parameters

Once the structural parameters of the colloidal crystals were quantified at RT conditions, the analysis of the *in-situ* GTSAXS data measured upon incremental heating of the samples was performed in a wide temperature range from RT to 385 K. Figure 6.3 shows GTSAXS patterns for the samples A, B and C at selected temperatures: 300, 355, 376, 381 and 385 K. The patterns are displayed for the q-range of 0.0643×0.0643 Å^{-1}

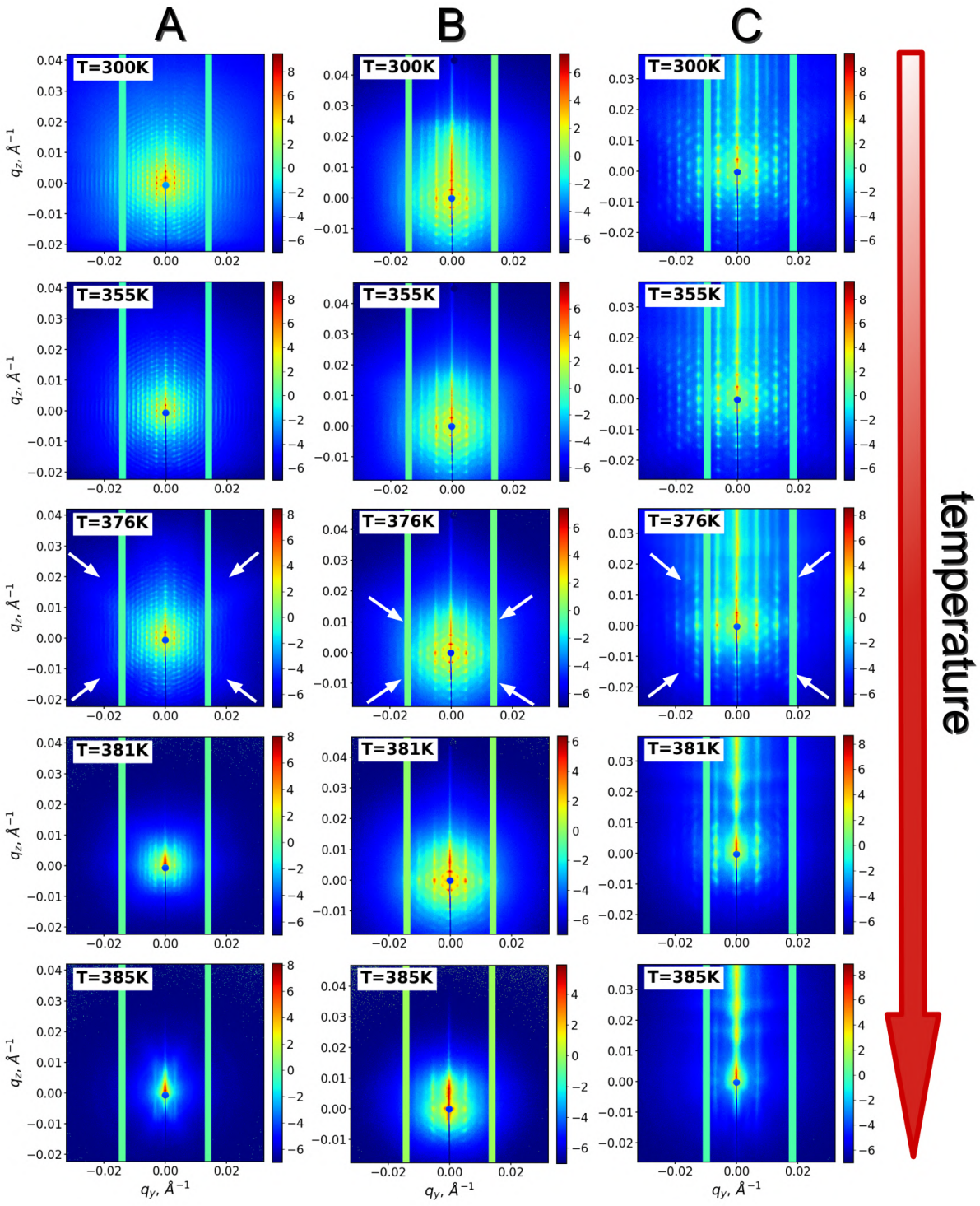

Figure 6.3: *In-situ* GTSAXS patterns for the PS colloidal crystal samples A (left column), B (middle column) and C (right column) measured during incremental heating in the range from RT to T = 385 K. Intensities are represented in logarithmic scale.

representing almost the full range of the 2D detector (square area of 487×487 px^2 of the Pilatus 300K detector). By visual inspection of diffraction peaks and diffuse scattering distribution one can identify the intermediate states of a colloidal crystal in the process of dry sintering. In the temperature range from RT to annealing temperature T_a = 355 K the peak shapes and positions exhibit no significant changes, while the isotropic diffuse scattering becomes suppressed. With a further increase of temperature up to T = 376 K the high-order diffraction peaks start to vanish, indicating a gradual loss of long-range ordering in a colloidal crystal. The fading of long-range order is accompanied by a transition from isotropic to anisotropic diffuse scattering distribution in the form of two inclined flares depicted by white arrows in Figure 6.3 at T = 376 K. The anisotropy of diffuse scattering indicates the onset of particle plastic deformation and shape transformation from a spherical to a faceted shape. Above T = 381 K the abrupt decay of lower diffraction orders signifies the total loss of ordering and the formation of an amorphous polymer film.

To unravel the behaviour of the colloidal crystals under dry sintering conditions, GTSAXS data was analyzed by evaluating the diffraction peak parameters, such as position, integrated intensity and widths as a function of temperature. The in-plane and out-of-plane directions in a colloidal crystal were probed by choosing the sets of (110) and (001) diffraction orders (Figure 6.2). The obtained temperature dependencies of the peak parameters for sample A are shown in Figure 6.4. At the initial stage of temperature raise up to T_a and the colloidal crystal undergoes thermal expansion while maintaining the long-range order. In this temperature range both in-plane and out-of-plane q-values of diffraction peaks decrease linearly. By converting q-values to interparticle distances the thermal expansion coefficient of the PS crystal was determined from a linear fit (Fig. 6.5). The obtained in-plane and out-of-plane linear coefficients α_L of thermal expansion of PS of 6.4×10^{-5} K^{-1} and 7.2×10^{-5} K^{-1} are in a good agreement with literature data [253] reporting the volumetric thermal expansion coefficient α_V=3α_L for PS as 1.7 - 2.4×10^{-4} K^{-1}. Further temperature increase up to the glass transition temperature of PS T_g = 373 K results in decreasing of particle size due to the faceting of colloidal spheres. In a range from T_g to the melting temperature T_m the particle size decreases more sharply which is caused by the fusion process of PS particles. From the integrated intensity plot (Figure 6.4b,e) one can directly determine the crystal melting temperature T_m, i.e. the temperature corresponding to the amorphisation of a colloidal crystal and the formation of a polymer film. T_m values of 378 K, 381 K and 377 K have been obtained for the samples A, B and C, respectively. The observed increase of T_m with an increase of the film thickness conforms with the results of earlier studies of glass transition in PS films [254]. Apart from T_m behavior, significant influence of the PS particle size on the evolution of structural parameters of colloidal crystals in the process of dry sintering was observed.

The temperature dependencies of peak widths $W_{q_{y,z}}$ were fitted using Williamson-

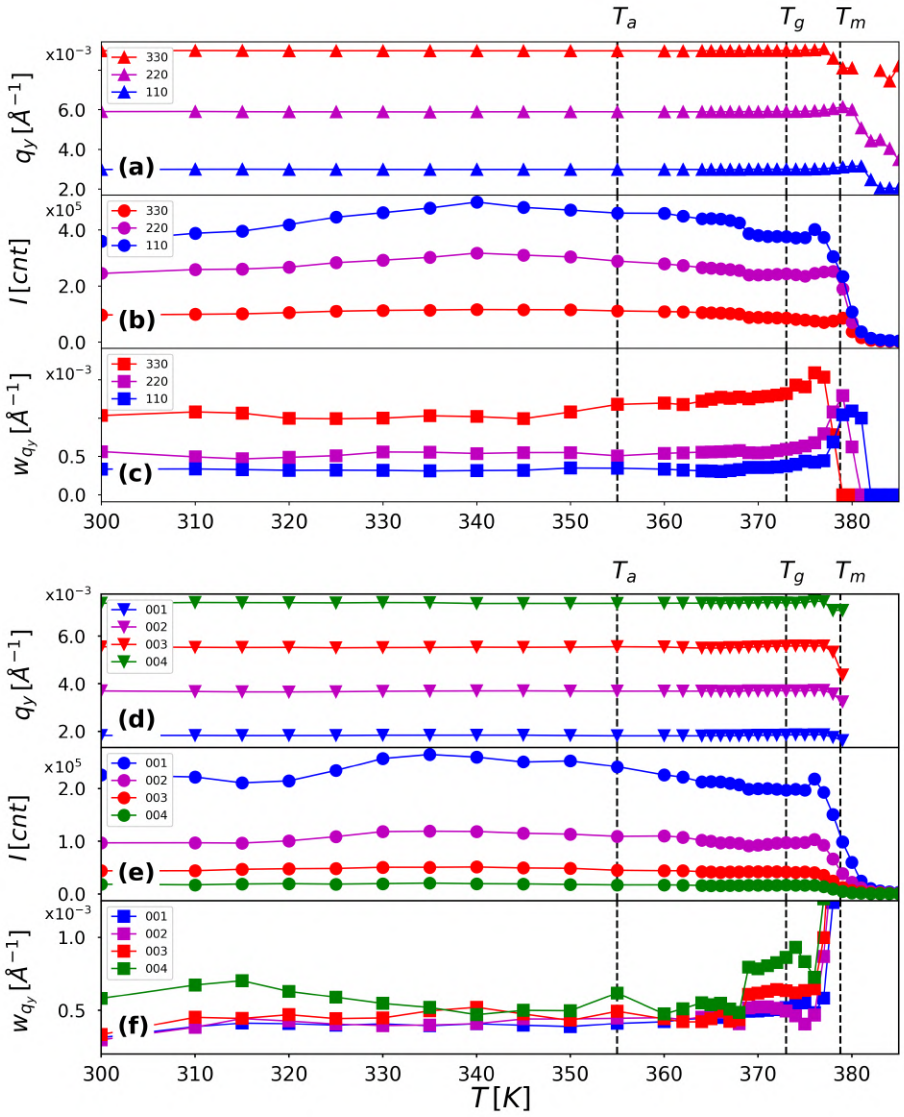

Figure 6.4: Temperature dependencies of GTSAXS peak positions, integrated peak intensities and widths of the PS colloidal crystal sample A for (a–c) in-plane and (d–f) out-of-plane directions.

Hall (WH) formula [255, 256]

$$W_{q_{y,z}}(T)^2 = (2\pi / L_{q_{y,z}}(T))^2 + (g_{q_{y,z}}(T)q)^2 , \tag{6.1}$$

where $L_{q_{y,z}}$ are the coherent scattering domain (CSD) sizes and $g_{q_{y,z}}$ represent the lattice deformation parameters. The temperature dependencies of CSD sizes and lattice deformation parameters obtained from the fitting analysis are plotted in Figure 6.6 for the sample A. The CSD size values of L_{q_y} = 4 µm and L_{q_z} = 3 µm and lattice deformation values of g_{q_y} = 4% and g_{q_z} = 6% for in-plane and out-of-plane directions, respectively, mainly remain constant in a range from RT to the annealing temperature T_a. At T = 365 K the in-plane CSD size exhibits a peak which coincides with a minimum of out-of-plane g parameter, indicating the initiation of an intermediate ordered phase in the

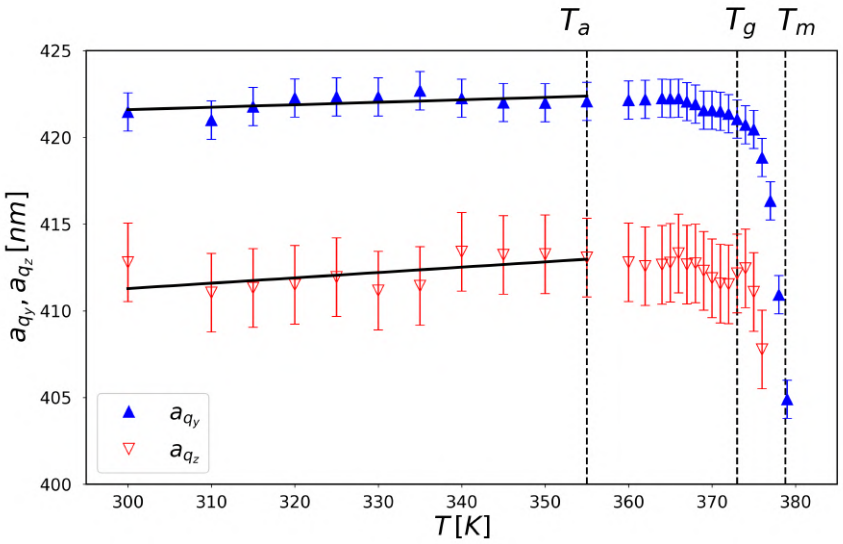

Figure 6.5: Temperature dependencies of in-plane a_{q_y} and out-of-plane a_{q_z} interparticle distances for the sample A. Linear fits are plotted by solid lines.

colloidal crystal due to thermal annealing. With further raising of temperature up to T_g the L values decrease while the g values increase, thus indicating the accommodation of lattice strains due to the fusion of colloidal particles.

At temperatures above T_a the transformation of spherical particle to a faceted shape sets in, as indicated by an enhancement of anisotropic diffuse scattering pattern in a form of inclined streaks (depicted by arrows in Figure 6.3(a,c)). The effect of particle shape transformation was analyzed by GTSAXS simulations implementing the scattering function of a rhombic dodecahedron, which can be computed as a sum of scattering functions of a cube and six equilateral square pyramids attached to the faces of a cube [257]. In Figure 6.7 the GTSAXS pattern measured for the sample A at T = 376 K is compared to the simulated GTSAXS patterns, corresponding to the scattering function of a single sphere (Figure 6.7b) and a 1:1 mixture of spheres and rhombic dodecahedrons (Figure 6.7c). As can be deduced from the scattering patterns the combination of spherical and dodecahedron shapes provides better description of the experiment as compared to the single sphere case. It worth to note that the diffuse scattering enhancement observed in GTSAXS geometry is less pronounced than in the case of SAXS geometry because of the averaging of scattering signal in GTSAXS due to a larger beam footprint. Similar enhancement of diffuse scattering due to particle faceting has been observed previously in transmission SAXS geometry [246, 255].

This result further implies that the shape transformation affects not all particles in a crystal, which is apparently caused by the presence of disordered domains. The transition of PS colloidal particles from spherical to a dodecahedron shape is also indicated by the decrease of lattice spacing at temperatures above T_g. As can be seen from Figure 6.5, the in-plane lattice spacing decreases from 420 nm down to 405 nm, reaching the value $D_{rd} \approx 0.96 D_{sp}$ This value is expected because the volume of a

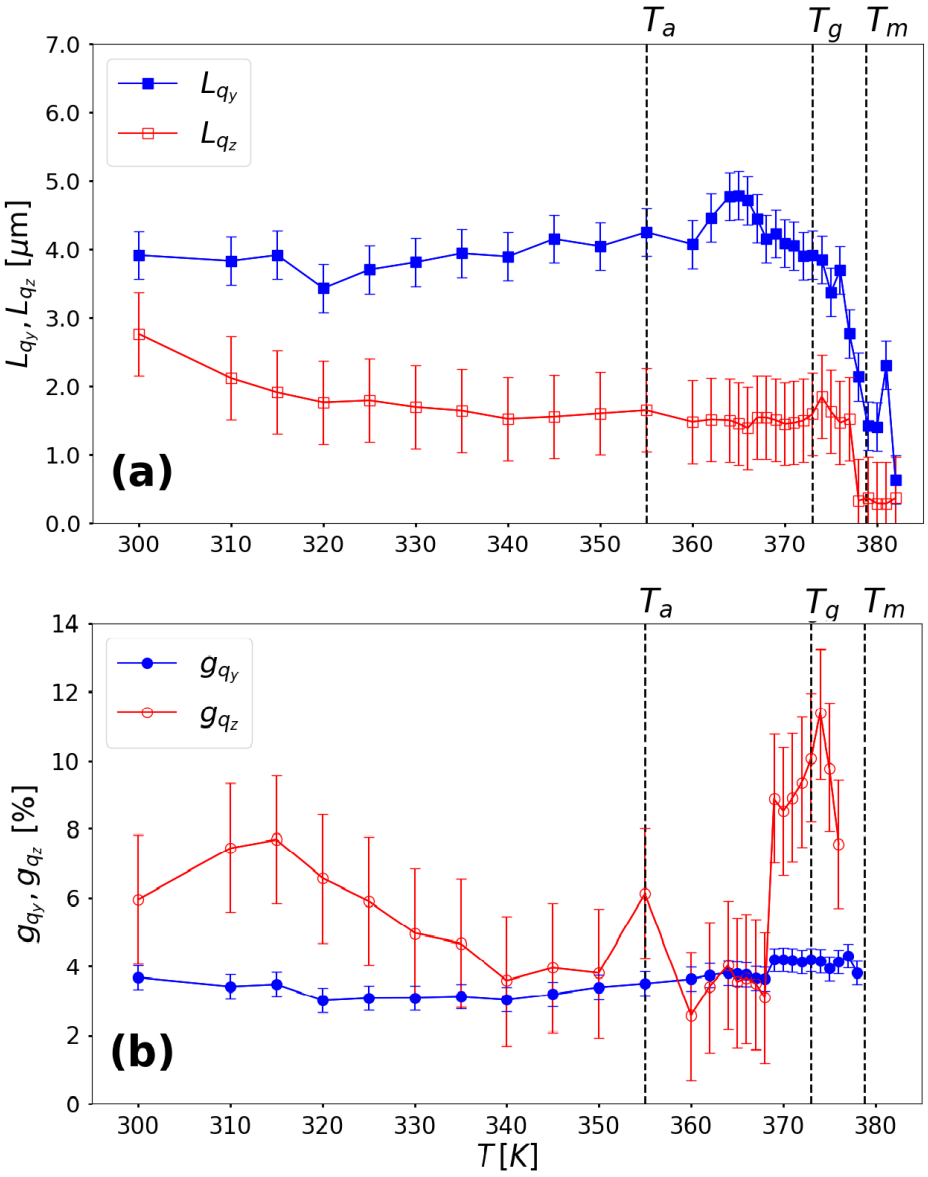

Figure 6.6: Temperature dependencies of (a) CSD sizes and (b) lattice deformation parameters for in-plane (blue filled dots) and out-of-plane (red open dots) directions of the sample A.

sphere $V_{sp} = (4/3)\pi R_{sp}^3$ has to be equal to the volume of a rhombic dodecahedron $V_{rd} = 16\sqrt{3}/9a^3$, where the radius of a sphere $R_{sp} = 0.5D_{sp}$ and a is the edge of a rhombic dodecahedron. From this condition, the lateral size of a rhombic dodecahedron $D_{rd} = \sqrt{3}a \approx 0.96D_{sp}$.

The structural evolution of a PS colloidal crystal in the process of dry sintering is visualised by a schematic 3D model in Figure 6.8, introducing a close-packed *fcc* arrangement of colloidal spheres with a central sphere surrounded by its 12 neighboring spheres. The middle layer consisting of the central sphere and its 6 neighboring spheres (shown in red) is sandwiched between the adjacent layers of 3 spheres each (shown in blue and green colors). The thermal expansion stage is followed by particle softening, which results in the particle shape transformation from a sphere to a rhom-

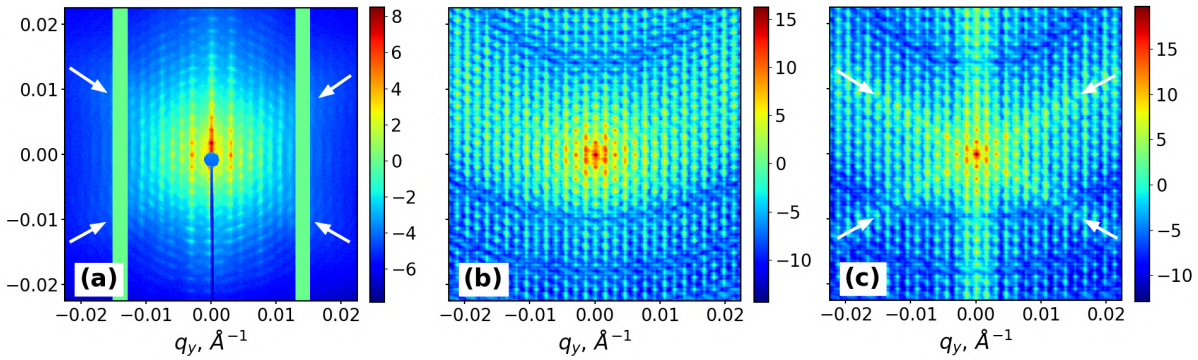

Figure 6.7: GTSAXS patterns for the sample A at T = 376 K: (a) experiment, (b) simulation using the scattering function of a single sphere and (c) simulation using the scattering functions of a sphere and a rhombic dodecahedron.

bic dodecahedron. The shape transformation is followed by the particle fusion stage, where the boundaries between particles merge together due to the interdiffusion of polymer chains.

6.4 Conclusions

In summary, the structural rearrangement of polymer colloidal crystals in the process of dry sintering has been revealed by *in-situ* GTSAXS measurements, which are sensitive to both in-plane and out-of-plane ordering. By simulations of GTSAXS patterns based on DWBA theory the structural characteristics such as particle size, number of layers, domain sizes, lattice disorder and mosaic spread have been determined at RT for the colloidal crystals made of spherical PS particles of different sizes. The in-plane lattice dilatation of 1-2% was observed, as compared to the out-of-plane direction in the PS colloidal crystals due to entropy-driven *rhcp* arrangement of particle layers and surface tension effects.

It was found that the PS colloidal crystals undergo several stages of structural evolution in the process of dry sintering: thermal expansion, particle shape transformation and crystal amorphisation. By analysing the peak positions as a function of temperature the linear coefficient of thermal expansion of polystyrene was determined, being in excellent agreement with literature data [253]. At temperatures around the glass transition temperature of PS, characteristic enhancement of diffuse scattering was observed indicating the particle transformation from spherical to polyhedron shape (see Fig. 6.8). The observed formation of polyhedral colloidal particles under dry sintering conditions in PS colloidal crystals has been supported by GTSAXS simulations using the particle shape functions of a sphere and a rhombic dodecahedron.

At temperatures approaching the crystal melting temperature T_m the softening of colloidal particles and interdiffusion of polymer chains lead to the blurring of interfaces between particles and the subsequent formation of an amorphous polymer film.

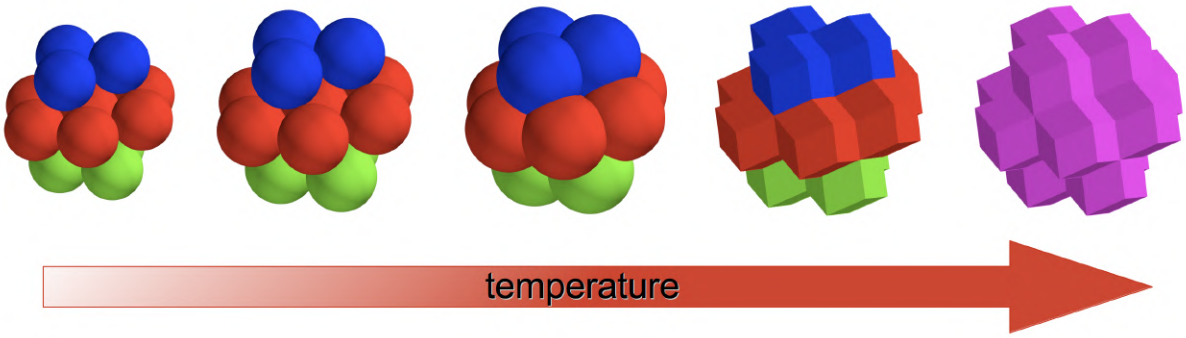

Figure 6.8: Schematic 3D model illustrating the structural rearrangement of *fcc* closed-packed colloidal spheres in the process of dry sintering.

A linear dependence of melting temperature T_m on the thickness of a colloidal crystal was observed, which is in agreement with previous studies of glass transition in PS films [254]. The observed decay of diffraction peak intensities and scattering domain sizes around T_m implies that the complete loss of ordering and the formation of a polymer film occur within a narrow temperature interval of less than 3 K.

Chapter 7

Probing dynamics in colloidal crystals with pump-probe experiments at LCLS

Acoustic motion in nanoscale objects induced by light is important for both fundamental science and applications. This interest is due to various potential applications in acousto-optical devices which can be used for ultrafast manipulation and control of electromagnetic waves by hypersonic (GHz) acoustic waves [167]. Colloidal crystals, formed by the self-assembly method, have shown phononic band gaps in the GHz frequency range [164–166]. Due to the recent progress in the fabrication of high-quality colloids, this provides an opportunity to produce inexpensive phononic crystals.

This chapter is based on the Reference [258]. In the first section, various studies of laser – induced vibrations in solids are discussed. Two pump-probe experiments on the colloidal crystals, previous to the study presented in this thesis are described in details. Further the infrared (IR) pump - X-ray probe diffraction experiment performed at XFEL on a periodic PS colloidal crystals is discussed. The periodicity of the sample allowed us to apply the Bragg peak analysis. The positions of the Bragg peaks and their radial and azimuthal widths were analyzed as a function of the time delay. Two sets of the experiments were performed - one with the IR laser intensity lower than the ionization threshold of the PS and one with higher IR laser intensity. In this chapter we discuss the experiment performed with the low IR laser intensity ($< 10^{14}$ W/cm^2), and in the next chapter the experiment performed with the IR laser intensity on the order of 10^{14} W/cm^2 is described. A theoretical analysis of the vibrations of the colloidal crystals was performed and applied to the analysis of the experimental results.

7.1 Pump-probe experiments on solid samples

Studies of coherent lattice vibrations (phonons) in solids is an exciting field of research in modern solid-state physics. In order to reveal the laser-induced phonon dynamics, the femtosecond pulse with duration shorter than the period of phonon oscillations is required. Such a short pulse excites only the electron subsystem while the lattice remains cold during the electron-phonon energy transfer time. To study the electron-phonon coupling a number of pump-probe experiments have been performed. In one of the type of the experiments the reflectivity oscillations at frequencies corresponding to the optical phonon modes of the material are measured. Such oscillations were observed in bismuth [259, 260], ferroelectric GeTe [261], gold [262] and colloidal crystals [263]

Using X-rays as a probe offers the possibility of measuring the atomic-scale motions directly. It was reported on the X-ray diffraction studies of the femtosecond structural changes of a bismuth crystal [264, 265]. Also, femtosecond X-ray diffraction was used to elucidate the dynamics of the high-amplitude phonons by direct measurement of the atomic positions within the unit cell in bismuth [266]. In the work of Sokolowski-Tinten the ultrashort X-ray pulses were generated by the microplasma source [264]. In another experiment femtosecond X-ray pulses were created using the synchrotron electron-beam slicing method [265]. However, the low scattering cross – sections of X-rays and relatively low number of photons in the ultrashort X-ray pulses limit the possibilities of these methods. In this respect, X-ray free-electron lasers, producing X-rays with unprecedented brightness, pulse duration and coherence, are especially well suited for investigating ultrafast structural dynamics.

It was also reported on the studies of the dynamical properties of single nanoparticles revealed by optical pump-probe experiment [262], and using electrons or X-rays [267, 268]. The application of advanced X-ray imaging methods, such as Bragg coherent diffraction imaging, allow characterization of lattice displacements in individual gold nanoparticles with atomic sensitivity [269].

This thesis is focused on the studies of the laser-induced dynamics in the colloidal crystals. There are several studies of the dynamical properties of the colloidal crystal using pump-probe technique. Dynamics in submicrometer colloidal crystals was investigated using different techniques such as Raman scattering [270], Brillouin light scattering [164], and optical pump-probe spectroscopy [166]. One of the examples of studies of the laser-induced dynamics of colloidal crystals by optical light is given in Ref. [263]. In this work silica colloidal crystals of 359 ± 10 nm in diameter were pumped and probed by the IR laser with 800 nm laser wavelength, 0.3 ps pulse duration and maximum energy of 1 μJ. In order to achieve higher absorption, all samples were covered by the 100 nm thick aluminum layer. The pump pulse was focused down to 200 μm on the aluminum layer, and the probe pulse was focused on the other side of

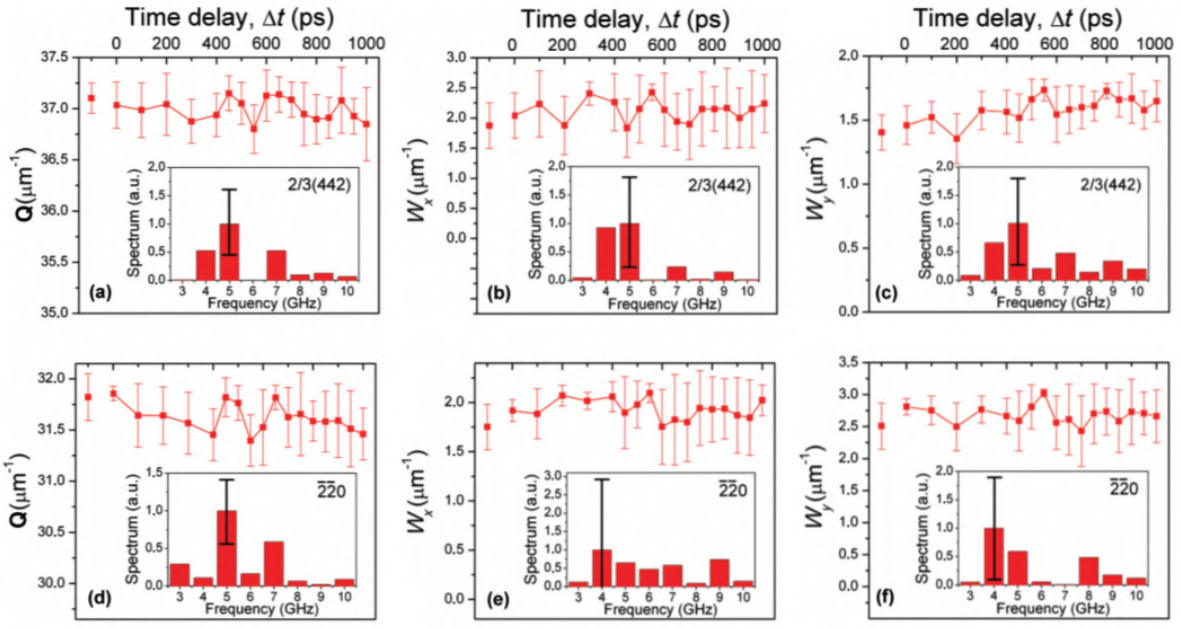

Figure 7.1: Time dependence of the momentum transfer Q (a) and (d), horizontal W_x (b) and (e) and vertical W_y (c) and (f) size (FWHM) for the selected Bragg peaks. Error bars are determined as a standard deviation for ten measurements. The insets show the power spectrum of the corresponding data. This figure was adapted from Reference [272].

the sample, which allowed to study $\mathbf{q}$ – vector perpendicular to the sample surface. The measured reflectivity curve shows the 11 GHz frequency oscillations with amplitude on the order of 10^{-4}. These oscillations correspond to the spheroidal mode of the vibrations of a colloidal crystal particle [271].

Later, another study of the laser-induced colloidal crystal vibrations was performed at FLASH [272]. In this experiment polystyrene colloidal crystal of 398 ± 11 nm in diameter were pumped by the IR laser with 800 nm wavelength and 1 μJ energy, and probed by the 8 nm FEL pulse with 0.1 ps pulse duration. The Bragg peaks originating from the colloidal crystal were observed and the parameters of the Bragg peak, such as intensity and FWHM were analyzed (see Fig. 7.1). This pump-probe experiment indicated the possibility of observation of the dynamics in the colloidal crystals by diffraction. To give a reliable interpretation of the observed results, it was necessary to investigate the dynamics with a larger time interval and better statistics. These studies motivated us to perform IR pump – hard X-ray probe diffraction experiment on a polystyrene colloidal crystal.

7.2 Experiment

7.2.1 Experimental setup

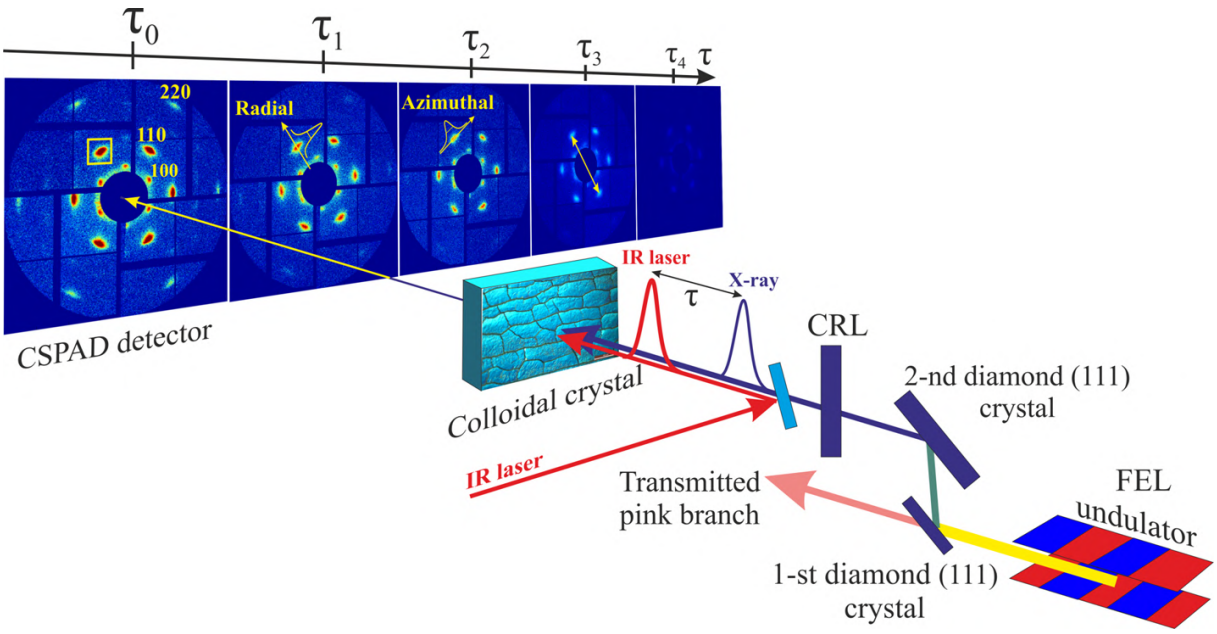

Figure 7.2: The scheme of the pump-probe experiment. X-ray free-electron laser (XFEL) pulses are generated by the undulator and reflected by the first diamond crystal. The second diamond crystal reflects the beam in the direction to the sample position. The beam is focused by the compound refractive lenses (CRLs) to the size of 50 µm at the sample position. The Cornell-SLAC Pixel Array Detector (CSPAD) is positioned 10 m downstream from the colloidal sample.

The pump-probe experiment was performed at the Linac Coherent Light Source (LCLS) [24] in Stanford, USA at the X-ray Pump Probe (XPP) beamline [273]. LCLS was operated in the Self Amplified Spontaneous Emission (SASE) mode. We used LCLS in the monochromatic regime with the photon energy of a single XFEL pulse of 8 keV (1.5498 $\AA$), energy bandwidth $\Delta E/E$ of $4.4 \cdot 10^{-5}$, and pulse duration of about 50 fs at a repetition rate of 120 Hz. The X-ray beam was focused using the Compound Refractive Lenses (CRL) on the sample down to 50 µm Full Width at Half Maximum (FWHM). The experimental setup is shown in Fig. 7.2. Series of X-ray diffraction images were recorded using the Cornell-SLAC Pixel Array Detector (CSPAD) [274] with a pixel size of 110×110 µm^2 positioned at the distance of 10 m and covering an area approximately 17×17 cm^2. Our experimental arrangement provided a resolution of 0.5 µm^{-1} per pixel in reciprocal space.

In our pump-probe experiment the Ti:Sapphire IR laser was used to pump the colloidal crystal film. The pump pulses were generated at the wavelength $\lambda = 800$ nm (1.55 eV) and duration about 50 fs (FWHM). The IR laser pulses were propagating collinear with XFEL pulses and were synchronized with the XFEL pulses with less than 0.5 ps jitter. The size of the laser footprint on the sample was 100 µm (FWHM)

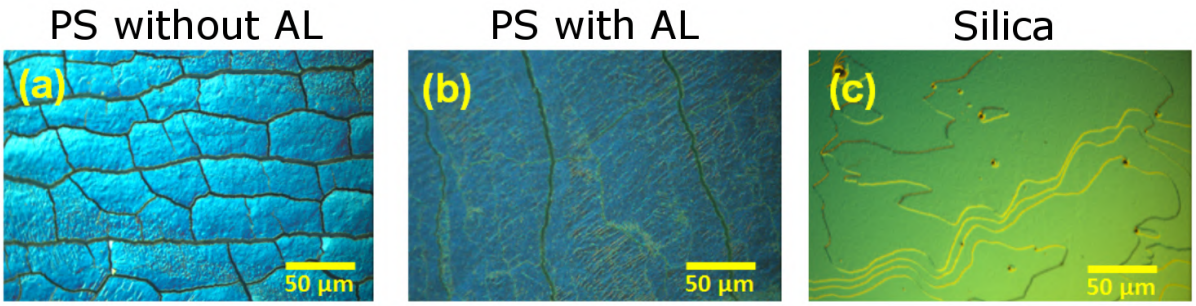

Figure 7.3: Microscopic images of colloidal crystals made from (a) polystyrene (PS), (b) PS covered with an Al layer, and (c) silica samples measured at Linac Coherent Light Source (LCLS).

and hence twice the size of the X-ray beam. The pump-probe experiment was performed with a time delay variation τ from 50 ps to +1000 ps, with a 10 ps time increment. This time delay region and the time interval were considered in order to resolve GHz frequency dynamics of colloidal crystals. In order to obtain sufficient statistics of the measured data, for each time delay a large number of diffraction patterns (600 for polystyrene and 120 for silica) with and without the IR laser were measured.

The colloidal crystal films were prepared from polystyrene spheres using the vertical deposition method [194]. The grown colloidal crystal films consisted of 30-40 layers of close-packed hexagonal planes. The thickness of the film was slightly depending on the position on a film along the growth direction. Due to the growing method, the dried colloidal crystal films used in our experiment contain cracks between single-crystal regions of about 50 µm in size. Different types of samples were investigated. The first type was polystyrene colloidal crystals with different particle diameters of $D = 420 \pm 9$ nm and $D = 376 \pm 8$ nm. After crystal growth, some of the films were covered with a 20 - 50 nm thick aluminum layer to increase interaction with the IR laser. Also we studied silica colloidal crystals with $D = 238 \pm 7$ nm. Microscopic images of these samples are shown in Figure 7.3.

7.2.2 Infrared laser calibration

The IR laser energy was controlled by the rotation of the optical axis of a waveplate, and was calibrated by a power sensor located at the sample position. The calibration curve showing the dependence of the laser pulse energy from the waveplate angle is presented in Fig. 7.4. The corresponding IR laser intensity is shown on the right vertical axis. The IR laser intensity was calculated from the IR laser energy assuming Gaussian shape of the pulse with 50 fs FWHM in the temporal domain and 100 µm FWHM in the spatial domain. Zero degrees of waveplate angle corresponds to the minimum and 15 degrees correspond to the maximum calibrated energy and intensity of the IR laser. The calibration curve was fitted with a sine function shown by the solid red line in Fig. 7.4.

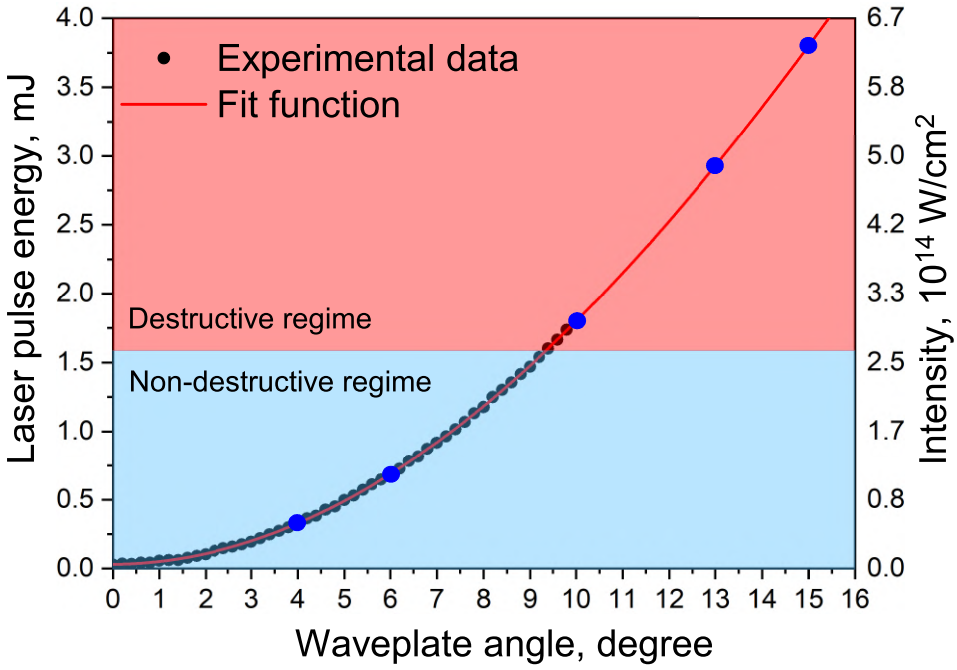

Figure 7.4: The infrared (IR) laser energy calibration curve. The measured data is shown by the black dots and the sine fit is shown by the solid red line. Destructive and non-destructive regimes are shown. The IR laser energy used in the experiments is marked with blue circles.

Depending on the IR laser intensity two regimes of the laser-matter interaction were achieved, namely destructive and non-destructive regime (see Fig 7.4). In this chapter we discuss a series of pump-probe experiments performed with the variation of the IR laser energy from 195 µJ to 691 µJ (3.2×10^{13} - 1.1×10^{14} W/cm^2) for polystyrene and silica samples and from 195 µJ to 326 µJ (3.2×10^{13} - 5.4×10^{13} W/cm^2) for polystyrene films covered by aluminum. Measurements with different IR laser energies were performed at the new position of the sample to avoid sample damage. The upper limit of IR laser energies was set due to the damage threshold of the colloidal crystals and was lower for Al-covered samples due to enhanced absorption of IR light by the Al film.

The experiment performed at higher IR laser intensities ($I_1 = 3.0 \cdot 10^{14}$ W/cm^2, $I_2 = 4.8 \cdot 10^{14}$ W/cm^2 and $I_3 = 6.3 \cdot 10^{14}$ W/cm^2) is discussed in chapter 8.

7.2.3 Data analysis

The following strategy was implemented for the data analysis. First, for the patterns with sufficiently high intensity (more than 5000 counts per single diffraction pattern), we selected Bragg peaks located far away from the detector gaps. Patterns with a lower signal were not treated. Using this procedure, typically three to four Bragg peaks were selected for the analysis. Next, the Bragg peak positions were extracted using the center of mass of their intensity distributions as well as the relative distances

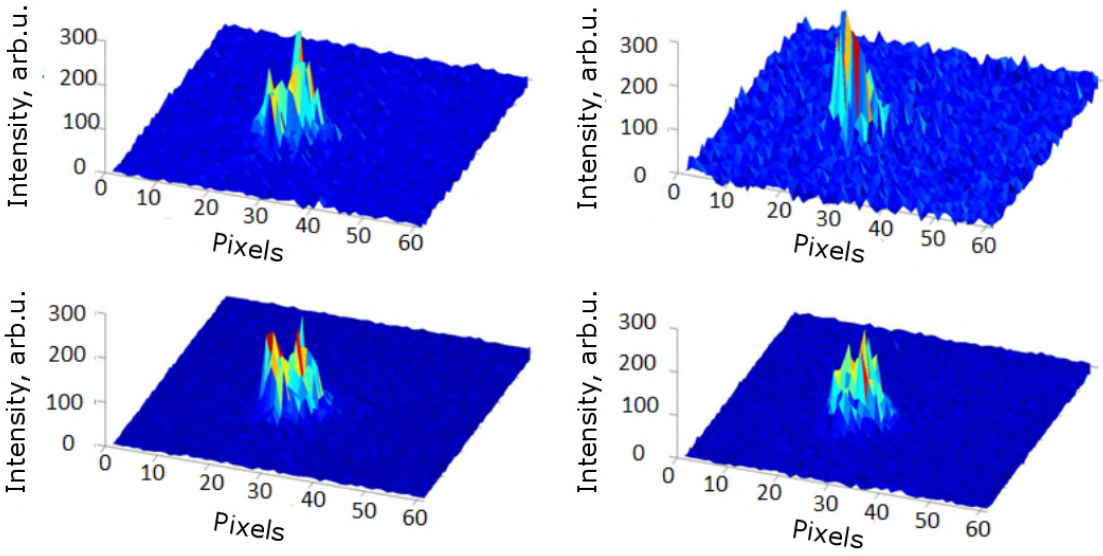

Figure 7.5: Four single-shot diffraction patterns measured at the same Bragg peak position. The spike-shaped peaks demonstrate an influence of the individual structure of each XFEL pulse on the Bragg peak.

between the opposite Bragg peaks. The change of the relative positions of the Bragg peaks as a function of the time delay allowed us to probe the lattice dynamics along specific crystal directions. The following parameters as a function of time delay were analyzed in order to reveal the dynamics of the colloidal crystals induced by the IR laser: Bragg peak position $q(\tau)$, as well as peak sizes (FWHMs) in the radial $w_q(\tau)$ and azimuthal $w_\varphi(\tau)$ directions in reciprocal space. The temporal variation of the momentum transfer vector $q(\tau)$ is related to the dynamics in the inter-particle spacing, while $w_q(\tau)$ corresponds to the dynamics of the average particle size, and $w_\varphi(\tau)$ defines the angular misorientation of coherent scattering domains [255].

Due to the nature of the SASE process, each XFEL pulse has a unique fine spatial structure that was mapped by the intensity distribution at each Bragg position. A multi-spiked structure of the Bragg peaks varying from pulse to pulse was observed in our experiment (see Figure 7.5). From these diffraction patterns spatial and temporal coherence properties of hard XFEL could be determined by spatial correlation analysis [71]. Due to the different shape of each FEL pulse (see Figure 7.5), it was not possible to perform deconvolution of each scattered pulse shape. For the same reason (non-Gaussian structure of Bragg peaks) fitting of the peaks with the two-dimensional Gaussian function was not reliable (see Figure 7.6a). In order to improve Bragg peak characterization, projections of their intensities on azimuthal and radial directions were performed. These data were fitted with the one-dimensional Gaussian function (see Figure 7.6b), and peak broadening in the radial (w_q) and azimuthal (w_φ) directions was determined.

In order to compare the dynamics of the collected data as a function of the time

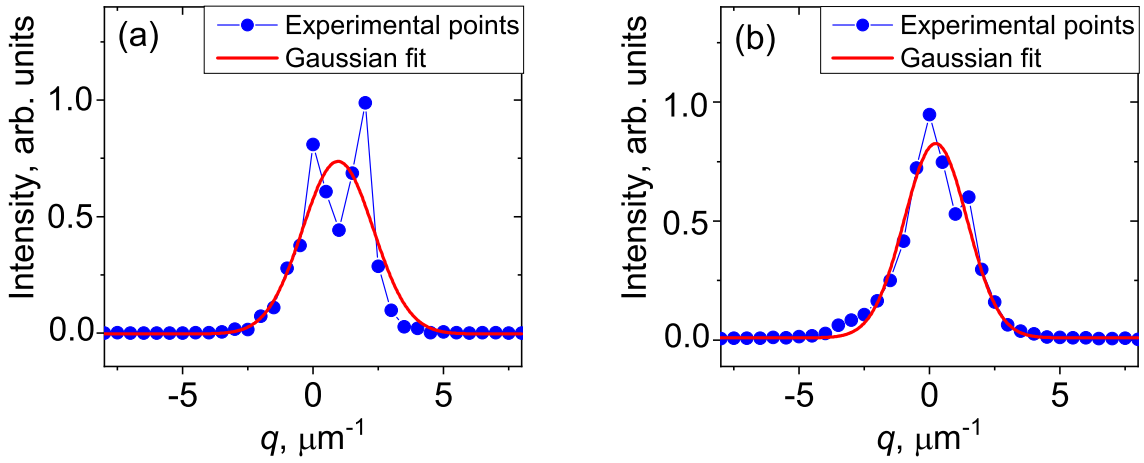

Figure 7.6: (a) The cross-section of a two-dimensional Bragg peak along azimuthal direction and (b) the projection of the same Bragg peak on the same direction. It is seen that the cross-section dataset (a) deviates from the Gaussian fit (red line), whereas the projection points are fitted with the Gaussian function with higher accuracy.

delay τ the following dimensionless parameters were used:

$$\frac{\Delta I(\tau)}{I} = \frac{\langle I_{on}(\tau) - \overline{I_{off}(\tau)}\rangle}{\overline{I_{off}(\tau)}}, \tag{7.1}$$

$$\frac{\Delta w(\tau)}{w} = \frac{\langle w_{on}(\tau) - \overline{w_{off}(\tau)}\rangle}{\overline{w_{off}(\tau)}}. \tag{7.2}$$

Subscript letters 'on' and 'off' define measurements with and without IR laser, respectively. Brackets $\langle \ldots \rangle$ correspond to averaging of the chosen Bragg peak parameter over the different positions at the sample. For the non-destructive regime both 'on' and 'off' pulses were averaged over each time delay, but for destructive regime only 'off' pulses were averaged due to the sample damage.

7.3 Experimental results

Typical single-shot diffraction patterns for the three different samples are shown in Fig. 7.2. The six-fold symmetry of the diffraction pattern is due to the hexagonal close-packed structure of the colloidal crystals. Two orders of Bragg peaks can be seen in single pulse diffraction patterns. A family of 110 Bragg reflections, indicated in Figure. 7.2 by squares, was used in further analysis.

Time dependencies of the momentum transfer vector $q(\tau)$, as well as radial $w_q(\tau)$ and azimuthal $w_\varphi(\tau)$ broadening of the Bragg peaks for three measured samples, are shown in Figure 7.7. Some points in this figure are excluded due to the unexpected

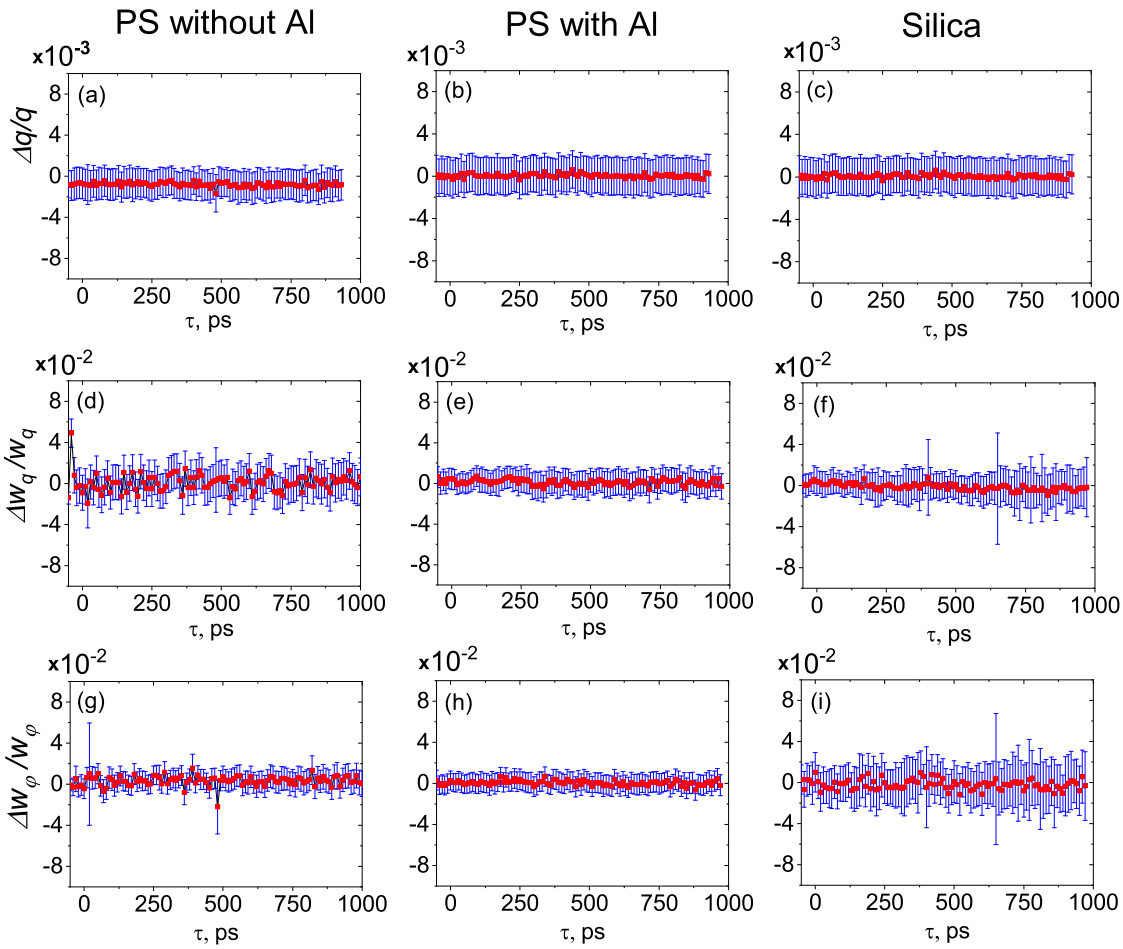

Figure 7.7: Time dependence of the relative change of the distance between the two opposite Bragg peaks $\Delta q(\tau)/q$ (ac) and Bragg peaks widths in radial $w_q(\tau)/w_q$ (d-f) and azimuthal $w_\varphi(\tau)/w_\varphi$ (g-i) directions for three selected samples. Analysis of the data was performed for the IR pump laser intensities shown by blue dots in Figure 7.4 and 110 Bragg peaks.

drops of intensity of the XFEL (such drops of intensity were observed when operation of some klystrons in the accelerator complex were failing). The statistical error of these parameters was determined using the standard approach for the error determination in the multi-parameter equation [275]. As clearly seen in Figure 7.7, the error of $\Delta q(\tau)/q$ values is one order of magnitude lower than for the Bragg peaks broadening parameters. This could be explained by the influence of the XFEL pulse shape on the shape of the Bragg peaks with a relatively stable position of each pulse. Due to this, the Gaussian fit of the Bragg peaks shape was not accurate, while the influence of the XFEL pulse spatial distribution on the variation of the center of mass was insignificant. The error values for the silica sample are higher than for the PS due to lower statistics (for the PS crystals 600 shots and for the silica crystals 120 shots were collected with the IR laser).

Figure 7.7 also clearly shows that variations of all parameters are around zero and in all cases, the signal is lower than the statistical error. To reveal characteristic frequencies excited by the IR laser, we performed the Fourier analysis of the time dependencies

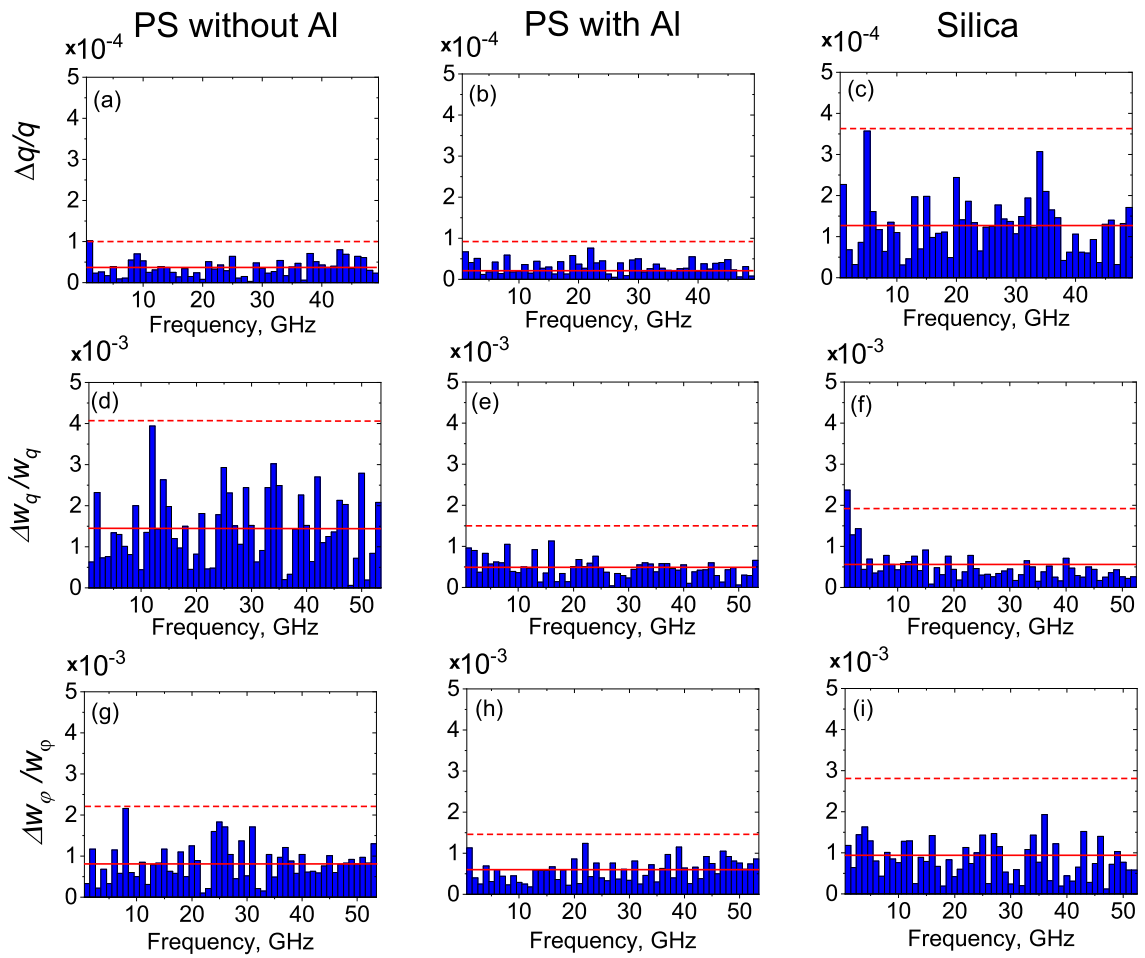

Figure 7.8: Fourier spectra from the distance between the two opposite Bragg peaks $\Delta q(\tau)/q$ (ac) and Bragg peaks widths in the radial $w_q(\tau)/w_q$ (d-f) and the azimuthal $w_\varphi(\tau)/w_\varphi$ (g-i) directions for three selected samples. These Fourier spectra are calculated from the results of the diffraction pattern analysis shown in Figure 7.7. Average value of all Fourier components is indicated by the solid red line. The dashed red line corresponds to the 3σ level above the average value, where σ is the standard deviation and is determined from the distribution of Fourier components.

of the Bragg peak parameters described above. The corresponding Fourier spectra are shown in Figure 7.8. Due to the more precise measurements of the momentum transfer vector $q(\tau)$, the average value of the Fourier components of $q(\tau)$ is one order of magnitude lower than for the Bragg peaks broadening $w(\tau)$. There was no significant enhancement of any particular Fourier component, for all Fourier spectra. We determined an average value of the Fourier components and the standard deviation σ from the distribution of these Fourier components. For all Fourier spectra shown in Figure 7.8, there is no Fourier component higher than 3σ above the average Fourier component value, which indicates that the periodic signal could not be reliably detected in these conditions.

7.4 Model simulations

To have better understanding of the obtained results, we performed simulations of the colloidal crystal dynamics induced by an external IR pulse excitation. In our model colloidal crystals consist of isotropic homogeneous spheres. The characteristic frequencies of vibration of a colloidal particle were determined using the Lamb theory describing vibrations of an isotropic elastic sphere [271]. Theoretically, two families of Lamb modes, namely spheroidal and torsional ones, can be derived from the equations of motion. The spheroidal modes cause the change of the sphere volume, and the torsional modes leave the sphere volume unperturbed. During the IR pulse propagation through a sphere, the changes of the sphere volume are expected and, therefore, we used spheroidal modes in our simulations. We determined the frequencies of the first spheroidal mode for all three measured samples using reference [276]. The sphere diameter, the longitudinal c_L and the transverse c_T sound velocities of PS and silica were obtained from reference [277]. These parameters, as well as the frequencies of the first spheroidal mode for the colloidal crystals, are summarized in Table 7.1.

The values of $\Delta q(\tau)/q$ were extracted from the experimental data with a smaller error in comparison to other Bragg peak parameters for all investigated samples (see Figure 7.7a-c). Therefore, the parameter $\Delta q(\tau)/q$ was considered for our simulations. Assuming an ideal close-packed crystal with the interparticle distances equal to the particles diameter, the unperturbed momentum transfer modulus of the 110 Bragg reflection can be described as $q_0 = 2\pi/D_{110} = 4\pi/D_0$, where D_0 is the unperturbed particle diameter. We simulated vibrations of the colloidal spheres with the diameter D_0 as a periodic sinusoidal signal

$$D(\tau) = D_0(1 - S \cdot \sin(\omega_v \tau)) \,, \tag{7.3}$$

where S is the relative amplitude and ω_v is the characteristic frequency of the vibration. The dynamics of the experimentally-observed 110 diffraction peak can be described as

$$q(\tau) = 4\pi/(D(\tau)) \approx 4\pi/D_0(1 + S \cdot \sin(\omega_v \tau)) \,, \tag{7.4}$$

where we used the Taylor series expansion of the momentum transfer vector $q(\tau)$ due to the small values of the amplitude $S \ll 1$. As a result, measured changes in the Bragg peak positions and $\Delta q(\tau)/q$ can be simulated as a periodic sinusoidal signal. We should also take into account systematic errors of the measurement as an additional noise. Finally, simulations of the parameter $\Delta q(\tau)/q$ in our model were described using the following expression

$$\Delta q(\tau)/q_0 = (q(\tau) - q_0)/q_0 = S \cdot \sin(\omega_v \tau) + N \cdot \eta_{noise}(\tau) \,, \tag{7.5}$$

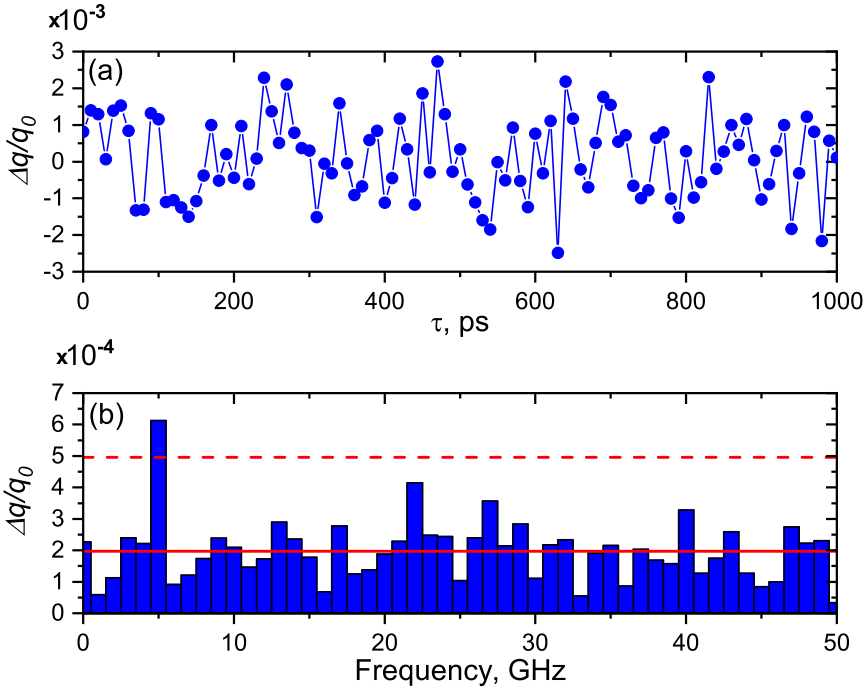

Figure 7.9: (a) Simulation of the signal $\Delta q(\tau)/q_0$ and (b) Fourier transform of this signal. The average value of all Fourier components is indicated by red line. The dashed red line corresponds to level of 3σ above the average value, where σ is a standard deviation and is determined from the distribution of Fourier components.

where N is the amplitude of a noise and $\eta_{noise}(\tau)$ is a random noise function with normal distribution and standard deviation value equal to one. The signal-to-noise ratio in this case is assumed to be equal to the ratio of the amplitudes S/N.

Next, we defined the criterion when the periodic signal is detected by the algorithm in our simulations. Due to the random behavior of the noise function $\eta_{noise}(\tau)$, each realization of the signal $\Delta q(\tau)/q_0$ (see Equation (7.5)) for a constant S/N is different. As an example, we demonstrate this for the experimental data of the polystyrene sample without aluminum. This sample was considered as one with the lowest noise level in our experiment. The time interval and increment of the simulated signal $\Delta q(\tau)/q_0$ were chosen the same as in our pump-probe experiment. One of the typical realizations of the $\Delta q(\tau)/q_0$ with the signal level $S = 0.7 \times 10^3$ and noise level $N = 1.4 \times 10^3$ is shown in Figure 7.9a. From this figure it is difficult to conclude on the presence or absence of the signal.

Similar to the analysis of the experimental data, the Fourier spectra were calculated for the simulated signal with the noise (see Figure 7.9b). Next, the behavior of the Fourier component amplitude A_{ω_v} corresponding to the first spheroidal mode frequency $\omega_v = 4.97$ GHz was studied. The criterion of detecting the signal was considered as

$$A_{\omega_v} > \bar{A} + 3\sigma\,, \tag{7.6}$$

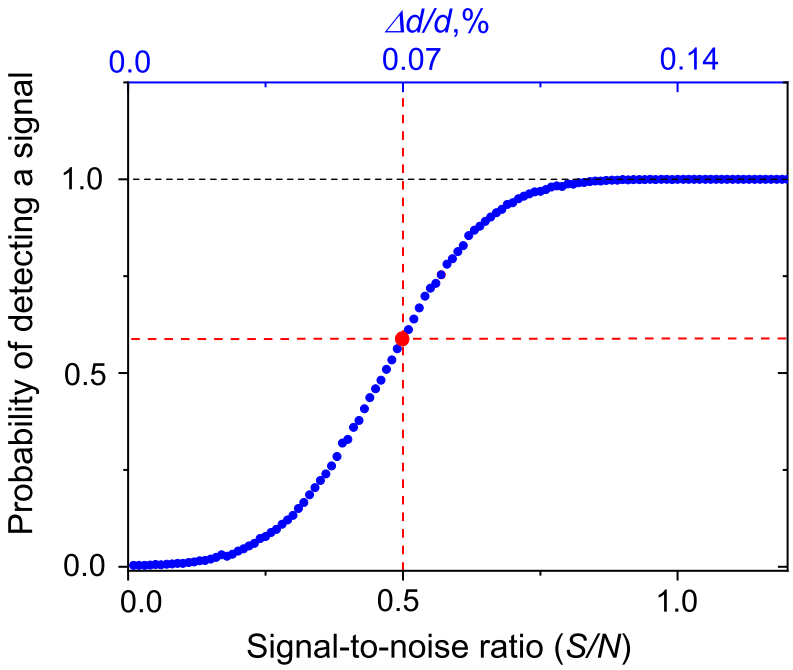

Figure 7.10: The probability of successful signal detection as a function of signal-to-noise ratio S/N. On the top horizontal axis, the change of the corresponding interparticle distance for the polystyrene sample without Al is shown. The red lines correspond to the value of $S/N = 0.5$ and $P(S/N) = 0.6$.

where $\bar{A}$ is the mean and σ is the standard deviation of all Fourier components in the spectrum. The Fourier spectrum of the simulated data (see Figure 7.9a), as well as its 3σ level are shown in Figure 7.9b. It can be seen that the contribution of the vibrational mode in the Fourier spectrum is higher than the criterion stipulated by Equation (7.6). Therefore, the algorithm detected the presence of the 4.97 GHz frequency signal.

We calculated the probability of successful signal detection as a function of signal-to-noise ratio S/N in the range of S/N from 0 to 1.5 with 0.01 increment. During the simulations the amplitude of the signal S was changing, while the noise level N was kept constant. The probability of detecting signal $P(S/N)$ was defined as

$$P(S/N) = \lim_{n\to\infty}\left(\frac{n_{detected}(S/N)}{n}\right), \tag{7.7}$$

where $n_{detected}(S/N)$ is a number of simulations with successful detection of signal (according to the criterion stipulated by Equation (7.6)) and $n = 10000$ is the total number of simulations for each S/N step. Results of these simulations for the experimental data of the polystyrene sample without aluminum are shown in Figure 7.10. As one can see from Figure 7.10 that, according to our criterion stipulated by Equation (7.6), the signal is 100% detectable if it is on the level of the noise $S/N = 1$.

Table 7.1: Parameters of PS and silica nanoparticles used in our model. The corresponding frequencies of the first spheroidal mode of colloidal particles were obtained from reference [276]. The noise level was derived from the experimental data. Relative and absolute deviation in the interparticle distance ($\Delta D/D_0$ and ΔD), which could be detected in our experiment with the probability of 60%, were calculated from the experimental data and simulations.

Sphere diameter, nm	PS without Al	PS with Al	Silica
Longitudinal sound velocity c_L, m/s	2350	2350	5950
Transverse sound velocity c_T, m/s	1210	1210	3760
Frequency of the breathing mode, GHz	4.97	5.54	19.06
Noise level $N \times 10^3$	1.4	1.8	1.8
Relative deviation in interparticle distance $\Delta d/d_0 \times 10^3$	0.7	0.9	0.9
Deviation in interparticle distance Δd, nm	0.29	0.35	0.22

7.5 Discussion

Simulations described previously, were performed for each sample (polystyrene sample without aluminum, polystyrene sample with aluminum, and silica samples) to derive the probability function $P(S/N)$ of detecting the periodic signal (see Figure 7.10) in each case. It is clearly visible from Figure 7.10 that even the value of the signal-to-noise ratio $S/N = 0.5$ gives 60% probability of detecting the signal. This condition was considered as a criterion for the minimum measurable signal. Using well-known relations between the deviations of the momentum transfer vectors and interparticle distances $\Delta q(\tau)/q_0 = \Delta D(\tau)/D_0$, as well as Equation (7.5), we can determine the relative (and absolute) values of the changes of the interparticle distances $\Delta D(\tau)/D_0(\Delta d(\tau))$ for the given values of the experimental noise N. As a result of this analysis, we can obtain the minimum values of these parameters which could be detected in our experimental conditions with the probability of 60%. For all measured samples results of this analysis are summarized in Table 7.1.

As it follows from Table 7.1, the minimum relative changes of the interparticle distance $\Delta D/D_0$ that can be detected with the probability of 60% for all samples were about 10^{-3}. Such values correspond to relatively large amplitudes of the deviations in interparticle distances of about 0.2 - 0.4 nm. Clearly, in our experimental conditions excited vibrations were lower than the noise level of the experiment that prevented us from their experimental determination.

7.6 Conclusions

In the present work the dynamics induced by IR laser in the polystyrene colloidal crystals was studied experimentally and by theoretical modelling. A pump-probe diffraction experiment was performed at LCLS with various IR laser intensities. The

periodic structure of the colloidal crystal allowed to measure Bragg peaks from the sample. The pump-probe experiments were performed in the wide range of the IR laser energies, from 195 μJ up to the upper limit of the non-destructive threshold of 691 μJ. The dynamics at different timescales was studied by the Fourier analysis of parameters associated with the momentum transfer and Bragg peak broadening in the radial and angular directions. Simulations of the colloidal crystal dynamics were performed and the probability function $P(S/N)$ was derived. Relative and absolute deviations in the interparticle distance ($\Delta D/D_0$ and ΔD), which could be detected in such an experiment with the probability of 60% (corresponding to the signal to noise level of 0.5), were calculated for all measured samples. From the experiment and simulations, one can conclude that, for all measured samples, the amplitudes of vibrational modes excited in colloidal crystals were less than the systematic error caused by the noise level.

Chapter 8

Femtosecond laser produced periodic plasma in a colloidal crystal probed by XFEL radiation

Studies of materials at high-pressure conditions above 1 Mbar are highly relevant to the physics of shock compressed matter [29, 30, 35, 89, 278], planetary formation [90, 279, 280], warm dense matter [29, 278, 281], and different types of plasma-matter interactions [87, 88]. Dynamic shock compression of aluminum [281], copper [282], graphite [29], and hydrocarbons [36], as well as other materials driven by high-power lasers, is a subject of recent extensive studies. The general understanding of processes in materials under high pressure and temperature, such as phase transitions [29] or phase separations [36] is of a great scientific interest. The invention of an ultrashort focused laser pulses with the intensities up to 10^{20} W/cm^2 and pulse duration of the tens of femtoseconds [31] boosted the studies of laser-matter interaction. Such a high laser intensity allows to ionize different kinds of matter and to create plasma from the material.

Results of this chapter are based on Reference [283]. The first section is focused on different ionisation regimes, the multiphoton, tunneling and above-barrier ionisation. The subsequent processes of the laser-plasma interaction, such as the inverse bremsstrahlung, plasma skin effect and electron-ion thermalisation are described. Further, the ablation and shock wave propagation processes are discussed in detail. In the last section the experiment performed with the IR laser intensity of the order of 10^{14} W/cm^2 is presented. With these extremely high intensities such a unique form of matter as periodic plasma [284] was created by the high-power laser interaction with the periodically ordered dielectric material. This confined hot periodic plasma exploded and generated a powerful shock wave that compressed the surrounding pristine material.

8.1 Physics of femtosecond pulse laser-matter interaction

8.1.1 Strong field ionisation

This section is focused on the different ionisation models. Fundamental works in the field of ionisation and plasma physics commonly use Hartree atomic units (AU) system named after the physicist Douglas Hartree [285]. In this system the following four fundamental physical constants: electron mass m_e, elementary charge e, reduced Planck constant $\hbar$ and inverse Coulomb constant $4\pi\epsilon_0$ are defined as unity: $m_e = e = \hbar = 4\pi\epsilon_0 = 1$. In this section atomic units are used, because this unit system radically simplifies the equations describing atomic processes

The ionisation of an atom can happen in different regimes, such as single-photon, multi-photon ionisation or quasi-static ionisation, depending on the incoming radiation intensity and wavelength (see Fig 8.1). In the single photon or multi-photon regime the incoming light is treated as a flux of photons while the quasi-static treats the incoming light as an electric field. An important parameter distinguishing multi-photon and quasi-static ionisation regimes is the Keldysh parameter γ [286]

$$\gamma = \frac{\omega\sqrt{2\mathcal{E}_I}}{E} = \begin{cases} > 1 \rightarrow \text{multi-photon regime}, \\ < 1 \rightarrow \text{quasi-static regime}, \end{cases} \tag{8.1}$$

where ω is the frequency of the laser field, $\mathcal{E}_I$ is the zero-field ionisation energy of an atom, and E is the external electric field generated by the laser. For low fields and high frequencies ($\gamma > 1$) the ionsation occurs in the multi-photon regime, while for strong fields and low frequencies ($\gamma < 1$) quasi-static ionisation prevails (see Fig. 8.2).

In the single-photon and multi-photon regimes, the shape of the potential of an atom is considered to be unperturbed by the external electric field. Therefore, ionisation of an atom requires a sufficient number of absorption processes in a short period of time. The single-photon ionisation, or photoionisation, occurs when energy of a sin-

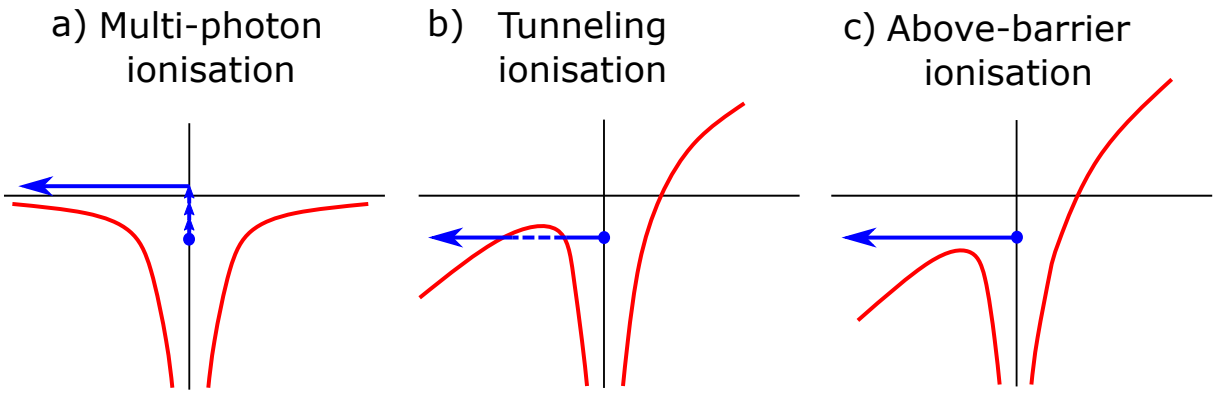

Figure 8.1: Schematic representation of three different ionisation regimes: (a) multi-photon, (b) tunneling, and (c) above-barrier.

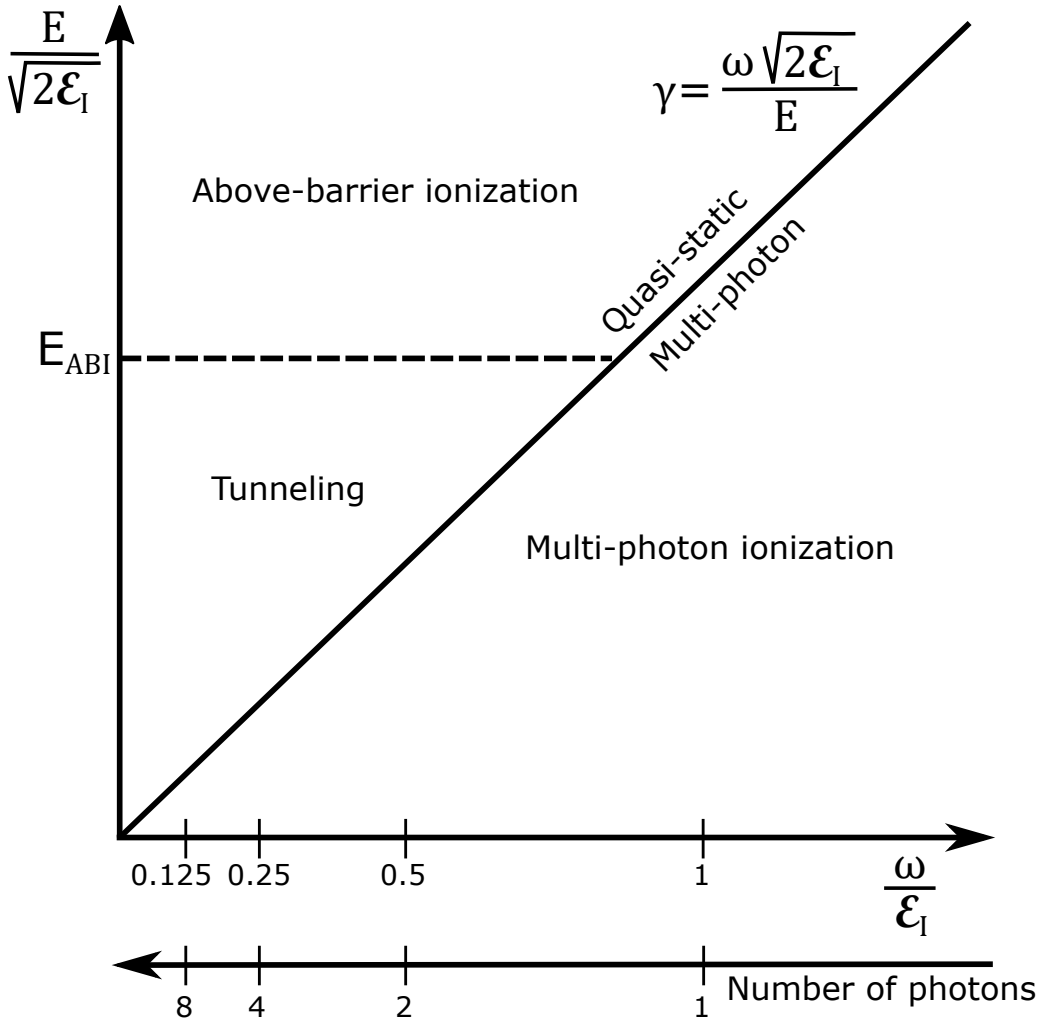

Figure 8.2: (a) Schematic map showing different ionization regions in the Keldysh theory. The quasi-static and multi-photon ionization regimes are determined by the value of the Keldysh parameter γ. E_{ABI}, defined only for the quasi-static regime, is the boundary between the tunneling ionization and the above-barrier.

gle photon is sufficient to ionise an atom (was described in Chapter 3). The number of photons n, which is sufficient for multi-photon ionisation can be estimated as

$$n = \left\lfloor \frac{\mathcal{E}_I}{\omega} \right\rfloor + 1\,, \tag{8.2}$$

where brackets $\lfloor ... \rfloor$ denote the integer part (floor function).

In the quasi-static regime, the incoming laser pulse is considered as an electric field curving the potential of an atom. Thus, the Coulomb effective potential barrier can be approximated as

$$V_{eff} = -\frac{Z}{r} + Er\,, \tag{8.3}$$

where Z is the ion charge, and r is coordinate from the center of an atom. The curved potential barrier of an atom V_{eff} is shown schematically in Fig. 8.3. The maximum of

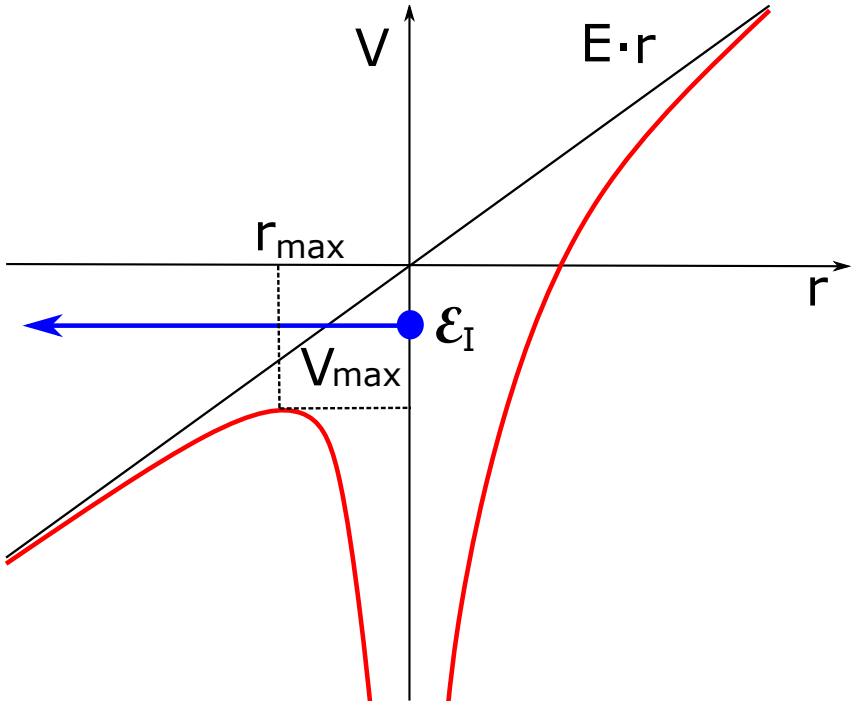

Figure 8.3: Schematic representation of the ionization in the quasi-static regime. The characteristic potential V_{eff} is shown by the solid red line. V_{max} is the value of characteristic potential at the local maximum at the position r_{max}. The blue line marks the path of the leaving electron.

this potential can be found according to

$$\frac{\partial V_{eff}}{\partial r} = \frac{\partial}{\partial r}\Big(-\frac{Z}{r} + Er\Big) = \frac{Z}{r^2} + E = 0\,, \tag{8.4}$$

and thus we obtain the position r_{max} and value V_{max} of the local maximum

$$r_{max} = -\sqrt{\frac{Z}{E}}\,, \tag{8.5}$$

$$V_{max} = -2\sqrt{ZE}\,. \tag{8.6}$$

Depending on the electric field E generated by the laser, two different ionisation regimes can be accessed in the quasi-static regime. If the maximum of the potential barrier V_{max} is below the energy level of electron $V_{max} < -\mathcal{E}_I$ the ionization is above-barrier ionization (ABI), and if it is higher $V_{max} > -\mathcal{E}_I$ the tunneling ionization is prevailing. The laser field strength required for the above-barrier ionization E_{ABI} is derived from Eq. (8.6) [287]

$$V_{max} = -2\sqrt{Z\mathcal{E}_{ABI}} = -\mathcal{E}_I\,, \tag{8.7}$$

and thus

$$E_{ABI} = \frac{\mathcal{E}_I^2}{4Z}\,. \tag{8.8}$$

The intensity of an oscillating electric field $E = e^{i\omega t}$ can be calculated in the following way

$$I = \frac{1}{\tau}\int_0^\tau E^*(t)E(t)dt, \tag{8.9}$$

where τ is the pulse length. Thus, combining Eq. (8.8) and Eq. (8.9) an intensity required for above-barrier ionization is obtained

$$I_{ABI} = \frac{\mathcal{E}_I^4}{16Z^2}\,. \tag{8.10}$$

In order to quantitatively describe the ionization process, we introduce the ionization rate $\Gamma(E)$, which is the probability of the ionization process per unit time. According to Bauer and Mulser [288], if an ionization rate $\Gamma[E(t)]$ is given, the probability for the electron to remain bound is

$$P_{bound} = \exp\Big(-\int_0^t \Gamma[E(t')]dt'\Big)\,. \tag{8.11}$$

The ionization probability, or the probability to find the electron in a small volume around the atomic nucleus, is defined as

$$P = 1 - P_{bound}\,. \tag{8.12}$$

Combining Eq. (8.11) and Eq. (8.12) and assuming the constant electric field during the time Δt, the ionization probability is obtained

$$P = 1 - e^{-\Gamma\Delta t}. \tag{8.13}$$

To calculate the ionization rate Γ, various models such as Ammosov-Delone-Krainov (ADK) [289], Keldysh [286], Keldysh-Faisal-Reiss (KFR) [290, 291], or Landau theory [292] have been developed . They are based on the solution of the time–dependent Schrödinger equation with a potential barrier of an atom from Eq. (8.3)

$$i\frac{\partial}{\partial t}\Psi(\mathbf{r},t) = \Big(\frac{\nabla^2}{2} - \frac{Z}{r} + \mathbf{r}\mathbf{E}(t)\Big)\Psi(\mathbf{r},t)\,, \tag{8.14}$$

where $\Psi(\mathbf{r},t)$ is the wave function of an electron.

The Landau theory was initially developed for hydrogen-like atoms and ions. It provides an exact solution for low field strengths E, but it overestimates ionization in the above-barrier regime and the Keldysh ionization theory is valid for the incoming electric field E small in comparison to the ionization potential E_I (tunneling regime). The ADK model [289] is based on the work of Landau and Lifshitz [292], and Keldysh [286], and also using KFR [290] approach. This model is applicable for both tunneling and above-barrier regime. Therefore in this thesis we will concentrate on the

ADK model of the quasi-static ionization.

Ammosov-Delone-Krainov ionization model

In this section the ADK ionization rate is discussed following [289]. The ADK ionization rate is based on the solution of the time–dependent Schrödinger for complex atoms in an electric field. The initial state of an atom is described by the angular quantum number l, the magnetic quantum number m and the effective principal quantum number

$$n^* = Z/\sqrt{2\mathcal{E}_I}\,, \tag{8.15}$$

which takes into account that the inner electrons do not entirely screen the charge of the core. The original ADK equation is taking into account contributions of all of the quantum numbers, and yields to a complicated equation [289]. In the simplified ADK equation and only s-state ($l = 0$) is considered, and the contribution of the magnetic quantum numbers other than $m = 0$ are neglected. Thus, the simplified ADK equation is obtained

$$\Gamma_{ADK} = \sqrt{\frac{3n^{*3}E}{\pi Z^3}}\frac{E}{8\pi Z}\left(\frac{4eZ^3}{En^{*4}}\right)^{2n*}\exp\left(-\frac{2Z^3}{3n^{*3}E}\right), \tag{8.16}$$

The ionization equations are only in this form if the atomic unit system is used. In Eq. (8.16), the first factor $\sqrt{3n^{*3}E/\pi Z^3}$ is obtained from the averaging over one laser cycle and is valid only for linearly polarized light. In the case of circularly polarized light $\sqrt{3n^{*3}E/\pi Z^3} = 1$ the ADK equation takes a more simple form

$$\Gamma_{ADK} = \frac{E}{8\pi Z}\left(\frac{4eZ^3}{En^{*4}}\right)^{2n*}\exp\left(-\frac{2Z^3}{3n^{*3}E}\right). \tag{8.17}$$

The exponential term $\exp(-2Z^3/3n^{*3}E)$ in the Eq. (8.16) and Eq. (8.17) describes the probability density for the electron to be found outside the barrier, and for very high electric fields it converges to one.

Ionization rates calculated according to ADK ionization model for H, C^{1+} and C^{2+} are shown in Fig. 8.4. The incoming electric field strength of 0.1 atomic units, similar to the electric field strength used in our experiment, is marked by the vertical dashed line. As can be seen from Fig. 8.4 for the C^{1+} the ionization rate is growing with the field strength up to 10^{17} s^{-1}. Acording to Eq. (8.13), for such a high ionization rate the probability for C^{1+} to be ionized in one femtosecond is

$$P_{C1} = 1 - e^{-100} \approx 1\,, \tag{8.18}$$

which indicates full ionization of C^{1+} in one femtosecond. For H the ionization rate is about 10^{15} s^{-1}, which results in full ionization in tens of femtoseconds. For C^{2+} the ionization rate is significantly lower, therefore for such an electric field intensity C^{2+} is

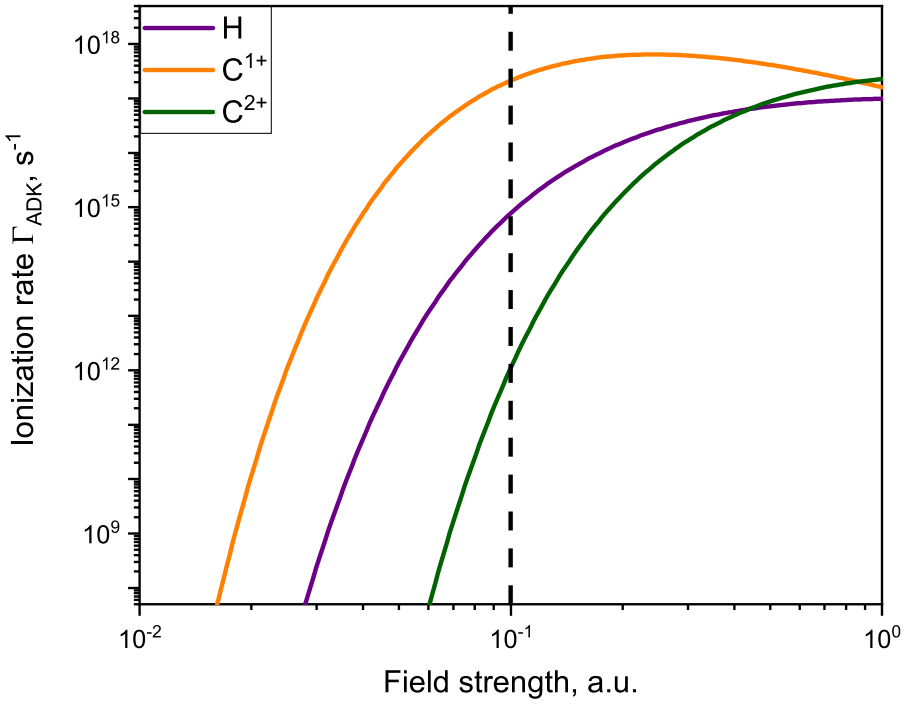

Figure 8.4: ADK ionization rates for H, C^{1+} and C^{2+}. The field strength of 0.1 a.u. similar to the electric field strength used in our experiment is marked by the vertical dashed line.

not fully ionized in femtoseconds. Thus, each carbon and hydrogen atoms are ionized up to C^{1+} and H^{1+} during the ultra-short femtosecond laser pulse.

In his subsequent work [293] Krainov incorporated ABI regime into ADK theory. As a result, he obtained an equation extending the ADK equation to the above-barrier regime

$$\Gamma_{ABI} = \frac{4\sqrt{3}}{\pi n^*}\frac{E}{(2E)^{1/3}}\left(\frac{4e|\mathcal{E}_I|^{3/2}}{En^*}\right)^{2n^*}\int_0^\infty \mathrm{Ai}^2\left(x^2+\frac{2|\mathcal{E}_I|}{(2E)^{3/2}}\right)x^2dx\,. \tag{8.19}$$

Here Ai stays for the Airy function. In tunneling limit this equation converges to the usual ADK ionization rate.

Thomas-Fermi ionization model

The second ionization mechanism is collisional ionization. Fast electrons collide inelastically with the atomic ions which causes ionization of the atom. The ionization rate of this process can be calculated according to the Thomas-Fermi (TF) ionization model [292]. TF theory is a semiclassical theory formulated in terms of the electronic density alone, and it is correct only in the limit of an infinite nuclear charge. In the TF model, electrostatic potential at each point of the atom is determined by the ion charge

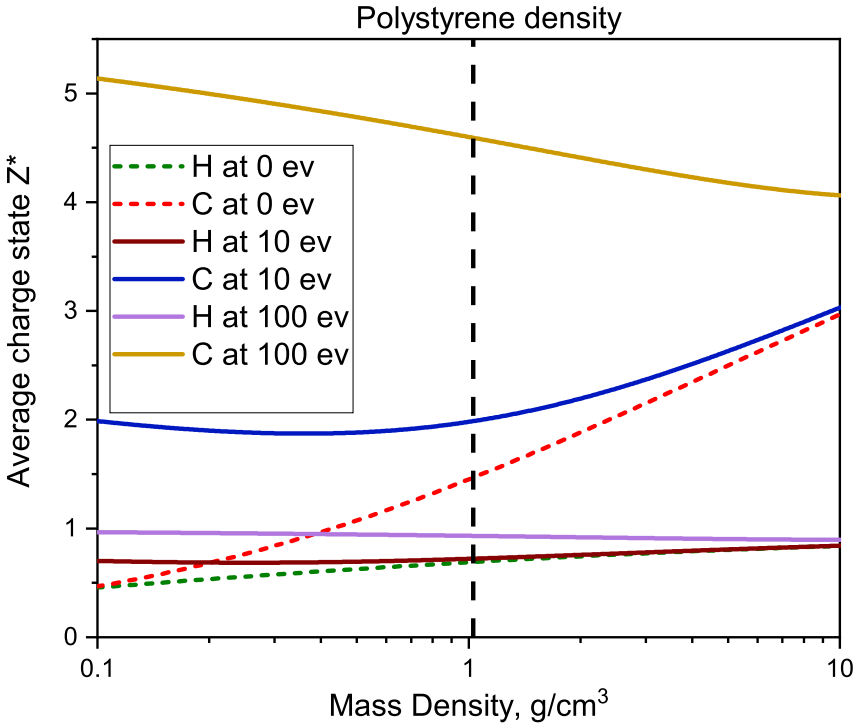

Figure 8.5: Thomas-Fermi ionization for H and C for 0 eV, 10 eV and 100 eV electron temperatures. For 10 eV and 100 eV charge state predictions are marked by solid lines, and for 0 eV the charge state predictions are marked by dashed lines because they show unphysical behavior.

and the electron density. An atom is considered to be ionized if an electron has energy higher than the maximum potential energy.

In our work collisional ionization was modelled according to [294]. In this model the electrostatic potential is approximately given by the ion-sphere formula based on a uniform free-electron distribution in an atom. The potential barrier height is approximately given by the centrifugal potential evaluated at the atom radius $r = R_0$. The ionization state $Z^*(\rho, T)$ is calculated using an approximate fit to the definition of the ionization state

$$Z^*(\rho, T) = 4/3\pi R_0^3 n(R_0)\,, \tag{8.20}$$

where $n(R_0)$ is the boundary electron density. These approximations lead to chain of algebraic equations which predict the conditions required for ionization. The parameters of the fit which can be used for modeling are available in Table 4 of Ref. [294].

The charge state estimates for carbon and hydrogen obtained from this model are shown in Fig. 8.5. From Fig. 8.5 one can see that in several cases prediction of the Thomas-Fermi model for carbon and hydrogen is completely unphysical. For example, at 0 eV electron temperature Thomas-Fermi model predicts a non-zero ionization state, which is not correct. Also, for temperature starting from 10 eV it estimates an increasing charge state for low ion densities (see carbon at 10 eV and at 100 eV in Fig 8.5).

Therefore in the modeling of Thomas-Fermi ionization different cut-off values should be introduced.

8.1.2 Heating of electrons during the laser pulse propagation

The next process occurring in the ionized solid is the heating of electrons. The first heating mechanism is inverse bremsstrahlung, which is an 'opposite' mechanism to bremstrahlung. During bremstrahlung process, electromagnetic radiation is produced by the deceleration of an electron by a heavy charged particles such as ions or atomic nuclei. In the inverse bremsstrahlung process, free electrons absorb electromagnetic radiation in a collision with heavy charged particles (see Fig. 8.6). In both processes the third particle, in this case ion or atomic nuclei, is required for energy and momentum conservation. Inverse bremstrahlung process is now discussed following [287]. Here only single-photon processes are assumed, and thus the first-order perturbation theory is applied. Therefore this theory is valid only for rather weak electromagnetic field.

The energy absorbed by a single electron in a single collision with a Coulomb center $\Delta\mathcal{E}$ is obtained from quantum electrodynamics [295]

$$\Delta\mathcal{E} = \frac{E^2}{2\omega^2}\,, \tag{8.21}$$

where E and ω are the electric field strength and electromagnetic frequency, respectively. The energy absorbed by an electron per unit time is the energy absorbed in a single collision $\Delta\mathcal{E}$ times frequency of electron-ion collisions ν_{ei}

$$\frac{d\mathcal{E}}{dt} = \Delta\mathcal{E}\nu_{ei}\,. \tag{8.22}$$

The definition of the electron-ion collision frequency ν_{ei} depends on the electron temperature T_e. For high energetic electrons, when electron temperature is higher than the ponderomotive energy ($T_e > E^2/4\omega^2$) the electron-ion collision frequency is ob-

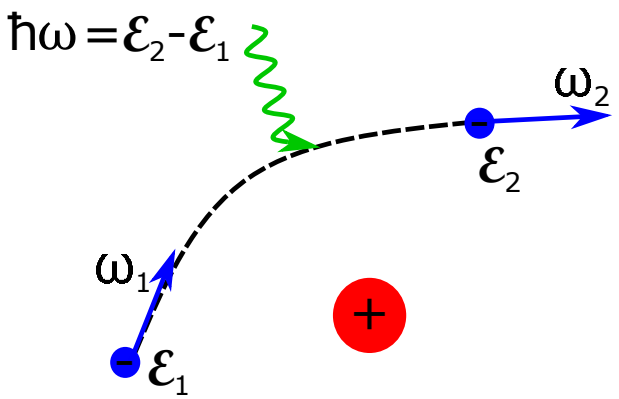

Figure 8.6: Scheme of the inverse bremsstrahlung process. An electron is absorbing a photon via the collision with a Coulomb center (ion).

tained from the kinetic theory of plasma [296]

$$\nu_{ei} = \frac{4\sqrt{2\pi}Zn_e}{3T_e^{3/2}} \ln\Lambda\,, \tag{8.23}$$

where n_e is the electron density, and $\ln\Lambda$ is the Coulomb logarithm. For low energetic electrons ($T_e < E^2/4\omega^2$) the electron-ion collision frequency is given by the relation [297]

$$\nu_{ei} = \frac{16Zn_e\omega^3}{E^3} \ln\Lambda\,. \tag{8.24}$$

It is worth to notice that in the case of a very intense electron-ion collisions $\nu_{ei} \gg \omega$ the absorbed energy is independent of ω

$$\frac{d\mathcal{E}}{dt} = \frac{16E^2}{3\pi\nu_{ei}}\,. \tag{8.25}$$

There are also absorption mechanisms that do not rely on collisions between electrons and ions [298]. One of these processes is resonance absorption when the incoming laser light excites a plasma wave. At low laser intensities, the resonance absorption mechanism is damped by the collisions and at high laser intensities – by the particle trapping. Therefore this mechanism becomes significant for the intermediate laser intensities $I\lambda^2 = 10^{16}$ W/cm^2, and it can cause rising of the absorption coefficient up to 70%.

8.1.3 Skin effect

In this section, the propagation of electromagnetic radiation through the free electron gas, or Fermi gas, is considered. Here skin effect, which is a very important aspect of the interaction of the incoming electromagnetic field with media is discussed following Reference [102]. Throughout this section CGS units are used.

Maxwell's equations for dielectric media are written in the form of

$$\operatorname{div}\mathbf{B} = 0\,, \tag{8.26}$$

$$\operatorname{div}\mathbf{D} = 4\pi\rho\,, \tag{8.27}$$

$$\operatorname{rot}\mathbf{E} = -\frac{1}{c}\frac{\partial\mathbf{B}}{\partial t}\,, \tag{8.28}$$

$$\operatorname{rot}\mathbf{H} = -\frac{4\pi}{c}\sigma\mathbf{E} + \frac{1}{c}\frac{\partial\mathbf{D}}{\partial t}\,. \tag{8.29}$$

Here $\mathbf{E}$ is the electric field, $\mathbf{B}$ is the magnetic field, $\mathbf{D}$ is the electric induction, $\mathbf{H}$ is the magnetizing field, σ is the electrical conductivity, ρ is the free charge density, and c is

the speed of light. The electric induction is defined by the equation

$$\mathbf{D} = \mathbf{E} + 4\pi\mathbf{P}\,, \tag{8.30}$$

where **P** is polarization.

Now let us derive the polarization induced by an incoming periodic electromagnetic field in a free electron gas. Newton second law of motion for a free electron in the electric field is written in the form

$$m_e \frac{d^2x}{dt^2} = -eE\,, \tag{8.31}$$

where m_e and e are the electron mass and charge respectively, E is an incoming electromagnetic field and x is the coordinate of an electron. If we assume the periodic electromagnetic field in the form of ($E \sim e^{-i\omega t}$) we obtain

$$-\omega^2 mx = -eE\,, \tag{8.32}$$

$$x = \frac{eE}{m\omega^2}. \tag{8.33}$$

Thus, the dipole moment of an electron p and the polarization of media P can be defined

$$p = -ex = -\frac{e^2E}{m\omega^2}\,, \tag{8.34}$$

$$P = -nex = -\frac{ne^2}{m\omega^2}E\,. \tag{8.35}$$

Here n is the electron density.

The displacement field in the frequency domain $D(\omega)$ is defined as

$$D(\omega) = \varepsilon(\omega)E(\omega)\,, \tag{8.36}$$

and thus the dielectric function is

$$\varepsilon(\omega) = \frac{D(\omega)}{E(\omega)} = 1 + 4\pi\frac{P(\omega)}{E(\omega)} = 1 - \frac{4\pi ne^2}{m\omega^2}\,. \tag{8.37}$$

The plasma frequency is defined as $\omega_p^2 = 4\pi ne^2/m$ and thus we can write the dielectric function in the form of

$$\varepsilon(\omega) = 1 - \frac{\omega_p^2}{\omega^2}\,. \tag{8.38}$$

The dependence of the dielectric function $\varepsilon(\omega)$ from the frequency ω/ω_p is shown in Fig. 8.7.

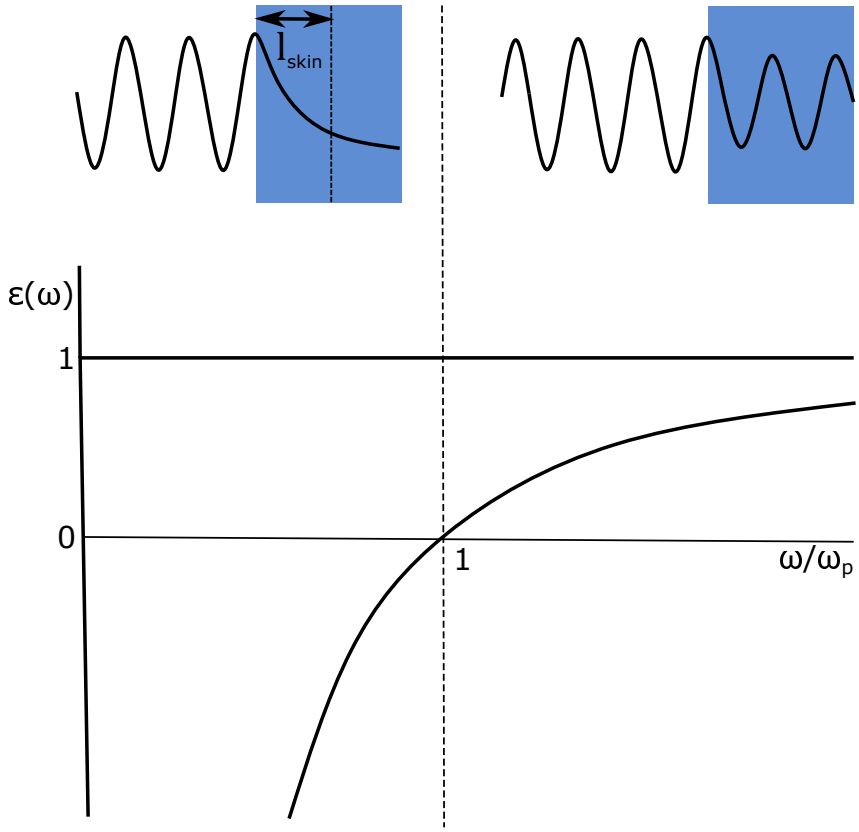

Figure 8.7: Frequency dependence of the dielectric function $\varepsilon(\omega)$. The electromagnetic waves are propagating inside the material only if $\varepsilon(\omega) > 0$. If $\varepsilon(\omega) < 0$ the electromagnetic waves penetrate only at the skin depth l_{skin}, and the rest is reflected. Figure was adapted from Reference [102].

The wave equation for the dielectric media is derived from Eq. (8.28) and Eq. (8.29)

$$\Delta \mathbf{E} = \frac{\varepsilon}{c^2} \frac{\partial^2 E}{\partial t^2} \,. \tag{8.39}$$

The solution of the wave equation is written in the form

$$E \propto \exp(-i\omega t) \exp(i\mathbf{K} \cdot \mathbf{r}) \,, \tag{8.40}$$

with the dispersion relation

$$\varepsilon(\omega, K)\omega^2 = c^2 K^2 \,, \tag{8.41}$$

where $\mathbf{K}$ is the wavevector. Combining Eq. (8.38) and Eq. (8.41) the dispersion relation for plasma is obtained

$$\omega^2 - \omega_p^2 = c^2 K^2 \,. \tag{8.42}$$

If $\omega > \omega_p$ then $\mathbf{K}$ is real and wave propagates with a phase velocity $c/\varepsilon^{1/2}$. If $\omega < \omega_p$ then $\mathbf{K}$ is imaginary and the wave is damped with characteristic length called the skin

depth. The skin depth is defined as

$$l_s = \frac{1}{|\mathbf{K}|} = \frac{c}{\sqrt{\omega_p^2 - \omega^2}}\,. \tag{8.43}$$

If $\omega \ll \omega_p$, ω in Eq. (8.43) can be neglected, and the skin depth depends only on the plasma frequency. The typical electron densities for the solid are of the order of 10^{21} electrons/cm^3. Thus, the skin depth is of the order of 10-20 nm.

8.1.4 Two-temperature model

At the end of the laser pulse, the absorbed laser energy is contained mostly in the electron sub-system, and the ion (lattice) sub-system remains cold. This system can be described by two different temperatures, ion temperature T_i and electron temperature T_e. The problem of electron energy transfer to the lattice was formulated by Kaganov et. al. [299], and further it led to the development of the two-temperature model [300]. We will now discuss the two-temperature model following the review by E.G. Gamaly and A.V. Rode [301].

In the two-temperature model the energy conservation law is written in the form

$$\begin{cases} \partial(C_e n_e T_e)/dt = Q_{abs} - \nabla Q_{e-th} - Q_{e-i}\,, \\ \partial(C_i n_i T_i)/dt = Q_{e-i}\,, \end{cases} \tag{8.44}$$

where $C_e(T_e)$ and $C_i(T_i)$ are the heat capacities for the electrons and the ions, respectively. Q_{abs} is the absorbed laser energy, depending on the position z inside the sample due to the skin effect

$$Q_{abs} = \frac{2A}{l_s} I(t) \exp\left(-\frac{2z}{l_s}\right). \tag{8.45}$$

Here A is the absorption coefficient, $I(t)$ is the time-dependent laser intensity and l_s is the skin depth.

Q_{e-th} is the electronic heat conduction flux

$$Q_{e-th} = \kappa_e \nabla T_e\,, \tag{8.46}$$

where κ_e is heat conduction coefficient.

Q_{e-i} is the energy transferred from hot electrons to the cold ions

$$Q_{e-i} = \nu_{e-i}^{en}(T_i) n_e (T_e - T_i)\,, \tag{8.47}$$

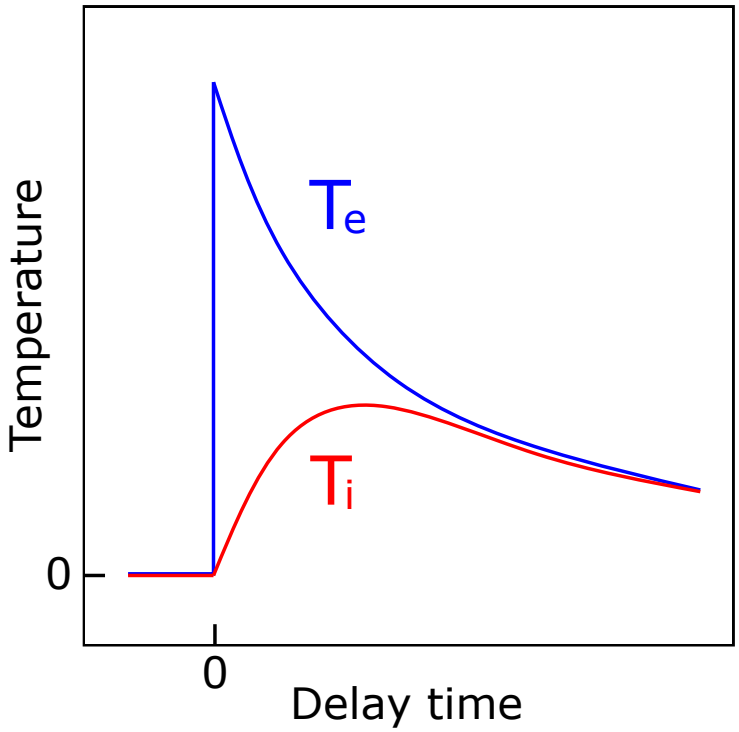

Figure 8.8: The two-temperature model showing the dynamics of the electron temperature (T_e) and ion temperature (T_i). This figure was adapted from Reference [302].

where ν_{e-i}^{en} is the electron-ion energy exchange rate

$$\nu_{e-i}^{en} = 12(2\pi)^{1/2} \frac{n_i Z^2 e^4 m_e^{1/2}}{T_e^{3/2} M_i} \ln \Lambda \,. \tag{8.48}$$

Here m_e and M_i are electron and ion mass respectively, and $\ln \Lambda$ is Coulomb logarithm. This equation is valid only if the solid is fully ionized. The solution of the Eq. (8.44) for the electron and ion temperature is shown in Fig. 8.8. The typical electron-ion relaxation time $t_{e-i}^{en} = (\nu_{e-i}^{en})^{-1}$ are of the order of 10 ps. It is important to note, that these timescales are longer than ultra-short laser pulse length ($\sim$ 100 fs) and shorter that the hydrodynamic expansion ($\sim$ 100 ps).

8.1.5 Ablation and shock wave propagation

In this section, we will discuss processes in a solid after the interaction with an ultrafast laser pulse. First, we will discuss ablation following [303] and further we will move to the shock wave formation and propagation.

The ablation threshold is defined by the binding energy of a material: if the atoms gain energy higher than the atomic binding energy, they escape from the surface. For metals the ablation threshold energy ε_a is equal to the sum of the atomic binding energy ε_b and the work function of the electron reaching a surface layer ε_{esc}

$$\varepsilon_a = \varepsilon_{esc} + \varepsilon_b \,. \tag{8.49}$$

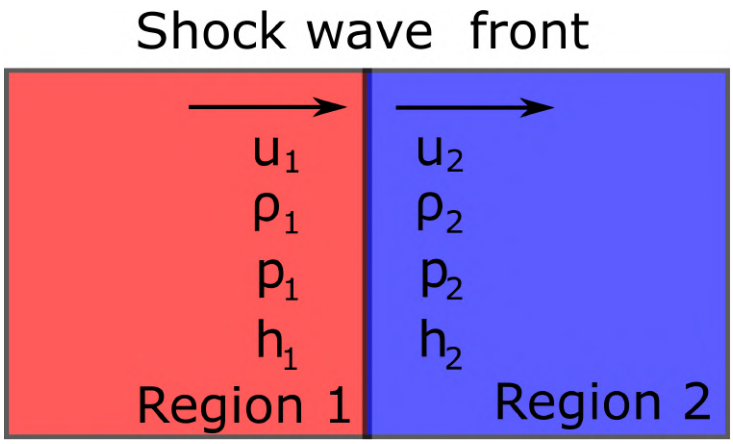

Figure 8.9: A schematic diagram of a shock wave front. Two regions with the densities ρ_1 and ρ_2, velocities u_1 and u_2 , pressures p_1 and p_2 and specific enthalpies h_1 and h_2 are shown.

The atomic binding energy ε_b and the electron work function ε_{esc} are typically of the order of 3-5 eV per atom [303]. For dielectrics, the ablation mechanism is the same, but an additional energy is needed to ionize the material and to create the free carriers. Therefore the ablation threshold for dielectric materials is higher than that for the metals. Also, the ablation in the dielectric materials occurs in the skin layer because all the atoms in the interaction zone must be at least singly ionized. The typical ablation timescales are of the order of the electron-ion thermalisation time (tens of picoseconds).

After the electron-ion thermalisation is finished, the hydrodynamic motion of atoms starts. The high pressure created by laser generates the shock wave compressing the surrounding unperturbed material. The shock wave is propagating with ultrafast speed, exceeding the speed of sound in solid. The relationship between both sides of a one-dimensional shock wave are described by the Rankine–Hugoniot conditions named after Scottish engineer and physicist William John Macquorn Rankine [304] and French engineer Pierre Henri Hugoniot [305]. We will now derive the equations defining the shock wave properties from the conservation laws, following [306] and [307]. In a coordinate system that is moving with the discontinuity, the conservation laws can be expressed as

$$\rho_1 u_1 = \rho_2 u_2 \equiv m \qquad \text{Conservation of mass}, \tag{8.50}$$

$$\rho_1 u_1^2 + p_1 = \rho_2 u_2^2 + p_2 \qquad \text{Conservation of momentum}, \tag{8.51}$$

$$h_1 + u_1^2/2 = h_2 + u_2^2/2 \qquad \text{Conservation of energy}, \tag{8.52}$$

where m is the mass flow rate per unit area, ρ_1 and ρ_2 are the mass density, u_1 and u_2 are the fluid velocities, p_1 and p_2 are the pressures, and h_1 and h_2 are the specific enthalpies in the region 1 and region 2 respectively. The variables from Eq. (8.50), Eq. (8.51), and Eq. (8.52) are shown in Figure 8.9.

Combining conservation of mass and conservation of momentum equations (Eq. (8.50)

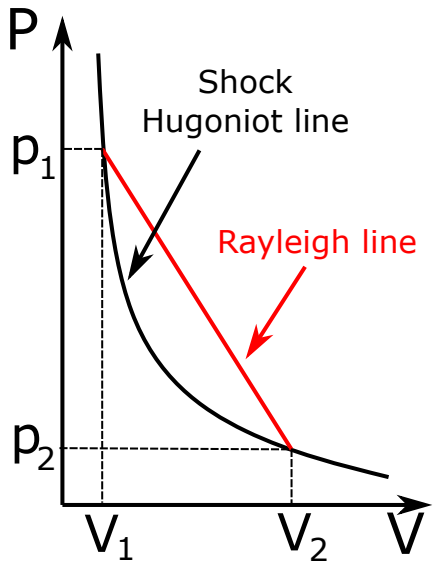

Figure 8.10: $P - V$ diagram of the shock Hugoniot adiabat (black) defined by Eq. (8.56) and Rayleigh line (red) defined by Eq. (8.53).

and Eq. (8.51)) and substituting density by the specific volume $V = \rho^{-1}$ an equation defining the Rayleigh line (see Figure 8.10) is obtained

$$m^2 = -\frac{p_2 - p_1}{V_2 - V_1}\,, \tag{8.53}$$

and equations defining both fluid velocities write as follows

$$u_1^2 = V_1^2 \frac{p_2 - p_1}{V_2 - V_1}\,, \tag{8.54}$$

$$u_2^2 = V_2^2 \frac{p_2 - p_1}{V_2 - V_1}\,. \tag{8.55}$$

From Eq. (8.54) it can be seen that the shock wave speed is proportional to the square root of pressure. The typical shock pressures are higher than a few GPa (higher than Young modulus of a material) and typical shock wave speed is of the order of a few kilometers per second.

Combining Eq (8.54), Eq (8.55) and conservation of energy law Eq (8.52) a Hugoniot equation is obtained

$$h_2 - h_1 - \frac{(p_2 - p_1)}{2}(V_1 + V_2) = 0\,. \tag{8.56}$$

This equation defines the shock wave parameters for a given thermodynamic condition. An example of the Hugoniot adiabat in the $P - V$ plane is shown in Fig. 8.10.

While propagating inside the solid, the shock wave is losing its speed due to the dissipation of energy and the pressure of the shock wave front is decreasing gradually. At the distance where the shock wave pressure is not sufficient to compress the material anymore, the shock wave effectively stops. The distance where the one-dimensional

shock wave stops can be estimated as

$$x_{stop} = \approx \frac{E_{abs}}{Y}, \tag{8.57}$$

where E_{abs} is total absorbed energy density, and Y is the Young modulus of a solid. At the stopping point, the shock wave converts into a sound wave, which propagates further into the material without inducing any permanent changes to a solid.

8.2 Experiment

In this section we discuss IR pump – X-ray probe experiments performed at the colloidal crystal film using three IR laser intensities I_1=3.0 $\cdot 10^{14}$ W/cm^2, I_2=4.8 $\cdot 10^{14}$ W/cm^2, and I_3=6.3 $\cdot 10^{14}$ W/cm^2. The colloidal crystal films were prepared from polystyrene spheres with a diameter of 163 $\pm$ 3 nm, using the vertical deposition method. The details of the experimental setup are given in chapter 7. The pump-probe experiment was conducted in the following way. First, for each position of the sample and each time delay 100 diffraction patterns without the IR laser were measured. Next, 100 diffraction patterns with the IR laser and a fixed time delay were measured. The fast CSPAD detector allowed us to determine the diffraction pattern just after the first irradiation by the IR laser pulse. For two lower IR laser intensities five diffraction patterns were measured at a new positions of the sample for each time delay. For higher IR laser intensity, the measurements were repeated nine times for the 6.5 ps time delay and 10 times for the 25.25 ps time delay. Each measurement was performed at a new position of the sample as in previous cases. For each IR laser intensity a pump-probe experiment was performed with a time delay variation τ from -10 ps to 1000 ps with 25.25 ps time increment. Additionally, for two higher IR laser intensities (I_2 and I_3) measurements from -10 ps to 48.5 ps with the 6.5 ps time increment were accomplished. For two lower IR laser intensities 5 diffraction patterns were measured for each time delay. For higher IR laser intensity measurements were repeated 9 times for 6.5 ps time delay and 10 times for 25.25 ps time delay.

8.2.1 Experimental results

For the three IR laser intensities variation of the Bragg peak intensity $\Delta I(\tau)/I$, the radial $\Delta w_q(\tau)/w_q$, and the azimuthal $\Delta w_\varphi(\tau)/w_\varphi$ the broadening of the Bragg peaks are shown in Fig. 8.11 as a function of the time delay. The experimental measurements are depicted by black dots for 25.25 ps time increment and by blue dots for 6.5 ps time increment. The decay of the relative Bragg peak intensity accompanied by the growth of the peaks size (FWHM) for all three measured IR laser intensities is well visible. For the two higher IR laser intensities, an additional fast drop of the relative

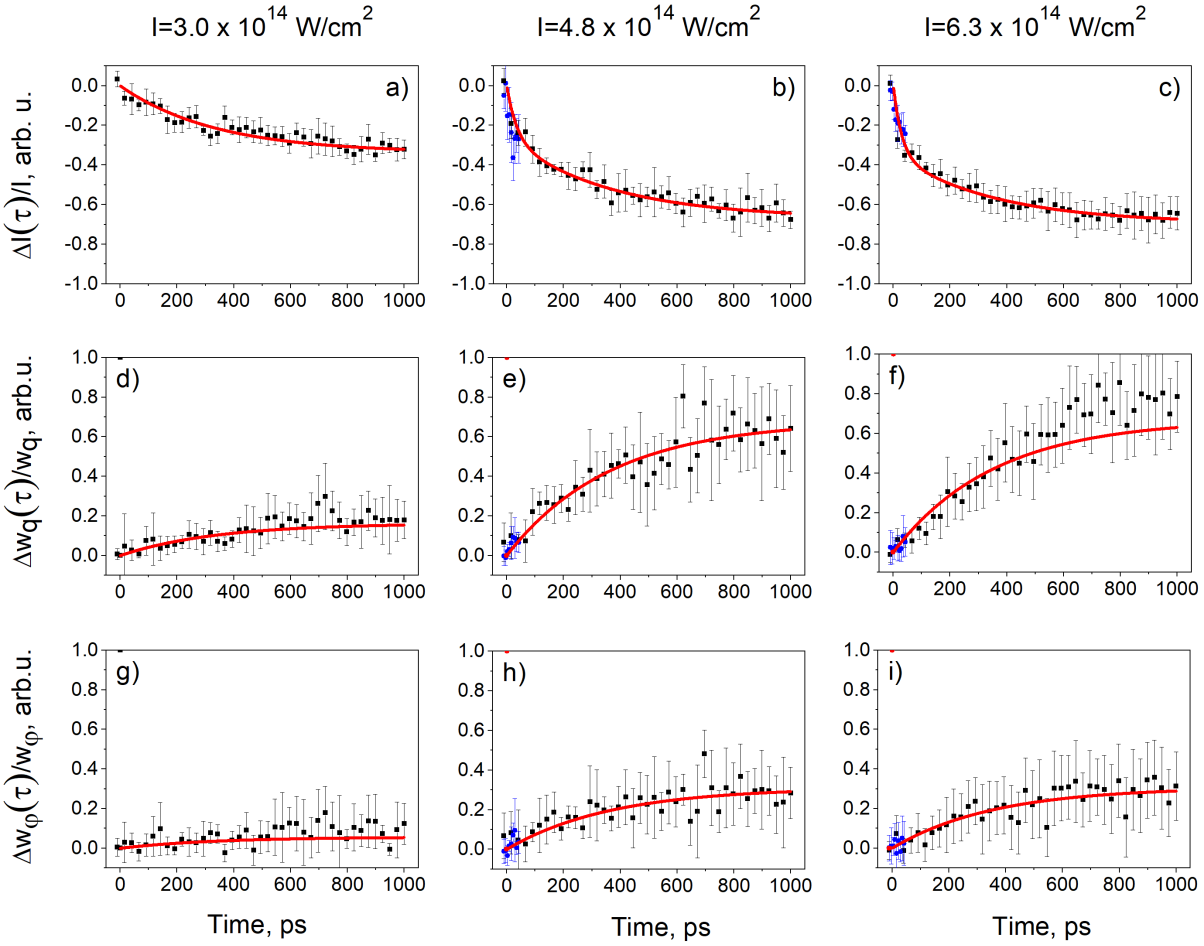

Figure 8.11: Time dependence of the relative change of the integrated intensity of the Bragg peaks $\Delta I(\tau)/I$ (a-c) and their widths in the radial $\Delta w_q(\tau)/w_q$ (d-f) and azimuthal $\Delta w_\varphi(\tau)/w_\varphi$ (g-i) directions at three measured IR laser intensities. Black (blue) dots are experimental data corresponding to 25.25 ps (6.5 ps) time delay increment and solid red lines are exponential fits.

intensity during the first picoseconds was also observed. From Fig. 8.11 this drop of intensity can be estimated to be about 10% of the initial intensity during the first 6.5 picoseconds. This intensity drop was not accompanied by significant changes in the radial or azimuthal peaks size.

In order to obtain the characteristic timescales, results of our measurements were fitted with exponential functions. For the lower IR laser intensity, the Bragg peak integrated intensity was fitted with one exponential function. For the two higher IR laser intensities, the Bragg peak intensity decay could not be fitted with a single exponential function due to the fast drop during the first picoseconds. Therefore, these data were fitted with the two exponential functions which took into account both short and long characteristic timescales. For the radial and azimuthal peaks sizes (FWHM) fitting was performed by a single exponential function for all IR intensities. The results of the fits are shown in Fig. 8.11 by red lines and they provide a good agreement with the experimental data. For all three IR laser intensities the exponential fit of Bragg peak parameters such as intensity and peaks size (FWHM) provided about 300-400 ps char-

acteristic timescales (see Fig. 8.11 and Table 8.4). For two higher IR laser intensities the short timescale of the order of 5 ps was also revealed by the analysis of the Bragg peak intensities.

8.3 Ionization of the colloidal crystal

To further analyze the obtained scattering results, the following model of the IR laser-matter interaction is proposed. At the first stage the incoming high-power IR laser pulse ionizes the top layer of colloidal particles, creating a confined plasma on the top of the colloidal crystal. The processes of plasma creation and expansion are modeled taking into account the periodicity of the colloidal crystal sample and the polystyrene properties and will be discussed below.

Polystyrene is a dielectric material and has no free electrons in the ground state. It is also known to be transparent for the incoming IR pulses with 1.55 eV energy at low laser intensities. However, the situation changes dramatically at high IR laser intensities. The tight focusing of a 50 fs IR laser pulse with the energy of a few millijoule produces an IR laser intensity of the order of hundreds of terawatts per cm^2. At such high IR laser intensities the so-called field ionization is important. It causes the plasma formation in the top layer of the colloidal crystal which may be described by the Keldysh theory [286] (see previous sections).

The dependence of the Keldysh parameter on the IR laser intensity is shown in Fig 8.12. For all three IR laser intensities and low ionization states of carbon and hydrogen the Keldysh parameter is lower than unity (see Fig. 8.12), so the quasi-static ionization regime prevails [308, 309]. As a result, during the first femtoseconds of the IR laser pulse propagation, periodic plasma is created on top of the colloidal crystal.

The ionization thresholds for above barrier ionization (ABI) are shown at the temporal and spatial profiles of the IR laser intensity in Fig. 8.12(b,c) by horizontal dashed lines. From Fig. 8.12(b,c) it is well seen that for lower laser intensity of $3 \cdot 10^{14}$ W/cm^2 only C^{1+} and H^{1+} are expected to be fully ionized. For two higher laser intensities we also have ionization of C^{2+}. It is interesting to look also at the spatial distribution of the IR laser pulse (see Fig. 8.12(c)). In the area of about 150 µm the sample is ionized to C^{1+} and H^{1+} for lower laser intensity, and to C^{2+} for two higher IR laser intensities. Therefore in the 50 µm focused X-ray beam the plasma is considered to be ionized.

Due to plasma creation and the well-known plasma skin effect described in previous sections [102, 310], the incoming IR radiation is not penetrating any more into the colloidal crystal sample. The depth of the skin layer l_{skin} depends on the frequency of the IR laser ω_{IR} and the plasma frequency and in our case, assuming single ionization of each atom, the skin depth is about 10 – 20 nm.

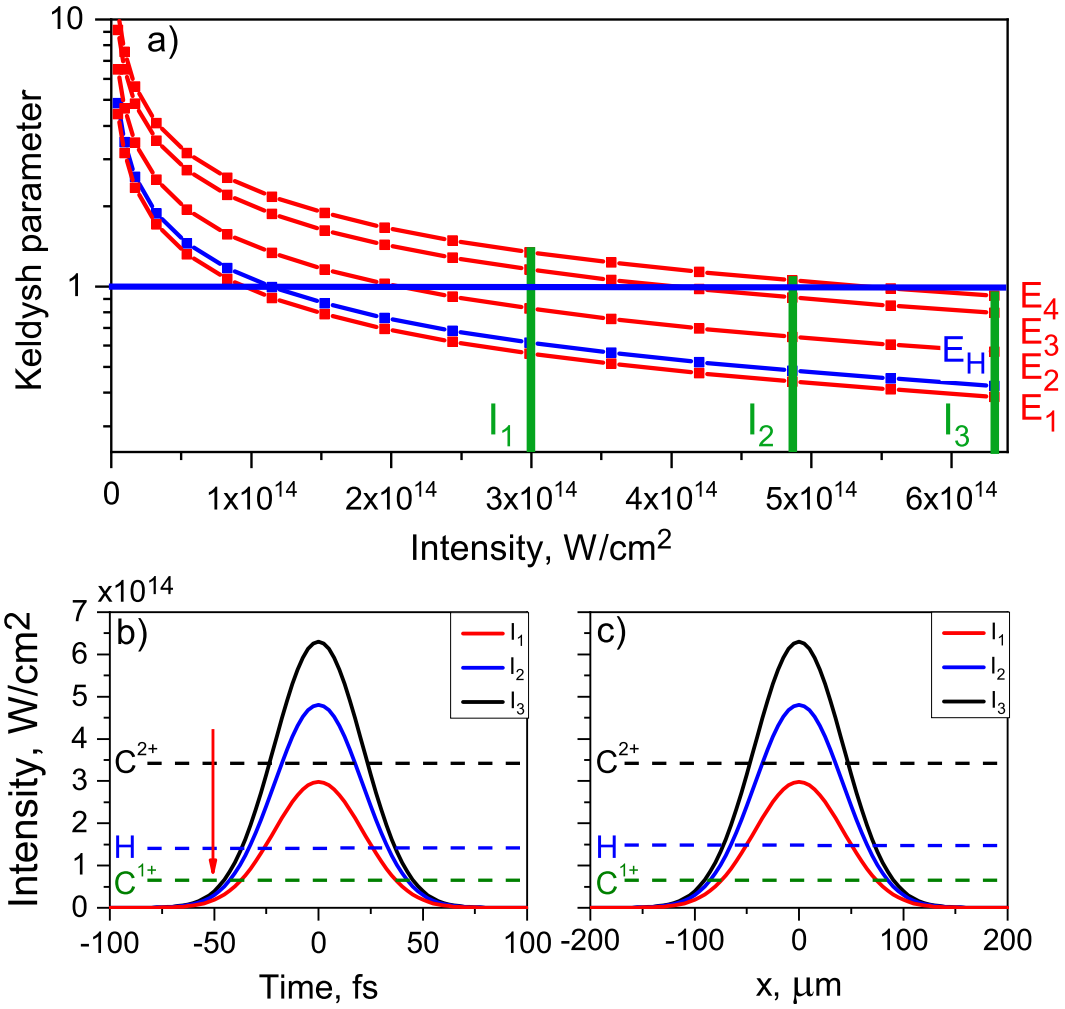

Figure 8.12: a) Keldysh parameter for 4 carbon ionization energies ($E_1 - E_4$) and hydrogen ionization energy E_H. Measured intensities $I_1 = 3.0 \cdot 10^{14}$ W/cm^2, $I_2 = 4.8 \cdot 10^{14}$ W/cm^2 and $I_3 = 6.3 \cdot 10^{14}$ W/cm^2 are shown by green vertical lines. For C^1+, C^2+ and H^+ Keldysh parameter is lower than one for all three intensities. Temporal b) and spatial c) Gaussian profile of the IR laser. Ionization thresholds for C and H are indicated by horizontal dashed lines. Beginning of the simulation is indicated as vertical red arrow.

Free electrons formed in the skin layer by the strong laser-matter ionization process are further accelerated by the inverse bremsstrahlung [287] and resonance absorption [298] mechanisms. As such, high-energetic electrons are propagating inside the first layer of the colloidal particles of the crystal. Accelerated electrons collide inelastically with the atomic ions inside the colloidal particle which causes additional collisional ionization of the C atoms. The ionization and IR laser energy absorption processes described above occur within the colloidal crystal which has a periodic structure. As a result, the created plasma also has the same periodicity as the colloidal crystal during the first picoseconds after the interaction with the IR laser pulse.

8.3.1 PIConGPU simulation details

To simulate plasma formation in the colloidal crystal during the first 1 picosecond of the IR laser pulse propagation, we used PIConGPU code version 0.4.0–dev developed at Helmholtz-Zentrum Dresden-Rossendorf [311, 312]. PIConGPU simulations were performed in the time interval from 0 to 1 ps for all three IR laser intensities measured in our pump-probe experiment. The start of the simulation time is indicated in Fig. 8.12(b) by the vertical red arrow 50 fs before the IR laser pulse reaches it's maximum. It is well seen that at the beginning of the simulation the IR laser intensity is below ionization thresholds for C and H.

Two different types of ionization processes are dominating in the colloidal crystal, namely field ionization and collisional ionization, and they were included in the simulations. The ionization rate of the field ionization process was calculated according to the Ammosov-Delone-Krainov (ADK) model [289], discussed in details before in this chapter.

The version of the ADK model that was used in the PIConGPU code is simplified due to the fact that our particles are carbon and hydrogen and do not have much inner structure. This model was applied for both the tunneling regime $E < E_{ABI}$ and above-barrier regime $E \approx E_{ABI}$. For strong fields $E > E_{ABI}$ where the potential barrier binding an electron is completely suppressed the so-called barrier-suppression ionization (BSI) regime is reached. Therefore, the ADK model was combined with a check for the BSI threshold. Also the ADK model used in this work is based on the assumption that the material investigated consists of independent atoms and it did not consider the molecular-orbital structure of covalently bonded materials. The collisional ionization was simulated using the Thomas-Fermi ionization model [294] described before in this chapter. Further simulation details are given in Appendix A.

8.3.2 PIConGPU simulation results

From PIConGPU simulations we obtained the 3D distributions of the charge state and of the electron energy density. The average charge state projections along the y-axis after 80 fs and after 1 ps of the IR laser pulse propagation are shown in Fig. 8.13. The IR laser pulse is coming from the top along the z-direction, and it initiates the ionization in the top layer of the colloidal crystal. As one can see from Fig. 8.13(a-c), after 80 fs only the first layer of the colloidal particles is ionized by the IR laser pulse. The highly ionized skin layer with the thickness of around 10 nm on top of the first layer of colloidal crystals is also well visible. The average charge state in the skin layer can reach up to 2.9 and is summarized in Table 8.1. Also, a high charge state is reached in the center of the colloidal particles for all three IR laser intensities, and their values are summarized in Table 8.1. As a result, the periodic plasma is formed on top of the colloidal crystal.

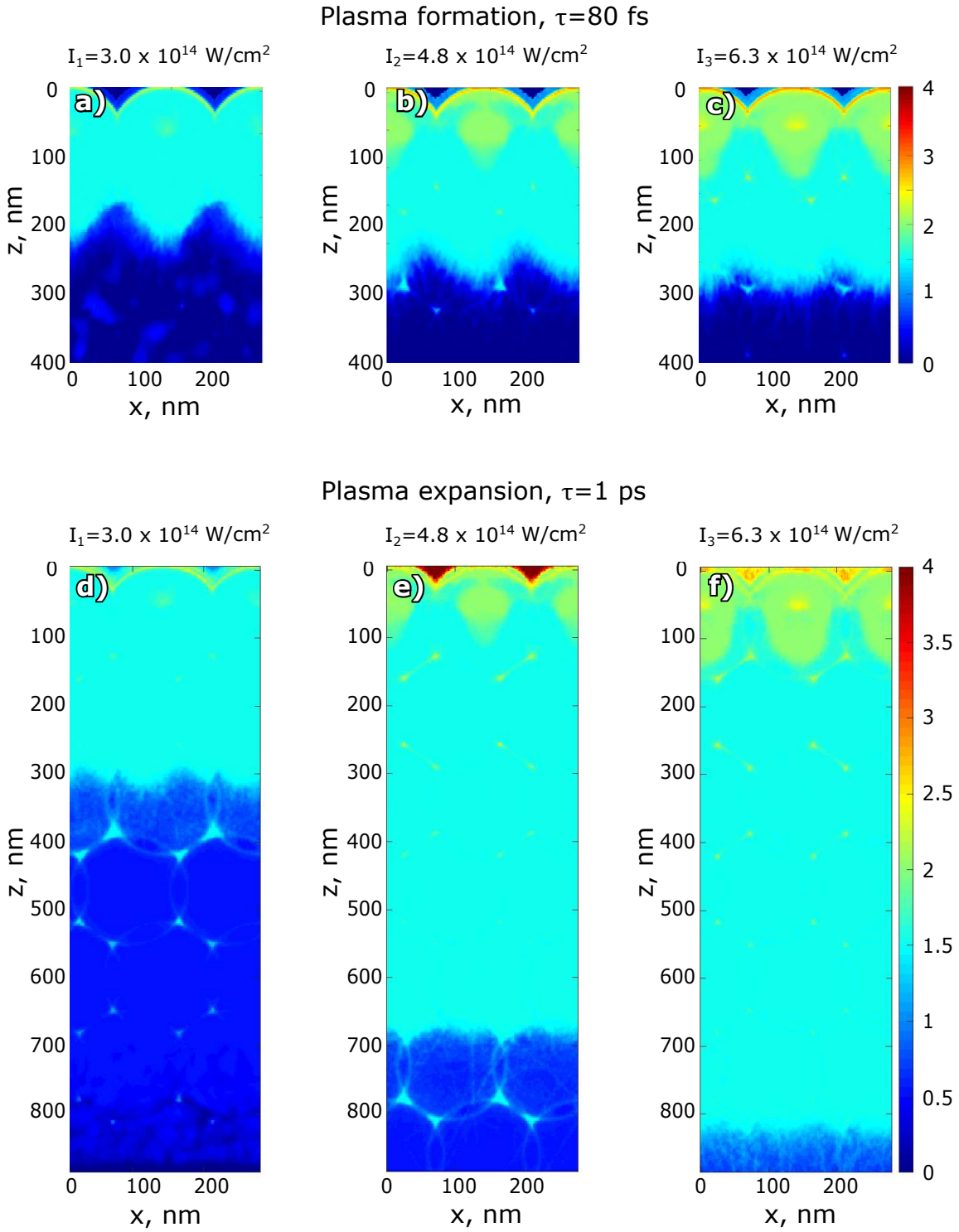

Figure 8.13: The average charge state distribution in the colloidal crystal at 80 fs (a-c) and at 1 ps (d-f) after the beginning of the IR laser pulse for three different IR laser intensities. Here the projection of the average charge state along the y-direction is shown.

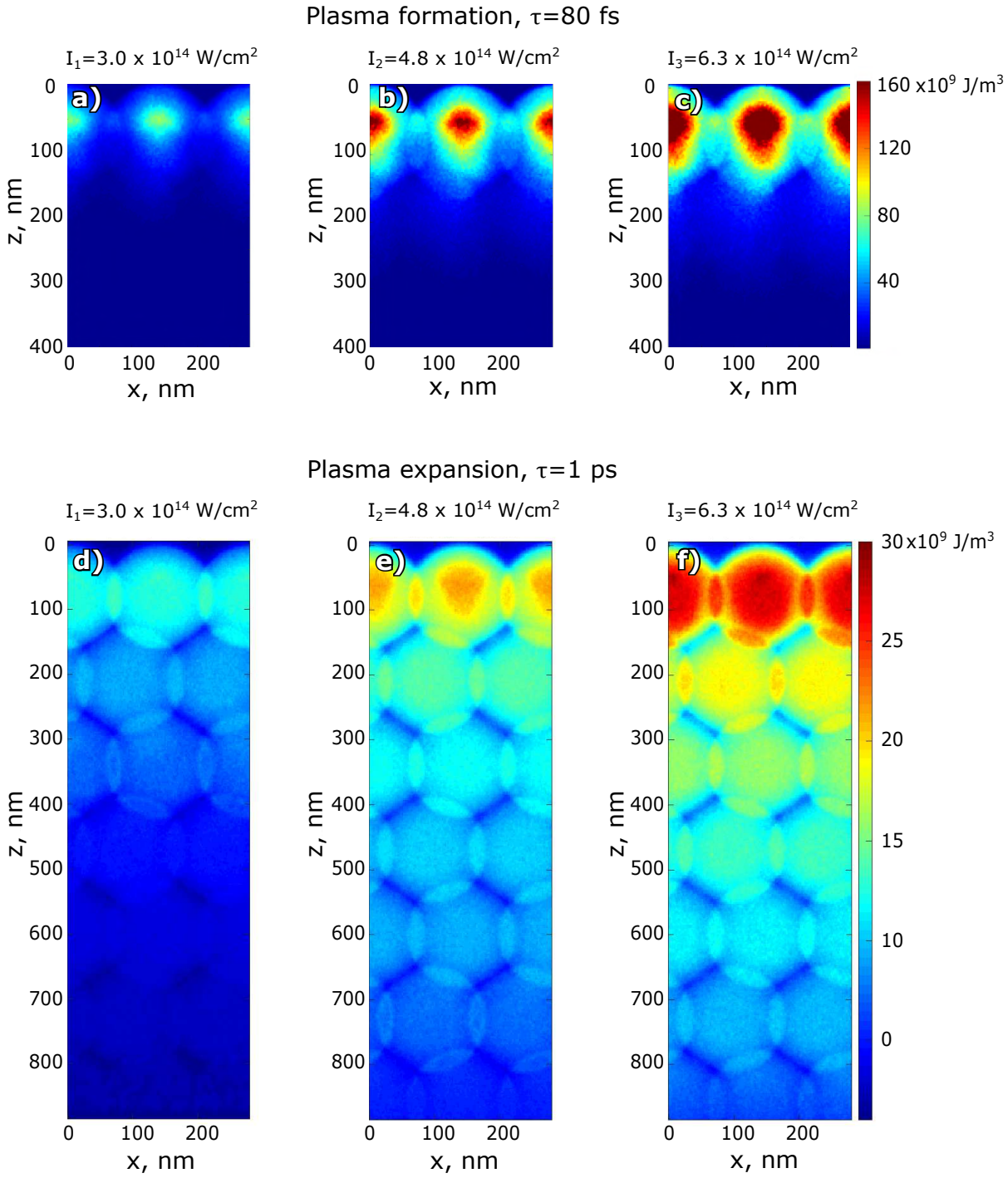

Figure 8.14: Electron energy density distribution in the colloidal crystal at 80 fs (a-c) and 1 ps (d-f) after the start of the IR laser pulse for three different IR laser intensities. The IR laser pulse is coming from the top along the z direction. Here the projection of the electron energy density along the y-direction is shown.

Table 8.1: IR laser parameters and results of the plasma simulations for our experiment. The corresponding average ionization state and ionization depth were calculated from the PIConGPU simulations.

Intensity, 10^{14} W/cm^2	3.0	4.8	6.3
Average charge state in the skin at 80 fs	2.1	2.7	2.9
Average charge state in the center of the first colloidal particle at 80 fs	1.8	2.1	2.4
Average charge state in the skin at 1 ps	2.1	2.7	2.7
Average charge state in the center of the first colloidal particle at 1 ps	1.7	2.1	2.4
Ionization depth, nm	300	700	820

At 600 fs after the beginning of the simulation, accelerated electrons collisionally ionized the inner part of the colloidal crystal and until 1 ps the ionization state of the colloidal crystal remained practically constant (see Fig. 8.13(d-f)). From Fig. 8.13(d-f) it can be observed that the ionization depth varies a lot with the IR laser intensity. The ionization depth is different for three IR laser intensities and is summarized in Table 8.1. Even at 1 ps after the start of the PIConGPU simulation, the highest ionization state remains at the center of the top layer of the colloidal particles.

The electron energy density distribution as a function of depth and transverse spatial coordinate at 80 fs and 1 ps after the start of the IR laser pulse propagation are shown in Fig. 8.14. As one can see from Fig. 8.14(a-c), at 80 fs only the first layer of the colloidal particles is strongly ionized by the IR laser pulse. Our simulations show that the maximum electron energy density was reached in the center of colloidal particles of the first layer 80 fs after the start of the IR laser pulse propagation (see Fig. 8.14(a-c)). The maximum electron energy density is summarized in Table 8.4 for three measured IR laser intensities.

At 1 ps after the beginning of the interaction of the IR laser with the colloidal crystal sample, accelerated electrons move deep inside the colloidal crystal and collisionally ionize the inner part of the crystal (see Fig. 8.14(d-f)). The electron energy density at 1 ps has its maximum still in the first layer of the colloidal crystal but its magnitude is much lower than at 80 fs (see Table 8.4). Even after 1 ps the electron energy density distribution resembles a periodic structure of the colloidal crystal.

To determine the evolution of the electron energy density distribution, simulated values were averaged over the transverse x- and y-coordinates. The time dependence of the maximum electron energy density is shown in Fig. 8.15(a). As shown in this figure the electron energy density reaches its maximum value at 80 fs for all IR laser intensities values, and after 0.6 ps remains practically constant. The z-dependence at 1 ps is shown in Fig. 8.15(b). It is clearly seen that the electron energy density is decaying along the z-direction with periodic modulations due to the colloidal crystal

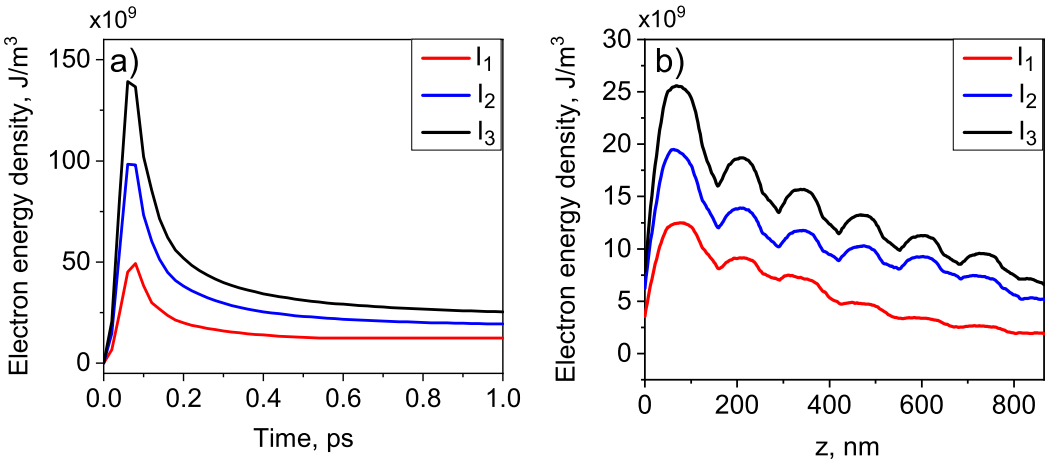

Figure 8.15: Time (a) and depth (b) dependencies of the electron energy density for three measured intensities $I_1 = 3.0 \cdot 10^{14}$ W/cm^2, $I_2 = 4.8 \cdot 10^{14}$ W/cm^2 and $I_3 = 6.3 \cdot 10^{14}$ W/cm^2. The time dependencies of the electron energy density are shown at 75 nm distance from the top of the sample that correspond to the center of colloidal particles in the first surface layer. The electron energy density-depth dependence is shown at 1 ps after the start of the interaction with the IR laser pulse.

structure. This periodicity is less visible for the lower IR laser intensity because of the low ionization level of the inner part of the colloidal crystal.

8.3.3 PIConGPU simulations coupled to HELIOS simulations

After the plasma formation, the electron-ion thermalisation occurs and further processes in the colloidal crystal are governed by the hydrodynamics. These processes are the ablation of the material and the propagation of a shock wave inside the cold material. This last hydrodynamic stage of our model, which was also observed in our experiment, will be discussed in this section. As can be seen from Fig. 8.15(a) the ionization of the colloidal crystal was practically finished at 1 ps. Around these times the high-pressure dense plasma in the top layers of the colloidal crystal induced ablation and shock wave propagation inside the sample.

In order to model structural changes in the colloidal crystal, hydrodynamic simulations using the HELIOS code were performed [313]. The HELIOS code is widely used to simulate the dynamics of plasma evolution created in high-energy density physics experiments [29, 36, 314]. The hydrodynamic simulation was one-dimensional, therefore the 3D structure of the colloidal crystal was modeled as layers with the periodic variation of a mass density. The simulations were performed using the two-temperature model (see Section 8.1), which takes into account the fact that the energy of hot electrons is not instantaneously transferred to cold ions, but is governed by the electron-phonon coupling.

The temperature distribution used as an input for hydrodynamic simulations is shown in Fig. 8.16 for three IR laser intensities. The PIConGPU simulations were per-

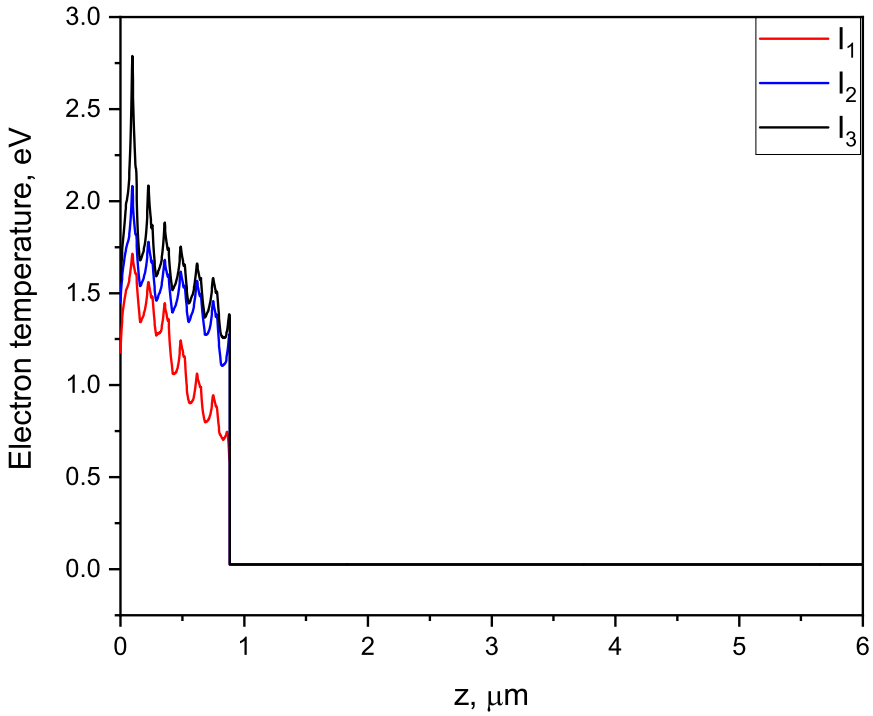

Figure 8.16: Electron temperature distribution in the colloidal crystal for three measured intensities $I_1 = 3.0 \cdot 10^{14}$ W/cm^2, $I_2 = 4.8 \cdot 10^{14}$ W/cm^2 and $I_3 = 6.3 \cdot 10^{14}$ W/cm^2 at 1 ps after the IR laser pulse.

formed only for the first 882.5 nm of the colloidal crystal, therefore the temperature distribution was obtained only up to this value. The oscillations of the electron temperature due to the periodic colloidal crystal structure are clearly visible. A drop of the electron temperature at 882.5 nm due to end of the PIConGPU simulation is well visible. The abrupt transition between two regimes was not smoothed due to several reasons. First, the ionization rate in the PIConGPU code was overestimated because recombination process was not included. Therefore, in the simulation the electrons in the deeper part of the sample are heated. Also the hydrodynamic simulations performed with such an initial conditions correspond quite well to the simulations performed only with hydrodynamic HELIOS code. These PIConGPU and HELIOS combined set of simulations is further noted as simulation Set 1.

8.4 Ablation and shock wave propagation inside the colloidal crystal

Hydrodynamic simulations were performed from 1 to 1000 ps with 1 ps time increment for the 6 μm thick polystyrene colloidal crystals. The pressure and mass density evolution obtained from the hydrodynamic simulations are shown in Fig. 8.17. The

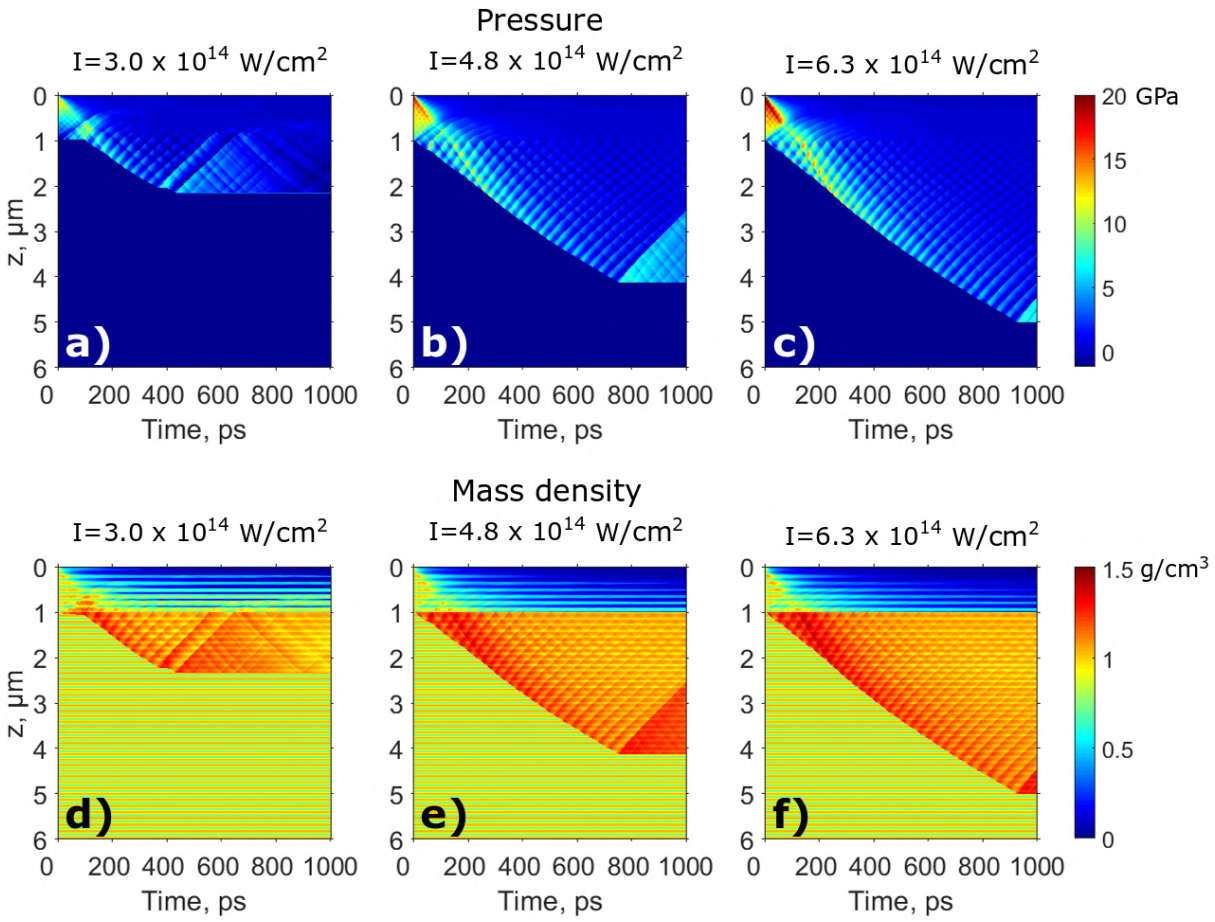

Figure 8.17: Hydrodynamic simulations of the shock wave propagation. Color plots show simulation results for the pressure (a-c) and mass density (d-f) for three different IR laser intensities: (a,d) I_1=3.0 · 10^{14} W/cm^2, (b,e) I_2=4.8 · 10^{14} W/cm^2, (c,f) I_3=6.3 · 10^{14} W/cm^2.

first process that was determined in the hydrodynamic simulations is the ablation of the material on the top of the colloidal crystal. The ablation threshold of polystyrene for 800 nm laser wavelength with 40 fs pulse duration as reported in [315] is of the order of 10 mJ/cm^2. The laser fluences used in our pump-probe experiment were three orders of magnitude higher than the polystyrene ablation threshold (see Table 8.4). During the first picoseconds the top layers of the colloidal crystal were already damaged by the ablation process, and a steep gradient of the mass density was observed in the hydrodynamic simulations (see in Fig. 8.17(d-f)s). After the first picoseconds the ablation process continues and results in a zero mass density on the top of the sample. Due to the ablation process of the top layers of the colloidal crystal a fast initial drop of the scattered intensity was observed (see Fig. 8.11(b,c)). The ablation process stops at about 180 nm – 450 nm depth which corresponds to about 1 – 3 layers (see Table 8.4).

The next process that occurs is the shock wave propagation inside the periodic colloidal crystal. As one can see from Fig. 8.17(a-c), the shock pressure is propagating along the z – direction and destroys the periodicity of the significant part of the sample. During the first picoseconds the maximum shock wave pressure is located in the top layer of the colloidal crystal (see Fig. 8.15, 8.17(a-c)). The shock wave speed is pro-

Table 8.2: The IR laser emitted and absorbed energy, and absorption coefficient estimated from PIConGPU simulations.

Intensity, 10^{14} W/cm^2	3.0	4.8	6.3
Laser emitted energy, 10^10 eV	3.5	5.5	7.2
Absorbed energy, 10^9 eV	3.5	5.7	7.0
Absorption coefficient, %	10.0	9.6	9.7

portional to the square root of pressure, and it reached about 6 km/s on the top of the sample and about 4 km/s on the border of the shock wave front with the cold material. Therefore, around 100 ps at the depth of about one micrometer (that corresponds to about 8 layers) the high pressure front reaches the low pressure front (see Fig. 8.17). After 100 ps the high pressure front propagates further inside the sample and destroys the sample periodicity. The average shock wave propagation speed obtained from our simulations is of the order of 5 km/s and the maximum mass velocity is of the order of 2 km/s which is in a good agreement with previous studies [316]. For the three IR laser intensities used in this experiment, the shock wave stopped after approximately 400 – 900 ps propagation time at a depth of 2 – 5 µm (exact values are provided in Table 8.4). The sample periodicity was not further destroyed beyond this point, because the shock wave converted into a sound wave, which did not induce any structural transformation of the colloidal crystal sample [301].

In order to compare PIConGPU coupled to HELIOS simulations (Set 1) and pure HELIOS simulations another set of hydrodynamic simulations was performed using only HELIOS program (Set 2). The simulations were performed for the three experimental laser intensities (I_1=3.0 $\cdot$ 10^{14} W/cm^2, I_2=4.8 $\cdot$ 10^{14} W/cm^2, I_3=6.3 $\cdot$ 10^{14} W/cm^2) with 800 nm wavelength. The FWHM of the laser pulse was 50 fs and the peak laser power was set at 50 fs after the beginning of the simulation. Percentage of power reflected at the critical surface was obtained from the PIConGPU simulations. The energy emitted by the IR laser and the energy absorbed by electrons for the three IR laser intensities are summarized in Table 8.3 and the absorption coefficient was around 10% for all three IR laser intensities. Therefore the reflection coefficient in the HELIOS simulations was set to 90%. This value of the reflection coefficient is also confirmed by simple estimations. In the case of a dense plasma the absorption coefficient derived from the Fresnel formulas can be written in the form $A = 4\pi l_s/\lambda$, where A is the absorption coefficient, l_s is the skin depth and λ is the IR laser wavelength [303]. For the estimated skin depth of 10 nm the absorption coefficient is about 15 %.

In the simulation Set 2, the two-temperature model was used, similar to the previous case. In the two-temperature model both electrons and ions were assumed to have a room temperature in the initial state. All other parameters of the simulation, except the laser parameters were the same as in the previous case (simulation Set 1). The initial mass density of the colloidal crystal was similar to the previous simulation

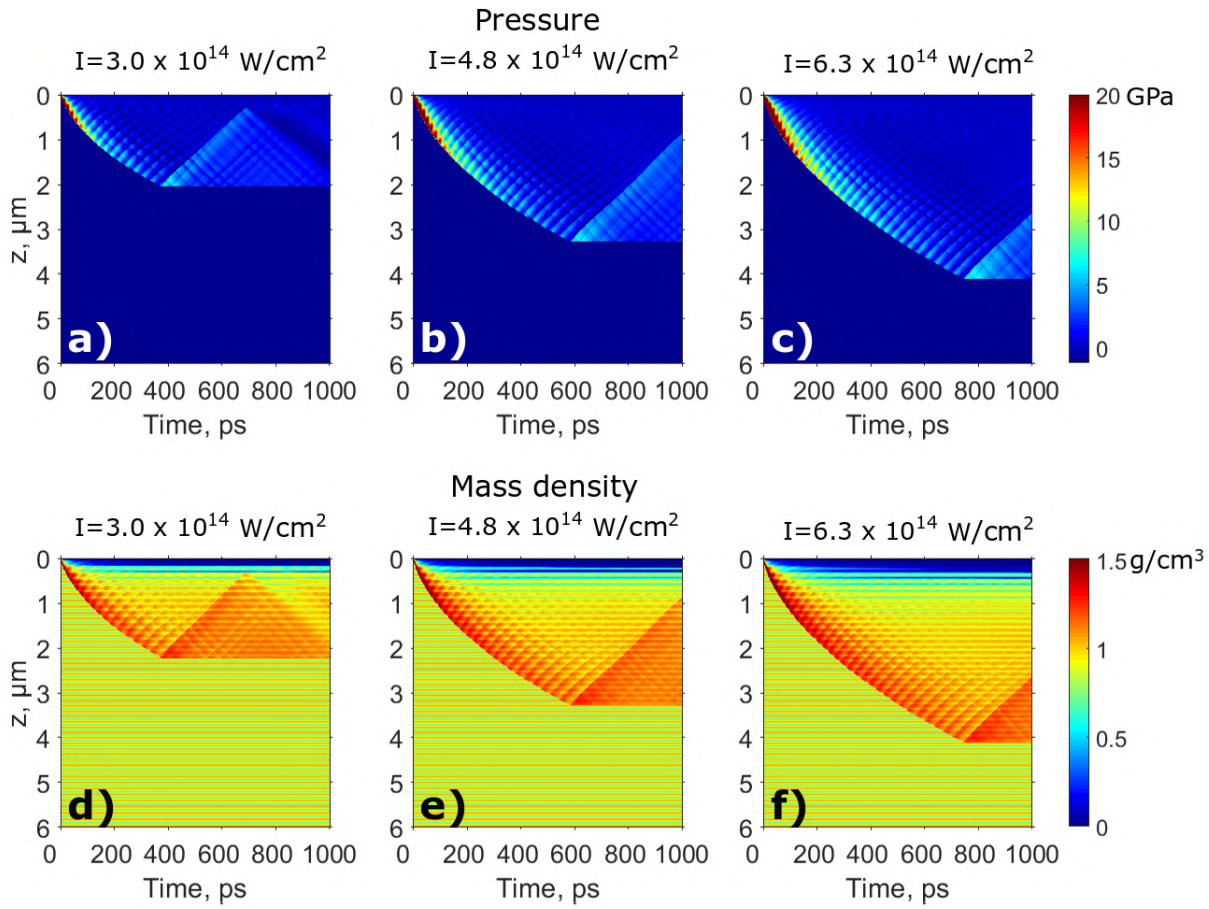

Figure 8.18: Hydrodynamic simulations of the shock wave propagation inside the periodic colloidal crystal. The simulations were performed using only the HELIOS code. Color plots show simulation results for the pressure (a-c) and mass density (d-f) for three different IR laser intensities: (a,d) I_1=3.0 · 10^{14} W/cm^2, (b,e) I_2=4.8 · 10^{14} W/cm^2, (c-f) I_3=6.3 · 10^{14} W/cm^2.

and had the same periodicity.

The pressure and mass density obtained from these set of simulations are shown in Figs. 8.18. Two processes occur in the simulated colloidal crystal sample - ablation and shock propagation (the same processes were observed in simulation Set 1). Ablation is well seen in Fig. 8.18(d-e) as the zero mass density on the top of the sample. The top 1-2 layers are ablated during the first picoseconds and the ablation depth is summarized in Table 8.3. In the simulation Set 2 the ablation depth is slightly smaller than in the simulation Set 1 (see Fig. 8.17 and Figure 8.18). Such a difference may be caused by the different IR laser absorption mechanisms implemented in the programs, and different penetration depth of the IR laser radiation.

The maximum shock wave pressure achieved at the first picosecond of the simulation is of the order of 150-200 GPa (see Table 8.3). At 20 ps the shock wavefront propagated through 0.5 μm of the colloidal crystal and destroyed the periodic structure of the sample. In the simulation Set 1 the periodicity of the first 1 μm was damaged 20 picoseconds after the beginning of the laser pulse. Therefore the simulation Set 2 is not explaining the fast drop of the diffracted intensity in the experimental results, while

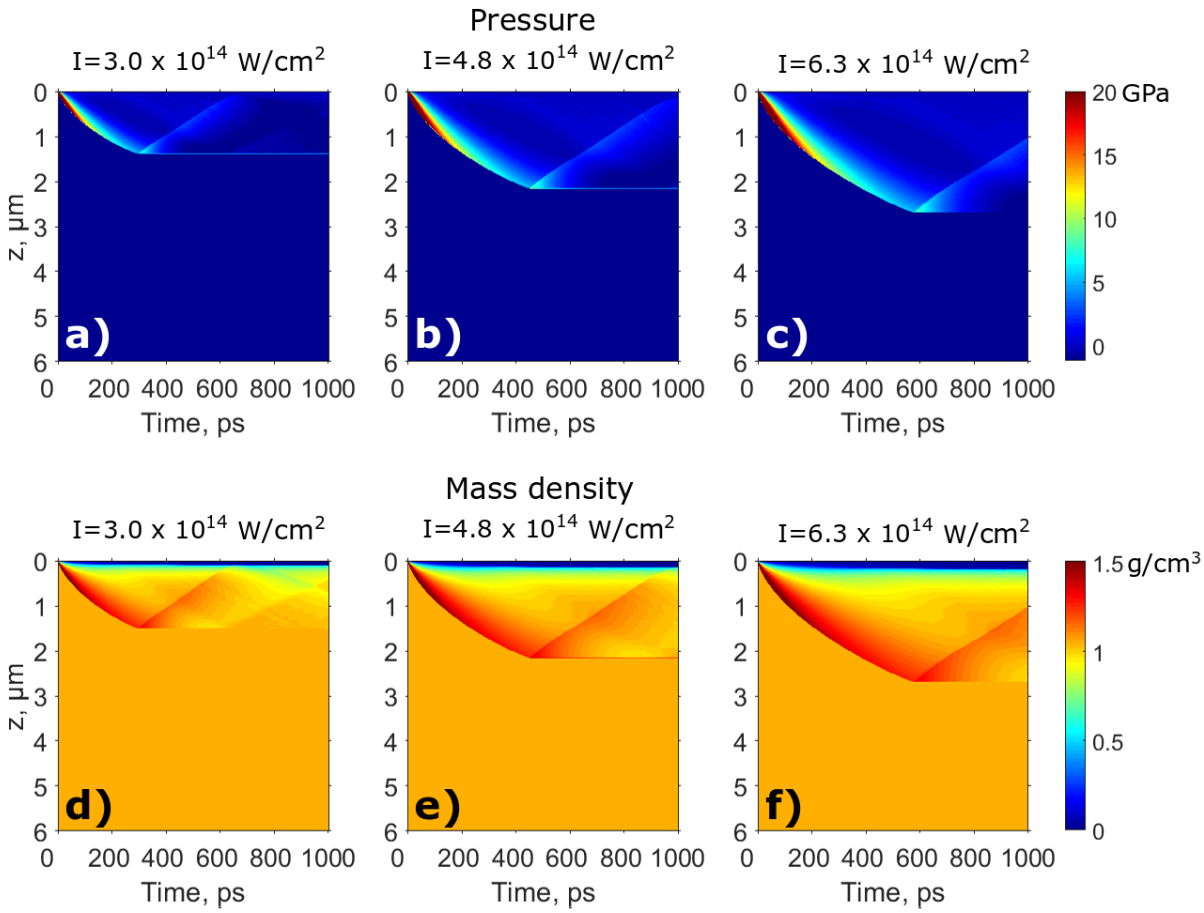

Figure 8.19: Hydrodynamic simulations of the shock wave propagation inside the bulk polystyrene sample. In this case only the HELIOS code was used. Color plots show simulation results for the pressure (a-c) and mass density (d-f) for three different IR laser intensities: (a,d) I_1=3.0 · 10^{14} W/cm^2, (b,e) I_2=4.8 · 10^{14} W/cm^2, (c-f) I_3=6.3 · 10^{14} W/cm^2.

the simulation Set 1 the changes in the colloidal crystal structure can be attributed to the reduced diffracted intensity.

Further the shock wave is propagating through the colloidal crystal sample. The shock wave stops at the different time and depth summarized in Table 8.3. It is worth to notice that compare to simulation Set 1, here the shock wave stops earlier and destroys less of the material. The difference in the shock wave depth is of the order of 25% for two higher IR laser intensities and approximately 1% for the lower IR laser intensity. Such a difference in the shock induced dynamics might be due to the different geometries (1D in HELIOS or 3D in PIConGPU). In the 3D PIConGPU simulations the colloidal crystal structure was properly set, while in the HELIOS simulation only a 1D projection of the mass density was used.

In order to study the influence of the sample periodicity on the shock wave propagation, hydrodynamic simulations were performed for the non-periodic polystyrene sample for all three IR laser intensities used in our XFEL experiment. The last set of hydrodynamics simulations was performed using only HELIOS code with the bulk polystyrene sample (Set 3). In this case all the simulations parameters were similar to

Table 8.3: Results of the HELIOS simulation for Set 1, Set 2 and Set 3 for three IR laser intensities.

Intensity, 10^{14} W/cm^2		3.0	4.8	6.3
Maximum shock wave pressure, GPa	Set 1	49	102	139
	Set 2	143	184	215
	Set 3	148	196	225
Ablation depth, nm	Set 1	180	280	450
	Set 2	150	180	300
	Set 3	80	120	180
Shock wave depth, µm	Set 1	2.36	4.15	5.00
	Set 2	2.24	3.30	4.10
	Set 3	1.53	2.16	2.69
Simulated shock wave stop times, ps	Set 1	437	756	931
	Set 2	377	589	751
	Set 3	301	454	581

the Set 2, except the initial polystyrene mass density. The polystyrene mass density was set to be constant along z – direction (1.05 g/cm^3) considering bulk polystyrene. The results of the simulation Set 3 are present in Fig. 8.19. The two main processes in the simulation Set 3 are ablation and the shock wave propagation, similar to simulation Set 1 and Set 2. The ablation of the material is already visible at 20 ps and it continues up to 100 ps (see Fig. 8.19. The ablation depth is of the order of 100-200 nm and is summarized in Table. 8.3. In the simulation Set 3 the ablation depth was approximately twice smaller than for simulation Set 2. The difference in the ablation depth can be explained by smaller average mass density in case of the simulation Set 2.

The maximum pressure is reached at the first picosecond of the simulation on the very top layer of the polystyrene sample (see Table. 8.3). The pressure–depth dependence had a periodic structure in the simulation Set 1 and Set 2 but in the simulation Set 3 it does not show any periodicity. Therefore one can conclude that such pressure modulations were caused by the periodic structure of the colloidal crystal sample. For the simulation Set 3 the shock wave stop time are much smaller than in case of simulation Set 2. The difference can be explained by the higher average mass density of the simulated sample.

From the comparison of two sets of simulations (Set 2 and Set 3) one can conclude that for the non-periodic sample the shock wave stops earlier and the depth of the shock wave propagation is about 30% smaller than for the periodic one. The ablation depth is also about twice shorter for the non-periodic sample Table 8.1. Such difference can be explained by the higher average mass density in the case of the non-periodic sample. A comparison of two simulation sets shows that the pressure modulations observed in Fig. 8.17(a-c) are caused by the periodic structure of the colloidal crystal sample.

8.5 Discussion

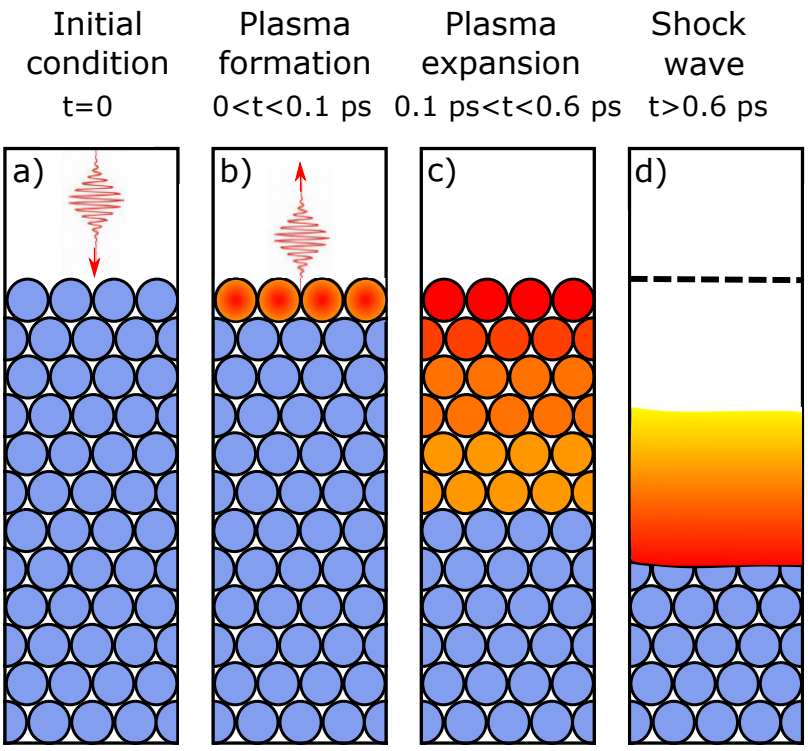

Figure 8.20: Three-stage model of the IR laser-matter interaction. The colloidal particles are shown as circles. The color of the particles corresponds to the temperature of the colloidal crystal - red is plasma and blue is the cold material. The incoming IR laser pulse is pointing in the direction of the pulse propagation. Initially, the IR laser pulse is propagating towards the colloidal crystal sample and after interaction with the sample it is reflected by the created plasma on the top layer of the colloidal crystal. The top surface level of the initial colloidal crystal is marked by the black dashed line in (d).

A three-stage model of interaction between the high-power IR laser pulse and the periodic colloidal crystal is proposed to explain the ultrafast changes in the colloidal sample (see Fig. 8.20). First, all colloidal particles are in the initial condition, unaffected by the laser pulse. The incoming IR laser pulse generates a plasma in the top layer of the colloidal crystal within the first few femtoseconds (see Fig. 8.20(a,b)). Due to the plasma skin effect the IR laser pulse is partially reflected (see Fig. 8.20(b)). This hot confined periodic plasma then propagates inside the colloidal crystal up to about 0.6 ps time (see Fig. 8.20(c)). The second stage is the ablation of a few layers on the top of the colloidal crystal. The top layers of the sample are damaged during the first few picoseconds and are completely destroyed afterwards (see Fig. 8.20(d)). During the third and last stage the shock wave is formed and propagates inside the colloidal crystal sample. This shock wave destroys the periodicity of the sample by compressing the structure in its deeper parts (see Fig. 8.20(d)).

The three-stage model of the laser-matter interaction allowed us to attribute the

Table 8.4: IR laser parameters and results of the plasma and shock wave simulations. The corresponding plasma pressure was calculated from the PIConGPU simulations. The ablation depth and the shock wave time and depth were calculated from the hydrodynamic HELIOS simulations. The experimental shock wave times were obtained from exponential fits of the measured data.

Intensity, 10^{14} W/cm^2	3.0	4.8	6.3
Laser fluence, J/cm^2	16	25.5	33.6
Short times of intensity decay, ps	-	3 ± 10	7.9 ± 1.1
Long times of intensity decay, ps	299 ± 33	300 ± 28	275 ± 28
Times of radial FWHM growth, ps	302 ± 32	279 ± 50	425 ± 90
Times of azimuthal FWHM growth, ps	345 ± 235	353 ± 86	410 ± 78
Maximum electron energy density at 80 fs, 10^9 J/m^3	49	98	149
Maximum electron energy density at 1 ps, 10^9 J/m^3	12	20	25
Ablation depth, nm	180	280	450
Shock wave depth, µm	2.36	4.15	5.00
Maximum mass velocity, km/s	2.3	2.7	2.8
Simulated shock wave stop times, ps	437	756	931

short 5 ps time scale determined in our diffraction pump-probe experiment to the ablation of the material. The long 300 ps time scale is related to the shock wave propagation. Simulations were performed for all three stages of the laser-matter interaction: plasma formation and expansion were simulated with the 3D PIConGPU code, ablation and shock wave propagation were simulated with the HELIOS code. From the results of plasma and hydrodynamic simulations, the time dependence of the structural changes in the colloidal crystal was obtained.

8.6 Conclusions

In the present work, a pump-probe diffraction experiment at LCLS was performed on a periodic plasma created from a colloidal crystal sample. The periodic structure of the colloidal crystal allowed us to reveal the picosecond dynamics of the propagating shock wave by Bragg peak analysis. A fast decay of the Bragg peak intensity and the growth of the radial and azimuthal peaks width were observed. From the analysis of the Bragg peak parameters 5 ps short and 300 ps long characteristic timescales were obtained. Such changes of scattering parameters indicate ultrafast dynamics of the colloidal crystal periodic structure, which is producing the scattering signal.

In order to understand the experimental results, a complex set of plasma and hydrodynamic simulations was performed. From these simulations one can conclude that the short and long characteristic timescales correspond to the ablation of the ma-

terial and shock wave propagation, respectively. At the same time our simulations predict much shorter times of evolution of plasma and ablation processes in polystyrene colloidal samples. This is still an open and intriguing question of investigation of the plasma dynamics and ablation process with sub-picosecond time resolution.

Chapter 9

Summary

This thesis presented three research projects focused on the use of X-ray scattering for studying structure and dynamics of mesoscopic materials.

The first project explored the superlattice of PbS nanocrystals linked by oleic acid molecules. The structure and orientational order of mesocrystals was studied using the angular X-ray cross-correlation analysis in conjunction with a X-ray nanodiffraction mapping. It was found that the superlattice forms an *fcc* structure and that the lattice constant is homogeneous within a single-crystalline domain. The domains of the superlattice were characterized by mesocrystalline polymorphs with two specific orientational orders. Close to the edges, the lattice constant decreased by 5 - 10%, which was often accompanied by a rotation of the superlattice with full preservation of their angular correlation. These findings were explained by the release of stress energy on the expense of specific nanocrystal – substrate interactions. The correlations between adjacent nanocrystals are conserved during the structural changes at most of the grain boundaries. Therefore the key to fabrication of the nanocrystal superlattices with macroscopic domain sizes is strengthening the interactions with the substrate. These results extend our knowledge about the origin of defects in nanocrystal superlattices, highlight the role of orientational order, and suggest a new opportunity to tailor the properties of nanocrystal-based materials.

The second project used *in-situ* grazing incidence X-ray scattering to study structural rearrangement of polystyrene colloidal crystals under dry sintering conditions. Measured diffraction patterns were analyzed using distorted wave Born approximation theory. The temperature evolution of the diffraction peaks' positions, integrated intensities, and widths revealed the evolution of colloidal crystal microstructure, including particle shape transformation, thermal expansion, and crystal amorphisation. These structural parameters for the in-plane and out-of-plane directions were determined for three colloidal crystal samples with different particle sizes. It was found that in the process of dry sintering the shape of colloidal particles in a crystal transforms from a sphere to a polyhedron. Results of this work deepen current understanding

of thermal annealing of polymer colloidal crystals and introduce a novel approach to study the structural evolution in such systems. The observed intermediate states of colloidal particles in the crystal provide new insights to the self-assembly of polymer-based nanostructures with desired optical properties.

In the third project, the laser-induced dynamics in polystyrene colloidal crystals was studied in a pump-probe experiment. Colloidal crystals were pumped with an infrared laser at a wavelength of 800 nm with varying power and probed by XFEL pulses at an energy of 8 keV with time delays in the range of -50 ps to 1000 ps. The crystalline order of the sample allowed using Bragg peaks to follow laser-induced ultrafast structural changes in the sample. By varying the pump laser intensity destructive and non-destructive regimes of the laser-matter interaction were explored.

In the non-destructive regime laser-induced vibrational modes in the colloidal particles were studied. Unexpectedly, the spectral analysis of the data did not reveal any significant enhancement of characteristic frequencies. This allowed to conclude that the amplitude of excited vibrational modes was less than the systematic error caused by the pulse-to-pulse variation. For the successful XFEL-based measurement of the lattice vibrations in colloidal crystals, some further improvements of the experiment are suggested. First, more accurate measurements of the incoming X-ray pulses intensity are required for the precise determination of the Bragg peak intensity. In the reported experiment this was not achieved due to the complicated structure of XFEL pulses and a relatively low accuracy (about 3%) in the measurement of the incoming X-ray pulse intensity. Second, covering the sample surface by a thicker aluminum layer could benefit with a more efficient energy transfer from an infrared laser to the colloidal crystal [317]. This would lead to a significant enhancement of the crystal lattice vibrations, and enable their detection in the pump-probe experiments.

The destructive experiment was performed with the infrared laser intensities on the order of 10^{14} W/cm^2. Such a high intensity of the IR laser was sufficient for non-linear ionization of carbon and hydrogen, therefore these atoms became ionized within the first femtoseconds after arrival of the pump pulse. Further, the incoming pulse heated the released electrons up to the temperature of several eV. This process created a confined periodic plasma which exploded and generated a powerful shock wave. The maximum pressure of the shock wave reached values about 100 GPa, resulting in the compression of the surrounding material. Performed simulations of the created high density plasma and shock wave propagation showed good agreement with the timescales obtained in the experiment (5 ps and 300 ps). Developed three-stage model allowed to attribute 5 ps timescale to the ablation and 300 ps to the shock wave propagation through the sample. This work demonstrates that the shock wave propagation inside colloidal crystals can be visualized with a high temporal resolution in an infrared pump – X-ray probe experiment. The described ideas pave a new way to the time-resolved studies of phase transitions in matter under extreme conditions.

Acknowledgements

First and foremost I thank Prof. Ivan Vartaniants for task-setting and great motivation for completing these tasks during my PhD. I am grateful to Prof. Ivan Vartaniants and Prof. Christian Schroer for agreeing to be my supervisors for this thesis. I want to thank Dr. Michael Sprung for being my mentor. I also thank Prof. Edgar Weckert for finding time for discussion despite his tight schedule. I am grateful to Dr. Sergey Yakunin for his supervision of my scientific activities in Russia.

Many thanks to the former and current members of the Coherent X-ray Scattering and Imaging group at DESY Anatoly Shabalin, Oleg Gorobtsov, Ivan Zaluzhnyy, Dmitry Dzhigaev, Max Rose, Sergey Lazarev, Ilya Besedin, Petr Skopintsev, Dameli Assalauova, Dmitry Lapkin, Ruslan Khubbutdinov, Luca Gelisio, Alexandr Ignatenko, Young Yong Kim and Jerome Carnis. I appreciate interesting discussions with you and your companionship during tea and coffee drinking. I thank especially Sergey Lazarev for helping me a lot during my first months at DESY, Oleg Gorobtsov for discussing plasma physics, Ivan Zaluzhnyy for exciting night shifts and Dmitry Lapkin for work on mesocrystal project. I also want to thank Rustam Rysov and Dmitry Lapkin for providing tasty food for our tea discussions.

I am grateful to all the people who read the text of my thesis or provided advises during its preparation: Jerome Carnis, Dmitry Lapkin, Anatoly Shabalin, Oleg Gorobtsov and Svitozar Serkez. Special thanks to Jerome Carnis who managed to read the full first draft of this thesis. I want to thank Maria Naumova and Edmund Welter for helping with abstract translation to German. I am very thankful to my friend Tamara Orlova for providing nice snail picture illustrating my struggles during writing this thesis.

I would like to express gratitude to the sample preparation people: Alexander André and Marcus Scheele for mesocrystals Janne-Mieke Meijer and Andrei V. Petukhov for colloidal crystals. Two experiments discussed in this thesis were performed at P10 beamline at PETRA III. Michael Sprung and the P10 beamline stuff is thanked for the excellent technical support. The pump-probe experiment on colloidal crystals was performed at LCLS and I thank LCLS XPP beamline and I thank beamline teams for their support. PIConGPU simulations were done in a close collaboration with Computational Radiation Physics Group at HZDR. I want to thank Axel Huebl, Thomas Kluge, Michael Bussmann and especially Marco Garten, for being very user-friendly software

developers.

I would like to acknowledge our funding. This work has been supported by the Helmholtz Associations Initiative, Networking Fund and the Russian Science Foundation grant HRSF-0002/18-41-06001

I want to thank my flatmate Maria Naumova for preventing our flat from total collapse while I was concentrated on writing. I enjoyed your company a lot. I am very thankful to Anatoly Shabalin for warm hugs and valuable emotional support before and during my PhD time. Special thanks to Ksenia Gasnikova and Andrei Fedulin for their support and encouragement. And I thank all my friends who were not mentioned before: Margarita Chudenkova, Nataliya Mezhetskaya, Nataliya Zolotova, Ivan Sobolev, Aleksandra Tolstikova, Aram Kalaydzhan, Pavel Lytaev, Yaryna Serkez, Sergey Riabchuk, Semyon Goncharov, Anton Sokolov, Olga Merkulova, Igor Khokhriakov, Tatiana Gurieva, Dina Sheyfer, Ruslan Kurta, Oleksandr Yefanov, Aleksandr Rogachev for having great time with you.

And last but not the least, I thank my parents, grandparents and other family members for supporting me throughout my life.

Own publications

Publications directly related to the thesis

1. N. Mukharamova, S. Lazarev, J.-M. Meijer, M. Chollet, A. Singer, R. P. Kurta, D. Dzhigaev, O. Gorobtsov, G. Williams, D. Zhu, Y. Feng, M. Sikorski, S. Song, A. G. Shabalin, I. Besedin, I. Zaluzhnyy, T. Gurieva, E. A. Sulyanova, O. M. Yefanov, A. V. Petukhov, and I. A. Vartanyants. Probing dynamics in colloidal crystals with pump-probe experiment at X-ray free-electron lasers. Applied Sciences **7.5**, 519 (2017).

2. N. Mukharamova, D. Lapkin, I. A. Zaluzhnyy, A. André, S. Lazarev, Y.Y.Kim, R. P. Kurta, F. Schreiber, I. A. Vartanyants, and M. Scheele. Revealing Grain Boundaries and Defect Formation in Nanocrystal Superlattices by Nanodiffraction. Small, **15**, 1904954 (2019).

3. N. Mukharamova, S. Lazarev, J.-M. Meijer, O. Yu. Gorobtsov, A. Singer, M. Chollet, M. Bussmann, D. Dzhigaev, Y. Feng, M. Garten, A. Huebl, T. Kluge, R. P. Kurta, V. Lipp, R. Santra, M. Sikorski, S. Song, G. Williams, D. Zhu, T. Cowan, A. V. Petukhov, and I. A. Vartanyants. Femtosecond-laser-produced plasma in colloidal crystal observed by FEL radiation. Scientific Reports **10.1**, 1-11 (2020).

4. A. Zozulya, I.A. Zaluzhnyy, N. Mukharamova , S. Lazarev, J.-M. Meijer, R.P. Kurta, A. Shabalin, M. Sprung, A.V. Petukhov and I.A.Vartanyants. Unravelling structural rearrangement of polymer colloidal crystals under dry sintering conditions. Soft Matter, **14**, 6849-6856 (2018).

Publications not directly related to the thesis

1. O. Gorobtsov, N. Mukharamova, S. Lazarev, M. Chollet, D. Zhu, Y. Feng, R. P. Kurta, J.-M. Meijer, G. Williams, M. Sikorski, S. Song, D. Dzhigaev, S.Serkez, A. Singer, A. V. Petukhov, and I. A. Vartanyants. Diffraction based Hanbury Brown and Twiss interferometry a hard x-ray free-electron laser. Scientific Reports **8.1**, 1-9 (2018).

2. I.A Zaluzhnyy, R.P. Kurta, N. Mukharamova, Y.Y.Kim, R.M. Khubbutdinov, D. Dzhigaev, V.V. Lebedev, E.S. Pikina, E.I. Kats, N.A. Clark, M. Sprung and I.A. Vartanyants. Evidence of a first-order smectic-hexatic transition and its proximity to a tricritical point in smectic films. Phys. Rev. E, **98**, 052703 (2018).

3. Y.Y. Kim, L. Gelisio, G. Mercurio, S. Dziarzhytski, M. Beye, L. Bocklage, A. Classen, C. David, O. Yu. Gorobtsov, R. Khubbutdinov, S. Lazarev, N. Mukharamova, Yu. Obukhov, K. Schlage, I. Zaluzhnyy, G. Brenner, R. Röhlsberger, J. von Zanthier, W. Wurth and I. A. Vartanyants. Ghost Imaging at an XUV Free-Electron Laser. Phys. Rev. A **101**, 013820 (2020).

4. A. Maier, D. Lapkin, N. Mukharamova, P. Frech, D. Assalauova, A. Ignatenko, R. Khubbutdinov, S. Lazarev, F. Laible, R. Löffler, N. Previdi, T. Chassé, M. Fleischer, M. Sprung, F. Schreiber, I.A. Vartanyants, M. Scheele. Structure-transport correlation reveals anisotropic charge transport in coupled PbS nanocrystal superlattices. Advanced Materials, **32**, 2002254 (2020).

List of Abbreviations

AXCCA	Angular X-ray Cross-Correlation Analysis
CCF	Cross-Correlation Function
SAXS	Small Angle X-ray Scattering
WAXS	Wide Angle X-ray Scattering
GISAXS	Grazing Incidence Small Angle X-ray Scattering
GISANS	Grazing Incidence Small Angle Naeutron Scattering
GTSAXS	Grazing Incidence Transmission Small Angle X-ray Scattering
GIWAXS	Grazing Incidence Wide Angle X-ray Scattering
DWBA	Distorted Wave Born Approximation
CXDI	Coherent X-ray Diffraction Imaging
XPCS	X-ray Photon Correlation Spectroscopy
EXAFS	Extended X-ray Absorption Fine Structure
XANES	X-ray Absorption Near-Edge Structure
FTH	Fourier Transform Holography
SEM	Scanning Electron Microscopy
FEL	Free-electron Laser
XFEL	X-ray Free-electron Laser
SASE	Self Amplification of Spontaneous Emission
HGHG	High-gain Harmonic Generation
EEHG	Echo-enable Harmonic Generation
SPI	Single Particle Imaging
LCLS	Linac Coherent Light Source
3D	Three-dimensional

2D	Two-dimensional
FWHM	Full Width at Half Maximum
LED	Light – Emitting Diod
GHz	Gigahertz
bcc	Body – centered cubic (structure)
bct	Body – centered tetragonal (structure)
fcc	Face – centered cubic (structure)
hcp	Hexagonal close-packed (structure)
rhcp	Random hexagonal close-packed (structure)
CTR	Crystal Truncation Rod
NC	Nanocrystal
AL	Atomic Lattice
SL	Superlattice
HOMO	Highest Occupied Molecular Orbital
LUMO	Lowest Unoccupied Molecular Orbital
COIN	Coupled Organic – Inorganic Nanostructures
PS	Polystyrene
WH	WilliamsonHall (method)
CSD	Coherently Scattering Domain
RT	Room Temperature
CRL	Compound Refractive Lens
CSPAD	Cornell – SLAC Pixel Array Detector
IR	Infrared
ABI	Above – Barrier Ionisation
ADK	Ammosov – Delone – Krainov (model)
KFR	Keldysh – Faisal – Reiss (model)
TF	Thomas – Fermi (model)

List of commonly encountered variables

c	Speed of light in vacuum
e	Elementary charge
$\mathbf{k}$	Wavevector
λ	Wavelength of radiation
m_e	Electron mass
n_e	Electron density
ω	Radiation frequency
$\mathbf{r}$	Vector of spatial coordinates
r_0	Classical electron radius
t	Time
x, y, z	Spatial coordinates
$\mathbf{F}$	Force
$\mathbf{n}$	Unit vector
h	Planck constant
$\mathbf{E}$	Electric field
$\mathbf{H}$	Magnetic field
$\mathbf{D}$	Electric induction
$\mathbf{H}$	Magnetizing field
Δ	Angular coordinate
$C(q_1, q_2, \Delta)$	Cross-correlation function

Chapter 2

$F(\lambda)$	Photon flux
$B(\lambda)$	Brilliance
$\varepsilon_{x,y}$	Horizontal and vertical emittance of the source
$\sigma_{x,y}$	Horizontal and vertical size of the source
$\sigma'_{x,y}$	Horizontal and vertical divergence of the source
γ	Lorenz factor
θ	Radiation angular spread
K_u	Undulator parameter
B_0	Magnetic field in the undulator
λ_u	Undulator period
N_p	Number of dipole magnets in the undulator
N_e	Number of electrons
ε_p	Photon beam emittance
ε_e	Electron beam emittance

Chapter 3

I	X-ray intensity
μ	Linear absorption coefficient
ρ_{at}	Atomic number density
σ_a	Absorption cross-section
E	Photon energy
Z	Atomic number
E_{in}	Magnitude of the incident plane wave electric field
$\mathbf{p}$	Polarization vector
$\mathbf{d}$	Dipole moment

$\mathbf{S}$	Poynting vector
Δ'	Phase difference
$\mathbf{k_i}$	Incident wavevector
$\mathbf{k_f}$	Diffracted wavevector
$A(\mathbf{q})$	Total diffracted amplitude
$f_{at}(\mathbf{q})$	Atomic formfactor
$P(\mathbf{q})$	Probability of elastic scattering
$f'(\omega), f''(\omega)$	Anomalous dispersion corrections
$\mathbf{a}_{1,2,3}$	Fundamental vectors of a crystal lattice
$\mathbf{R_n}$	Translation vector of a crystal lattice
$\rho(\mathbf{r})$	Electron density of the material
$\rho_{uc}(\mathbf{r})$	Electron density of the unit cell
$s(\mathbf{r})$	Shape function of the crystal
$\mathbf{G_n}$	Vectors of a reciprocal crystal lattice
$\mathbf{b}_{1,2,3}$	Fundamental vectors of a reciprocal crystal lattice
$F_{uc}(\mathbf{q})$	Structure factor (of the unit cell)
$W(\mathbf{q})$	Debye-Waller factor
$L_{1,2,3}$	Length, width and height of the crystal
V	Crystal volume
$s'(\mathbf{q})$	Fourier transform of the crystal shape function
d_{hkl}	Spacing between crystal planes
θ_B	Bragg angle
n	Diffraction order
α_f	In-plane incoming angle
α_f	In-plane scattering angle
θ_f	Out-of-plane scattering angle

$q_{\|\|}$	Lateral component of the scattering vector
R_α	Reflection coefficient
n_s	Complex refractive index
$M(q, \varphi)$	Mask function

Chapter 4

$\mathbf{u}(\mathbf{r})$	Displacement vector field
$\mathbf{b}$	Burgers vector

Chapter 5

A	Bragg peak intensity
σ	Bragg peak size

Chapter 6

D	Colloidal particle diameter
T_a	Annealing temperature
T_g	Glass-transition temperature
T_a	Melting temperature
α_i	Linear thermal expansion coefficient
L	Coherent scatering domain size
g	Lattice deformation patameter

Chapter 7

A	Bragg peak intensity
σ	Bragg peak FWHM
D	Colloidal particle diameter
S	Relative amplitude of the vibration

ω_v	Characteristic frequency of the vibration
N	Noise amplitude
$\eta(\tau)$	Random noise function
P	Probability of detecting signal
c_L	Longitudinal sound velocity
c_T	Transverse sound velocity

Chapter 8

γ	Keldysh parameter
$\mathcal{E}_I$	Ionisation energy
Z	Ion charge
E_{ABI}	Above-barrier ionisation laser field strength
I_{ABI}	Above-barrier ionisation laser field intensity
P	Ionisation probability
P_{bound}	Probability of an electron to remain bound
Γ	Ionisation rate
$\Psi(\mathbf{r}, t)$	Wave-function of an electron
n^*	Effective principal quantum number
l	Angular quantum number
m	Magnetic quantum number
Γ_{ADK}	ADK ionisation rate
Z^*	Average ionisation state
ν_{ei}	Electron-ion collision frequency
$\mathbf{P}$	Polarization
$\varepsilon(\omega)$	Dielectric function
ω_p	Plasma frequency

l_s	Skin depth
T_e	Electron temperature
T_i	Ion temperature
C_e	Electron heat capacity
C_i	Ion heat capacity
Q_{abs}	Absorbed laser energy
Q_{e-th}	Electron heat conduction flux
Q_{e-i}	Energy transferred from electrons to ions
A	Absorption coefficient
ν_{e-i}^{en}	Electron-ion energy exchange rate
t_{e-i}^{en}	Electron-ion relaxation time
κ_e	Heat conduction coefficient
ε_a	Ablation threshold energy
ε_b	Atomic binding energy
ε_{esc}	Electron work function
m	Mass flow rate per unit area
ρ	Mass density
u	Fluid velocity
p	Pressure
h	Specific enthalpy
V	Specific volume
Y	Young modulus of a solid
x_{stop}	Distance where the shock wave stops
E_{abs}	Total absorbed energy density

Bibliography

[1]R. Paolesse, F. Mandoj, A. Marini, and C. Di Natale, "Encyclopedia of nanoscience and nanotechnology, Vol. X", American Scientific Publisher (2003).

[2]D. V. Talapin, J.-S. Lee, M. V. Kovalenko, and E. V. Shevchenko, "Prospects of colloidal nanocrystals for electronic and optoelectronic applications", Chem. Rev. **110**, 389–458 (2009).

[3]M. Scheele, W. Brütting, and F. Schreiber, "Coupled organic–inorganic nanostructures (COIN)", Phys. Chem. Chem. Phys. **17**, 97–111 (2015).

[4]J. Als-Nielsen and D. McMorrow, *Elements of modern X-ray physics* (John Wiley & Sons, 2011).

[5]J. Miao, P. Charalambous, J. Kirz, and D. Sayre, "Extending the methodology of X-ray crystallography to allow imaging of micrometre-sized non-crystalline specimens", Nature **400**, 342–344 (1999).

[6]H. N. Chapman and K. A. Nugent, "Coherent lensless X-ray imaging", Nat. Photon. **4**, 833–839 (2010).

[7]I. A. Vartanyants, D. Grigoriev, and A. V. Zozulya, "Coherent X-ray imaging of individual islands in GISAXS geometry", Thin Solid Films **515**, 5546–5552 (2007).

[8]J. Rodenburg, A. Hurst, A. Cullis, B. Dobson, F. Pfeiffer, O. Bunk, C. David, K. Jefimovs, and I. Johnson, "Hard-X-ray lensless imaging of extended objects", Phys. Rev. Lett. **98**, 034801 (2007).

[9]P. Thibault, M. Dierolf, A. Menzel, O. Bunk, C. David, and F. Pfeiffer, "High-resolution scanning X-ray diffraction microscopy", Science **321**, 379–382 (2008).

[10]G. Grübel and F. Zontone, "Correlation spectroscopy with coherent X-rays", J. Alloys Compd. **362**, 3–11 (2004).

[11]X. Lu, K. G. Yager, D. Johnston, C. T. Black, and B. M. Ocko, "Grazing-incidence transmission X-ray scattering: surface scattering in the Born approximation", J. Appl. Crystallogr. **46**, 165–172 (2013).

[12]P. Wochner, C. Gutt, T. Autenrieth, T. Demmer, V. Bugaev, A. D. Ortiz, A. Duri, F. Zontone, G. Grübel, and H. Dosch, "X-ray cross correlation analysis uncovers hidden local symmetries in disordered matter", Proc. Natl. Acad. Sci. **106**, 11511–11514 (2009).

[13]M. Altarelli, R. P. Kurta, and I. A. Vartanyants, "X-ray cross-correlation analysis and local symmetries of disordered systems: general theory", Phys. Rev. B **82**, 104207 (2010).

[14]I. A. Zaluzhnyy, R. P. Kurta, A. André, O. Y. Gorobtsov, M. Rose, P. Skopintsev, I. Besedin, A. V. Zozulya, M. Sprung, F. Schreiber, et al., "Quantifying angular correlations between the atomic lattice and the superlattice of nanocrystals assembled with directional linking", Nano Lett. **17**, 3511–3517 (2017).

[15]I. A. Zaluzhnyy, R. P. Kurta, E. A. Sulyanova, O. Y. Gorobtsov, A. G. Shabalin, A. V. Zozulya, A. P. Menushenkov, M. Sprung, B. Ostrovskii, and I. A. Vartanyants, "Spatially resolved X-ray studies of liquid crystals with strongly developed bond-orientational order", Phys. Rev. E **91**, 042506 (2015).

[16]M. C. Weidman, D.-M. Smilgies, and W. A. Tisdale, "Kinetics of the self-assembly of nanocrystal superlattices measured by real-time in situ X-ray scattering", Nat. Mater. **15**, 775 (2016).

[17]H. Franz, O. Leupold, R. Röhlsberger, S. V. Roth, O. H. Seeck, J. Spengler, J. Strempfer, M. Tischer, J. Viefhaus, E. Weckert, et al., "Technical report: PETRA III: DESY's New High Brilliance Third Generation Synchrotron Radiation Source", Synchrotron Radiat. News **19**, 25–29 (2006).

[18]P. F. Tavares, S. C. Leemann, M. Sjöström, and Å. Andersson, "The MAX IV storage ring project", J. Synchrotron Radiat. **21**, 862–877 (2014).

[19]J.-L. Laclare, "ESRF X-ray synchrotron radiation source", Rev. Sci. Instrum. **60**, 1399–1402 (1989).

[20]H. Tanaka, "Current status of the spring-8 upgrade project", Synchrotron Radiat. News **27**, 23–26 (2014).

[21]D. Moncton, E. Crosbie, and G. Shenoy, "Overview of the advanced photon source", Rev. Sci. Instrum. **60**, 1403–1405 (1989).

[22]V. Ayvazyan, N. Baboi, J. Bähr, V. Balandin, B. Beutner, A. Brandt, I. Bohnet, A. Bolzmann, R. Brinkmann, O. Brovko, et al., "First operation of a free-electron laser generating GW power radiation at 32 nm wavelength", The European Physical Journal D - Atomic, Molecular, Optical and Plasma Physics **37**, 297–303 (2006).

[23]M. Altarelli, R. Brinkmann, M. Chergui, W. Decking, B. Dobson, S. Düsterer, G. Grübel, W. Graeff, H. Graafsma, J. Hajdu, et al., "The European X-ray free-electron laser", Technical Design Report, DESY **97**, 1–26 (2006).

[24]P. Emma, R. Akre, J. Arthur, R. Bionta, C. Bostedt, J. Bozek, A Brachmann, P. Bucksbaum, R. Coffee, F.-J. Decker, et al., "First lasing and operation of an ångstrom-wavelength free-electron laser", Nat. Photon. **4**, 641–647 (2010).

[25]T. Ishikawa, H. Aoyagi, T. Asaka, Y. Asano, N. Azumi, T. Bizen, H. Ego, K. Fukami, T. Fukui, Y. Furukawa, et al., "A compact X-ray free-electron laser emitting in the sub-ångström region", Nat. Photon. **6**, 540 (2012).

[26]M. M. Seibert, T. Ekeberg, F. R. Maia, M. Svenda, J. Andreasson, O. Jönsson, D. Odić, B. Iwan, A. Rocker, D. Westphal, et al., "Single mimivirus particles intercepted and imaged with an X-ray laser", Nature **470**, 78–81 (2011).

[27]M. Rose, S. Bobkov, K. Ayyer, R. P. Kurta, D. Dzhigaev, Y. Y. Kim, A. J. Morgan, C. H. Yoon, D. Westphal, J. Bielecki, et al., "Single-particle imaging without symmetry constraints at an X-ray free-electron laser", IUCrJ **5**, 727–736 (2018).

[28]E. Biasin, T. B. Van Driel, K. S. Kjær, A. O. Dohn, M. Christensen, T. Harlang, P. Chabera, Y. Liu, J. Uhlig, M. Pápai, et al., "Femtosecond X-ray scattering study of ultrafast photoinduced structural dynamics in solvated [Co (terpy) 2]2+", Phys. Rev. Lett. **117**, 013002 (2016).

[29]D. Kraus, A. Ravasio, M. Gauthier, D. Gericke, J. Vorberger, S. Frydrych, J. Helfrich, L. Fletcher, G. Schaumann, B. Nagler, et al., "Nanosecond formation of diamond and lonsdaleite by shock compression of graphite", Nat. Commun. **7**, 10970 (2016).

[30]C. A. Stan, D. Milathianaki, H. Laksmono, R. G. Sierra, T. A. McQueen, M. Messerschmidt, G. J. Williams, J. E. Koglin, T. J. Lane, M. J. Hayes, et al., "Liquid explosions induced by X-ray laser pulses", Nat. Phys. **12**, 966 (2016).

[31]E. Cunningham, E. Galtier, G. Dyer, J. Robinson, and A. Fry, "Pulse contrast enhancement via non-collinear sum-frequency generation with the signal and idler of an optical parametric amplifier", Appl. Phys. Lett. **114**, 221106 (2019).

[32]J. M. Glownia, J Cryan, J. Andreasson, A Belkacem, N Berrah, C. Blaga, C Bostedt, J Bozek, L. DiMauro, L Fang, et al., "Time-resolved pump-probe experiments at the LCLS", Opt. Express **18**, 17620–17630 (2010).

[33]J. M. Glownia, K. Gumerlock, H. T. Lemke, T. Sato, D. Zhu, and M. Chollet, "Pump–probe experimental methodology at the linac coherent light source", J. Synchrotron Radiat. **26** (2019).

[34]S. Wandel, F. Boschini, E. da Silva Neto, G. Welch, M. Seaberg, J. Koralek, G. Dakovski, W. Hettel, M. Lin, S. Moeller, et al., "Probing charge density wave dynamics in superconducting YBCO via ultrafast X-ray scattering", in CLEO: QELS Fundamental science (Optical Society of America, 2018), FM1F–7.

[35]R. Briggs, M. G. Gorman, A. L. Coleman, R. S. McWilliams, E. E. McBride, D. McGonegle, J. S. Wark, L. Peacock, S. Rothman, S. G. Macleod, et al., "Ultrafast X-ray diffraction studies of the phase transitions and equation of state of scandium shock compressed to 82 GPa", Phys. Rev. Lett. **118**, 025501 (2017).

[36]D. Kraus, J. Vorberger, A. Pak, N. Hartley, L. Fletcher, S. Frydrych, E. Galtier, E. Gamboa, D. Gericke, S. Glenzer, et al., "Formation of diamonds in laser-compressed hydrocarbons at planetary interior conditions", Nat. Astron. **1**, 606 (2017).

[37]W. C. Röntgen, "On a new kind of ray, a preliminary communication", Wurzburg Physico-Médical Society on December **28** (1895).

[38]W. Friedrich, P. Knipping, and M. Laue, "Interferenzerscheinungen bei Röntgenstrahlen", Annalen der Physik **346**, 971–988 (1913).

[39]W. H. Bragg and W. L. Bragg, "The reflection of X-rays by crystals", Proc. R. Soc. Lond. A Math. Phys. **88**, 428–438 (1913).

[40]A. Thompson, D. Attwood, E. Gullikson, M. Howells, K. J. Kim, J. Kirz, J. Kortright, I. Lindau, P. Pianetta, A. Robinson, J. Scofield, J. Underwood, D. Vaughan, and G. Williams, "X-ray data booklet (Lawrence Berkeley National Laboratory, Berkeley, CA)", (2001).

[41]J. Stöhr, "Two-photon X-ray diffraction", Phys. Rev. Lett. **118**, 024801 (2017).

[42]D. Iwanenko and I. Pomeranchuk, "On the maximal energy attainable in a betatron", Phys. Rev. **65**, 343 (1944).

[43]F. Elder, A. Gurewitsch, R. Langmuir, and H. Pollock, "Radiation from electrons in a synchrotron", Phys. Rev. **71**, 829 (1947).

[44]R. Madden and K. Codling, "New autoionizing atomic energy levels in He, Ne, and Ar", Phys. Rev. Lett. **10**, 516 (1963).

[45]K. Codling and R. Madden, "New Rydberg series in molecular oxygen near 500 Å", J. Chem. Phys. **42**, 3935–3938 (1965).

[46]E. Rowe and F. E. Mills, "Tantalus I. A dedicated storage ring synchrotron radiation source", Part. Accel. **4**, 211–227 (1973).

[47]H Kamitsubo, "Spring-8 program", J. Synchrotron Radiat. **5**, 162–167 (1998).

[48]V. Ginzburg, "On the radiation of microradiowaves and their absorbtion in the air", Isvestia Akad. Nauk SSSR (Fizika) **11**, 165 (1947).

[49]H. Motz, "Applications of the radiation from fast electron beams", J. Appl. Phys. **22**, 527–535 (1951).

[50]J. A. Clarke, *The science and technology of undulators and wigglers*, Vol. 4 (Oxford University Press, 2004).

[51]I. A. Vartanyants and O. M. Yefanov, "Coherent x-ray diffraction imaging of nanostructures. In the book *X-ray Diffraction. Modern Experimental Techniques*. Edited by O. H. Seeck and B. M. Murphy.", in (Pan Stanford Publishing, Singapore, 2015), pp. 341–384.

[52]S. Lindaas, M. Howells, C. Jacobsen, and A. Kalinovsky, "X-ray holographic microscopy by means of photoresist recording and atomic-force microscope readout", JOSA A **13**, 1788–1800 (1996).

[53]A. Rosenhahn, R. Barth, F. Staier, T. Simpson, S. Mittler, S. Eisebitt, and M. Grunze, "Digital in-line soft x-ray holography with element contrast", JOSA A **25**, 416–422 (2008).

[54]I. McNulty, J. Kirz, C. Jacobsen, E. H. Anderson, M. R. Howells, and D. P. Kern, "High-resolution imaging by fourier transform X-ray holography", Science **256**, 1009–1012 (1992).

[55]S. Eisebitt, J. Lüning, W. Schlotter, M. Lörgen, O. Hellwig, W. Eberhardt, and J. Stöhr, "Lensless imaging of magnetic nanostructures by X-ray spectro-holography", Nature **432**, 885–888 (2004).

[56]A. Singer and I. A. Vartanyants, "Coherence properties of focused X-ray beams at high-brilliance synchrotron sources", J. Synchrotron Rad. **21**, 5–15 (2014).

[57]I. A. Vartanyants and A. Singer, *Coherence properties of third-generation synchrotron sources and free-electron lasers*, 2016.

[58]C. G. Schroer, I. Agapov, W. Brefeld, R. Brinkmann, Y.-C. Chae, H.-C. Chao, M. Eriksson, J. Keil, X. Nuel Gavaldà, R. Röhlsberger, et al., "PETRA IV: the ultralow-emittance source project at DESY", J. Synchrotron Radiat. **25**, 1277–1290 (2018).

[59]K.-J. Kim, "Characteristics of synchrotron radiation", in AIP conference proceedings, Vol. 184, 1 (American Institute of Physics, 1989), pp. 565–632.

[60]T. Tanaka and H. Kitamura, "Universal function for the brilliance of undulator radiation considering the energy spread effect", J. Synchrotron Radiat. **16**, 380–386 (2009).

[61]T. E. Fornek, *Advanced photon source upgrade project preliminary design report*, tech. rep. (Argonne National Laboratory (ANL)(United States), 2017).

[62]P. Raimondi, *Hybrid multi bend achromat: from SuperB to EBS*, tech. rep. (2017).

[63]R. Khubbutdinov, A. P. Menushenkov, and I. A. Vartanyants, "Coherence properties of the high-energy fourth-generation X-ray synchrotron sources", J. Synchrotron Radiat. **26**, 1851–1862 (2019).

[64]D. Einfeld, J. Schaper, and M. Plesko, "A pure insertion device synchrotron light source utilizing the MBA-optics", Le Journal de Physique IV **4**, C9–373 (1994).

[65]J. M. Madey, "Stimulated emission of bremsstrahlung in a periodic magnetic field", J. Appl. Phys. **42**, 1906–1913 (1971).

[66]D. A. Deacon, L. Elias, J. M. Madey, G. Ramian, H. Schwettman, and T. I. Smith, "First operation of a free-electron laser", Phys. Rev. Lett. **38**, 892 (1977).

[67]A. Kondratenko and E. Saldin, "Generating of coherent radiation by a relativistic electron beam in an ondulator", Part. Accel. **10**, 207–216 (1980).

[68]R. Bonifacio, C. Pellegrini, and L. Narducci, "Collective instabilities and high-gain regime free electron laser", in AIP conference proceedings, Vol. 118, 1 (American Institute of Physics, 1984), pp. 236–259.

[69]J. Murphy and C. Pellegrini, "Generation of high-intensity coherent radiation in the soft X-ray and vacuum-ultraviolet region", JOSA B **2**, 259–264 (1985).

[70]I. A. Vartanyants, A. Singer, A. P. Mancuso, O. M. Yefanov, A Sakdinawat, Y. Liu, E Bang, G. J. Williams, G. Cadenazzi, B. Abbey, et al., "Coherence properties of individual femtosecond pulses of an X-ray free-electron laser", Phys. Rev. Lett. **107**, 144801 (2011).

[71]O. Y. Gorobtsov, N. Mukharamova, S. Lazarev, M. Chollet, D. Zhu, Y. Feng, R. P. Kurta, J.-M. Meijer, G. Williams, M. Sikorski, et al., "Diffraction based Hanbury Brown and Twiss interferometry at a hard X-ray free-electron laser", Sci. Rep **8**, 2219 (2018).

[72]R. Ganter, *SwissFEL-conceptual design report*, tech. rep. (Paul Scherrer Institute (PSI), 2010).

[73]I. S. Ko, H.-S. Kang, H. Heo, C. Kim, G. Kim, C.-K. Min, H. Yang, S. Y. Baek, H.-J. Choi, G. Mun, et al., "Construction and commissioning of PAL-XFEL facility", Appl. Sci. **7**, 479 (2017).

[74]C Pellegrini, A Marinelli, and S Reiche, "The physics of x-ray free-electron lasers", Rev. Mod. Phys. **88**, 015006 (2016).

[75]L. H. Yu, "Generation of intense uv radiation by subharmonically seeded single-pass free-electron lasers", Phys.Rev. A **44**, 5178 (1991).

[76]L.-H. Yu, M. Babzien, I. Ben-Zvi, L. DiMauro, A. Doyuran, W. Graves, E. Johnson, S. Krinsky, R. Malone, I. Pogorelsky, et al., "High-gain harmonic-generation free-electron laser", Science **289**, 932–934 (2000).

[77]E. Allaria, D. Castronovo, P. Cinquegrana, P. Craievich, M. Dal Forno, M. Danailov, G. D'Auria, A. Demidovich, G. De Ninno, S. Di Mitri, et al., "Two-stage seeded soft X-ray free-electron laser", Nat. Photon. **7**, 913 (2013).

[78]G. Stupakov, "Using the beam-echo effect for generation of short-wavelength radiation", Phys. Rev. Lett. **102**, 074801 (2009).

[79]D. Xiang and G. Stupakov, "Echo-enabled harmonic generation free electron laser", Phys. Rev. Accel. Beams **12**, 030702 (2009).

[80]J. Feldhaus, E. Saldin, J. Schneider, E. Schneidmiller, and M. Yurkov, "Possible application of X-ray optical elements for reducing the spectral bandwidth of an X-ray SASE FEL", Opt. Commun. **140**, 341–352 (1997).

[81]G. Geloni, V. Kocharyan, and E. Saldin, "A novel self-seeding scheme for hard x-ray fels", J. Mod. Opt. **58**, 1391–1403 (2011).

[82]J. Amann, W. Berg, V. Blank, F.-J. Decker, Y. Ding, P. Emma, Y. Feng, J. Frisch, D. Fritz, J. Hastings, et al., "Demonstration of self-seeding in a hard X-ray free-electron laser", Nat. Photon. **6**, 693–698 (2012).

[83]D. Ratner, R. Abela, J. Amann, C. Behrens, D. Bohler, G. Bouchard, C. Bostedt, M. Boyes, K. Chow, D. Cocco, et al., "Experimental demonstration of a soft X-ray self-seeded free-electron laser", Phys. Rev. Lett. **114**, 054801 (2015).

[84]R. Neutze, R. Wouts, D. Van der Spoel, E. Weckert, and J. Hajdu, "Potential for biomolecular imaging with femtosecond X-ray pulses", Nature **406**, 752–757 (2000).

[85]H. N. Chapman, P. Fromme, A. Barty, T. A. White, R. A. Kirian, A. Aquila, M. S. Hunter, J. Schulz, D. P. DePonte, U. Weierstall, et al., "Femtosecond X-ray protein nanocrystallography", Nature **470**, 73–77 (2011).

[86]A. V. Martin, J. Andreasson, A. Aquila, S. Bajt, T. R. Barends, M. Barthelmess, A. Barty, W. H. Benner, C. Bostedt, J. D. Bozek, et al., "Single particle imaging with soft X-rays at the Linac Coherent Light Source", in Advances in X-ray free-electron lasers: radiation schemes, X-ray optics, and instrumentation, Vol. 8078 (International Society for Optics and Photonics, 2011), p. 807809.

[87]R. P. Drake, *High-energy-density physics: fundamentals, inertial fusion, and experimental astrophysics* (Springer, Berlin, 2006).

[88]O. Ciricosta, S. Vinko, B. Barbrel, D. S. Rackstraw, T. R. Preston, T. Burian, J. Chalupskỳ, B. I. Cho, H.-K. Chung, G. L. Dakovski, et al., "Measurements of continuum lowering in solid-density plasmas created from elements and compounds", Nat. Commun. **7**, 11713 (2016).

[89]A. Schropp, R. Hoppe, V. Meier, J. Patommel, F. Seiboth, Y. Ping, D. G. Hicks, M. A. Beckwith, G. W. Collins, A. Higginbotham, et al., "Imaging shock waves in diamond with both high temporal and spatial resolution at an XFEL", Sci. Rep **5**, 11089 (2015).

[90]F. Coppari, R. Smith, J. Eggert, J. Wang, J. Rygg, A. Lazicki, J. Hawreliak, G. Collins, and T. Duffy, "Experimental evidence for a phase transition in magnesium oxide at exoplanet pressures", Nat. Geosci. **6**, 926–929 (2013).

[91]P. Vester, I. A. Zaluzhnyy, R. P. Kurta, K. B. Møller, E. Biasin, K. Haldrup, M. M. Nielsen, and I. A. Vartanyants, "Ultrafast structural dynamics of photo-reactions observed by time-resolved X-ray cross-correlation analysis", Struct. Dyn. **6**, 024301 (2019).

[92]S. Sinha, E. Sirota, S. Garoff, and H. Stanley, "X-ray and neutron scattering from rough surfaces", Phys. Rev. B **38**, 2297 (1988).

[93]C. Giacovazzo, H. L. Monaco, G. Artioli, D. Viterbo, G. Ferraris, and C Giacovazzo, *Fundamentals of crystallography*, Vol. 7 (Oxford University Press Oxford, 2002).

[94]P. Bouguer, *Essai d'optique sur la gradation de la Lumière*, 1729.

[95]J. Baruchel, J.-Y. Buffiere, and E. Maire, *X-ray tomography in material science*, Vol. 31 (Hermes Science, 2000).

[96]R. A. Quinn, C. C. Sigl, et al., *Radiography in modern industry* (Eastman Kodak, 1980).

[97]L. Landau and E. Lifchitz, *The Classical Theory of Fields* (Pergamon Press, 1971).

[98]A. H. Compton, "A quantum theory of the scattering of X-rays by light elements", Phys. Rev. **21**, 483 (1923).

[99]O. Klein and Y. Nishina, "The scattering of light by free electrons according to Dirac's new relativistic dynamics", Nature **122**, 398–399 (1928).

[100]T. Hahn, U. Shmueli, and J. W. Arthur, *International tables for crystallography*, Vol. 1 (Reidel Dordrecht, 1983).

[101]M. Eckert, "Max von Laue and the discovery of X-ray diffraction in 1912", Annalen der Physik **524**, A83–A85 (2012).

[102]C. Kittel, *Introduction to Solid State Physics* (Wiley, New York, 2005).

[103]P. Ewald, "Contributions to the theory of the interferences of X-rays in crystals", Phys. Z **14**, 465–472 (1913).

[104]P. Debye, "Interference of X-ray and thermal motion", Annalen der Physik **43**, 49–95 (1914).

[105]M. Rauscher, T. Salditt, and H. Spohn, "Small-angle X-ray scattering under grazing incidence: the cross section in the distorted-wave Born approximation", Phys. Rev. B **52**, 16855 (1995).

[106]R. Lazzari, "IsGISAXS: a program for grazing-incidence small-angle X-ray scattering analysis of supported islands", J. Appl. Crystallogr. **35**, 406–421 (2002).

[107]J. R. Levine, J. Cohen, Y. Chung, and P. Georgopoulos, "Grazing-incidence small-angle X-ray scattering: new tool for studying thin film growth", J. Appl. Crystallogr. **22**, 528–532 (1989).

[108]A. Naudon, "Grazing-incidence small-angle X-ray scattering, application to layers and surface layers", in *Modern aspects of small-angle scattering* (Springer, 1995), pp. 181–202.

[109]S. Hazra, A. Gibaud, A. Desert, C. Sella, and A Naudon, "Morphology of nanocermet thin films: X-ray scattering study", Physica B: Condensed Matter **283**, 97–102 (2000).

[110]A. Hexemer and P. Müller-Buschbaum, "Advanced grazing-incidence techniques for modern soft-matter materials analysis", IUCrJ **2**, 106–125 (2015).

[111]J. S. Pedersen, "Modelling of small-angle scattering data from colloids and polymer systems", in *Neutrons, X-rays and light* (Elsevier, 2002), pp. 391–420.

[112]S. V. Roth, M. Burghammer, C. Riekel, P. Müller-Buschbaum, A. Diethert, P. Panagiotou, and H. Walter, "Self-assembled gradient nanoparticle-polymer multilayers investigated by an advanced characterization method: microbeam grazing incidence X-ray scattering", Appl. Phys. Lett. **82**, 1935–1937 (2003).

[113]S. V. Roth, G. Herzog, V. Körstgens, A. Buffet, M. Schwartzkopf, J. Perlich, M. A. Kashem, R. Döhrmann, R. Gehrke, A. Rothkirch, et al., "In situ observation of cluster formation during nanoparticle solution casting on a colloidal film", J. Phys. Condens. Matter **23**, 254208 (2011).

[114]S. V. Roth, M. Kuhlmann, H. Walter, A. Snigirev, I. Snigireva, B. Lengeler, C. Schroer, M. Burghammer, C. Riekel, and P. Müller-Buschbaum, "Colloidal silver nanoparticle gradient layer prepared by drying between two walls of different wettability", J. Phys.: Condens. Matter **21**, 264012 (2009).

[115]G. Renaud, R. Lazzari, and F. Leroy, "Probing surface and interface morphology with grazing incidence small angle X-ray scattering", Surf. Sci. Rep. **64**, 255–380 (2009).

[116]P. Müller-Buschbaum, "Grazing incidence small-angle X-ray scattering: an advanced scattering technique for the investigation of nanostructured polymer films", Anal. Bioanal. Chem. **376**, 3–10 (2003).

[117]J. Wernecke, H. Okuda, H. Ogawa, F. Siewert, and M. Krumrey, "Depth-dependent structural changes in PS-b-P2VP thin films induced by annealing", Macromolecules **47**, 5719–5727 (2014).

[118]V. Holỳ, J. Kubena, I. Ohli, K. Lischka, W. Plotz, et al., "X-ray reflection from rough layered systems", Phys. Rev. B **47**, 15896 (1993).

[119]V. Holỳ and T. Baumbach, "Nonspecular X-ray reflection from rough multilayers", Phys. Rev. B **49**, 10668 (1994).

[120]D. Babonneau, S. Camelio, D. Lantiat, L. Simonot, and A. Michel, "Waveguiding and correlated roughness effects in layered nanocomposite thin films studied by grazing-incidence small-angle X-ray scattering", Phys. Rev. B **80**, 155446 (2009).

[121]D. Gollmer, F. Walter, C. Lorch, J. Novák, R. Banerjee, J. Dieterle, G. Santoro, F. Schreiber, D. Kern, and M. Fleischer, "Fabrication and characterization of combined metallic nanogratings and ito electrodes for organic photovoltaic cells", Microelectronic engineering **119**, 122–126 (2014).

[122]M. Soccio, D. R. Rueda, M. C. García-Gutiérrez, N. Alayo, F. Pérez-Murano, N. Lotti, A. Munari, and T. A. Ezquerra, "Morphology of poly (propylene azelate) gratings prepared by nanoimprint lithography as revealed by atomic force microscopy and grazing incidence X-ray scattering", Polymer **61**, 61–67 (2015).

[123]Y. Gu, C. Wang, and T. P. Russell, "Multi-length-scale morphologies in PCPDTBT/PCBM bulk-heterojunction solar cells", Adv. Energy Mater. **2**, 683–690 (2012).

[124]P. Müller-Buschbaum, "The active layer morphology of organic solar cells probed with grazing incidence scattering techniques", Adv. Mater. **26**, 7692–7709 (2014).

[125]L. H. Rossander, N. K. Zawacka, H. F. Dam, F. C. Krebs, and J. W. Andreasen, "In situ monitoring of structure formation in the active layer of polymer solar cells during roll-to-roll coating", AIP Advances **4**, 087105 (2014).

[126]G. Renaud, R. Lazzari, C. Revenant, A. Barbier, M. Noblet, O. Ulrich, F. Leroy, J. Jupille, Y. Borensztein, C. R. Henry, et al., "Real-time monitoring of growing nanoparticles", Science **300**, 1416–1419 (2003).

[127]M. Schwartzkopf, A. Hinz, O. Polonskyi, T. Strunskus, F. C. Loöhrer, V. Köorstgens, P. Müller-Buschbaum, F. Faupel, and S. V. Roth, "Role of sputter deposition rate in tailoring nanogranular gold structures on polymer surfaces", ACS applied materials & interfaces **9**, 5629–5637 (2017).

[128]Z. Kam, "Determination of macromolecular structure in solution by spatial correlation of scattering fluctuations", Macromolecules **10**, 927–934 (1977).

[129]Z. Kam, "The reconstruction of structure from electron micrographs of randomly oriented particles", J. Theor. Biol. **82**, 15–39 (1980).

[130]W. Griffin and P. Pusey, "Anticorrelations in light scattered by nonspherical particles", Phys. Rev. Lett. **43**, 1100 (1979).

[131]N. A. Clark, B. J. Ackerson, and A. J. Hurd, "Multidetector scattering as a probe of local structure in disordered phases", Phys. Rev. Lett. **50**, 1459 (1983).

[132]I. A. Zaluzhnyy, R. P. Kurta, M. Scheele, F. Schreiber, B. I. Ostrovskii, and I. A. Vartanyants, "Angular x-ray cross-correlation analysis (AXCCA): basic concepts and recent applications to soft matter and nanomaterials", Materials **12**, 3464 (2019).

[133]R. P. Kurta, M. Altarelli, E. Weckert, and I. A. Vartanyants, "X-ray cross-correlation analysis applied to disordered two-dimensional systems", Phys. Rev. B **85**, 184204 (2012).

[134]R. P. Kurta, M. Altarelli, and I. A. Vartanyants, "Structural analysis by x-ray intensity angular cross correlations", Adv. Chem. Phys **161**, 1–39 (2016).

[135]J. R. Fienup, "Phase retrieval algorithms: a comparison", Appl. Opt. **21**, 2758–2769 (1982).

[136]V. Elser, "Phase retrieval by iterated projections", JOSA A **20**, 40–55 (2003).

[137]S. Marchesini, "Invited article: a unified evaluation of iterative projection algorithms for phase retrieval", Rev. Sci. Instrum. **78**, 011301 (2007).

[138]J. R. Fienup, "Phase retrieval algorithms: a personal tour", Appl. Opt. **52**, 45–56 (2013).

[139]R. P. Kurta, M. Altarelli, and I. A. Vartanyants, "X-ray cross-correlation analysis of disordered ensembles of particles: potentials and limitations", Adv. Condens. Matter Phys. **2013** (2013).

[140]R. P. Kurta, R. Dronyak, M. Altarelli, E. Weckert, and I. A. Vartanyants, "Solution of the phase problem for coherent scattering from a disordered system of identical particles", New J. Phys. **15**, 013059 (2013).

[141]H. Poon and D. Saldin, "Beyond the crystallization paradigm: structure determination from diffraction patterns from ensembles of randomly oriented particles", Ultramicroscopy **111**, 798–806 (2011).

[142]R. A. Kirian, "Structure determination through correlated fluctuations in X-ray scattering", J. Phys. B At. Mol. Opt. Phys. **45**, 223001 (2012).

[143]R. A. Kirian and D. K. Saldin, "Structure determination from disordered ensembles of identical particles", Synchrotron Radiat. News **26**, 20–25 (2013).

[144]F. Lehmkühler, G. Grübel, and C. Gutt, "Detecting orientational order in model systems by X-ray cross-correlation methods", J. Appl. Crystallogr. **47**, 1315–1323 (2014).

[145]B. Pedrini, A. Menzel, M. Guizar-Sicairos, V. A. Guzenko, S. Gorelick, C. David, B. D. Patterson, and R. Abela, "Two-dimensional structure from random multiparticle X-ray scattering images using cross-correlations", Nat. Commun **4**, 1647 (2013).

[146]D. K. Saldin, H. C. Poon, M. Bogan, S. Marchesini, D. A. Shapiro, R. A. Kirian, U. Weierstall, and J. Spence, "New light on disordered ensembles: ab initio structure determination of one particle from scattering fluctuations of many copies", Phys. Rev. Lett. **106**, 115501 (2011).

[147]H.-C. Poon, P. Schwander, M. Uddin, and D. K. Saldin, "Fiber diffraction without fibers", Phys. Rev. Lett. **110**, 265505 (2013).

[148]D. Starodub, A. Aquila, S. Bajt, M. Barthelmess, A. Barty, C. Bostedt, J. D. Bozek, N. Coppola, R. B. Doak, S. W. Epp, et al., "Single-particle structure determination by correlations of snapshot X-ray diffraction patterns", Nat. Commun **3**, 1276 (2012).

[149]K. A. Seu, S. Roy, R. Su, D. Parks, E. Shipton, E. Fullerton, and S. Kevan, "Momentum transfer resolved memory in a magnetic system with perpendicular anisotropy", Appl. Phys. Lett. **98**, 122505 (2011).

[150]R. Su, K. A. Seu, D. Parks, J. J. Kan, E. E. Fullerton, S. Roy, and S. D. Kevan, "Emergent rotational symmetries in disordered magnetic domain patterns", Phys. Rev. Lett. **107**, 257204 (2011).

[151]D. Mendez, T. J. Lane, J. Sung, J. Sellberg, C. Levard, H. Watkins, A. E. Cohen, M. Soltis, S. Sutton, J. Spudich, et al., "Observation of correlated X-ray scattering at atomic resolution", Philos. Trans. R. Soc. Lond., B, Biol. Sci. **369**, 20130315 (2014).

[152]D. Mendez, H. Watkins, S. Qiao, K. S. Raines, T. J. Lane, G. Schenk, G. Nelson, G. Subramanian, K. Tono, Y. Joti, et al., "Angular correlations of photons from solution diffraction at a free-electron laser encode molecular structure", IUCrJ **3**, 420–429 (2016).

[153]A. V. Martin, "Orientational order of liquids and glasses via fluctuation diffraction", IUCrJ **4**, 24–36 (2017).

[154]M. A. Schroer, C. Gutt, F. Lehmkühler, B. Fischer, I. Steinke, F. Westermeier, M. Sprung, and G. Grübel, "Nano-beam X-ray microscopy of dried colloidal films", Soft matter **11**, 5465–5472 (2015).

[155]F. Lehmkühler, B. Fischer, L. Müller, B. Ruta, and G. Grübel, "Structure beyond pair correlations: X-ray cross-correlation from colloidal crystals", J. Appl. Crystallogr. **49**, 2046–2052 (2016).

[156]M. Schroer, F. Westermeier, F. Lehmkühler, H. Conrad, A. Schavkan, A. Zozulya, B. Fischer, W. Roseker, M. Sprung, C. Gutt, et al., "Colloidal crystallite suspensions studied by high pressure small angle X-ray scattering", J. Chem. Phys. **144**, 084903 (2016).

[157]I. Zaluzhnyy, R. Kurta, E. Sulyanova, O. Y. Gorobtsov, A. Shabalin, A. Zozulya, A. Menushenkov, M. Sprung, A. Krówczyński, E. Górecka, et al., "Structural studies of the bond-orientational order and hexatic–smectic transition in liquid crystals of various compositions", Soft Matter **13**, 3240–3252 (2017).

[158]R. P. Kurta, L. Grodd, E. Mikayelyan, O. Y. Gorobtsov, I. A. Zaluzhnyy, I. Fratoddi, I. Venditti, M. V. Russo, M. Sprung, I. A. Vartanyants, et al., "Local structure of semicrystalline P3HT films probed by nanofocused coherent X-rays", Phys. Chem. Chem. Phys. **17**, 7404–7410 (2015).

[159]C. Gutt, L. Grodd, E. Mikayelyan, U. Pietsch, R. J. Kline, and S. Grigorian, "Local orientational structure of a P3HT π–π conjugated network investigated by X-ray nanodiffraction", J. Phys. Chem. Lett. **5**, 2335–2339 (2014).

[160]R. P. Kurta, L. Grodd, E. Mikayelyan, O. Y. Gorobtsov, I. Fratoddi, I. Venditti, M. Sprung, S. Grigorian, and I. A. Vartanyants, "Structural properties of π-π conjugated network in polymer thin films studied by X-ray cross-correlation analysis", in J. Phys. Conf. Ser. Vol. 499, 1 (IOP Publishing, 2014), p. 012021.

[161]N. Mukharamova, D. Lapkin, I. A. Zaluzhnyy, A. André, S. Lazarev, Y. Y. Kim, M. Sprung, R. P. Kurta, F. Schreiber, I. A. Vartanyants, et al., "Revealing grain boundaries and defect formation in nanocrystal superlattices by nanodiffraction", Small **15**, 1904954 (2019).

[162]E. Uchaker and G. Cao, "Mesocrystals as electrode materials for lithium-ion batteries", Nano Today **9**, 499–524 (2014).

[163]S. G. Johnson and J. D. Joannopoulos, *Photonic crystals: the road from theory to practice* (Springer Science & Business Media, 2001).

[164]W. Cheng, J. Wang, U. Jonas, G. Fytas, and N. Stefanou, "Observation and tuning of hypersonic bandgaps in colloidal crystals", Nat. Mater. **5**, 830 (2006).

[165]T. Still, W. Cheng, M. Retsch, R. Sainidou, J. Wang, U. Jonas, N. Stefanou, and G. Fytas, "Simultaneous occurrence of structure-directed and particle-resonance-induced phononic gaps in colloidal films", Phys. Rev. Lett. **100**, 194301 (2008).

[166]E. L. Thomas, T. Gorishnyy, and M. Maldovan, "Phononics: colloidal crystals go hypersonic", Nat. Mater. **5**, 773–774 (2006).

[167]T. Gorishnyy, C. K. Ullal, M. Maldovan, G. Fytas, and E. L. Thomas, "Hypersonic phononic crystals", Phys. Rev. Lett. **94**, 115501 (2005).

[168]I. Lokteva, M. Koof, M. Walther, G. Grubel, and F. Lehmkuhler, "Coexistence of hcp and bct phases during in situ superlattice assembly from faceted colloidal nanocrystals", J. Phys. Chem. Lett. **10**, 6331–6338 (2019).

[169]P. Krishna, D. Pandey, and C. A. Taylor, *Close-packed structures* (University College Cardiff Press Cardiff, United Kingdom, 1981).

[170]F. Selmi, "Studies on the demulsion of silver chloride", Nuovi Ann. Sci. Nat. Di Bologna series II **4**, 146 (1845).

[171]L. Onsager, "Theories of concentrated electrolytes.", Chem. Rev. **13**, 73–89 (1933).

[172]W. G. McMillan Jr. and J. E. Mayer, "The statistical thermodynamics of multicomponent systems", J. Chem. Phys. **13**, 276–305 (1945).

[173]P. C. Hiemenz, "The role of van der Waals forces in surface and colloid chemistry", J. Chem. Educ. **49**, 164 (1972).

[174]T. Tadros, *Colloid stability: the role of surface forces - part i General principles of colloid stability and the role of surface forces* (Wiley, 2007).

[175]G. Fritz, V. Schädler, N. Willenbacher, and N. J. Wagner, "Electrosteric stabilization of colloidal dispersions", Langmuir **18**, 6381–6390 (2002).

[176]J. G. Kirkwood, "Molecular distribution in liquids", J. Chem. Phys. **7**, 919–925 (1939).

[177]J. G. Kirkwood and E. Monroe, "Statistical mechanics of fusion", J. Chem. Phys. **9**, 514–526 (1941).

[178]T. Alfrey, E. Bradford, J. Vanderhoff, and G. Oster, "Optical properties of uniform particle-size latexes", JOSA **44**, 603–609 (1954).

[179]J. B. Jones, J. V. Sanders, and E. R. Segnit, "Structure of opal", Nature **204**, 990–991 (1964).

[180]P. J. Darragh, A. J. Gaskin, and J. V. Sanders, "Opals", Scientific American **234**, 84–95 (1976).

[181]P. Jiang, J. F. Bertone, K. S. Hwang, and V. L. Colvin, "Single-crystal colloidal multilayers of controlled thickness", Chem. Mater. **11**, 2132–2140 (1999).

[182]L. Rayleigh, "XXVI. on the remarkable phenomenon of crystalline reflexion described by prof. stokes", London Edinburgh and Dublin Philos. Mag. J. Sci. **26**, 256–265 (1888).

[183]E. Yablonovitch, "Inhibited spontaneous emission in solid-state physics and electronics", Phys. Rev. Lett. **58**, 2059 (1987).

[184]S. John, "Strong localization of photons in certain disordered dielectric superlattices", Phys. Rev. Lett. **58**, 2486 (1987).

[185]N. D. Denkov, O. D. Velev, P. A. Kralchevsky, I. B. Ivanov, H. Yoshimura, and K. Nagayama, "Two-dimensional crystallization", Nature **361**, 26 (1993).

[186]A. Blanco, E. Chomski, S. Grabtchak, M. Ibisate, S. John, S. W. Leonard, C. Lopez, F. Meseguer, H. Miguez, J. P. Mondia, et al., "Large-scale synthesis of a silicon photonic crystal with a complete three-dimensional bandgap near 1.5 micrometres", Nature **405**, 437 (2000).

[187]Y. A. Vlasov, X.-Z. Bo, J. C. Sturm, and D. J. Norris, "On-chip natural assembly of silicon photonic bandgap crystals", Nature **414**, 289 (2001).

[188]A. Singer, L. Boucheron, S. H. Dietze, K. E. Jensen, D. Vine, I. McNulty, E. R. Dufresne, R. O. Prum, S. G. Mochrie, and O. G. Shpyrko, "Domain morphology, boundaries, and topological defects in biophotonic gyroid nanostructures of butterfly wing scales", Sci. Adv. **2**, e1600149 (2016).

[189]H. S. Lee, T. S. Shim, H. Hwang, S.-M. Yang, and S.-H. Kim, "Colloidal photonic crystals toward structural color palettes for security materials", Chem. Mater. **25**, 2684–2690 (2013).

[190]J. B. Kim, S. Y. Lee, J. M. Lee, and S.-H. Kim, "Designing structural-color patterns composed of colloidal arrays", ACS Appl. Mater. Interfaces **11**, 14485–14509 (2019).

[191]V. A. Vasantha, W. Rusli, C. Junhui, Z. Wenguang, K. V. Sreekanth, R. Singh, and A. Parthiban, "Highly monodisperse zwitterion functionalized non-spherical polymer particles with tunable iridescence", RSC Advances **9**, 27199–27207 (2019).

[192]M. Soljačić, C. Luo, J. D. Joannopoulos, and S. Fan, "Nonlinear photonic crystal microdevices for optical integration", Opt. Lett. **28**, 637–639 (2003).

[193]D.-K. Hwang, B. Lee, and D.-H. Kim, "Efficiency enhancement in solid dye-sensitized solar cell by three-dimensional photonic crystal", RSC Advances **3**, 3017–3023 (2013).

[194]J.-M. Meijer, *Colloidal crystals of spheres and cubes in real and reciprocal space* (Springer, 2015).

[195]J. Zhang, Z. Sun, and B. Yang, "Self-assembly of photonic crystals from polymer colloids", Curr. Opin. Colloid Interface Sci. **14**, 103–114 (2009).

[196]Z. Zhou and X. S. Zhao, "Opal and inverse opal fabricated with a flow-controlled vertical deposition method", Langmuir **21**, 4717–4723 (2005).

[197]L. V. Woodcock, "Entropy difference between the face-centred cubic and hexagonal close-packed crystal structures", Nature **385**, 141 (1997).

[198]P. G. Bolhuis, D. Frenkel, S.-C. Mau, and D. A. Huse, "Entropy difference between crystal phases", Nature **388**, 235 (1997).

[199]A. Petukhov, I. Dolbnya, D. Aarts, G. Vroege, and H. Lekkerkerker, "Bragg rods and multiple X-ray scattering in random-stacking colloidal crystals", Phys. Rev. Lett. **90**, 028304 (2003).

[200]I. P. Dolbnya, A. V. Petukhov, D. Aarts, G. Vroege, and H. Lekkerkerker, "Coexistence of rhcp and fcc phases in hard-sphere colloidal crystals", EPL **72**, 962 (2005).

[201]H. Cölfen and M. Antonietti, "Mesocrystals: inorganic superstructures made by highly parallel crystallization and controlled alignment", Angew. Chem. Int. Ed. **44**, 5576–5591 (2005).

[202]J. Cañaveras, S. Sánchez-Moral, J. Calvo, M. Hoyos, and S. Ordóñez, "Dedolomites associated with karstification. an example of early dedolomitization in lacustrine sequences from the tertiary madrid basin, central spain", Carbonates Evaporites **11**, 85–103 (1996).

[203]W. Depmeier, "Mesocrystallography", Ann. Chim. Sci. Mat. **23**, 43–48 (1998).

[204]K. Bian, J. J. Choi, A. Kaushik, P. Clancy, D.-M. Smilgies, and T. Hanrath, "Shape-anisotropy driven symmetry transformations in nanocrystal superlattice polymorphs", ACS Nano **5**, 2815–2823 (2011).

[205]J. J. Choi, C. R. Bealing, K. Bian, K. J. Hughes, W. Zhang, D.-M. Smilgies, R. G. Hennig, J. R. Engstrom, and T. Hanrath, "Controlling nanocrystal superlattice symmetry and shape-anisotropic interactions through variable ligand surface coverage", J. Am. Chem. Soc. **133**, 3131–3138 (2011).

[206]B. W. Goodfellow, Y. Yu, C. A. Bosoy, D.-M. Smilgies, and B. A. Korgel, "The role of ligand packing frustration in body-centered cubic (bcc) superlattices of colloidal nanocrystals", J. Phys. Chem. Lett. **6**, 2406–2412 (2015).

[207]R. Li, K. Bian, T. Hanrath, W. A. Bassett, and Z. Wang, "Decoding the superlattice and interface structure of truncate PbS nanocrystal-assembled supercrystal and associated interaction forces", J. Am. Chem. Soc. **136**, 12047–12055 (2014).

[208]J. J. Choi, K. Bian, W. J. Baumgardner, D.-M. Smilgies, and T. Hanrath, "Interface-induced nucleation, orientational alignment and symmetry transformations in nanocube superlattices", Nano Lett. **12**, 4791–4798 (2012).

[209]A. D. McFarland, M. A. Young, J. A. Dieringer, and R. P. Van Duyne, "Wavelength-scanned surface-enhanced Raman excitation spectroscopy", J. Phys. Chem. B **109**, 11279–11285 (2005).

[210]L. Bahrig, S. G. Hickey, and A. Eychmüller, "Mesocrystalline materials and the involvement of oriented attachment – a review", CrystEngComm **16**, 9408–9424 (2014).

[211]M. I. Bodnarchuk, E. V. Shevchenko, and D. V. Talapin, "Structural defects in periodic and quasicrystalline binary nanocrystal superlattices", J. Am. Chem. Soc. **133**, 20837–20849 (2011).

[212]C. Wang, C. Siu, J. Zhang, and J. Fang, "Understanding the forces acting in self-assembly and the implications for constructing three-dimensional (3D) supercrystals", Nano Res. **8**, 2445–2466 (2015).

[213]R.-Q. Song and H. Cölfen, "Mesocrystal - ordered nanoparticle superstructures", Adv. Mater. **22**, 1301–1330 (2010).

[214]E. V. Sturm and H. Cölfen, "Mesocrystals: Past, presence, future", Crystals **7** (2017).

[215]J. Seto, Y. Ma, S. A. Davis, F. Meldrum, A. Gourrier, Y.-Y. Kim, U. Schilde, M. Sztucki, M. Burghammer, S. Maltsev, et al., "Structure-property relationships of a biological mesocrystal in the adult sea urchin spine", Proc. Natl. Acad. Sci. **109**, 3699–3704 (2012).

[216]X. Li, Z.-H. Xu, and R. Wang, "In situ observation of nanograin rotation and deformation in nacre", Nano Lett. **6**, 2301–2304 (2006).

[217]J. Perrin, D. Vielzeuf, A. Ricolleau, H. Dallaporta, S. Valton, and N. Floquet, "Block-by-block and layer-by-layer growth modes in coral skeletons", Am. Mineral. **100**, 681–695 (2015).

[218]D. Vielzeuf, N. Floquet, D. Chatain, F. Bonneté, D. Ferry, J. Garrabou, and E. M. Stolper, "Multilevel modular mesocrystalline organization in red coral", Am. Mineral. **95**, 242–248 (2010).

[219]D. Vielzeuf, J. Garrabou, A. Baronnet, O. Grauby, and C. Marschal, "Nano to macroscale biomineral architecture of red coral (corallium rubrum)", Am. Mineral. **93**, 1799–1815 (2008).

[220]N. Floquet and D. Vielzeuf, "Ordered misorientations and preferential directions of growth in mesocrystalline red coral sclerites", Cryst. Growth Des. **12**, 4805–4820 (2012).

[221]Y. Oaki, A. Kotachi, T. Miura, and H. Imai, "Bridged nanocrystals in biominerals and their biomimetics: classical yet modern crystal growth on the nanoscale", Adv. Funct. Mater. **16**, 1633–1639 (2006).

[222]E. Shevchenko, D. Talapin, A. Kornowski, F. Wiekhorst, J. Kötzler, M. Haase, A. Rogach, and H. Weller, "Colloidal crystals of monodisperse fept nanoparticles grown by a three-layer technique of controlled oversaturation", Adv. Mater. **14**, 287–290 (2002).

[223]M. Nagel, S. G. Hickey, A. Frömsdorf, A. Kornowski, and H. Weller, "Synthesis of monodisperse PbS nanoparticles and their assembly into highly ordered 3D colloidal crystals", Z. Phys. Chem. **221**, 427–437 (2007).

[224]L. Meng, W. Chen, Y. Tan, L. Zou, C. Chen, H. Zhou, Q. Peng, and Y. Li, "Fe3O4 octahedral colloidal crystals", Nano Res. **4**, 370–375 (2011).

[225]S. M. Rupich, E. V. Shevchenko, M. I. Bodnarchuk, B. Lee, and D. V. Talapin, "Size-dependent multiple twinning in nanocrystal superlattices", J. Am. Chem. Soc. **132**, 289–296 (2009).

[226]P. Podsiadlo, G. Krylova, B. Lee, K. Critchley, D. J. Gosztola, D. V. Talapin, P. D. Ashby, and E. V. Shevchenko, "The role of order, nanocrystal size, and capping ligands in the collective mechanical response of three-dimensional nanocrystal solids", J. Am. Chem. Soc. **132**, 8953–8960 (2010).

[227]Y. Wang, Q. Dai, B. Zou, W. W. Yu, B. Liu, and G. Zou, "Facile assembly of size-and shape-tunable IV – VI nanocrystals into superlattices", Langmuir **26**, 19129–19135 (2010).

[228]N. Goubet and M. Pileni, "Analogy between atoms in a nanocrystal and nanocrystals in a supracrystal: Is it real or just a highly probable speculation?", J. Phys. Chem. Lett. **2**, 1024–1031 (2011).

[229]M. C. Weidman, M. E. Beck, R. S. Hoffman, F. Prins, and W. A. Tisdale, "Monodisperse, air-stable PbS nanocrystals via precursor stoichiometry control", ACS Nano **8**, 6363–6371 (2014).

[230]I. Moreels, K. Lambert, D. Smeets, D. De Muynck, T. Nollet, J. C. Martins, F. Vanhaecke, A. Vantomme, C. Delerue, G. Allan, et al., "Size-dependent optical properties of colloidal PbS quantum dots", ACS Nano **3**, 3023–3030 (2009).

[231]S. Kalbfleisch, H. Neubauer, S. P. Krüger, M. Bartels, M. Osterhoff, D. D. Mai, K. Giewekemeyer, B. Hartmann, M. Sprung, and T. Salditt, "The Göttingen holography endstation of beamline P10 at PETRA III/DESY", in AIP conference proceedings, Vol. 1365, 1 (American Institute of Physics, 2011), pp. 96–99.

[232]M. P. Boneschanscher, W. H. Evers, J. J. Geuchies, T. Altantzis, B. Goris, F. T. Rabouw, S. Van Rossum, H. S. van der Zant, L. D. Siebbeles, G. Van Tendeloo, et al., "Long-range orientation and atomic attachment of nanocrystals in 2D honeycomb superlattices", Science **344**, 1377–1380 (2014).

[233]D. Zherebetskyy, M. Scheele, Y. Zhang, N. Bronstein, C. Thompson, D. Britt, M. Salmeron, P. Alivisatos, and L.-W. Wang, "Hydroxylation of the surface of PbS nanocrystals passivated with oleic acid", Science **344**, 1380–1384 (2014).

[234]P. Simon, L. Bahrig, I. A. Baburin, P. Formanek, F. Röder, J. Sickmann, S. G. Hickey, A. Eychmüller, H. Lichte, R. Kniep, et al., "Interconnection of nanoparticles within 2D superlattices of PbS/oleic acid thin films", Adv. Mater. **26**, 3042–3049 (2014).

[235]M. Stimulak and M. Ravnik, "Tunable photonic crystals with partial bandgaps from blue phase colloidal crystals and dielectric-doped blue phases", Soft Matter **10**, 6339–6346 (2014).

[236]P. F. Damasceno, M. Engel, and S. C. Glotzer, "Crystalline assemblies and densest packings of a family of truncated tetrahedra and the role of directional entropic forces", ACS Nano **6**, 609–614 (2012).

[237]P. F. Damasceno, M. Engel, and S. C. Glotzer, "Predictive self-assembly of polyhedra into complex structures", Science **337**, 453–457 (2012).

[238]A. V. Petukhov, J.-M. Meijer, and G. J. Vroege, "Particle shape effects in colloidal crystals and colloidal liquid crystals: small-angle x-ray scattering studies with microradian resolution", Curr. Opin. Colloid Interface Sci. **20**, 272–281 (2015).

[239]A. V. Petukhov, R. Tuinier, and G. J. Vroege, "Entropic patchiness: effects of colloid shape and depletion", Curr. Opin. Colloid Interface Sci. **30**, 54–61 (2017).

[240]M. N. O'Brien, H.-X. Lin, M. Girard, M. Olvera de la Cruz, and C. A. Mirkin, "Programming colloidal crystal habit with anisotropic nanoparticle building blocks and dna bonds", J. Am. Chem. Soc. **138**, 14562–14565 (2016).

[241]U. Agarwal and F. A. Escobedo, "Mesophase behaviour of polyhedral particles", Nat. Mater. **10**, 230–235 (2011).

[242]J.-M. Meijer, A. Pal, S. Ouhajji, H. N. Lekkerkerker, A. P. Philipse, and A. V. Petukhov, "Observation of solid–solid transitions in 3D crystals of colloidal superballs", Nat. Commun. **8**, 1–8 (2017).

[243]J. Gong, R. S. Newman, M. Engel, M. Zhao, F. Bian, S. C. Glotzer, and Z. Tang, "Shape-dependent ordering of gold nanocrystals into large-scale superlattices", Nat. Commun. **8**, 1–9 (2017).

[244]B. Gates, S. H. Park, and Y. Xia, "Tuning the photonic bandgap properties of crystalline arrays of polystyrene beads by annealing at elevated temperatures", Adv. Mater. **12**, 653–656 (2000).

[245]H. R. Vutukuri, A. Imhof, and A. Van Blaaderen, "Fabrication of polyhedral particles from spherical colloids and their self-assembly into rotator phases", Angew. Chem., Int. Ed. **53**, 13830–13834 (2014).

[246]A. Zozulya, J.-M. Meijer, A. Shabalin, A. Ricci, F. Westermeier, R. Kurta, U. Lorenz, A. Singer, O. Yefanov, A. Petukhov, et al., "In situ X-ray crystallographic study of the structural evolution of colloidal crystals upon heating", J. Appl. Crystallogr. **46**, 903–907 (2013).

[247]J.-M. Meijer, F. Hagemans, L. Rossi, D. V. Byelov, S. I. Castillo, A. Snigirev, I. Snigireva, A. P. Philipse, and A. V. Petukhov, "Self-assembly of colloidal cubes via vertical deposition", Langmuir **28**, 7631–7638 (2012).

[248]N. Mahadevapuram, J. Strzalka, and G. E. Stein, "Grazing-incidence transmission small angle X-ray scattering from thin films of block copolymers", J. Polym. Sci. B Polym. Phys. **51**, 602–610 (2013).

[249]Y. Yoneda, "Anomalous surface reflection of X-rays", Phys. Rev. **131**, 2010 (1963).

[250]B. Lee, I. Park, J. Yoon, S. Park, J. Kim, K.-W. Kim, T. Chang, and M. Ree, "Structural analysis of block copolymer thin films with grazing incidence small-angle X-ray scattering", Macromolecules **38**, 4311–4323 (2005).

[251]M. P. Tate, V. N. Urade, J. D. Kowalski, T.-C. Wei, B. D. Hamilton, B. W. Eggiman, and H. W. Hillhouse, "Simulation and interpretation of 2D diffraction patterns from self-assembled nanostructured films at arbitrary angles of incidence: from grazing incidence (above the critical angle) to transmission perpendicular to the substrate", J. Phys. Chem. B **110**, 9882–9892 (2006).

[252]J.-M. Meijer, A. Shabalin, R. Dronyak, O. Yefanov, A. Singer, R. Kurta, U. Lorenz, O. Gorobstov, D. Dzhigaev, J. Gulden, et al., "Double hexagonal close-packed structure revealed in a single colloidal crystal grain by Bragg rod analysis", J. Appl. Crystallogr. **47**, 1199–1204 (2014).

[253]G. Beaucage, R. Composto, and R. Stein, "Ellipsometric study of the glass transition and thermal expansion coefficients of thin polymer films", J. Polym. Sci. B Polym. Phys. **31**, 319–326 (1993).

[254]J. L. Keddie, R. A. Jones, and R. A. Cory, "Size-dependent depression of the glass transition temperature in polymer films", EPL **27**, 59 (1994).

[255]E. A. Sulyanova, A. Shabalin, A. V. Zozulya, J.-M. Meijer, D. Dzhigaev, O. Gorobtsov, R. P. Kurta, S. Lazarev, U. Lorenz, A. Singer, et al., "Structural evolution of colloidal crystal films in the process of melting revealed by Bragg peak analysis", Langmuir **31**, 5274–5283 (2015).

[256]G. K. Williamson and W. H. Hall, "X-ray line broadening from filed aluminium and wolfram", Acta Metall. **1**, 22–31 (1953).

[257]A. Senesi and B. Lee, "Scattering functions of polyhedra", J. Appl. Crystallogr. **48**, 565–577 (2015).

[258]N. Mukharamova, S. Lazarev, J.-M. Meijer, M. Chollet, A. Singer, R. P. Kurta, D. Dzhigaev, O. Y. Gorobtsov, G. Williams, D. Zhu, et al., "Probing dynamics in colloidal crystals with pump-probe experiments at LCLS: methodology and analysis", Appl. Sci. **7**, 519 (2017).

[259]M. Hase, K. Mizoguchi, H. Harima, S. Nakashima, M. Tani, K. Sakai, and M. Hangyo, "Optical control of coherent optical phonons in bismuth films", Appl. Phys. Lett. **69**, 2474–2476 (1996).

[260]D. Boschetto, E. G. Gamaly, A. V. Rode, B. Luther-Davies, D. Glijer, T. Garl, O. Albert, A. Rousse, and J. Etchepare, "Small atomic displacements recorded in bismuth by the optical reflectivity of femtosecond laser-pulse excitations", Phys. Rev. Lett. **100**, 027404 (2008).

[261]M. Hase, M. Kitajima, S.-I. Nakashima, and K. Mizoguchi, "Forcibly driven coherent soft phonons in GeTe with intense THz-rate pump fields", Appl. Phys. Lett. **83**, 4921–4923 (2003).

[262]M. A. van Dijk, M. Lippitz, and M. Orrit, "Detection of acoustic oscillations of single gold nanospheres by time-resolved interferometry", Phys. Rev. Lett. **95**, 267406 (2005).

[263]A. V. Akimov, Y. Tanaka, A. B. Pevtsov, S. F. Kaplan, V. G. Golubev, S. Tamura, D. R. Yakovlev, and M. Bayer, "Hypersonic modulation of light in three-dimensional photonic and phononic band-gap materials", Phys. Rev. Lett. **101**, 033902 (2008).

[264]K. Sokolowski-Tinten, C. Blome, J. Blums, A. Cavalleri, C. Dietrich, A. Tarasevitch, I. Uschmann, E. Förster, M. Kammler, M. Horn-von Hoegen, et al., "Femtosecond X-ray measurement of coherent lattice vibrations near the Lindemann stability limit", Nature **422**, 287–289 (2003).

[265]S. L. Johnson, P. Beaud, C. J. Milne, F. S. Krasniqi, E. S. Zijlstra, M. E. Garcia, M. Kaiser, D. Grolimund, R. Abela, and G. Ingold, "Nanoscale depth-resolved coherent femtosecond motion in laser-excited bismuth", Phys. Rev. Lett. **100**, 155501 (2008).

[266]D. M. Fritz, D. A. Reis, B. Adams, R. A. Akre, J. Arthur, C. Blome, P. H. Bucksbaum, A. L. Cavalieri, S. Engemann, S. Fahy, et al., "Ultrafast bond softening in bismuth: mapping a solid's interatomic potential with x-rays", Science **315**, 633–636 (2007).

[267]C.-Y. Ruan, Y. Murooka, R. K. Raman, and R. A. Murdick, "Dynamics of size-selected gold nanoparticles studied by ultrafast electron nanocrystallography", Nano Lett. **7**, 1290–1296 (2007).

[268]A. Plech, V. Kotaidis, S. Grésillon, C. Dahmen, and G. Von Plessen, "Laser-induced heating and melting of gold nanoparticles studied by time-resolved X-ray scattering", Phys. Rev. B **70**, 195423 (2004).

[269]J. N. Clark, L. Beitra, G. Xiong, A. Higginbotham, D. M. Fritz, H. T. Lemke, D. Zhu, M. Chollet, G. J. Williams, M. Messerschmidt, et al., "Ultrafast three-dimensional imaging of lattice dynamics in individual gold nanocrystals", Science **341**, 56–59 (2013).

[270]E. Duval, A. Boukenter, and B. Champagnon, "Vibration eigenmodes and size of microcrystallites in glass: observation by very-low-frequency Raman scattering", Phys. Rev. Lett. **56**, 2052 (1986).

[271]H. Lamb, "On the vibrations of an elastic sphere", Proc. London Math. Soc. **1**, 189–212 (1881).

[272]R. Dronyak, J. Gulden, O. Yefanov, A. Singer, T. Gorniak, T. Senkbeil, J.-M. Meijer, A. Al-Shemmary, J. Hallmann, D. Mai, et al., "Dynamics of colloidal crystals studied by pump-probe experiments at FLASH", Phys. Rev. B **86**, 064303 (2012).

[273]M. Chollet, R. Alonso-Mori, M. Cammarata, D. Damiani, J. Defever, J. T. Delor, Y. Feng, J. M. Glownia, J. B. Langton, S. Nelson, et al., "The X-ray pump–probe instrument at the linac coherent light source", J. Synchrotron Radiat. **22**, 503–507 (2015).

[274]P. Hart, S. Boutet, G. Carini, M. Dubrovin, B. Duda, D., G. Haller, R. Herbst, S. Herrmann, C. Kenney, et al., "The CSPAD megapixel X-ray camera at LCLS", in Proc. SPIE, Vol. 8504 (2012), p. 85040C.

[275]M. Hazewinkel, *Encyclopedia of mathematics: an updated and annotated translation of the soviet mathematical encyclopaedia*, Vol. 2 (Springer Science & Business Media, 2013).

[276]L. Saviot, D. B. Murray, and M. D.C. M. De Lucas, "Vibrations of free and embedded anisotropic elastic spheres: application to low-frequency Raman scattering of silicon nanoparticles in silica", Phys. Rev. B **69**, 113402 (2004).

[277]J. E. Mark, *Polymer data handbook* (Oxford University Press, 2009).

[278]M. Koenig, A. Benuzzi-Mounaix, A. Ravasio, T. Vinci, N. Ozaki, S. Lepape, D. Batani, G. Huser, T. Hall, D. Hicks, et al., "Progress in the study of warm dense matter", Plasma Phys. Controlled Fusion **47**, B441 (2005).

[279]M. Ross, "The ice layer in Uranus and Neptune diamonds in the sky?", Nature **292**, 435–436 (1981).

[280]L. R. Benedetti, J. H. Nguyen, W. A. Caldwell, H. Liu, M. Kruger, and R. Jeanloz, "Dissociation of CH4 at high pressures and temperatures: diamond formation in giant planet interiors?", Science **286**, 100–102 (1999).

[281]L. Fletcher, H. Lee, T. Döppner, E. Galtier, B. Nagler, P. Heimann, C. Fortmann, S. Lepape, T. Ma, M. Millot, et al., "Ultrabright X-ray laser scattering for dynamic warm dense matter physics", Nat. Photon. **9**, 274 (2015).

[282]R. Kraus, J.-P. Davis, C. Seagle, D. Fratanduono, D. Swift, J. Brown, and J. Eggert, "Dynamic compression of copper to over 450 GPa: a high-pressure standard", Phys. Rev. B **93**, 134105 (2016).

[283]N. Mukharamova, S. Lazarev, J.-M. Meijer, O. Y. Gorobtsov, A. Singer, M. Chollet, M. Bussmann, D. Dzhigaev, Y. Feng, M. Garten, et al., "Femtosecond laser produced periodic plasma in a colloidal crystal probed by XFEL radiation", Sci. Rep. **10**, 1–11 (2020).

[284]G. Lehmann and K. Spatschek, "Laser-driven plasma photonic crystals for high-power lasers", Phys. Plasmas **24**, 056701 (2017).

[285]D. R. Hartree, "The wave mechanics of an atom with a non-Coulomb central field. Part I. Theory and methods", in Math. Proc. Camb. Philos. Soc. Vol. 24, 1 (Cambridge University Press, 1928), pp. 89–110.

[286]L. V. Keldysh, "Ionization in the field of a strong electromagnetic wave", Sov. Phys. JETP **20**, 1307–1314 (1965).

[287]V. P. Krainov and M. B. Smirnov, "Cluster beams in the super-intense femtosecond laser pulse", Phys. Rep. **370**, 237–331 (2002).

[288]D. Bauer and P. Mulser, "Exact field ionization rates in the barrier-suppression regime from numerical time-dependent Schrödinger-equation calculations", Phys. Rev. A **59**, 569 (1999).

[289]N. B. Delone and V. P. Krainov, "Tunneling and barrier-suppression ionization of atoms and ions in a laser radiation field", Physics-Uspekhi **41**, 469–485 (1998).

[290]H. R. Reiss, "Effect of an intense electromagnetic field on a weakly bound system", Phys. Rev. A **22**, 1786 (1980).

[291]F. H. Faisal, "Multiple absorption of laser photons by atoms", J. Phys. B At. Mol. Opt. Phys. **6**, L89 (1973).

[292]L. D. Landau and E. M. Lifshitz, *Quantum mechanics: non-relativistic theory*, Vol. 3 (Elsevier, 2013).

[293]V. P. Krainov, "Ionization rates and energy and angular distributions at the barrier-suppression ionization of complex atoms and atomic ions", JOSA B **14**, 425–431 (1997).

[294]R. More, "Pressure ionization, resonances, and the continuity of bound and free states", Adv. Atom Mol. Opt. Phys. **21**, 305–356 (1985).

[295]V. Krainov, "Absorption of electromagnetic energy by slow electrons under scattering from Coulomb centers", Sov. Phys. JETP **92**, 960–968 (2001).

[296]L. Spitzer, *Physics of fully ionized gases* (Courier Corporation, 2006).

[297]V. Silin, "Nonlinear high-frequency plasma conductivity", Sov. Phys. JETP **20**, 1510–1516 (1965).

[298]P. Gibbon and E. Förster, "Short-pulse laser-plasma interactions", Plasma Phys. Controlled Fusion **38**, 769 (1996).

[299]M. Kaganov, E. Lifshitz, and L. Tanatarov, "Relaxation between electrons and the crystalline lattice", Sov. Phys. JETP **4**, 173–178 (1957).

[300]S. Anisimov, B. Kapeliovich, T. Perelman, et al., "Electron emission from metal surfaces exposed to ultrashort laser pulses", Sov. Phys. JETP **66**, 375–377 (1974).

[301]E. G. Gamaly and A. V. Rode, "Physics of ultra-short laser interaction with matter: from phonon excitation to ultimate transformations", Prog. Quantum Electron. **37**, 215–323 (2013).

[302]I. Robinson, J. Clark, and R. Harder, "Materials science in the time domain using Bragg coherent diffraction imaging", J. Opt. **18**, 054007 (2016).

[303]E. G. Gamaly, A. V. Rode, B. Luther-Davies, and V. T. Tikhonchuk, "Ablation of solids by femtosecond lasers: ablation mechanism and ablation thresholds for metals and dielectrics", Phys. Plasmas **9**, 949–957 (2002).

[304]W. J. M. Rankine, "XV. on the thermodynamic theory of waves of finite longitudinal disturbance", Philos. Trans. R. Soc. Lond., 277–288 (1870).

[305]H. Hugoniot, "Memoir on the propagation of movements in bodies, especially perfect gases (first part)", J. de l'Ecole Polytechnique **57**, 3–97 (1887).

[306]L. Landau and E. Lifchitz, *Fluid Mechanics*, Vol. 6 (1959).

[307]I. B. Zeldovich and I. P. Raĭzer, *Physics of shock waves and high-temperature hydrodynamic phenomena*, Vol. 2 (Academic Press, 1968).

[308]H. Reiss, "The tunnelling model of laser-induced ionization and its failure at low frequencies", J. Phys. B At. Mol. Opt. Phys. **47**, 204006 (2014).

[309]H. Reiss, "Limits on tunneling theories of strong-field ionization", Phys. Rev. Lett. **101**, 043002 (2008).

[310]L. Pitaevskii and E. Lifshitz, *Physical Kinetics*, Vol. 10 (Butterworth-Heinemann, 2012).

[311]H. Burau, R. Widera, W. Honig, G. Juckeland, A. Debus, T. Kluge, U. Schramm, T. E. Cowan, R. Sauerbrey, and M. Bussmann, "PIConGPU: a fully relativistic particle-in-cell code for a GPU cluster", IEEE Trans. Plasma. Sci. **38**, 2831–2839 (2010).

[312]M. Bussmann, H. Burau, T. E. Cowan, A. Debus, A. Huebl, G. Juckeland, T. Kluge, W. E. Nagel, R. Pausch, F. Schmitt, U. Schramm, J. Schuchart, and R. Widera, "Radiative signatures of the relativistic Kelvin-Helmholtz instability", in Sc '13 (2013), 5:1–5:12.

[313]J. J. MacFarlane, I. E. Golovkin, and P. R. Woodruff, "HELIOS-CR–a 1-D radiation – magnetohydrodynamics code with inline atomic kinetics modeling", J. Quant. Spectrosc. Radiat. Transf. **99**, 381–397 (2006).

[314]D. Kraus, N. J. Hartley, S. Frydrych, A. K. Schuster, K. Rohatsch, M. Rödel, T. E. Cowan, S. Brown, E. Cunningham, T. van Driel, et al., "High-pressure chemistry of hydrocarbons relevant to planetary interiors and inertial confinement fusion", Phys. Plasmas **25**, 056313 (2018).

[315]R. Suriano, A. Kuznetsov, S. M. Eaton, R. Kiyan, G. Cerullo, R. Osellame, B. N. Chichkov, M. Levi, and S. Turri, "Femtosecond laser ablation of polymeric substrates for the fabrication of microfluidic channels", Appl. Surf. Sci. **257**, 6243–6250 (2011).

[316]S. P. Marsh, *LASL shock Hugoniot data*, Vol. 5 (Univ of California Press, 1980).

[317]G. Tas and H. J. Maris, "Electron diffusion in metals studied by picosecond ultrasonics", Phys. Rev. B **49**, 15046 (1994).

[318]R. Courant, K. Friedrichs, and H. Lewy, "On the partial difference equations of mathematical physics", Math. Ann. **100**, 32–74 (1928).

[319]K. Yee, "Numerical solution of initial boundary value problems involving maxwell's equations in isotropic media", IEEE Trans. Antennas Propag. **14**, 302–307 (1966).

[320]A. Huebl, R. Lehe, J.-L. Vay, D. P. Grote, I. Sbalzarini, S. Kuschel, and M. Bussmann, *openPMD 1.0.0: A meta data standard for particle and mesh based data.* Version 1.0.0, Nov. 2015.

Appendix A

PIConGPU simulations

PIConGPU is a relativistic Particle-in-Cell (PIC) code running on graphic processing units (GPUs) developed in Helmholtz-Zentrum Dresden-Rossendorf [311]. This code uses the Particle-in-Cell algorithm, which calculates plasma dynamics by computing the motion of electrons and ions in the plasma based on Maxwell - Vlasov equations. Electrons and ions are modeled by macro-particles carrying both charge q and mass m. This macro particles consist of up to several hundred particles. The simulated volume is divided into cells, and electric and magnetic fields are interpolated on this grid.

The PIC algorithm consists of the following four steps, calculated at each time step in each cell on the mesh

1. The Lorentz force $F_{Lorentz}$ is calculated from the given distribution of the electric field **E** and magnetic field **B**

$$\mathbf{F}_{\text{Lorentz}} = q(\mathbf{E} + \mathbf{v} \times \mathbf{B})\,. \tag{A.1}$$

2. The velocity **v** and the position **r** of the particle is calculated from the equation of motion

$$m\ddot{\mathbf{r}} = \mathbf{F}_{\text{Lorentz}}\,. \tag{A.2}$$

   This step is usually called the particle pusher.

3. The current **J** is calculated from the new positions and velocity of particles.

$$\mathbf{J} = qN\mathbf{v}\,, \tag{A.3}$$

   where N is th number of particles.

4. Electric and magnetic fields are calculated from the local current following Maxwells equations.

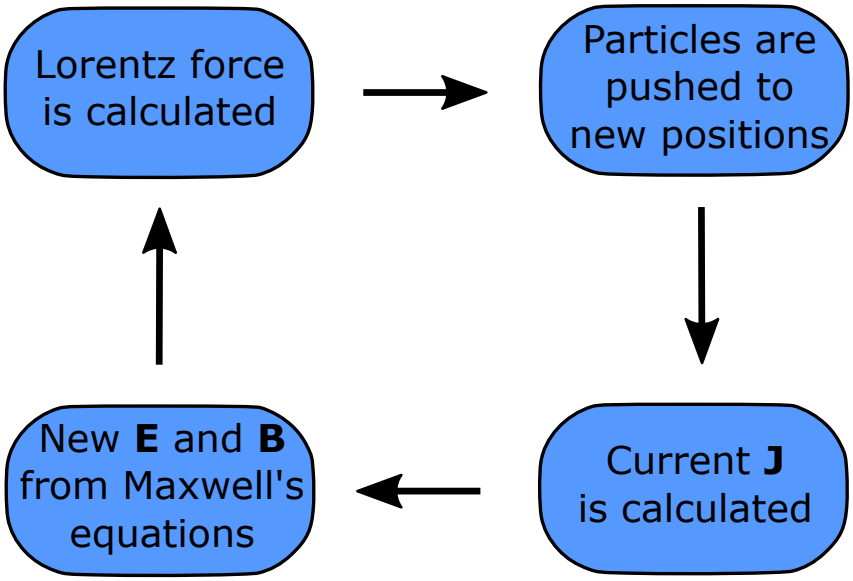

Figure A.1: Scheme of the PIC algorithm.

PIConGPU was used to simulate the plasma formation in the colloidal crystal and here simulation details are discussed. In the PIConGPU simulation we considered a rectangular simulation box. The simulated volume of the colloidal crystal was chosen according to the colloidal particle size ($d = 163$ nm). The simulation box is shown in Fig. A.2 and was $284 \times 163 \times 1280$ nm^3 in $x \times y \times z$ directions ($d \times d\sqrt{3}$ in $x \times y$ direction). The top view on the simulation box is shown in Fig. A.2(a) and two layers of the hexagonal-close-packed colloidal crystal are represented by red and blue color. From Fig. A.2(a) it is clear that such a simulation box is periodic in x and y direction. Therefore, the size of the simulation box was chosen in order to apply periodic boundary conditions on the sides ($x = 0$ nm, $x = 284$ nm and $y = 0$ nm, $y = 163$ nm planes). On the top and bottom of the simulation box additional absorbing layers were introduced. To optimize the simulation process, the simulation box consisted of $128 \times 64 \times 512$ cells in $x \times y \times z$ directions. From that condition, the size of one cell was chosen to be 2.2 nm in x and 2.5 nm in y and z directions. On the top of the simulation box 128 cells or 320 nm were not filled with any colloidal particles. This empty space was introduced in the simulation box to initialize the incoming IR laser.

In order to satisfy Courant Friedrichs Lewy condition [318] the simulations were performed with 4.25 attosecond time increment. Such a time increment allows to resolve the plasma frequency oscillations in the $2.2 \times 2.5 \times 2.5\times$ nm cell size in $x \times y \times z$ directions. The output of the simulation was saved each 5 fs during the first 100 fs and each 20 fs up to 1 ps due to a huge amount of the output data. Simulations were performed using a standard Yee solver scheme, which requires information from the next-neighbor cells [319] and the HDF5 openPMD output [320] implemented in the PIConGPU code.

To simulate the ionisation processes in the colloidal crystal ADK ionisation model

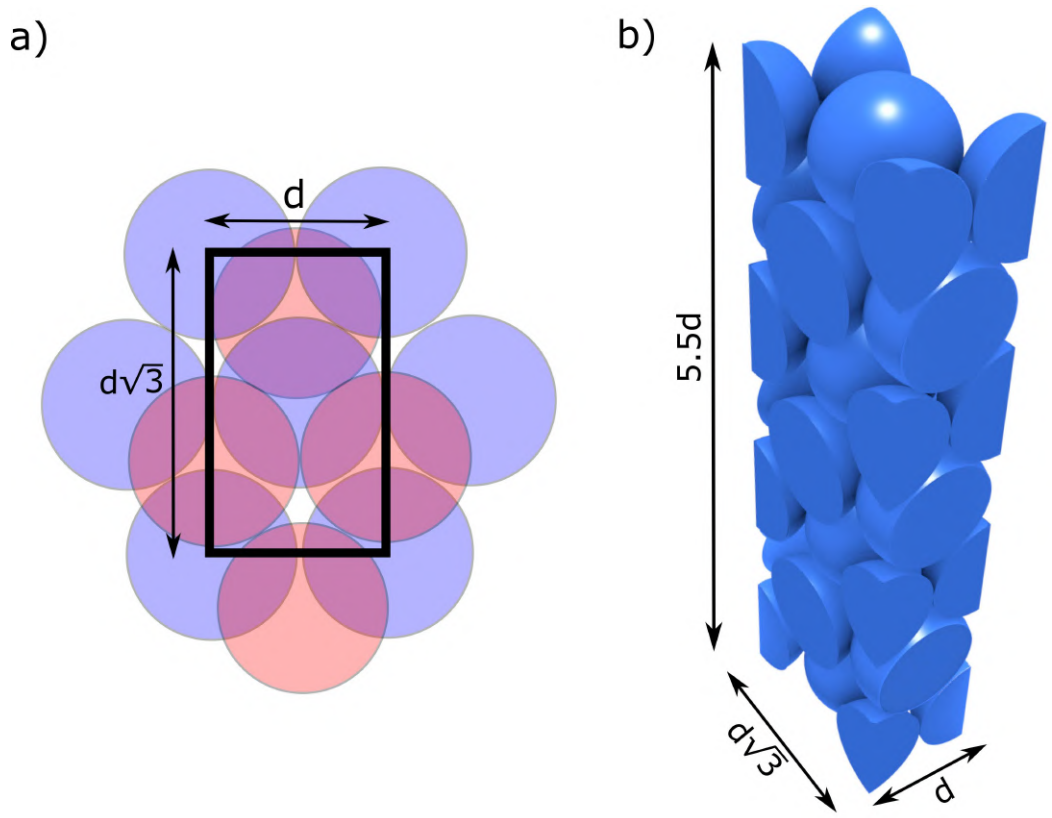

Figure A.2: Simulation cell used in PIConGPU simulations. a) The top view on the simulation box. Two different layers of the hexagonal-close-packed colloidal particles are shown in blue and red color. b) 3D view on the simulation box.

was used for the field ionisation and Thomas-Fermi ionisation model was used for collisional ionisation. The Thomas-Fermi model displays unphysical behavior in several cases (see Fig. 8.5 in Chapter 8), thus the cutoff values were introduced, to exclude some particles from the calculation. For carbon and hydrogen it predicts non-zero charge states at zero temperature, therefore the lower electron-temperature cut-off value should be defined, and in our model it was 1 eV. For low ion densities Thomas-Fermi model predicts an increasing charge state for decreasing ion densities (see Fig. 8.5). This occurs already for electron temperatures of 10 eV and the effect increases with the temperature. Therefore a low ion-density cutoff value of $1.74 \cdot 10^{21}$ ions/cm^3 was used. Also, a cutoff value for super-thermal electrons was introduced to exclude electrons with kinetic energy above 50 keV. That is motivated by a lower interaction cross-section of particles with high relative velocities.

Appendix B

HELIOS simulations

HELIOS is a 1-D radiation-hydrodynamics code designed to study the hydrodynamic evolution of plasmas heated by laser beams or by external radiation sources [313]. This code solves Lagrangian hydrodynamics equations in either planar, cylindrical, and spherical geometries. The equation of state is obtained from Prism Opacity and Equation Of State (PROPACEOS) or SESAME data. The equation of motion is solved for a single fluid (co-moving ions and electrons). Electrons and ions are assumed to have Maxwellian distributions with different electron and ion temperature (two temperature model). The simulated sample may be composed of a single material or multiple layers of materials.

The hydrodynamic simulations were coupled to the plasma PIConGPU simulations in the following way. The 1D projection of the electron energy density profile at 1 ps was obtained from the PIConGPU simulations. The electron energy density distribution was further converted to the electron temperature using PROPACEOS (PRism OPACity and Equation Of State code) data tables (see Fig. B.1). The horizontal axis is the electron internal energy and the vertical axis is the electron temperature. The PROPACEOS data for polystyrene with a typical polystyrene density of 1.05 g/cm^3 is shown by the black dots. This data was fitted with 7th order polynomial function and the polynomial fit is shown by the red line in Fig. B.1. Subsequently, this polynomial function was used to convert the electron energy density to electron temperature. The electron temperature was extended up to 6 µm according to the room temperature conditions (0.025 eV). The ions were assumed to have room temperature.

Hydrodynamic simulations using HELIOS code were performed from 1 to 1000 ps with 1 ps time increment for the 6 µm thick polystyrene colloidal crystals. The boundaries of the plasma were allowed to expand freely. The quiet start temperature was set to 0.044 eV which is equal to the polystyrene melting temperature. The time increment in the HELIOS simulations was chosen according to Courant condition, and other criteria which constrain the fractional change of various physical quantities used in the simulation. The simulation results were saved each 1 ps due to a huge amount of the

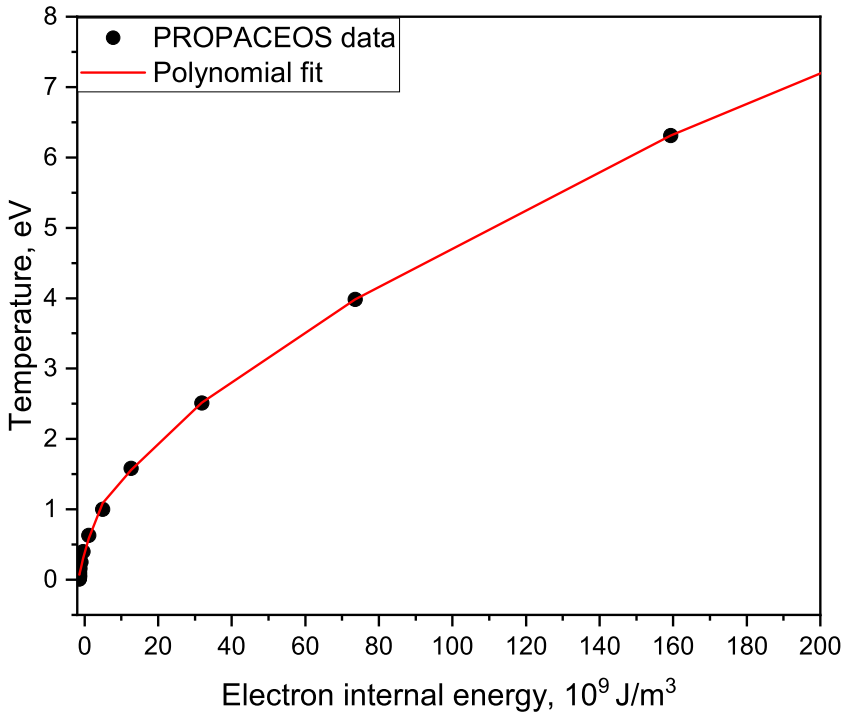

Figure B.1: Polystyrene equation of state obtained from PROPACEOS data tables (black dots) and polynomial fit (solid red line).

output data.